INTERFACE PROPERTIES OF CARBON NANOSTRUCTURES AND NANOCOMPOSITE MATERIALS

A Dissertation
Presented to
The Academic Faculty

by

Dhaval Deepak Kulkarni

In Partial Fulfillment
of the Requirements for the Degree
Doctor of Philosophy in the
School of Materials Science and Engineering

Georgia Institute of Technology
August, 2013

INTERFACE PROPERTIES OF CARBON NANOSTRUCTURES AND NANOCOMPOSITE MATERIALS

Approved by:

Dr. Vladimir V. Tsukruk, Advisor
School of Materials Science and Engineering
Georgia Institute of Technology

Dr. Zhiqun Lin
School of Materials Science and Engineering
Georgia Institute of Technology

Dr. Andrei G. Fedorov
Woodruff School of Mechanical Engineering
Georgia Institute of Technology

Dr. Gleb Yushin
School of Materials Science and Engineering
Georgia Institute of Technology

Dr. Seung Soon Jang
School of Materials Science and Engineering
Georgia Institute of Technology

Date Approved: May 29, 2013

Dedicated to my loving family

ACKNOWLEDGEMENTS

Prof. Tsukruk gave me the valuable opportunity to join his research group when I had no credentials or research background in the field of Materials Science and Engineering and I cannot thank him enough for being compassionate and generous throughout these years. He nurtured curiosity, inspired creativity, and fostered the desire in me towards achieving my goal. During this stint as a graduate research assistant, everyday has been a learning experience and I will cherish these memories for the rest of my life. I would also like to thank Prof. Andrei Fedorov, Prof. Zhiqun Lin, Prof. Seung Soon Jang, and Prof. Gleb Yushin for their helpful feedback, suggestions, and kind willingness to be a part of my dissertation committee.

It is only because of the supportive and congenial nature of the SEMA lab members that my PhD tenure had been a memorable one. Particularly, I would like to thank Prof. Srikanth Singamaneni, Dr. Michael McConney, and Prof. Konrad Rykaczewski for their constant support and guidance. Prof. Srikanth Singamaneni has always been a source of motivation and inspiration and I would like to specially thank him for his support and guidance during the initial years of my Ph.D. I would also like to thank current and former SEMA lab members, Dr. Maneesh Gupta, Dr. Rajesh Kodiyath, Dr. Sehoon Chang, Ikjun Choi, Zachary Combs, and Kesong Hu for their support. Special thanks are due to Songkil Kim for his significant contribution to the work presented here.

I am extremely grateful to my family and friends for their unconditional love and support. Sincere thanks goes to all my friends, Ganesh Narayan, Aashay Shringarpure, Ram Thanumoorthy, Aayush Sharan, Ranbir Jamwal, Praveesh Govindan, and Ajay Seshadri for their moral support over the years.

TABLE OF CONTENTS

LIST OF TABLES

LIST OF FIGURES

SUMMARY

To truly realize and exploit the unique properties of carbon nanomaterials, it is essential to understand, design, and fabricate efficient interfaces and develop techniques which would enable and probe the transfer of charge carriers, phonons, and photons in devices and stress transfer in structural materials. The study presented in this dissertation investigated the different interfaces commonly encountered while fabricating carbon-based devices, monitored the changes in the physical structure and chemical composition of different materials, probed the effect of processing conditions, and developed techniques for optimizing the interface properties which would help in improving the device performance.

Two different interfaces were the focus of study: 1) the interface between disordered amorphous carbon and inorganic materials (metal nanostructures and silicon), and 2) the interface between partially ordered graphene (graphene oxide) and synthetic polymer matrix. Specifically, the uniqueness of this study can be summarized through the following novel findings, fabrication processes, and characterization techniques:

- A simple and efficient process for faster, greener, less-expensive, and highly localized transformation of amorphous carbon nanostructures into graphitic nanostructures using low temperature heat and light treatments was developed for the fabrication of low-resistance interfaces between carbon nanomaterials and inorganic metal surfaces.
- A new protocol for high resolution mapping the charge distribution and electronic properties of nanoscale chemically heterogeneous domains on non-homogeneous surfaces such as graphene oxide was established.
- High strength laminated mechanical nanocomposites based on high interfacial stress transfer between polymer matrices and large area, flat, and non-wrinkled graphene oxide sheets were suggested and demonstrated.

- Scanning Thermal Twist Microscopy – a thermal microscopy based technique was developed and demonstrated for characterizing the thermal properties of homogeneous and heterogeneous interfaces with nanoscale spatial resolution and high thermal sensitivity unachievable using traditional techniques.

We suggest that the understanding of the interface between carbon nanomaterials and organic-inorganic surfaces combined with the fabrication and characterization processes discussed in this study can be important for the addressing some of the challenges facing the integration of carbon-based electronic, photonic, and thermal devices and structural materials.

CHAPTER 1

INTRODUCTION

1.1 Background

Carbon is one of the most widely studied elements to date and can exist in different forms owing to its tendency to undergo three different types of hybridizations; sp^1, sp^2, and sp^3.[1] A wide range of electronic properties ranging from insulating/semiconducting to metal-like (graphite, nanotubes and graphene) can be tuned by adjusting the sp^3/sp^2 content and nanostructure morphologies of carbon materials. In particular, carbon nanotubes and graphene consisting of an sp^2 hybridized carbon structure has attracted enormous attention owing to their unique electronic properties supported by their excellent mechanical and thermal characteristics.[2,3] On the other hand, diamond consisting of all sp^3 bonded carbon atoms is known for its high mechanical strength and wear resistance.[4,5,6]

Carbon materials have always intrigued the minds of researchers for several decades due to their unique structural and physical properties. The last few decades have seen the discovery and emergence of zero-dimensional fullerenes, one-dimensional carbon nanotubes, and two-dimensional graphene.[7] All these materials with thicknesses less than 1 nm have been demonstrated for their unique electronic, optical, thermal, mechanical, and chemical properties. Thus, expectation for improving the performance of electronic devices, efficiency of photovoltaics, heat sinks, charge storage in batteries and supercapacitors, chemical sensors, structural composites, and in bioengineering as scaffolds for bone growth has increased over the years.[8,9,10,11,12,13] Early work in all these areas have demonstrated the working principle and high performance output, however, the issues related with high-purity synthesis with low defects and structural uniformity,

large area assembly over the device substrates, and integration with the existing device fabrication protocol have limited the use of these materials for commercial applications. However, recent advances in large area device fabrication and efforts to address the issues related to integration continue to attract the research community towards these unique materials.

1.1.1 Carbon interfaces in electronic devices

Looking from a fundamental perspective, fabrication of carbon-based electronic devices obviously involves formation of several interfaces between carbon nanomaterial and different surfaces such as metals like copper or gold, semiconductor materials such as silicon, oxide surfaces such as silicon oxide and even synthetic polymers. The efficient transfer of the charge carriers, phonons, and photons across the devices depends on the characteristics of these interfaces. A low resistance contact interface is necessary to avoid current crowding, which could result in a localized heat generation leading to eventual device failure or can increase the power consumption, both of which are undesirable.

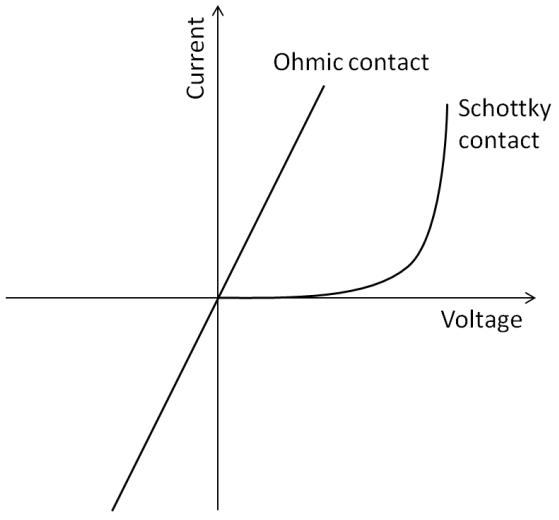

Figure.1.1 Typical current (I) - voltage (V) curves for Ohmic and Schottky contacts

Fabricating an electrical interface requires the knowledge about the work function of the metal and the adhesion of the metal to the underlying substrate. Typically, the metal deposition process on the semiconductor surfaces results in the formation of two types of electrical contacts; Ohmic contact and a Schottky contact (Figure 1.1).[14,15,16]

From an electrical viewpoint, Ohmic contact refers to the formation of an interface between a metal and semiconductor surface such that the applied voltage results in a linear change in the current. On the contrary, Schottky or rectifying junctions are formed if the current-voltage characteristics are non-linear and asymmetric. A Schottky contact can be thought to be a barrier which prevents the flow of charge carriers below certain energy to cross the junction. The formation of these contacts depends on the difference in the work function of the metal and the electron affinity of the semiconductor material. A good match of the work function and electron affinity can offer a minimum barrier for the transfer and result in an efficient transfer of charge carriers across the interface. A Schottky barrier is formed if the metal work function is greater than the work function of an n-type semiconductor or lower than the work function of a p-type semiconductor. Obtaining an Ohmic contact with low resistance is important to exploit the unique properties of carbon nanomaterials for electronic applications.

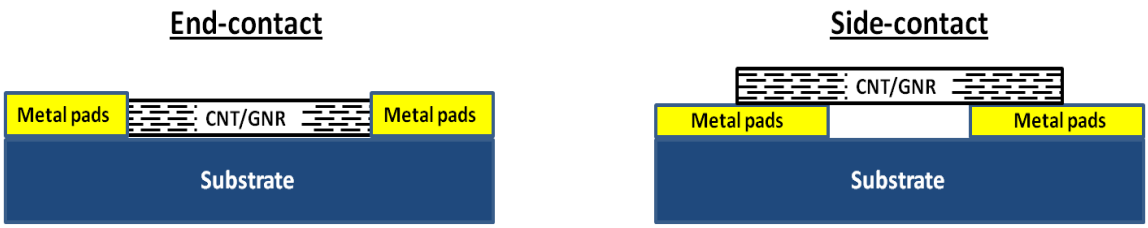

Figure 1.2 “End-contact" and “Side-contact” device configuration for carbon-based electronics

Fabrication of the metal contacts is usually done by lithographically patterning the substrate at desired locations followed by metal deposition via sputtering, thermal evaporation, or chemical vapor deposition.[17,18,19,20] Particularly, for carbon-based electronics, the metal contacts can be termed as "end-contact" or "side-contact" depending on the position of the carbon nanomaterial with respect to the metal surface, as shown in Figure 1.2.[21,22,23]

Depending on the requirement of the lateral dimensions of the contact the lithography patterning can be done either by the conventional photolithography technique or electron beam lithography. Electron beam lithography generates small features and better resolution than optical lithography, however, is limited by its slow speed. Further, the deposition techniques used also have influence the formation of the contact. Typically, sputtering results in rougher metal films than thermal evaporation or CVD deposition and can significantly affect the device performance. All these techniques result in the formation of a conformal contact between the two materials and mostly results in a physical interaction with weak electronic coupling.

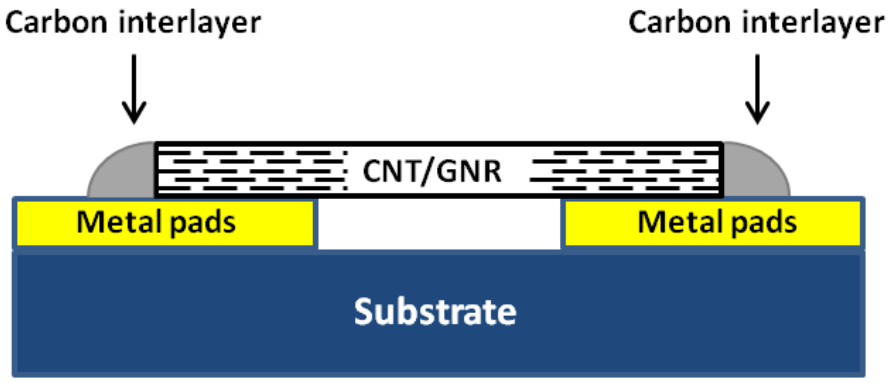

Figure 1.3 Application of a carbon interlayer for lowering the contact-resistance and fabricating a robust interface

The potential of carbon interlayer connection has been demonstrated in different areas, including the establishment of an improved carbon nanotube-metal electrical connection and a robust mechanical interface (Figure 1.3).[24] Localized deposition of nanoscale amorphous carbon deposits can be achieved using Electron Beam Induced Deposition (EBID) technique.[25,26] However, little attention has been dedicated towards the fundamental understanding of the carbon composition itself after EBID deposition. As shown in Figure 1.2, carbon nanotubes (CNT) or graphene nanoribbons (GNRs) aligned between metal pads are known to show a high contact resistance (few GΩs) owing to the weak electronic coupling at the interface. Fabrication of a localized EBID carbon interlayer having a similar work function as the carbon nanomaterials and good interfacial adhesion owing to the similar chemistry at the junction between the carbon nanotube or graphene nanoribbon and metal electrodes can be particularly promising for establishing a low resistance Ohmic connection at the interface (Figure 1.3).[27]

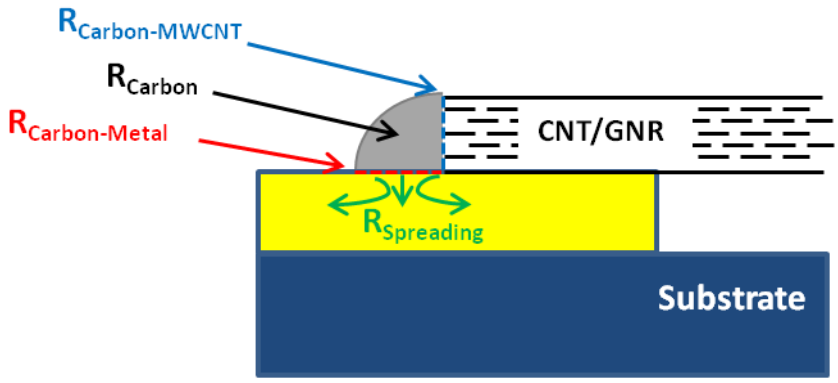

Figure 1.4 Factors contributing towards the contact resistance of CNT/graphene nanoribbon-carbon-metal interface

Figure 1.4 shows a more detailed understanding of the factors contributing to the interface resistance. The spreading resistance depends on the resistivity of the metal and area of the EBID carbon contact. If the contact area is small (< 1 μm^2), the spreading

resistance would be significantly low and can be neglected (< 1Ω).[28] Also, the resistances of a typical interconnect with 5 μm CNT is on the order of few GΩs, while the intrinsic resistance of the CNT itself is only a few kΩs. Thus, initially the resistance of the carbon nanotube itself is negligible in comparison to the total resistance of the interconnect. Further, if one assumes that the contact resistance of one of the ends to be much smaller than the other (for example, of one of the ends has already established a good electrical connection using EBID, then the total resistance of the interconnect reduces to

$$R_{Total} = R_{Contact} = R_{Carbon-MWCNT} + R_{Carbon} + R_{Carbon-Metal}$$

The total resistance of interconnect relies on the contact made by the EBID carbon deposit with the CNT and the metal. This suggests that the composition of the EBID carbon deposits, their structure and dimensions along with their interaction with the underlying metal electrode would have a strong control over the overall performance of the interconnect. Also, this technique can offer an added advantage of establishing a multiple-shell conduction pathway at the interface between CNT or graphene and metal interface for further lowering of contact resistance. Thus, in order to address these possibilities, fundamental understanding of the physical and chemical characteristics of EBID carbon contacts would be of prime importance. As deposited EBID carbon is known to be amorphous with poor electrical conductivity owing to a disordered network of sp^2 bonded carbon. Tuning the structure of the insulating EBID carbon deposits towards highly conductive carbon materials with significant ordering of sp^2 domains will be one of the key factors in lowering the interfacial resistance.

1.1.2 Carbon interfaces in mechanical nanocomposites

On the other hand, mechanical interfaces also form a key role in the fabrication of carbon-based mechanical nanocomposites.[29,30] Carbon nanomaterials offer an advantage

of fabricating multi-functional composites with high electrical and thermal conductivities along with strong mechanical properties. The most important factor is the stress transfer at the interface and the composite will be strong if the transfer is efficient. This requires a strong interaction between the carbon materials and the polymer matrix which can be achieved by means of covalent bonding, electrostatic interaction, hydrogen bonding, or van der Waals interaction. Polymer composites are conventionally fabricated by melt-mixing, laminating, electrospinning, Layer-by-Layer (LbL) assembly, and in-situ polymerization techniques.[31,32,33] High contact surface area and strong interfacial interaction between the carbon nanomaterials and polymer is an important factor for designing a robust composite.

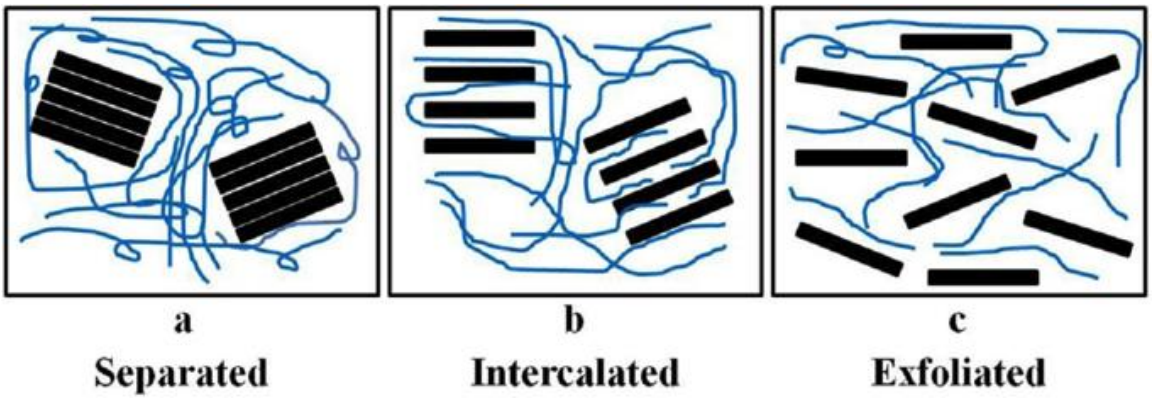

Figure 1.5 Possible dispersion characteristics of filler inside the polymer matrix in a nanocomposite. (a) Separation of the filler due to aggregation, (b) intercalation of the polymer chains inside the filler, and (c) exfoliation of the filler within the polymer with a uniform distribution[34]

Carbon nanomaterials are known for their poor dispersibility in organic solvents, commonly used for polymer processing. Thus, it is difficult to get a good dispersion of carbon nanomaterials inside the polymer matrix.[33] Figure 1.5 shows a schematic of the different scenarios encountered during polymer composite fabrication.[34] Poor dispersion leads to aggregation of the carbon materials in the polymer and results in a weak interface

thereby leading to poor mechanical properties. On the other hand, an efficient intercalation and exfoliation can improve the interfacial surface area and result in a stronger composite. Although intercalation can lead to stronger interaction, it would result in a localized improvement in the properties of the composite. Areas with stronger interaction would show better properties compared to other. However, uniform exfoliation of filler inside the polymer matrix is best suited for improved performance. Further, carbon nanomaterials can be functionalized to ease the dispersion and improve the chemical interaction with the polymer matrix.

The mechanical properties of a composite are judged based on the elastic modulus, tensile strength, elongation, and toughness.[35] Typically, it is difficult to obtain a material exhibiting record values for all these factors. Efforts to improve one of these factors show an adverse effect on the other factors. Thus, efforts are being made to selective improve one or more of these mechanical aspects depending on requirements of the end-application. Some applications demand high strength whereas some applications require high toughness. However, the toughness values are considered to be the important parameter in comparing the properties of different materials since it combines the effect of strength and flexibility. Mathematically, the toughness value is simply calculated by the area under the stress-stain curve. Thus, a material that can withstand a very high stress under maximum elongation will have a very high mechanical toughness. On a macroscopic level, the stress-strain curve can be considered as an effect of the interaction between polymer chains and the filler particles. The mobility of the polymer chains inside the polymer matrix defines the elongation but the interaction and stress transfer efficiency between the polymer chains and the filler material defines the load bearing capacity of the composite. A strong polymer-filler interaction suggests as higher strength but lower elongation. However, a weaker interaction would result in a slippage past the polymer-filler interface and the composite would eventually fail under higher loads.

1.1.3 Summary of carbon interfaces

Thus, in terms of performance issues related with carbon electronics and mechanical composites, the interface plays a key role in dominating the transfer of charge carriers and phonons or transferring the external stress. While the efforts so far have been primarily dedicated to fine tune the device fabrication processes, we address the problem from a different viewpoint. The physical properties (morphology and chemical composition) of the interface, which are often overlooked, are extremely important for fabrication of efficient electronic devices and mechanical composites. EBID is the only method to have a controlled and localized fabrication of nanoscale carbon deposits and the interfacial properties of these amorphous deposits with different organic and inorganic substrates would be a key towards addressing the issue with contacts with high electrical resistance. Also, functionalization of carbon nanomaterials, such as a 2D graphene with a large surface area and understanding the surface properties would be a key towards fabrication of a robust interface for strong mechanical composites. Thus, prior to addressing these issues, in the next sections we will highlight some of the material properties and the briefly introduce some of the studies on carbon based devices and composites.

1.2 Materials

Here, we discuss the different carbon materials of interest with a focus on their structural aspects and chemical composition. The knowledge of these intrinsic properties of carbon materials is essential to address the material change during fabrication and processing and to tune these properties to suit our need. In this section, we give a brief introduction on the properties of ordered carbon materials (CNTs and graphene), and disordered carbon materials (graphene oxide and amorphous carbon).

1.2.1 Ordered carbon nanomaterials

Carbon nanomaterials with a long range structural ordering are considered to be ordered carbon nanomaterials. These include fullerenes, carbon nanotubes, graphite, and graphene. Brief introduction on the structure and properties of CNTs and graphene most relevant to this study are discussed below

1.2.1.1 Carbon nanotubes – structure and properties

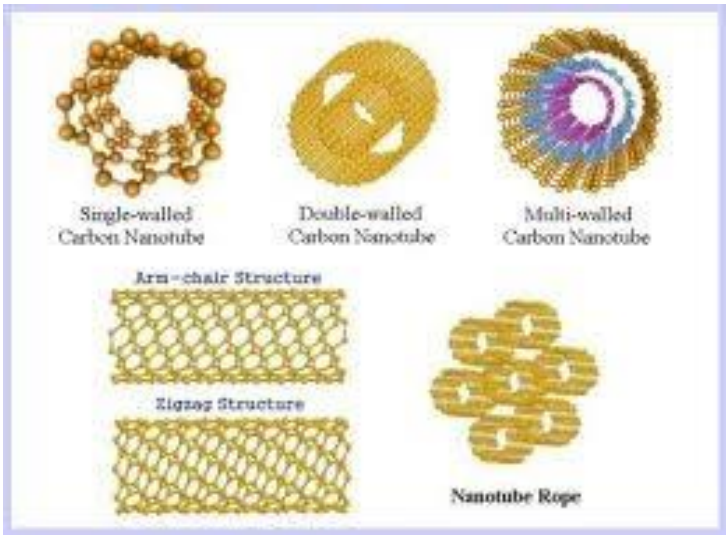

Figure 1.6 Different structural types of carbon nanotubes[43]

Since the first report in 1991, CNTs have been around for a while and have been suggested to be promising for fabrication of high-strength composites, energy and hydrogen storage devices, field emission displays, nanobioelectronics, drug delivery, and high performance semiconductor components and interconnects.[36,37,38,39,40,41,42] CNTs exist in two forms; single walled carbon nanotubes (SWCNTS) and multi-walled carbon nanotubes (MWCNTs) (Figure 1.6).[43] MWCNTs consisting of concentric cylinders of

graphene sheets wrapped into a cylindrical tube are often preferred over SWNTs owing to their multi-channel conduction and simpler manufacturing process.[44,45] CNTs are typically synthesized using carbon-arc discharge, laser ablation of carbon, or chemical vapor deposition over catalytic particles. SWCNTs with diameters ranging from 0.4 nm to over 3 nm and MWCNTs with diameter over 100 nm have been reported in literature.[46,47,48]

CNTs can be either metallic or semiconducting, depending on the chirality of the structure. The synthesis process typically results in a mixed population of metallic and semiconducting tubes with over 2/3rd of the mixture known to be of the semiconducting type.[49,50,51] The electronic properties of perfect MWCNTs and SWCNTs are similar with a nearly one-dimensional electronic structure resulting in a ballistic conduction over the entire length of the tube and high current carrying capacities with no heating.[52] Also, CNTs are known to be stiff with a very high Young's modulus and tensile strength.2[,53,54] Thus, the application of CNTs for the fabrication of multi-functional light structural materials has been an area of intensive study.

1.2.1.2 Graphene – structure and properties

Graphene a monolayer form of graphite, has attracted tremendous attention since its discovery in 2004.[55,56] Graphene, a sp^2 bonded sheet of carbon atoms densely packed in a honeycomb-like crystal, can be thought of as an analog of CNT slit along its length (Figure 1.7).[57] Thus, graphene also shows all the unique electrical, thermal, and mechanical properties exhibited by the CNTs. Intrinsic graphene is considered to be a semi-metal with a zero band gap and has recorded remarkably high carrier mobility at room temperature.3[,58,59] It is highly transparent with a visible light transmission over

97.3%.[60] Further, these properties can be easily modified by strain and deformation making it applicable for a wide range of applications.

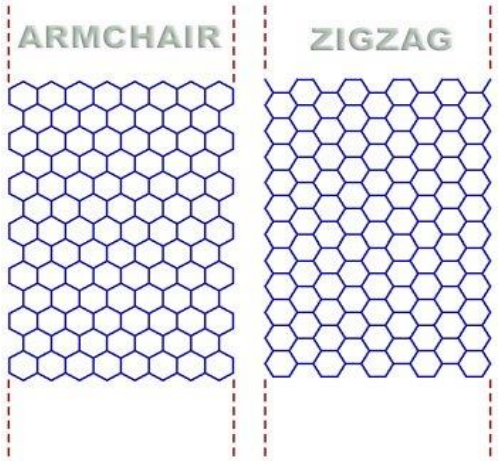

Figure 1.7 Different structural configurations of graphene nanoribbons: arm-chair and zig-zag configurations[57]

Moreover, monolayer graphene flakes can be deposited easily by simple mechanical exfoliation of Highly Oriented Pyrolytic Graphite (HOPG), thereby making it a preferred choice over CNTs demanding similar applications.[55] Till date, the use of graphene has been demonstrated for a number of applications including fabrication of electronic devices, as transparent conducting electrodes, component of photovoltaic devices, chemical and biosensors, supercapacitors, energy storage, optical modulators, and as reinforcement in light-weight composites.[61,62,63,64,65]

1.2.2 Disordered carbon nanomaterials

Carbon nanomaterials with non-homogeneous chemical composition and short range structural ordering are referred as disordered carbon nanomaterials. Graphene oxide and a broad range of amorphous carbon materials come under this category. Brief

introduction on the structure and properties of graphene oxide and amorphous carbon nanostructures are discussed below:

1.2.2.1 Graphene oxide – A precursor of graphene

One of the most common methods for synthesis of large area monolayer graphene sheets in liquid phase is via reduction of graphene oxide.[66,67] Graphene oxide commonly considered as a precursor of graphene has been widely studied and emerged to be a promising material owing to its ease of synthesis, dispersibility in aqueous and organic solvents, and the subsequent large area transfer on different flexible and rigid substrates.[68] A typical graphene oxide flake can be considered equivalent to a graphene flake randomly decorated with defects and functional groups such as carboxyl, epoxy, and hydroxyl over its basal plane (Figure 1.8).[69,70,71] The presence of different chemical functionalities over the surface makes graphene oxide dispersible in different solvents; however, it disrupts the pi-conjugated structure of graphene responsible for its excellent electronic properties. Moreover, the functionalities are randomly located on the surface of graphene oxide.[72]

The functionalization process is difficult to control and generally results in a random distribution of oxygenated functionalities on the surface with a carbon : oxygen ratio of 2:1.[66,73] Graphene oxide is an insulator but can be made conductive by subsequent reduction using hydrazine, high temperature treatments, laser, or flash reduction techniques.[74,75,76] The reduction process removes most of the oxygen functionalities but does not fix the defect sites in the structure. Thus, the conversion of graphene oxide to pristine graphene like structure is never achieved but has been an area of interest. Also, efforts to identify the distribution of functionalities on the surface of graphene oxide are on-going and can be a good resource to develop an efficient reduction process.

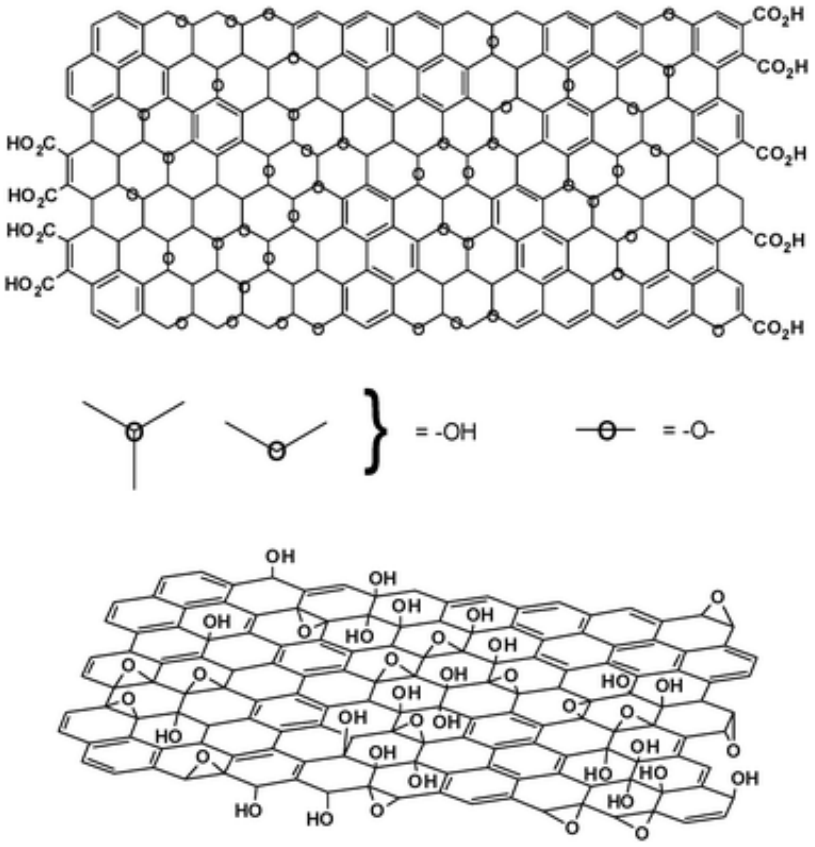

Figure 1.8 Lerf-Klinowski model of graphene oxide[70]

The chemical composition and structure of graphene oxide has been verified using NMR, XPS, UV-vis spectroscopy, and Raman spectroscopy.[68,76] XPS has been shown to be a useful tool to identify the presence of different functional groups and probe the degree of oxidation of graphene oxide. However, most of these optical techniques are resolution limited and provide average information of the sample over a given area. Also, Scanning Tunneling Microscopy (STM) and Transmission Electron Microscopy (TEM) have been used to probe the presence of defects sites on the surface of graphene oxide.[77,78] The studies have clearly shown that the surface of graphene oxide consists of defects due to chemical functionalities as well as bond disorder. STM in particular has clearly probed the different functional groups such as carboxyl, epoxy, and hydroxyl owing to the difference in the electron charge densities over different areas along the surface.

However, STM and TEM require the material to be deposited on special substrates (conductive films or TEM grids) which limits the use of these techniques for characterizing graphene oxide for device applications. Also, the effect of the synthesis parameters on the distribution of functionalities over the surface of individual graphene oxide flakes is yet to be addressed.

1.2.2.2 Amorphous carbon structures

Disordered carbon materials have been of importance for over centuries. They encompass a broad range of materials and exhibit different properties. Disordered carbon materials consist of a mixed proportion of sp^2 and sp^3 domains and are classified as glassy carbon, amorphous carbon, microcrystalline carbon, tetrahedral amorphous carbon, and hydrogenated amorphous carbon depending on the relative ratio (Figure 1.9).[79,80] Also, it is expected that the electronic and mechanical properties of these materials will also depend on the relative sp^2/sp^3 ratio.[81,82] For eg., glassy carbon is metallic with order range of 0.5 nm but disordered over a 3 nm scale whereas amorphous carbon is a semiconductor consisting of sp^2 ordering of over 1.5 nm surrounded by a sp^3 matrix. Hydrogenated amorphous carbon known for its hardness consists of a near equal proportion of sp^2 and sp^3 domains. Hydrogen helps in the stabilization of the sp3 domains, however, inversely affects the hardness of the material.[79]

Disordered carbon films are deposited using plasma chemical vapor deposition, sputter deposition, pulsed vapor deposition, ion-beam deposition, and cathodic arc deposition techniques.[83,84,85,86,87] Different deposition techniques results in the formation of films with different sp^2/sp^3 content. Also, the sp^2/sp^3 ratio can be tuned by applying high pressure or by thermal annealing. The use of these materials have been demonstrated for the fabrication of antireflective coatings for improving the efficiency of solar cells, field-

emission displays, as a coating material for biological implants, micro-electro mechanical systems (MEMS), and as gate insulators in thin film transistors.[88,89,90,91,92]

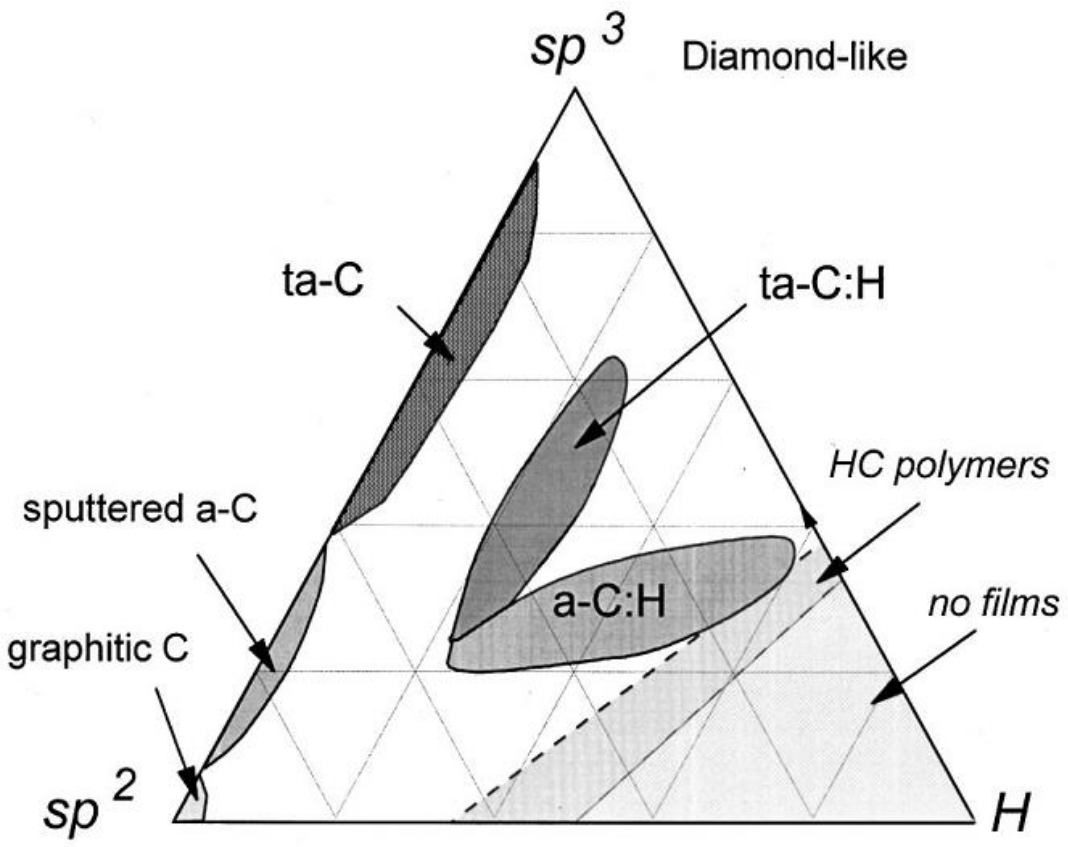

Figure 1.9 Phase diagram of carbon showing the composition of carbon materials with as a function of sp^2, sp^3, and hydrogen content[79]

As mentioned above, EBID is another technique for deposition of amorphous carbon in the form of nanodeposits. This is the only technique where localized fabrication of nanostructures can be achieved with a high degree of spatial control (Figure 1.10). In this process a tightly focused, high-energy electron beam impinges on a substrate and the high-energy primary electrons interact with the substrate to produce low energy secondary electrons (SE) and backscattered electrons (BSE).[93] As demonstrated by Fedorov *et al*., significant electron beam induced heating of the deposit and substrate

occurs only under conditions rarely achievable in SEM, namely when the electron beam currents are higher than microampere.[94]

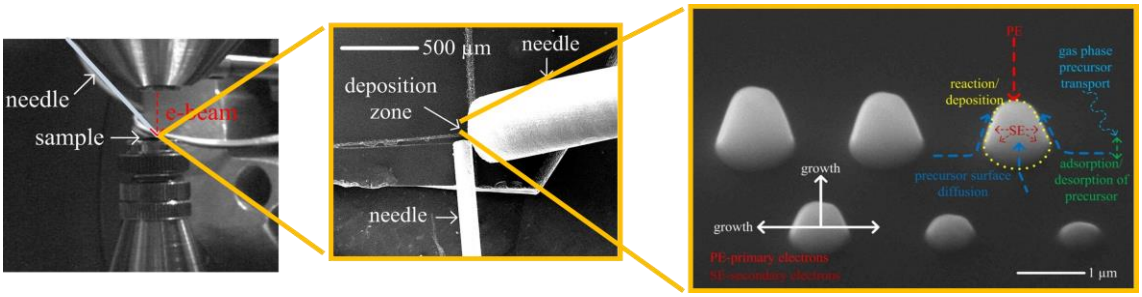

Figure 1.10 Instrumental setup and the corresponding EBID nanostructures[93]

The precursor delivery methods can be subdivided into two categories: gas-phase and surface adsorbed phase delivery.[93,94,95] In the first method, precursor gas is introduced locally near the deposition area via a needle or globally by partial to complete flooding of the reaction chamber. In the second method, surface adsorbed residual hydrocarbons, sometimes supplemented by placing a hydrocarbon, in the vicinity of the deposition area are used as a precursor.[96,97] Since, the surface adsorbed phase delivery method can be used in conjunction with an unmodified Scanning Electron Microscope (SEM), this method has been widely utilized in CNT processing and is the main focus of this work (Figure 1.10).[98] Regardless of the precursor supply method, once adsorbed on the surface the molecules redistribute by surface diffusion. Interactions of adsorbed molecules with backscattered primary and secondary electrons of the appropriate energy result in their dissociation forming a deposit. The vertical growth rates depend on the deposition procedure and the geometry of the deposit and can vary from ~20 nm/min to ~3 µm/min.[99,100] The deposits can grow both opposite to and perpendicular to the direction of the primary electron beam due to electron scattering within the deposit and surface transport of the precursor.[101]

1.3 Applications of carbon nanomaterials

In this section, we briefly describe some of the key research highlights involving the demonstration of carbon nanotubes and graphene for the fabrication of high performance electronic devices and mechanical reinforcements.

1.3.1 Electronic devices

One of the significant bottlenecks realized with the miniaturization of electronic devices is the large resistivity of copper based devices such as interconnects, due to grain and boundary scattering of electrons and electromigration effects as they approach the nanoscale.[102,103] Recent advances in the CNT research have speculated that the issues with down-sizing, electromigration, and breakdown of electronic devices can be addressed based on the ballistic transport properties, high current carrying capacities, and exceptional mechanical strength of the carbon nanotubes.[37,104] However, the ballistic transport property of the CNTs can be envisioned in a device only after the fabrication of contacts with low contact resistance. Also, the overall resistance will be limited by the quantum resistance of a single shell of CNT (~6.5 komhs) but can be lowered further by contacting all the inner shells of a MWCNT.[105,106]

Field-effect transistors (FETs) based on CNTs operating at room temperature were reported back in 1998. Tans *et al.* modulated the conductivity by over five orders of magnitude by applying an electric field to a SWCNT using a back gate.[107] Over the years enormous progress has been made in developing CNT-based FETs by optimizing the gate material and the contact metal to achieve a high performance.[108,109,110] Li *et al.* demonstrated that intermediate and global interconnects based on MWCNTs can outperform both copper and random chirality SWCNT-bundle based interconnects.[111]

Close *et al*. demonstrated GHz-range operation of an integrated circuit with MWCNT interconnects (Figure 1.11).[112]

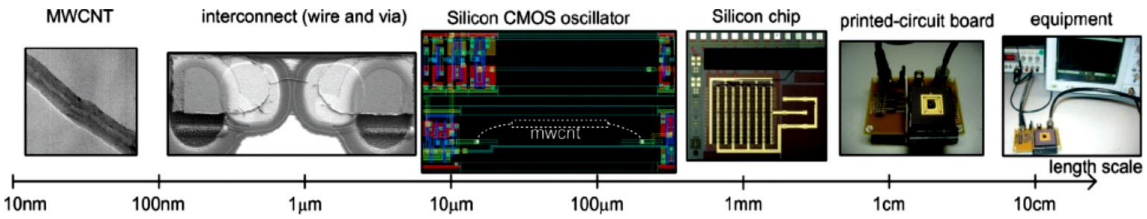

Figure 1.11 Length scale showing the transitioning of MWCNTs into a 1 GHz operating integrated circuit[112]

Pristine graphene is a zero band gap material and not suitable for fabrication of high performance FETs.[113] However, graphene nanoribbons with widths lower than 20 nm opens up a band gap and have been used for FETs.[114] A 15 nm graphene nanoribbon exhibits a bang gap of 200 meV due to the lateral confinement of charge carriers.[115,116] Sub-10 nm graphene nanoribbons are known to be semi-conducting and the FETs showed an on-off ratio of ~10^7 at room temperature. A recent developed in the area of graphene-based transistors was achieved by Avouris *et al.* who fabricated transistors operating at 100 GHz on a wafer-scale epitaxial graphene substrate (Figure 1.12).[117] The performance of the graphene transistors exceeds the state-of-the art silicon-based transistors but requires the use of expensive silicon carbide substrate and temperatures higher than 1350^{o}C, which are incompatible with the existing silicon based technology.[118]

Studies on the use of hexagonal boron nitride as a substrate for fabricating graphene-based electronic devices have also been an area of recent interest owing to its atomically smooth surfaces relatively free of dangling bonds and charge traps.[119,120] Thus, the interface between the graphene and underlying substrate is critical to achieve a high device performance. Graphene is also proposed to be a promising material for

transparent conducting electrode owing to its high thermal and mechanical stability along with its high transparency.[121,122] Easy synthesis, large scale production, and chemical inertness towards water and oxygen makes graphene a viable candidate for fabrication of future photovoltaic devices. [123,124] Reports on the use of graphene for hydrogen storage and energy storage have also been promising.[125,126,127,128]

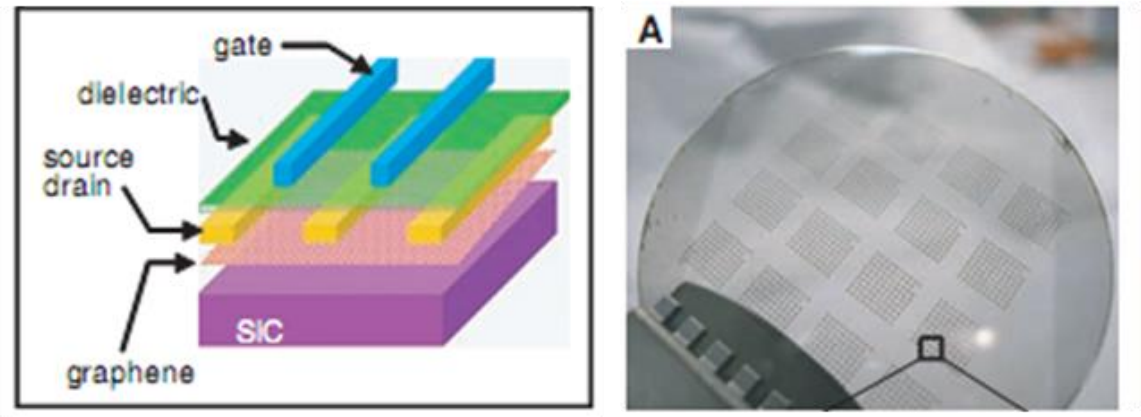

Figure 1.12 Graphene FETs on silicon carbide along with the optical image demonstrating the large-area fabrication[117]

Also, amorphous EBID carbon deposits have been used as soldering material to improve the contact of heterogeneous materials at the interface (e.g metal-metal or metal-semiconductor interface).[24] In addition to this, it can be deposited over a relatively small area (<1000 nm^2) which makes it important for nano-scale patterning of surfaces and in electronic circuits, where localized fusion of the metal joints is required (Figure 1.13).[95,129,130,131] But, as deposited the EBID carbon is amorphous and has low electrical conductivity, thus limiting its use in electronic circuits as materials for interconnects.[27] Thus, post-deposition treatment, including microstructure modification (dehydrogenation and residual stress relaxation) and directed phase transformation (i.e., towards much higher electrically conductive graphitic phase) is required after EBID process.[132]

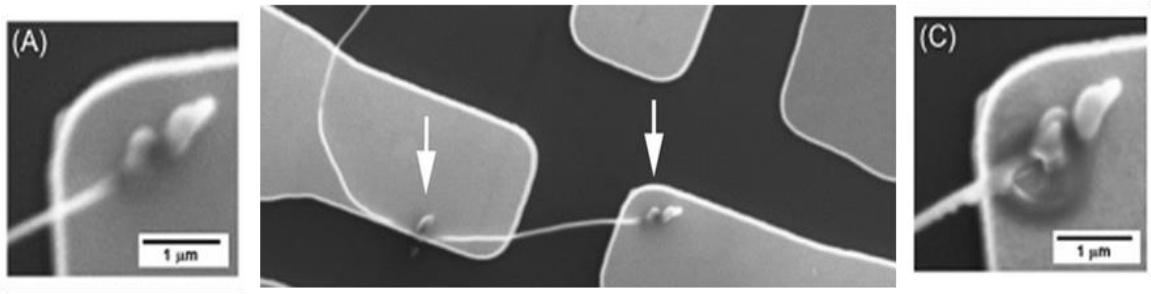

Figure 1.13 Application of EBID carbon deposits as soldering joints to carbon nanotubes[129]

Studies involving the transformation of amorphous carbon to graphene have also been reported in literature. This transformation process typically involves subjecting the amorphous carbon films to high temperature and pressure.[133] Javey *et al*. reported a metal-catalyzed transformation of amorphous carbon films deposited on a silicon oxide surface to graphene.[134] This process was further developed to fabricate a graphitic interlayer to carbon nanotubes for lowering the electrical contact resistance.[135] A catalyst-free process for the transformation of amorphous carbon to graphene by joule heating has also been demonstrated recently.[136] Thus, amorphous carbon has emerged to be a promising material for the fabricating as well as improving the performance of electronic components and also serves the purpose of a chemically inert protective coating.

1.3.2 Structural reinforcements

Reinforcement of carbon nanomaterials have been known to increase the strength and toughness of the polymer matrix by absorbing the strain energy due to their high flexibility during loading.[137,138] CNTs can offer multifunctionality to the composite owing to its unique electrical and thermal properties.[139,140] Several studies have been reported on the use of carbon nanotubes as a filler material for polymer

nanocomposites.[141,142,143,144] MWCNT-PVA composites were reported by Shaffer and Windle. However, the stiffness and the elastic modulus of the composite were lower than the expected values for CNT-based composities. This was attributed to the poor stress transfer between the CNTs and the polymer matrix. MWCNT-PS composites showed improved mechanical properties with the Young's modulus increasing from 1.9 to 4.5 GPa with the increase in the MWCNT content.[145] However, the dependence of the tensile strength on the loading fraction was more complex with the lower filler concentration adversely affecting the mechanical properties of the polymer matrix.[146] In all these studies, the interfacial properties between the carbon nanotubes and the polymer matrix were found to significantly affect the composite performance and have been an area of interest for several years.

Graphene being mechanically robust as well as electrically conductive makes it an ideal filler material for fabrication of multi-functional polymer composities.[147,148] Graphene has been included in a variety of polymer matrices such as epoxy, polystyrene, polyaniline, nafion, and poly (3,4-ethyldioxythiophene).[149,150,151] The percolation threshold, conductivity, and mechanical properties of the composites were tested for applications including supercapacitors, transparent conducting electrodes, gas barrier membranes, and biosensors.[152,153,154,155] However, improved performance of the nanocomposite requires efficient dispersion of the graphene inside the polymer matrix without aggregation. Graphene being inert to most of the solvent and the strong van der Waals interaction between the graphene layers in graphite makes it difficult to disperse in the commonly used organic solvents and also in the polymer matrices. Thus, efforts to decorate the surface of graphene with different functionalities such as hydroxyl, epoxy and carboxyl group for subsequent functionalization such as amidation of carboxylic groups, or nucleophilic substitution to epoxy groups are on-going for improving the dispersibility and interaction with the polymer matrix.[148,153,156]

1.4 Challenges in integrating ordered carbon nanostructures into devices and nanocomposites

Although studies have been reported on the application and performance of electronic devices and mechanical composites based on these carbon materials, several fundamental limitations are still in the way of applying these materials on a real-device platform.[55,157] Below, we address the critical issues, some of the possible solutions, along with some of the opportunities for addressing these issues.

1.4.1 Electronic device fabrication

Firstly, it is difficult have a controlled, high-density, preferential, and defect-free growth of carbon nanotubes. CNTs are typically grown in a CVD process on top of metal catalysts.[37,158,159] The chirality of the CNTs depends on the metal catalyst used and control over the process is yet to be achieved. Two-thirds of all CNTs obtained are known to show a semiconducting behavior whereas only one-third are metallic in nature.[160,161] Separation of the metallic from the semiconducting types involves selective functionalization with an organic molecule or the use of surfactants.[162,163,164] Further, purification of CNTs to remove amorphous carbon and catalyst particles results in the introduction of additional functionalities on the surface.[165,166] These techniques introduce defects in the CNT structure and adversely affect the electronic properties, thereby reducing the device performance

Also, graphene can be incorporated in the form of few-layer or multi-layer graphene nanoribbons (GNRs). Few-layer arrangements of GNRs can significantly reduce the capacitance and electrostatic coupling between adjacent interconnects. The reduction in capacitance helps to reduce the delay and power dissipation of local interconnects. This arrangement is particularly interesting for local interconnects in which the delay is

dominated by capacitive loading and not resistivity. However, wafer-level synthesis of high quality graphene with temperatures compatible with the CMOS technology still remains a major challenge. Also, resistance of narrow GNR is sensitive to edge quality because electrons interact with the edges frequently when the GNR width becomes comparable to the intrinsic mean free path of non-patterned 2D graphene.[167,168]

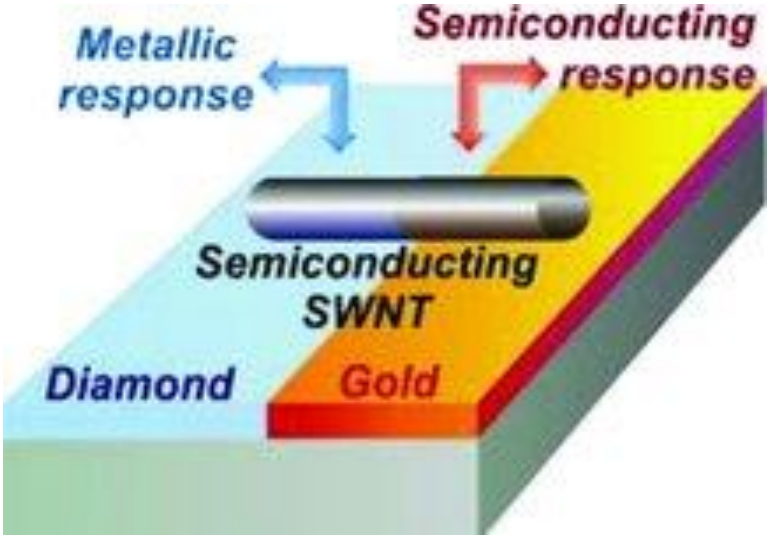

Figure 1.14 Effect of the contact metal on the electrical characteristics of CNT[183]

Several methods for production of graphene have been reported in literature. Single-layer graphene has been generally prepared by micromechanical exfoliation of highly oriented pyrolitic graphite (HOPG).[169] Large area graphene sheets have been prepared by epitaxial growth on insulator surface (such as SiC), chemical vapor deposition (CVD) on top of copper or nickel and arc discharge of graphite under suitable conditions.[170,171] Also, liquid phase exfoliation of graphite in different solvents has been reported. However, the yield of monolayer graphene is very low and not suitable for practical device applications.[172,173]

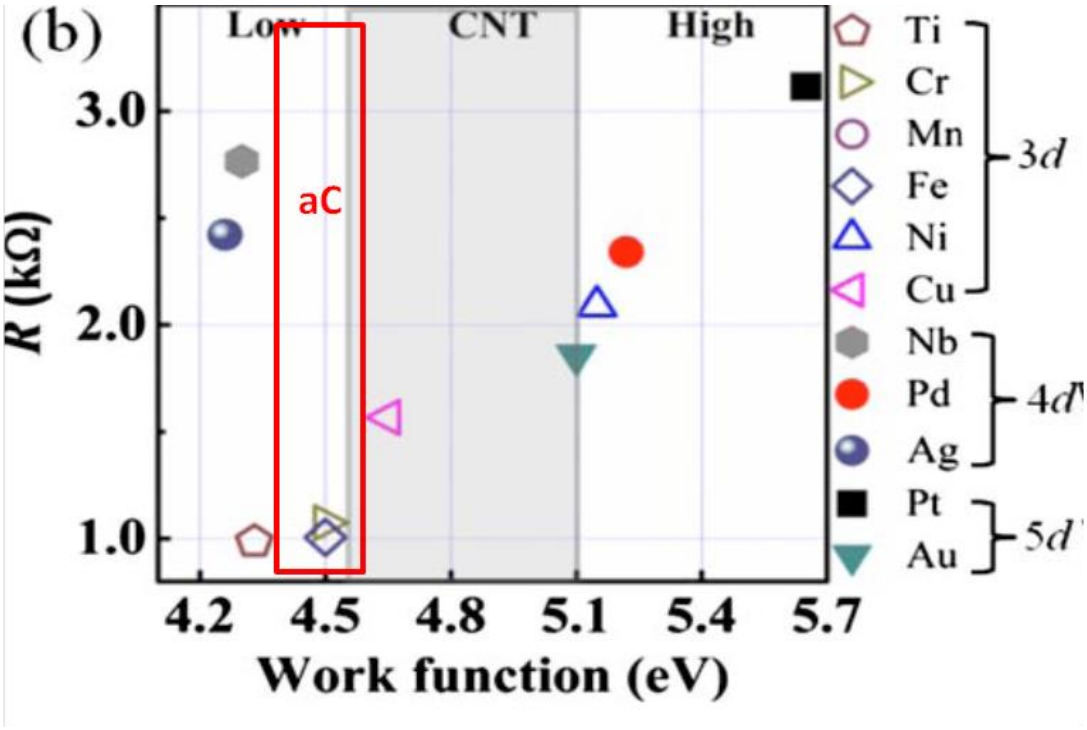

Figure 1.15 Work function of different metals commonly used for fabricating contacts to carbon nanomaterials[182]

Further, it is important to establish low resistance contacts between the CNTs and metal using methods which would be compatible with the existing semiconductor processing technology.[174,175,176] In the case of MWCNTs based devices, establishment of electrical connection with inner shells of the tube poses an additional challenge.[177] Several groups were able to demonstrate very low contact resistance in vertically aligned or free-standing MWCNTs.[178] However, the methods used involved dipping the ends of MWCNTs in a liquid metal or by growing from preformed catalyst nanoparticles which limits the control over the orientation of the tube and are difficult to practically implement in 'on-the-substrate' configuration.[177]

In this type of device geometry, methods such as Electron Beam Lithography (EBL) of metal pads, joule heating, and gold nanoparticle ("nano-ink") suspensions deposition have been applied for lowering of the contact resistance.[179,180] In application of these methods it is difficult to establish contact with the inner shells of tube because the conductor deposition occurs predominantly in the vertical direction. In addition these methods produce side-contacted rather than end-contacted CNT-metal geometries, which according to Tersoff *et al.* results in a weak electronic coupling at the Fermi surfaces and thus a higher intrinsic contact resistance.[181]

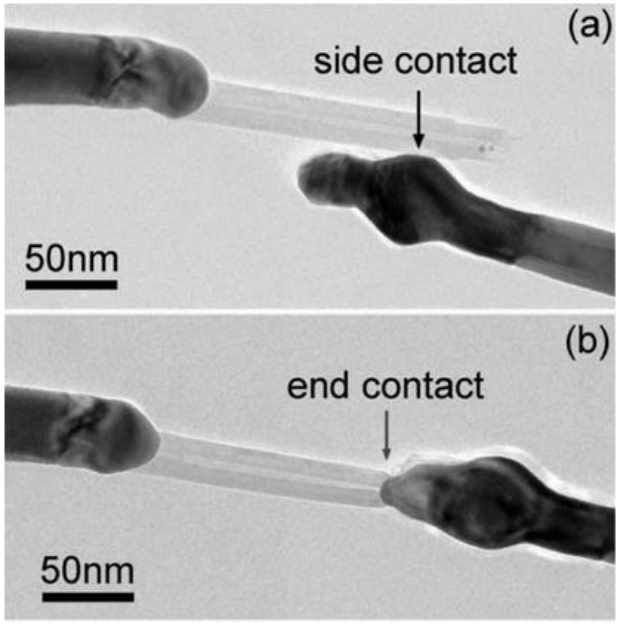

Figure.1.16 Fabrication of side-contact and end-contact to MWCNTs by fusing the ends using joule heating[185]

Two major considerations while selecting an interface material are the adhesion properties with the different surfaces and the work-function difference with the carbon materials.[16,182]. Different metals have different adhesion properties owing to the difference in the surface energies. For eg., gold typically binds weakly with the silicon oxide surface whereas chromium adheres well with both these materials. Thus,

chromium is used as an adhesion layer to fabricate a gold contact on a silicon oxide surface. Moreover, it is essential to have a good match between the work function of the metal and the carbon materials in order to have a good electron transport across the junction. As shown in figure 1.14, the interaction between the CNT and the substrate plays an important role in tune the electrical behavior of the device.[183] Typically, carbon materials like CNTs have a work function in the range of 4.7-5.1 eV. Thus, metals such as titanium (Ti), chromium (Cr), copper (Cu), and gold (Au) are considered to be form a good electrical contact across the interface (Figure 1.15).

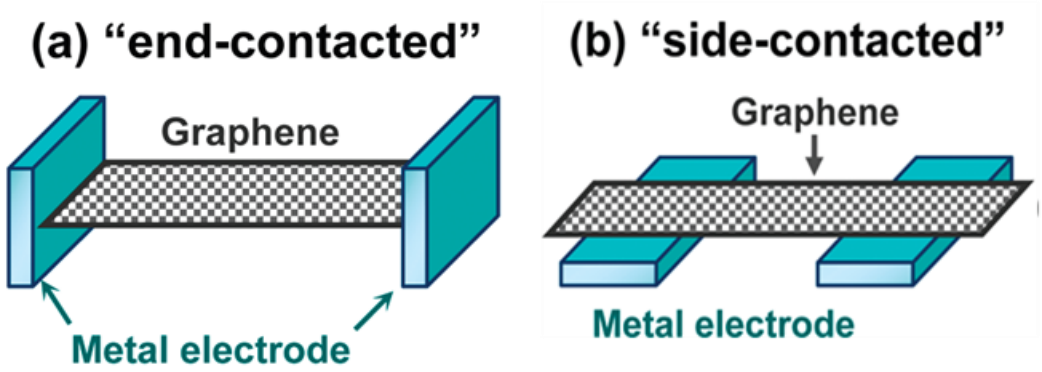

Figure 1.17 Different contact geometries for graphene-based devices[184]

For electronic applications, the qualities of the contact at the interface are judged by the contact resistance values. Efforts to lower the contact resistance at the interface have been of prime interest and several studies and techniques have been reported in literature.[181] The conventional techniques for contact fabrication discussed in the earlier section results in the formation of a physical contact to the carbon materials. This results in a weak electronic coupling at the Fermi surfaces and a high electrical resistance at the interface. For e.g., commonly used e-beam lithography technique for fabricating metal contacts to a multi-walled carbon nanotube results in the connection to the outer shell

only and all the inner shells are electronically decoupled and do not contribute to the conduction.

Several techniques have been demonstrated for establishing a good electrical contact and lowering the resistance at the CNT-metal interface. The configuration of the CNT-metal contact has also been demonstrated to play an important role in the device resistance.[184] Bando *et al.* demonstrated a side contact and end contact geometry of the carbon nanotube-metal interface obtained by fusing the open end of the carbon nanotube with tungsten via joule heating in an SEM chamber (Figure 1.16).[185] The resistance for the end contact geometry was reported to be over an order of magnitude lower than the side contact geometry. Also, simulation studies have been reported for understanding the effect of side-contact and end-contact geometry for fabricating graphene devices (Figure 1.17). Even in the case of graphene the end-contacted geometry is expected to have a lower interfacial resistivity. However, end-contacted geometry with a low interfacial resistance is difficult to fabricate using conventional metal deposition techniques and the techniques mentioned above cannot be applied for fabricating contact on the substrates used for electronic devices.

1.4.2 Structural reinforcement materials - Role of interfaces

On the other hand, the properties of the interfaces also play an important role in enhancing the mechanical properties of composites. Interfaces transfer the stress applied to filler material in the composite and the transfer relies on the strength of the interfaces. Typical filler materials include nanomaterials such as metal nanoparticles, clay, silica, CNTs, and graphene.[186,187,188,189] It is expected that the strength of the filler material would dominate the properties of the composite material but in fact, it is the interface between the filler and the polymer matrix which controls the mechanical properties.

Carbon nanotubes have been known for their exceptional strength with a tensile strength of 50 GPa. However, the composites based on carbon nanotubes reached a tensile strength of only 220 MPa.[190]

Carbon nanomaterials are typically difficult to disperse in the polymer matrix and results in the formation of a weak interface and aggregation leading to poor mechanical properties.[191,192] Several studies on functionalization of the carbon materials to improve the dispersion and interaction with the polymer matrix have been reported. However, the properties of these composites still fall short of the expected numbers. Carbon nanomaterials are promising materials for the fabrication of robust composites. Theoretically, it is not possible to achieve a complete stress transfer across the interface but fabrication and designing of a strong interface for efficient stress transfer is essential to maximize the composite strength.[137,193]

Currently, multifunctional nanocomposites with improved mechanical performance are primarily fabricated by adding carbon nanotubes,[190,194] inorganic nanoparticles,[186,188] and metal nanowires.[187,195,196] However, further development is hindered due to poor dispersion of these reinforcing nanostructures in the polymer matrix. Inorganic materials such as clay and metal nanoparticles form a poor interface owing to their lack of surface functionality. Clay obtained in the form of inter-lamellar sheets is known to be an excellent filler for applications requiring reduced permeation to atmospheric gases and moisture, e.g., food packaging. However, it difficult to uniformly disperse the non-functionalized clay nanosheets in polymer matrices and the composite thus obtained exhibits a very little improvement in the mechanical properties.

1.5 Motivation

Fabrication of high performance carbon-based devices involves formation of several heterogeneous interfaces between the carbon nanomaterials and organic or inorganic surfaces. In order to exploit the unique properties of these carbon materials, fabrication of a low-resistance electrical interface for efficient charge and phonon transfer and a robust mechanical interface for stress transfer is of prime importance.[197] Conventional metal deposition techniques results in the formation of an interface with high electrical resistance between the carbon nanomaterials and the metal electrode. Although several techniques have been demonstrated to lower the interfacial resistivity, they are either nor reliable or not applicable for 'on-substrate' configuration. Also, commonly used techniques for fabricating carbon-based nanocomposite result in the formation of poor polymer-filler interfaces with weak mechanical properties.

It is well established that different materials and techniques can be used for the contact fabrication; however the performance of the device would be dominated by the properties of the interface and needs to be understood to achieve a high performance output.[198,199] Carbon nanostructures with tunable chemical composition at CNT/graphene-metal interface can offer an alternative to control and lower the interfacial contact resistance. In this regard, EBID technique offers an advantage over conventional technique and can be used to fabricate a localized contact with high precision at the CNT/graphene-metal junction and resolve the issue of high interfacial contact resistance.[129,200,201,202] However, as deposited EBID carbon are disordered amorphous nanostructures with a high sp^3/sp^2 ratio resulting in a low electrical conductivity. This offers an additional advantage of tuning the sp^3/sp^2 ratio and modulating the work function to create an interface with Ohmic behavior.

Further, the effect of fabrication and processing conditions on the morphology and chemical composition can be critical in tailoring the electrical and mechanical aspects of the deposits. Transformation of these amorphous carbon nanostructures of different shape and sizes with high sp^3/sp^2 contact into graphitic structures with predominantly sp^2 fraction on top of all sp^2 carbon nanomaterials can be a means of forming a robust interface with strong electrical coupling and lower resistivity. Typically, transformation of amorphous carbon films requires high temperature treatment not suitable for 'on-substrate' configuration. Thus, it is essential to develop the deposition, fabrication, and integration processes to be compatible with the existing semiconductor processing technology. Effect of the substrate on the transformation of the amorphous carbon and understanding the structural-property relationship for improving the interfacial electrical conductivity is a fundamental task to validate the use of this novel fabrication technique for electronic applications.

On the other hand, graphene can be used for fabricating a robust mechanical interface for efficient stress transfer in a nanocomposite. Graphene with a high surface areas and similar mechanical properties to carbon nanotubes is considered to be efficient filler for fabricating strong structural composites. However, it is difficult to exfoliate graphite and disperse graphene in aqueous or organic solvents, commonly used for fabricating polymer composites. Thus, graphite is typically subjected to strong oxidation which results in the formation of different oxygen functionalities on the surface and helps in the exfoliation and dispersion. This exfoliated and oxygenated graphene, also known as graphene oxide can help in fabricating a mechanically robust polymer nanocomposite via formation of a robust graphene oxide-polymer interface. Functionalization of graphene surface for improved interaction with the polymer matrix also necessitates the understanding of the composition and the distribution of functional groups along the surface of graphene oxide and will be addressed in this study.

Graphene oxide nanocomposites with thicknesses on the order of few microns were found to be robust and exhibited interesting physical properties including, good electrical and thermal conductivity and controlled electron transport.[149,203,204,205,206] Several studies have been reported on the use of graphene oxide as a filler material for fabricating a multi-functional composite. Though these nanocomposites show a significant improvement in their mechanical properties, they still fall short of the expected theoretical numbers. This can be attributed to the weak dispersion and interaction between the graphene oxide flakes and the polymer matrix resulting in a weaker stress transfer across the polymer-graphene oxide interface.

Overcoming this critical limitation primarily relies on obtaining laminated and un-crumpled sheets of graphene oxide finely dispersed into polymer matrix. Maximum interaction can be achieved by increasing the interfacial contact areas between the filler and the polymer matrix. This can be accomplished by precisely sandwiching and stacking the flat graphene oxide sheets between the polymer layers. This also ensures uniform properties along the surface of the resulting composite. Even though graphene shows excellent intrinsic properties, the best among the known reinforcing agents, its full potential is yet to be witnessed. Efforts to improve the interface between uncrumpled graphene oxide sheers and the polymer matrix to fabricate a robust polymer nanocomposite material would be an essential part of this study.

CHAPTER 2

RESEARCH GOALS, OBJECTIVES, AND DISSERTATION OVERVIEW

2.1 Goals

The goal of the proposed study is to ***facilitate the fabrication of low-resistance electrical contacts*** via comprehensive understanding of the interface properties between ordered and disordered carbon nanomaterials and inorganic surfaces for efficient transport of charge carriers, phonons, and photons across the junction, as well as, ***to understand, design, and fabricate a mechanically robust interface*** between carbon nanomaterials and organic surfaces for efficient stress transfer in structural nanocomposites.

Thus, in an effort to address the electrical interface and mechanical interface separately, the study has been divided into two parts. In the first part, amorphous carbon nanostructures will be the prime materials of this study and addressing ***the physical and chemical characteristics*** of these nanostructures fabricated on different substrates and their ***transformation from amorphous to crystalline state*** under different processing conditions is the key area of focus. In the second part, the morphology, ***surface functionality, and chemical composition*** of individual graphene oxide sheets will be ***locally and globally probed with high precision*** and the knowledge obtained will be directed towards ***designing and fabrication of a strong interface*** between graphene oxide and synthetic polymer in order to fabricate mechanically tough, free-standing polymer nanocomposites.

2.2 Objectives

In this comprehensive study, the two tasks will be accomplished through the following specific ***technical objectives***:

Task 1:

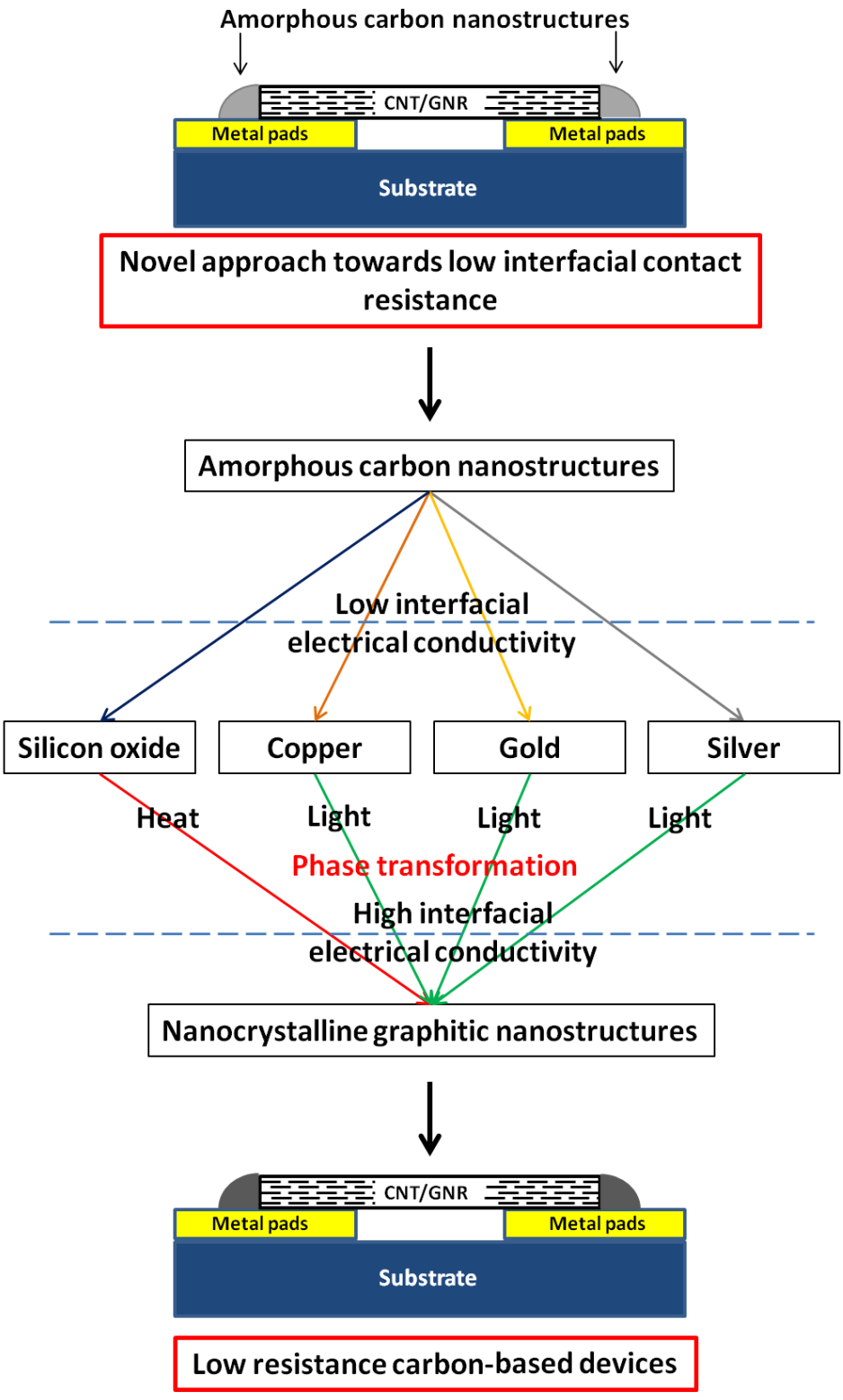

Figure 2.1 Motivation, goals, and objectives of task 1

- *Fabrication of amorphous carbon nanodeposits under different conditions and addressing the effect of e-beam deposition on the morphology, microstructure, and composition on these nanostructures.*
- *Effect of temperature and processing conditions on the physical state and chemical composition of amorphous carbon nanostructures of different sizes and geometries.*
- *Fabrication of amorphous carbon nanostructures on different metal and semiconductor substrates and addressing the effect substrate composition on the morphology, microstructure, and composition.*
- *Understanding the optical properties of the metal surfaces and development of a localized low temperature process for inducing the phase transformation of amorphous carbon structure via surface plasmons induced heating effect.*
- *Development of a highly sensitive probing technique for mapping the localized nanoscale thermal characteristics of the different materials.*
- *Application of the established protocols for understanding the physical state and composition of amorphous carbon towards lowering the contact resistance of CNT/Graphene-metal interface .*

Task 2:

- *Oxidation of graphite for synthesis of graphene oxide and assembling a monolayer over large areas on different substrates along with an extensive characterization of surface morphology and chemical composition.*
- *Establishment of Electrostatic Force Microscopy - an Atomic Force Microscopy (AFM)-based technique, to locally probe the functionalized domains on the surface of graphene oxide assembled over a device-based substrate and compare it with other AFM-based techniques.*

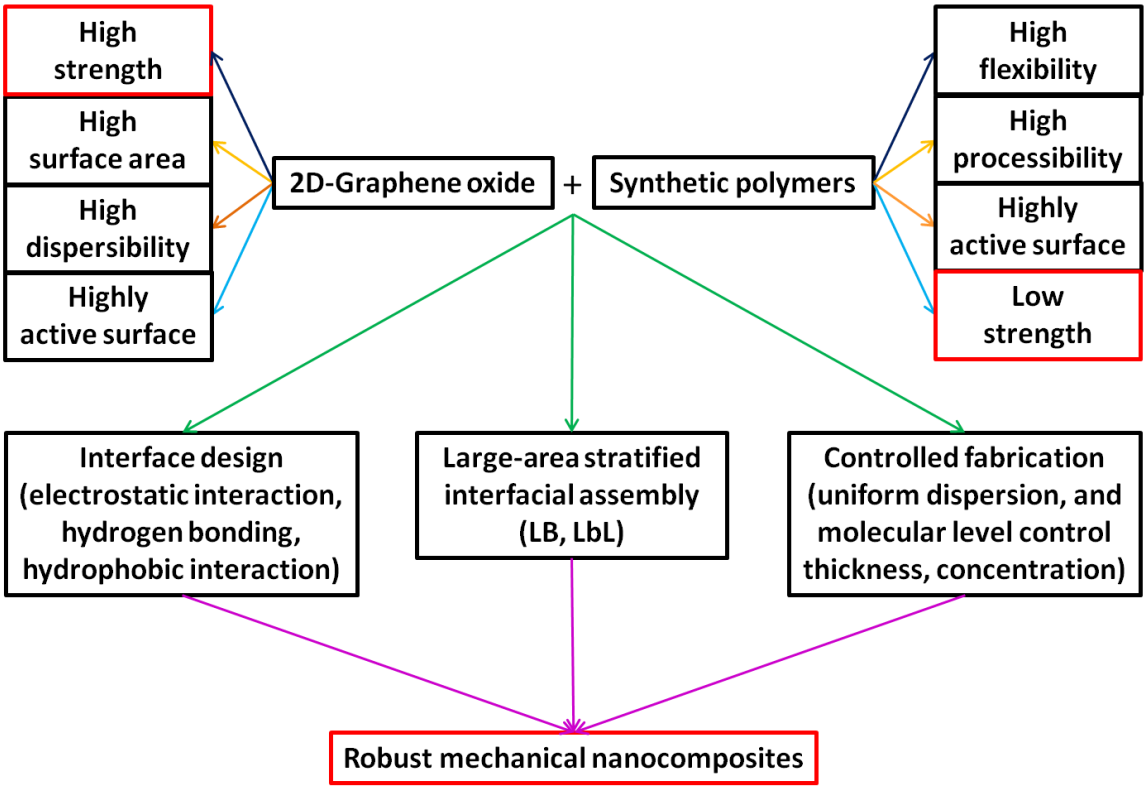

Figure 2.2 Motivation, goals, and objectives of task 2

- *Address the effect of the external environment while imaging of oxidized domains on the surface of graphene oxide and monitor the effect of chemical reduction on the surface composition of graphene oxide over time.*
- *Fabrication of a mechanically robust graphene oxide-polymer nanocomposite via formation of a strong interface aided by the presence of oxygenated functionalities on the surface of graphene oxide.*

Formation of heterogeneous interface is unavoidable during electronic device and mechanical composite fabrication. Efforts to understand the functionality of the interface and tune it to suit the need using techniques which would not interfere with the other fabrication processes is essential to develop a device with improved performance. The two tasks described in this study highlights the properties of the interfaces formed

between amorphous and crystalline carbon nanomaterials and different substrates commonly encountered during device fabrication.

The significance of this study is that, first, we show that the properties of the interface formed between carbon nanomaterials such as amorphous carbon and different inorganic substrates such as metals and silicon oxide, can be locally probed and modulated using techniques compatible with the semiconductor processing. This includes methods to characterize and modulate the morphology and chemical composition of carbon nanomaterials, transformation of amorphous carbon to nanocrystalline carbon, as well as development of a novel technique to probe the nanoscale thermal characteristics of different materials.

Second, the surface chemical composition of graphene oxide was locally probed using a novel technique and used towards designing and fabricating a mechanically robust polymer nanocomposite via improvement of the graphene oxide-polymer interface. This includes characterization of morphology, composition, and determination of defects on the graphene oxide surfaces which could act as anchor sites for improving the interaction with the polymer matrix followed by the fabrication of a layered hierarchical structure for improved strength and toughness.

2.3 Organization and Composition of Dissertation

Chapter 1 is a critical review of problems facing the miniaturization of electronic devices and nanocomposite materials, prospective materials solutions along with the challenges limiting their use. This chapter includes a synopsis of ordered carbon materials (CNTs and graphene) and disordered carbon materials (graphene oxide and

amorphous carbon), their application in electronic devices and mechanical composites, issues with their integration, and motivation for this study.

Chapter 2 includes a concise description of the goals and technical objectives of the work presented in this dissertation. Furthermore, it provides a brief overview of the organization of the dissertation, with brief descriptions of the contents of each chapter.

Chapter 3 includes the experimental techniques that played a critical role in the studies presented in this dissertation. It includes substrate preparation, materials synthesis, fabrication, and characterization techniques. Substrate preparation and materials fabrication processes include cleaning of silicon substrate, sputter deposition of metal nanostructures on silicon substrate, synthesis of graphene oxide, fabrication of amorphous carbon nanostructures, layer-by-layer (LbL) technique, and Langmuir-Blodgett (LB) assembly. Characterization techniques include atomic force microscopy for measuring topography, mechanical properties, and electrical conductivity of the sample, Raman spectroscopy and X-ray photoelectron spectroscopy to understand the chemical composition, and techniques for measuring the mechanical properties of free-standing nanocomposite films. In several subsequent chapters the experimental techniques are supplemented with specific protocols used for the particular studies presented.

Chapter 4 relates to the thermally-induced phase transformations of amorphous carbon nanostructures by correlating the changes in its morphology with internal microstructure by using combined AFM and high resolution confocal Raman microscopy. These carbon nanodeposits can be used to create heterogeneous junctions in electronic devices commonly known as carbon-metal interconnects. We compared two basic shapes of amorphous carbon deposits: dots/pillars with widths from 50 to 600 nm and heights from

50 to 500 nm and lines with variable heights from 10 to 150 nm but having a constant length of 6 μm. We observed that during thermal annealing, the nanoscale amorphous deposits go through multi-stage transformation including dehydration and stress-relaxation around 150^{o}C, dehydrogenation within 150-300^{o}C, followed by graphitization (350^{o}C) and formation of nanocrystalline, highly densified graphitic structures around 450^{o}C. The later stage of transformation occurs well below commonly observed graphitization for bulk carbon (600-800^{o}C). It was observed that the shape of the deposits contribute significantly to the phase transformations. We suggested that this difference is controlled by different contributions from interfacial footprints area. Moreover, the rate of graphitization was different for deposits of different shapes with the lines showing a much stronger dependence of its structure on the density than the dots.

Chapter 5 reports on highly localized light-induced transformation of amorphous carbon nanostructures (dots and squares) on noble metal surfaces. The phase transformation from the amorphous phase to the disordered graphitic phase was analyzed using the characteristic Raman signatures for amorphous and graphitized carbon and conductive force microscopy. The extent of the transformation was found to be largely dependent on the plasmon absorption properties of the underlying metal film. It was observed that the amorphous carbon deposits on the silver films consisting of 12 nm particles with the plasmon absorption near the laser excitation wavelength (514 nm), undergo fast graphitization to a nanocrystalline or a disordered graphitic phase. This transformation results in the formation of a highly conductive carbon-metal interface with atleast six orders of magnitude lower electrical resistivity than the initial insulating interface. We suggest that the fast graphitization of nanoscale carbon deposits might serve as an efficient path for the formation of complex patterned nanoscale metal-carbon interconnects with high electrical conductivity.

In **Chapter 6,** we discuss about a novel technique to measure the local thermal characteristics of a surface known as Scanning Thermal Twist Microscopy (STTM). The thermal bimorph is a very popular thermal sensing mechanism used in various applications from meat thermometers to uncooled infrared cameras. While thermal bimorphs have remained promising for scanning thermal microscopy, unfortunately the bending of the bimorph directly interferes with the bending associated with topographical information. We circumvented this issue by creating bimorphs that twist instead of bending and demonstrate the superior properties of this approach as compared to conventional scanning thermal microscopy. This technique was found to be highly sensitive and can be an important tool to identify the properties of different surfaces and interfaces.

In **Chapter 7**, we highlight the use of EFM to probe the defect sites on a surface. This technique was applied to locally probe the graphitic and oxidized areas on the surface of an individual graphene oxide flake and measured the local surface potential of these regions using EFM. Conventional optical characterization techniques such as Raman and XPS were resolution-limited and could not identify the localized domains on the surface of graphene oxide but give average information of a given area. Interestingly, high resolution topography and adhesion maps did not show any significant difference over the graphene oxide surface but the EFM phase images of the same area clearly showed areas with different response. We attributed this phenomenon the different in the dielectric response of the graphitic and oxidized domains on the graphene oxide towards the conductive tip as it was scanned across the surface.

Chapter 8 discusses the mechanical properties of ultrathin laminated nanocomposites can be significantly enhanced by the incorporation of small amount of a dense monolayer of planar graphene oxide flakes. Negatively charged functionalized graphene oxide

layers were incorporated into polyelectrolyte multilayers (PEMs) assembled with LbL via LB deposition. These LbL-LB graphene oxide nanocomposite films were released as robust freely standing membranes with large lateral dimensions (cm) and thickness of around 50 nm. Micromechanical measurements showed enhancement of the elastic modulus by an order of magnitude, from 1.5 GPa for pure LbL membranes to about 20 GPa, for only 8.0 vol. % graphene oxide encapsulated LbL membranes. These tough nanocomposite PEMs can be freely suspended over large (few mm) apertures and sustain large mechanical deformations.

Finally, **Chapter 9** provides general conclusions for the overall work in the dissertation with a specific focus on impact and future directions.

CHAPTER 3

EXPERIMENTAL DETAILS

The following chapter is intended to provide a brief description and experimental details for the techniques and instruments used throughout this work.

3.1 Synthesis and fabrication

3.1.1 Synthesis of graphene oxide

Graphene oxide is synthesized from natural graphite flakes (325 mesh, 99.8% metal basis) purchased from Alfa Aesar as per Hummer's method.[66] Briefly, 5g of graphite flakes and 2.5g of sodium nitrate ($NaNO_3$) are added to 107 ml of 98% sulfuric acid (H_2SO_4) maintained at 0^oC. Further, 15g of $KMnO_4$ is added to the mixture with vigorous stirring by maintaining the temperature below 20^oC during addition. The solution is heated to 35^oC and maintained for 30 mins until the effervescence get reduced. After 30 mins, 214 ml of water is added. The temperature increases to 98^oC. After 15 mins, 850 ml of warm water is added along with 10 ml of hydrogen peroxide. Finally, graphene oxide solution is obtained after subjecting the above solution to several cycles of filtration and washing to remove the excess acid.

3.1.2 Fabrication of graphene oxide films

Assembly of a monolayer of graphene oxide sheets on silicon substrate is carried out using a KSV 2000 minitrough Langmuir-Blodgett (LB) setup.[207] Specifically, 1-2 ml of the synthesized graphene oxide solution in water-metanol (1:5) mixture is dispersed evenly on the air-water interface. The barriers were then compressed at the rate of 5 mm/min. The graphene oxide monolayer was transferred from the air-water interface by

vertically pulling out the substrate submerged in the water sub-phase at the rate of 2 mm/min.

3.1.3 Fabrication of amorphous carbon nanostructures

Residual hydrocarbons and acetone is used as a precursor molecule to induce the growth of the deposits over different substrates. EBID carbon joints are fabricated using Quanta 200 environmental scanning electron microscope (ESEM) operated under 0.01 Pa.[27] Cone-shaped carbon deposits are deposited by keeping the electron beam in spot mode for varying period depending on the size required. Electron beam energy in 10 to 30 keV range and electron beam current (spot size) in the 5-140 pA range is be used for deposition. The carbon lines and carbon rectangles are deposited under line mode and area mode respectively, with similar SEM settings by varying the exposure time depending on the required dimensions.

3.1.4 Fabrication of free-standing Layer-by-Layer (LbL) assembled graphene oxide-polyelectrolyte membranes

Poly(4-vinylphenol) (M_w = 25,000), Poly(allylamine hydrochloride) (PAH, M_w = 56,000) and poly(sodium 4-styrene sulphonate) (PSS, M_w = 70,000) were purchased from Aldrich and used as received. A PHS droplet (2.0 wt.% solution in dioxane) was spincoated onto a clean silicon wafer. Alternating positive and negative PAH and PSS layers were spin-coated to form ‘m’ bottom PAH/PSS bilayers terminated with PAH, followed by deposition of graphene oxide flakes using LB technique. In between casting steps, the coated surface was rinsed once again with Nanopure water. Another ‘n’ PAH/PSS bilayers is assembled on the top. The concentration of the graphene oxide inside the polyelectrolyte matrix was manipulated by depositing graphene oxide sheets at regular intervals inside the matrix. Films with graphene oxide sandwiched between

$(PAH/PSS)_mPAH$ are designated as $(PAH/PSS)_mPAH$ GO $(PAH/PSS)_n$ PAH (φ), where φ refererred to the volume fraction of graphene oxide within the matrix. The volume fraction was calculated as the volume occupied by 2D graphene oxide sheets divided by the total volume of the membrane. The above procedure was performed in a class 100 clean air hood.

Finally, the LbL films were cut into approximately 2 mm x 2 mm squares using a stainless steel microneedle. They were then released by submersion in acetone, which preferentially dissolves PHS layer. For easy deposition on a 3 mm diameter copper substrate with a 150 μm opening or a TEM grid, the floating membranes are transferred into another petri dish containing nanopure water. For thickness determination, some membranes were deposited on a silicon substrate and a micrometer wide scratch was made. The membrane thickness was measured by AFM cross-sectional analysis across the edge of the film or across the scratch mark.

3.2 Characterization techniques

The research involves the application of a wide range of characterization techniques for the comprehensive study of physical and chemical properties of different materials. Different techniques were used for getting detailed information about the structure and composition of the materials. Common techniques such as scanning electron microscopy (SEM), optical microscopy, and contact angle measurements are relatively well established and will not be discussed. Some of the techniques, which are specific to the current research in that they are either custom built or tailored for specific requirements, will be briefly described.

3.2.1 Atomic Force Microscopy (AFM)

Tapping mode was commonly used for surface characterization and done using the Dimension 3000, Icon, and Innova AFMs (Bruker AXS, Santa Barbara). The technique relies on a micro-fabricated tip that deflects a focused laser when interacting with the sample surface. This deflection is detected by optical methods onto a photodiode position sensor that can translate both normal and lateral deflection signal. The result is a three-dimensional map of the sample surface with nanometer resolution allowing for quantitative analysis of the surface roughness.[208] Tapping mode AFM allows for the high resolution imaging of soft polymeric and biological samples without damage to tip or sample since contact with the surface is minimized. This is achieved by using specially designed probes that oscillate above the surface at their resonant frequencies of 100 – 500 kHz.[209,210] Different capabilities of AFM were also used extensively in this studied and are discussed below

3.2.1.1 Peak-Force Quantitative NanoMechanics (QNM)

The nanomechanical properties of different surfaces were quantified using the Dimension Icon (Bruker AXS, Santa Barbara) AFM under the Peak Force QNM (quantitative NanoMechanics) mode.[211] Peak Force QNM enables quantitative measurement of nanoscale material properties such as modulus, adhesion, deformation and dissipation. Peak force mode performs a very fast force curve at every pixel in the image. The peak interaction force of each of these force curves is then used as the imaging feedback signal. Peak force tapping mode modulates the z-piezo at ~2kHz with a default Peak Force amplitude of 150 nm. Analysis of the force curve data is done while scanning to provide a map of multiple mechanical properties that has the same resolution as the height image.[212]

3.2.1.2 Conductive Atomic Force Microscopy (CAFM)

The electrical properties of the materials were analyzed using Innova AFM (Bruker AXS, Santa Barbara). Conductive Atomic Force Microscopy (CAFM) module was used to map the electrical properties of the amorphous carbon nanostructures after phase transformation. The topography and electrical mapping of the surface was obtained simultaneously by rastering a tip coated with a conductive metal (Au/Pt) across the samples under bias. Depending on the resistivity of different domains on the sample, the current flowing under the applied sample bias is plotted along with the morphology as the probe moves across the surface.[211]

3.2.1.3 Electrostatic Force Microscopy (EFM)

Surface charge distribution over the graphene oxide surface was mapped using the Icon AFM (Bruker AXS, Santa Barbara) using the Electrostatic Force Microscopy (EFM) module.[211] In this technique, the system records the surface topography in the 1st pass and records the electrostatic interaction between the tip and the sample during the 2nd pass by lifting the tip by a known distance and applying a constant bias. The tip experience electrostatic forces as it scans over the sample which results in the change in the amplitude of oscillation or a shift in the phase of the cantilever. The system maps these parameters along with the topography and gives the surface charge distribution across the surface.[213]

3.2.2 Confocal Raman microscopy

Raman microscopy was used to understand the composition of different carbon nanomaterials as well as to monitor the changes in phase and composition of the amorphous carbon upon different treatment.[214] Raman microscopy relies on vibrational

spectroscopy which can provide chemical composition, structure of the material by monitoring the frequency shifts between excitation laser and scattered light. It is one of the most important tools for characterizing the microstructure of various carbon materials (graphite, amorphous carbon, carbon nanotubes, graphene), primarily due to its non-destructive approach, presence of sharp bands, and high intensity of these characteristic bands. This technique provides a wide range of critical information for bulk carbon materials, nanoscale structures, carbon-based nanocomposites, and individual carbon structures, including the composition, internal stresses and crystal orientation inside the material.[215,216,217,218] Raman spectroscopy is a unique technique for probing the physical state of different carbon materials in a nondestructive manner. WiTec (Alpha 300 R) confocal Raman microscope equipped with a Nd:YAG laser (514 nm) is employed for the purpose. The Raman microscope provides a lateral resolution of ~250 nm and vertical resolution of 1µm.[219]

3.2.3 X-ray Photoelectron Spectroscopy (XPS)

Thermo K-alpha XPS was used to understand the composition of graphene oxide. XPS is an analytical technique that directs a monochromatic beam of X-rays on a sample and detects the characteristic electrons that are ejected. The energies and number of electrons are used to determine the elements present, their abundance and chemical bonding state. This technique is highly surface sensitive and the typical detection depth is ~5nm. It can detect light elements such as Silicon at about 1% of the total surface composition and heavier elements down to ~0.1% with an accuracy of 20-50% of the given value.[220]

3.2.4 Ellipsometery

Ellipsometry was performed using spectroscopic ellipsometer M2000U (Woolam). Ellipsometry is a non-destructive optical technique, which deals with the measurement

and interpretation of changes of the polarization state of polarized light undergoing oblique reflection from a sample surface.[221] The quantities measured by an ellipsometer are ellipsometric angles Ψ and Δ which are related to the complex ratio of the Fresnel reflection coefficients R_p and R_s for light polarized parallel (p) and perpendicular (s) to the plane of incidence such as

$$\rho = R_p / R_s = \tan \Psi \exp(i \Delta) \quad (1)$$

The complex reflectance ratio ρ is completely determined by an amplitude (tan Ψ) and a phase (Δ).[222,223] These changes are related to a transformation of a shape and orientation of the ellipse of polarization, respectively. In order to deduce unknown parameters of a sample under investigation, a model for the sample structure is first constructed with initial estimates of the parameters. These parameters (e.g. thickness and refractive index) are then varied to generate a set of calculated Ψ^{exp} and Δ^{exp}. The initial parameters of the model parameters are transformed finally into true parameters of the sample, such as thickness and optical constants.

Measurement of the metal film thicknesses and optical constants was carried out for three incident angles 65º, 70º, and 75º. The psi(polarized angle) and delta (phase) values are measured and fitted with the stored parameters for gold, silver and copper to determine the thickness and optical constants (refractive index (n) and extinction coefficient (k)) over wavelengths 300 to 900 nm.

3.2.5 Mechanical testing of polymer nanocomposites

Mechanical aspects of free-standing Graphene-oxide polymer nanocomposite membranes were analyzed using the following techniques

3.2.5.1 Bulging

Bulging tests are performed according to procedures described in detail in the literature.[224,225] The bulging test data is analyzed using a model for the elastic deformation of circular membranes, according to the procedure described previously. The bulging tests are performed using a custom-made interferometer equipped with a charge coupled device (CCD) camera (Logitech) and a He-Ne Laser (λ=632.8 nm). Pressures up to 6000 Pa are exerted using a 60ml syringe regulated by an automatic pump (Kent Scientific Inc.) and monitored with an automatic pressure gauge, DPM 0.1 (SI Pressure Instruments).

The LbL membranes freely suspended over a copper substrate with a 150 μm aperture are first inspected under an optical microscope and a minimal pressure was exerted to check for symmetrical Newton's ring patterns that indicate membrane homogeneity. While monitoring pressure, the slightly pressurized membrane is allowed to stand idle for a few minutes to ensure the absence of any leaks. The mounted membrane is then tilted at a minimum angle, θ, to form a vertical interference pattern. For bulging measurements conducted between 0 and 6000 Pa, the maximum membrane deflection did not exceed 8μm. Under these conditions, the maximum error due to tilting is about 6nm, which is within the resolution of the interference pattern ($1/4\lambda$ or 160 nm). During measurements, a transparent crosshair window is laid over the digital image of the membrane such that the central vertical interference pattern coincided with the vertical line of the crosshair. As the pressure increased, the interference pattern moves laterally across the crosshair. Concomitantly, the deflection of the copper substrate is also monitored using a mouse cursor as the target marker. A minimum of three randomly selected specimens are measured for each membrane with different densities of graphene oxide.

3.2.5.2 Buckling

Buckling tests were conducted to independently evaluate the elastic modulus of LbL membranes.[226,227] For an isotropic thin membrane, a uniform buckling pattern with a characteristic wavelength, λ, is observed when it is subjected to a critical compressive stress.[228] The spacing of this pattern which is directly related to the elastic modulus is calculated using AFM and verified from optical images. To initiate the buckling pattern, a 2 mm x 2 mm membrane piece was placed over a 0.6 cm x 0.6 cm x 0.4 cm PDMS substrate, which was slowly compressed with micrometer-sized increments. The total compressive distance is generally less than 15 μm. The compression was monitored in differential interference contrast (DIC) mode adjusted for maximum contrast. Optical images are captured with a Leica MZ16 microscope in reflection mode.

CHAPTER 4

THERMALLY-INDUCED TRANSFORMATIONS OF AMORPHOUS CARBON NANOSTRUCTURES

4.1 Introduction

Several fabrication techniques can be used for the deposition of carbon in the form of ultrathin coatings and individual nanostructures. These methods include chemical vapor deposition,[229] cathodic arc deposition,[230] pulsed laser deposition,[231] and sputtering.[232] Depending on the deposition methods and settings, amorphous carbon films with different microstructures and sp^2/sp^3 contents have been produced.[233,234,235] The characterization of these microstructures basically involves determining the atomic order and chemical composition as the sp^3/sp^2 ratio. Different techniques such as diffraction, NMR, X-ray reflectivity, electron energy loss spectroscopy and Raman spectroscopy have been used for obtaining these parameters. Most of these techniques were used to study the properties of bulk amorphous carbon films deposited on a substrate.[133,236,237,238]

Raman spectroscopy is one of the most important tools for characterizing the microstructure of various carbon materials (graphite, amorphous carbon, carbon nanotubes, graphene), primarily due to its non-destructive approach, presence of sharp bands, and high intensity of these characteristic bands. This technique provides a wide range of critical information for bulk carbon materials, nanoscale structures, carbon-based nanocomposites, and individual carbon structures, including the composition, internal stresses and crystal orientation inside the material.[215,216,217,218]

All amorphous and graphitic carbon structures have been known to show characteristic peaks for D-band and G-band near 1350 cm^{-1} and 1580 cm^{-1} respectively. Raman spectra

of carbon structures is greatly dominated by the sp^2 sites owing their 50-230 times larger Raman scattering cross-section than the sp^3 sites.[239] Thus, the Raman spectrum of tetrahedral amorphous carbon which contains only 10-15% sp^2 content is still dominated by the presence of the characteristic peaks. G-mode is associated with the stretching vibrations of any pair of sp^2 sites, whether in C=C chains or in aromatic rings. The D-mode is the breathing mode of those sp^2 sites located only in rings but not in chains.[235,237,240]

In recent study, Tuinstra and Koenig reported that the intensity ratio of the D and G peaks varies inversely with the in-plane correlation length, *La* or grain size of the graphite.[241] In another fundamental work, Ferrari *et al.* found that it is possible to classify the transformation of carbon microstructure as deduced from Raman spectra of all disordered carbons within a three-stage model of increasing disorder starting from perfect graphite, as follows: 1) transformation of graphite to nanocrystalline graphite; 2) transformation of nanocrystalline graphite to sp^2 amorphous carbon with presence of aromatic rings; 3) further transformation of mostly sp^2 amorphous carbon to completely disordered sp^3 amorphous carbon with fragmented and chain configurations. In these transformations, stage 1 corresponds to the progressive reduction in the grain size of ordered graphite layers, while keeping the aromatic rings. Second, stage 2 corresponds to the topological disordering of a graphite layer (odd membered rings) and loss of aromatic bonding, but with a purely sp^2 network. In stage 3, the sp^3 content increases from 0 to 100%. This changes the sp^2 configuration from mainly rings to short chains.[240,242] These changes in the microstructure are also associated with the changes in the density of the substrate. Finally, amorphous carbon which is insulator is reported to show a density between 1.8-2.1 g/cm^3 whereas graphite with high electrical conductivity has a density of 2.3 g/cm^3, thus resulting in decrease in specific volume by 15%.[243,244] Complete graphitization and formation of nanocrystalline graphite is usually observed at temperatures above 600^{o}C.

Recently, EBID has been shown to be a useful tool for localized (nanoscale) deposition of amorphous carbon and metals with complex 2D/3D geometry over different substrates. At room temperature, organic molecules present on the substrate have sufficient mobility to migrate and become a precursor for deposition reaction. A precursor molecule, when interacts with an electron of appropriate energy (i.e., secondary electrons generated upon impact of electron beam on a substrate), dissociates and results in the formation of an immobile carbon deposit.[99,101,245] As has been demonstrated, electron beam in conventional SEM can be used for the growth of such carbon deposits.

These EBID deposits can be used as soldering material to improve the contact of heterogeneous materials at the interface (e.g metal-metal or metal-semiconductor interface).[24] In addition to this, it can be deposited over a relatively small area (<1000 nm^2) which makes it important for nano-scale patterning of surfaces and in electronic circuits, where localized fusion of the metal joints is required.[95,130,131] But, as deposited the EBID carbon is amorphous and has low electrical conductivity, thus limiting its use in electronic circuits as materials for interconnets.[27] Thus, post-deposition treatment, including microstructure modification (dehydrogenation and residual stress relaxation) and directed phase transformation (i.e., towards much higher electrically conductive graphitic phase) is required after EBID process.[132]

Several methods have been proposed to lower the electrical resistance of the amorphous carbon via graphitization. Thermal annealing has been widely used for graphitization of amorphous carbon films. On subjecting a carbon film to high temperature, several processes can take place. Studies on thermal annealing of thin amorphous carbon films have shown that significant structural changes occur around 400^oC followed by completed graphitization at 600-800^oC.[246,247,248,249,250,251252] However, no studies have been reported on the microstructure and morphology of the amorphous carbon deposits

having nanoscale dimensions (well below a micrometer scale) where the role of the interfaces become dominant and thermal behavior can be much different from that observed for bulk carbon materials.

Here, we demonstrate that dramatic and complex thermally-induced changes in chemical and physical states of EBID amorphous carbon nanostructures can be revealed by using a combination of atomic force microscopy (AFM) and confocal Raman microscopy techniques. Amorphous carbon deposits in the form of one-dimensional (lines) and zero-dimensional (dots) having characteristic dimensions within 50-500 nm were analyzed for their changes in microstructure with annealing temperature up to 500^{o}C. The size of the deposits was also varied to account for the effect of confinement on the process of phase transition. The change in the density of the deposits upon change in the microstructure was analyzed by recording the changes in their shape by using AFM. Concurrently, confocal Raman measurements were performed on the same individual carbon deposits with lateral resolution of 300 nm.[253]

Correlating the Raman data with the AFM measurements revealed multi-stage transformations of the amorphous carbon deposits, well-known for bulk carbon materials but at much lower annealing temperatures. Complete graphitization along with formation of densified nanocrystalline carbon structures was achieved at temperatures around 400^{o}C which is much lower than that for bulk amorphous carbon. Both dots and lines undergo similar thermally-induced transformations but more transitions are observed for carbon lines owing to their higher structural dependency on the density (height^{2}~1/density) than the dots (height^{3}~1/density).

4.2 Experimental details

Residual hydrocarbons and acetone was used as a precursor molecule to induce the growth of the deposits over clean Au/Cr substrates. EBID amorphous carbon joints are fabricated using Quanta 200 ESEM operated under 0.01 Pa. The cone-shaped carbon deposits shown in Figure 4.2 were deposited by keeping the electron beam in spot mode for a period of 20 minutes. Electron beam energy in 10 to 30 keV range and electron beam current (spot size) in the 5-140 pA range was used for deposition. The carbon dots shown in Fig. 4.4 were are made by scanning the electron beam at energy of 25 keV and current of ~20 pA at a frame time of 0.411s and resolution of 2048x1768 pixels for a period varying from 5 sec to 240 sec. The carbon lines shown in Figure 4.5 were deposited under line mode with similar SEM settings by varying the exposure time from 30 sec to 20 mins. These deposits were annealed under atmospheric conditions at different temperatures for 3 minutes and analyzed for their structural and compositional changes using AFM and Raman microscopy, as discussed in chapter 3.

4.3 Results and discussion

4.3.1 Amorphous carbon nanostructures fabrication

The carbon deposits were grown over a 50 nm layer of gold layer deposited on 10 nm layer of chrome over a silicon oxide layer on a silicon substrate as shown in Figure 4.1. EBID deposits are known to be hydrogenated amorphous carbon containing more sp^2 than sp^3 bonded carbon. Electron beam focused at a spot for prolonged period of time lead to the formation of "dot" like structures from residual hydrocarbons ("contamination") as a precursor, as shown in Figure 4.2a. SEM images of deposits upon tilting the substrate at 45^o with respect to the electron beam, reveal a pillar like

morphology of these deposits (Figure 4.2b). These deposits were obtained by varying the e-beam current from 1.5 pA to 400 pA and accelerating voltage from 10 keV to 30 keV. Although, the electron beam exposure time was maintained constant for all deposits, their morphology showed a significant variation with EBID parameters. The widths of these nanostructures can be controlled in the range from 100 nm to 1000 nm and their heights can be varied from 50 nm to several microns (Figure 4.2b). The details of the carbon deposit morphology with the deposition settings are discussed elsewhere.

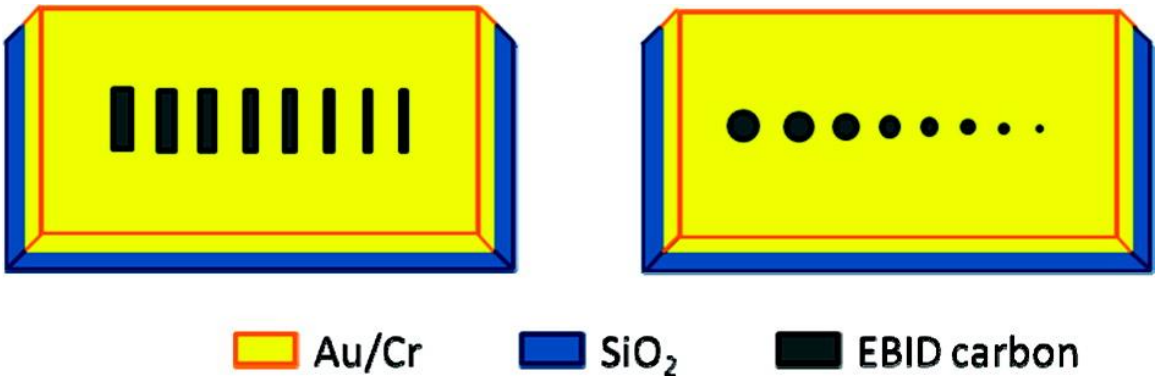

Figure 4.1 Deposition geometry of amorphous carbon nanostructure arrays with different shapes and size of dots and lines

The intrinsic physical state of these carbon deposits was confirmed from their characteristic Raman spectra collected from individual carbon structures with Raman micromapping under minimum laser power (Figure 4.3). The images were obtained by integrating the intensity of the peaks between 1000 cm^{-1} and 1800 cm^{-1} to account for the characteristic D- and G- peaks.[236] Thus, the deposits which show peaks in this range appear brighter as compared to other regions. Figure 4.3b shows the high-resolution Raman spectra in this selected range obtained from the corresponding deposits by averaging over 400 individual spectra. Though, the deposits show a different morphology (see Figure 4.2b), their Raman spectra are virtually identical with the G-band

peak position varying between 1560 cm^{-1} - 1565 cm^{-1} and D/G ratio around 1.3. Thus, although the deposits were fabricated under different electron beam conditions and showed different morphologies and dimensions, they had a similar composition and microstructure with significant sp^3 content suggesting the dominance of amorphous and highly fragmented carbon material.[240]

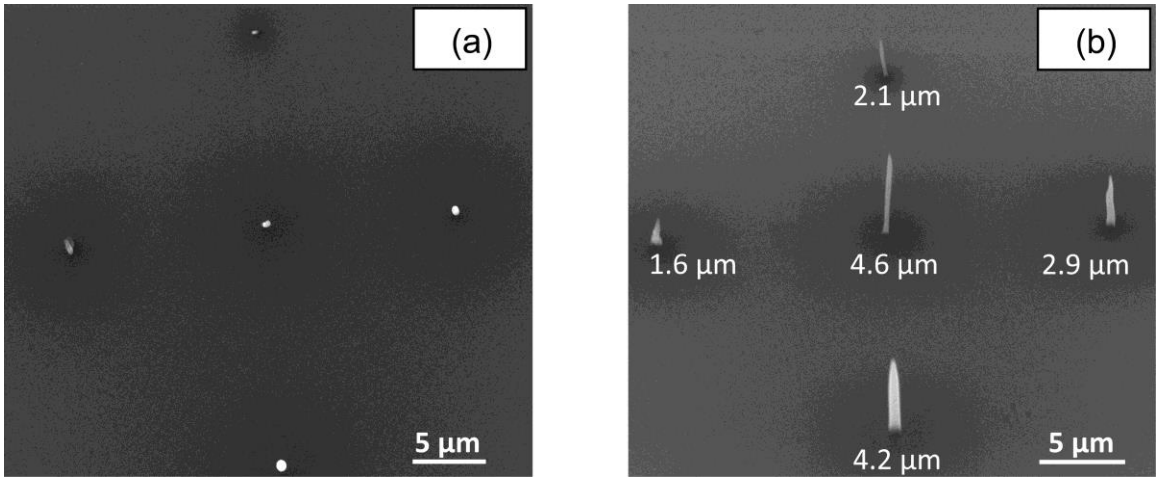

Figure 4.2 SEM image of amorphous carbon dots deposited under different settings. (a) top view of the deposits showing dot like structures, (b) 45^o view of the deposits showing pillar like morphology with the values underneath indicating its height

After evaluating the effect of e-beam deposition settings, carbon dots of different dimensions were grown by varying the exposure time at fixed e-beam parameters for detail studies. The electron beam parameters were kept constant by maintaining the e-beam current and accelerating voltage at 25 pA and 20 keV respectively, with the exposure time varying from 5 sec to 240 sec. Figure 4.4 shows the AFM image of these carbon dots (Figure 4.4a) and cross-sectional profile (Figure 4.4b) with the corresponding 3D AFM image (Figure 4.4c). A uniform gradient in the size of these deposits is observed with height and width of dots increasing, as the exposure time increases. The smallest dot with the height of 60 nm was obtained at an exposure time of 5 sec with the

largest dot having the height of 450 nm. To study the microstructure of these deposits, Raman maps were obtained as described before (Figure 4.4d). The measurements were made under minimum laser power (0.5mW) to avoid any laser light induced thermal effects. The smallest deposits were practically invisible on Raman maps owing to their very low signal-to-noise ratio and thus were excluded from further Raman spectral analysis (two smallest dots on left in Figure 4.4a).

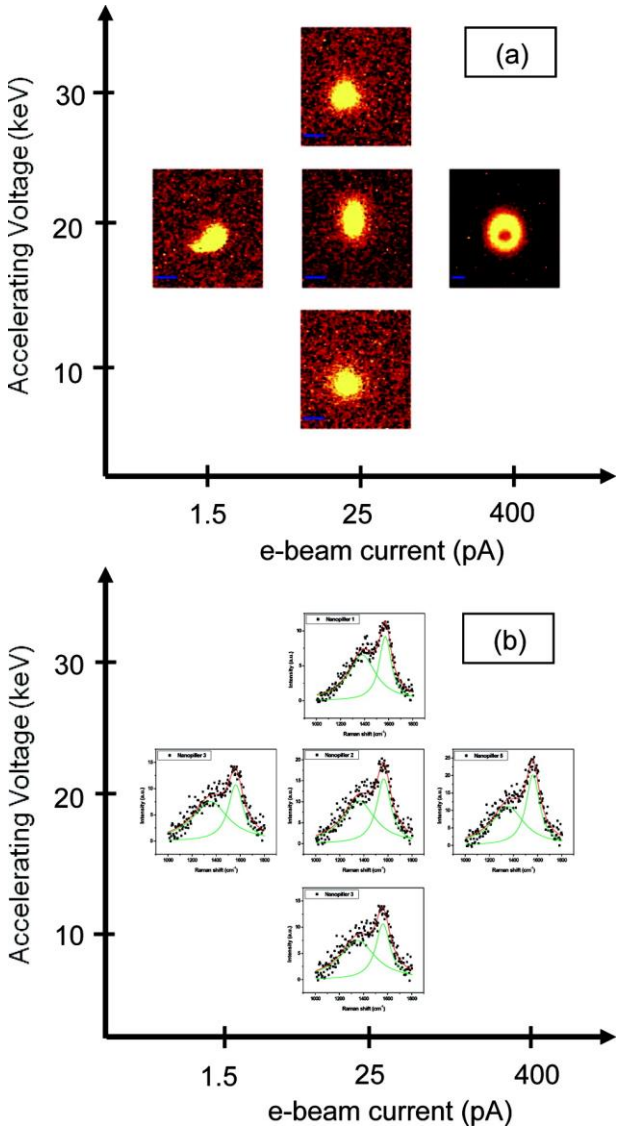

Figure 4.3 Raman micromapping of the carbon deposits fabricated under different e-beam settings. (a) Raman map (scale bar: 1 um); (b) corresponding Raman spectra

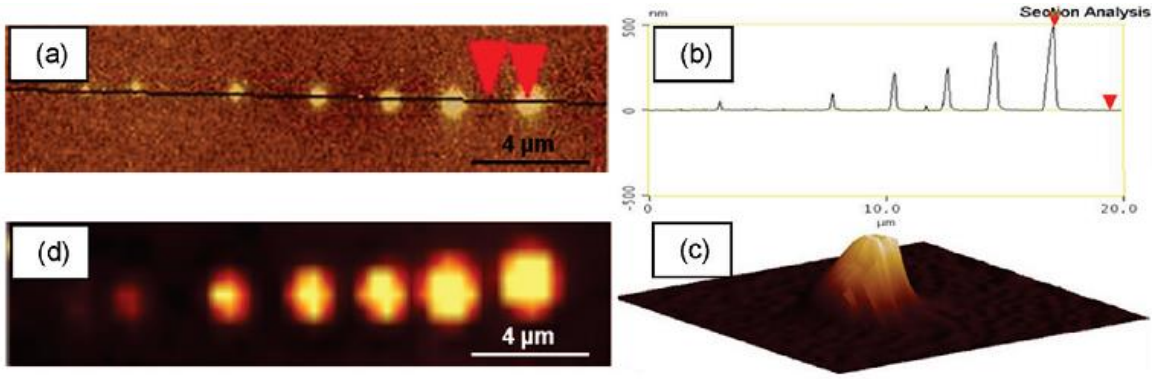

Figure 4.4 Linear array of EBID-fabricated amorphous carbon dots with different dimensions. (a) AFM image showing the section line; (b) cross-section; (c) representative 3D image (z-scale: 450 nm); (d) Raman map

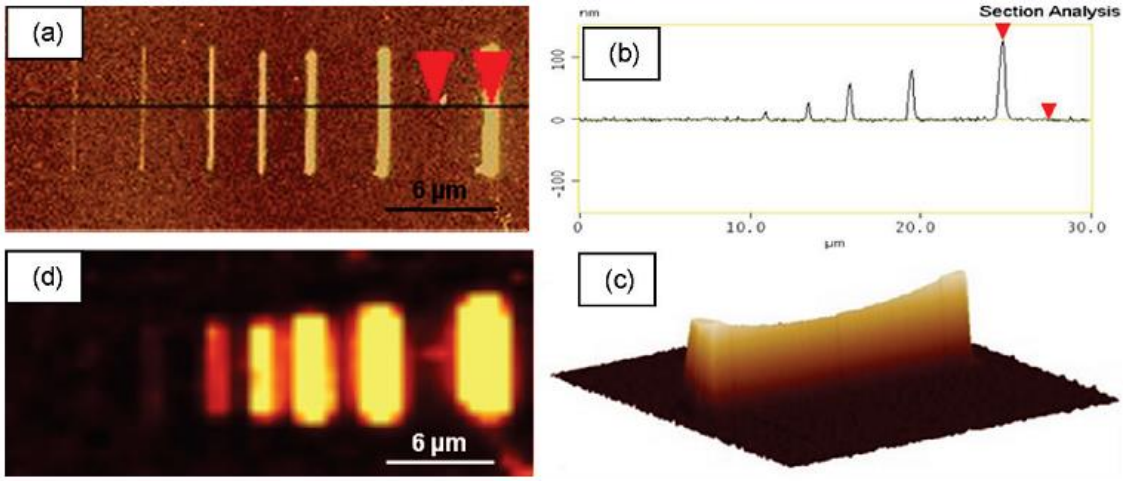

Figure 4.5 Linear array of EBID-fabricated amorphous carbon lines with different dimensions. (a) AFM image showing the section line; (b) cross-section; (c) representative 3D image (z-scale: 150 nm); (d) Raman map

Carbon deposits in the form of line with identical length and different cross-sections were grown by scanning the e-beam back and forth across the surface. The length of the line was kept constant by maintaining a constant scan area but its height was varied by changing the exposure time. Figure 4.5a shows the AFM of the lines having the same lengths but with increasing thickness/height from left to right. The thinnest line having the height and width of 2 nm and 270 nm respectively was obtained at an exposure time of 30 sec. Sectional analysis (Figure 4.5b) shows a systematic increase in the height of these lines from left to right. Figure 4.5c displays a representative 3D image of the line with the height of the line varying along its length with the height gradually decreasing toward the center. This is due to a higher rate of diffusional supply of precursor molecules at the corners as compared to the edges and is common for EBID deposits.

The array of carbon lines were also analyzed using Raman micromapping (Figure 4.5d). The smallest carbon line deposits (<10 nm) did not show up in the Raman image (similar to dots) and thus were excluded from further Raman spectral analysis (two thinnest lines on left in Figure 4.5a). The substrate with the line deposits was also annealed at same range of temperatures and analyzed for its morphology and microstructure at every step by AFM measurements and Raman spectroscopy under conditions identical to those applied to variable-size carbon dots.

4.3.2 Thermal annealing of amorphous carbon nanostructures

4.3.2.1 Morphological changes.

AFM and Raman measurements were collected for exactly the same deposits for each thermal annealing cycle. Measurements were performed at each thermal annealing step by moving the substrate with microscopic location marks using a micromanipulator to

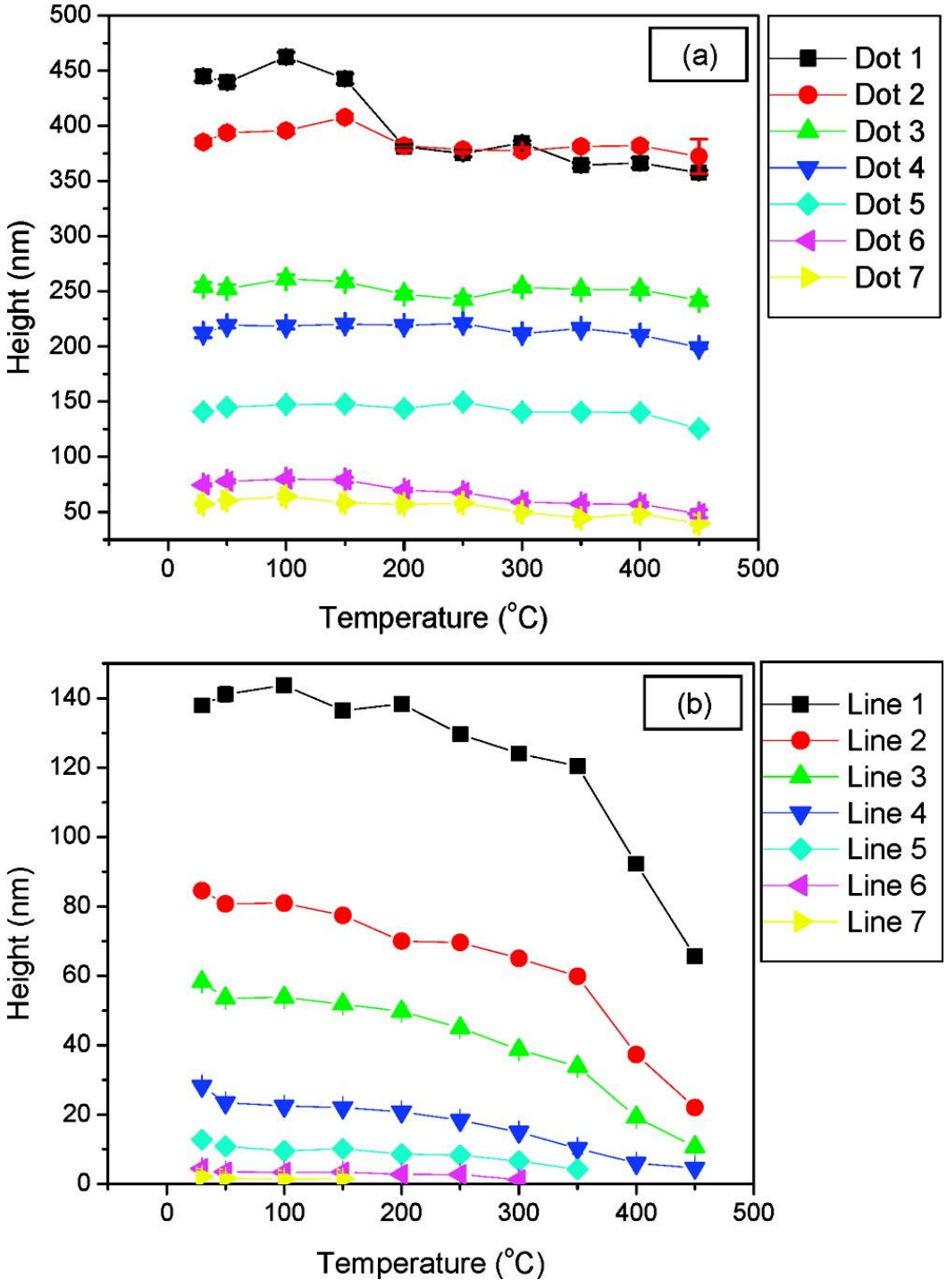

Figure 4.6 AFM height analysis of (a) amorphous carbon dots, and (b) amorphous carbon lines at different annealing temperatures

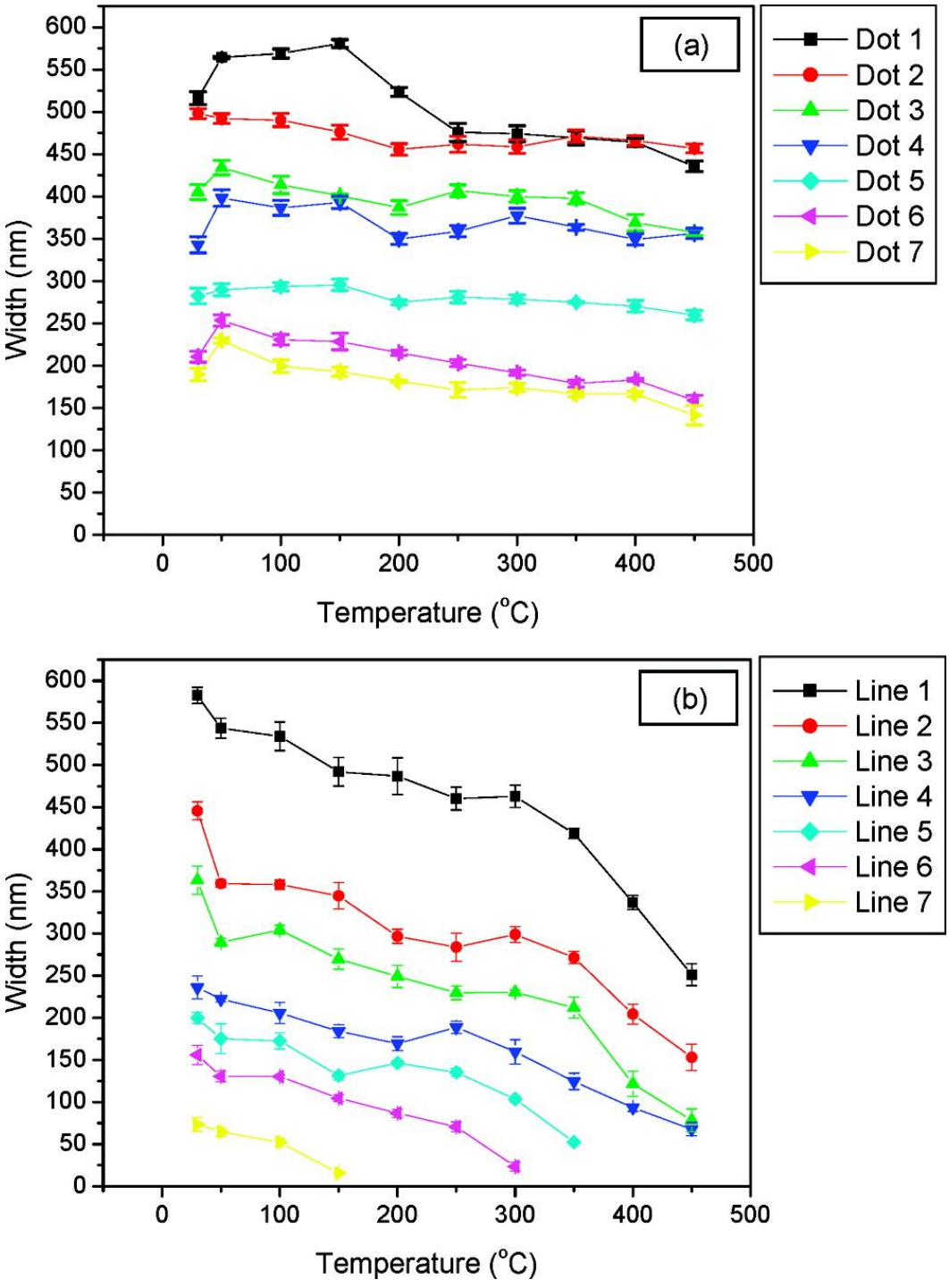

Figure 4.7 AFM width analysis of (a) amorphous carbon dots, and (b) amorphous carbon lines at different annealing temperatures

exactly locate the same surface area for all the readings. Thus, all data points presented here, represent the same selected deposits which go through all thermal transformations. One-time capturing of both AFM and Raman images for all carbon deposits annealed at given temperature minimize instrumentation variations related to differences in sample preparation, thermal treatment, and imaging; thus providing for the highest resolution and a solid base for comparative studies of these very small amounts of carbon deposits.

Figure 4.6 demonstrates the variation in height of the carbon deposits with different sizes (heights) annealed at different temperatures as measured from averaging multiple cross-sections of AFM images. As clear from this data, all the carbon dots show a small decrease in their size with the increase in annealing temperature from 30^{o}C to 250-300^{o}C. However, some decrease in size is observed above 300^{o}C with a higher rate observed for smaller dots. On the contrary, carbon lines show a much more distinct change in their size on annealing at higher temperatures (Figure 4.6b). All the carbon lines show a steady decrease in height up to 300^{o}C followed by a sharp decrease, the most prominent (~75%) being for the smallest line (60 nm). Modest structural changes (10-30%) were also observed for the lines with the smallest cross-section.

A similar trend is observed for the widths of these deposits annealed at different temperatures (Figure 4.7). All the dots show a slight decrease in their widths with the increase in annealing temperature. It is interesting to note that the dots with relatively smaller widths (< 200 nm) show a more pronounced decrease in their widths. However, a distinct transition is difficult to interpret from this data alone. On the contrary, lines show a gradual decrease in their widths on annealing from 30^{o}C to 300^{o}C followed by a step decrease around 450^{o}C. Interestingly, it was observed that the length of the line does not change with the annealing temperature. Thus, for simplification, all the discussions henceforth will focus on the analyzing the variation in height of the deposits, keeping into

consideration that the widths will follow a similar trend and the volume of deposits decreases with thermal annealing as well .

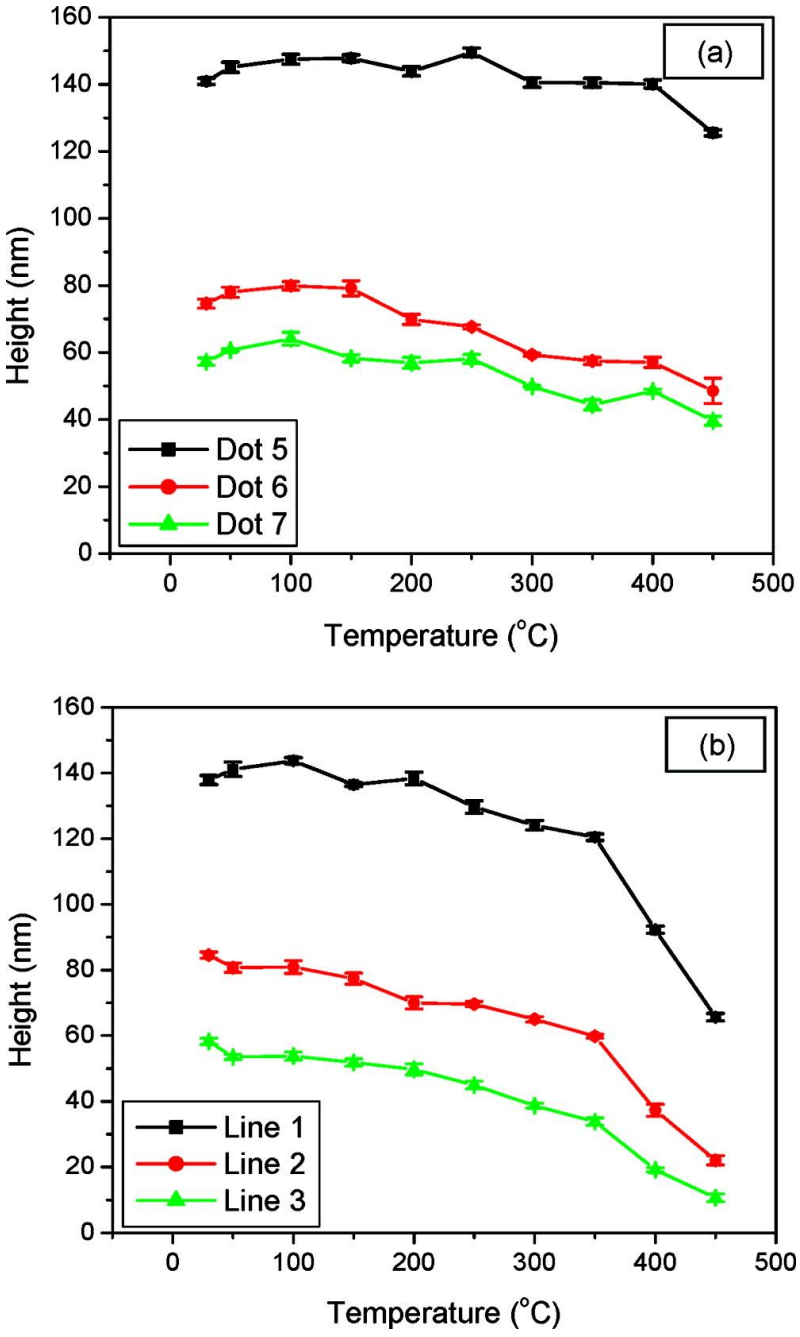

Figure 4.8 AFM height analysis of (a) amorphous carbon dots, and (b) amorphous carbon lines having similar initial heights, at different temperatures

On analyzing the separate plots for carbon dots and lines with approximately similar cross-sections, a significant change in the height (~75%) was observed for smallest line as compared to a mere 20% decrease for smallest dot at the highest annealing temperatures (Figure 4.8). Smallest lines (<15nm) were not visible at temperatures above 300^{o}C due to greatly diminished dimensions because of densification and partial ablation. Decreasing height of the carbon deposits suggests that they are undergoing significant densification during thermal annealing at elevated temperatures that can be related to both graphitization and clustering of initially amorphous and porous carbon deposits.

These trends indicate that the transformation process primarily depends on the cross-sectional area of the deposits. The most significant structural changes are observed for carbon deposits having feature size less than 100 nm. Intense transformation for the smallest deposits suggests that the reorganization process relies on the efficient transfer of thermal energy across the deposit which further implies that the metal (Au/Cr) – carbon interface should have a significant contribution in this process. It is worth to note that the surface area of the substrate covered by the lines is much higher than that occupied by the dots. Comparing the deposits having the similar heights, it is seen that the line footprint covers a surface area of 2.9 $\pm$ 1.0 μm^2 whereas the dot footprint cover just 0.047 $\pm$ 0.025 μm^2. Even the bigger dots show an average footprint of 0.6 $\pm$ 0.35 μm^2 which is much lower than that for the smallest line again.

In fact, the interface with metal substrate might act as a site for nucleation of the graphitic crystallites inside the amorphous carbon structure during extensive annealing as caused by thermally-induced interfacial stresses between materials with different thermal properties. Thus, the first nucleation should occur at the low energy gold surface and at the interface of the carbon deposit. In case of the deposits with similar heights, the surface area per unit volume available for the nucleation is the same. We suggest that at

elevated temperatures, the formation of the interfacial layer of graphitic crystalline domains takes place inside the deposits. With the further increase in annealing temperature, the growth of the crystal domains takes place resulting in further densification of deposits. The rapid decrease in the height of the lines, implying a higher growth rate of crystalline domains is likely due to the $height^2 \sim 1/density$ or even $height \sim 1/density$ (for taller lines) dependence for lines simply because at least one dimension – the line length is largely fixed and the change of volume occurs due to a change in other dimensions.

For the dots, on the other hand, since all three dimensions are likely to shrink at approximately the same rate as the density increases upon graphitization, the height vs. density dependence is much weaker: $height^3 \sim 1/density$. Thus, a steady decrease in the height is observed for the lines with the increase in the annealing temperature. Apparently, much higher energy is required to drive the crystal growth inside the dots due to significant space constraints and small footprint as compared to carbon lines. Considering that further increase in annealing temperature leads to a dramatic reduction in size which well exceeds the expected densification caused by complete graphitization (15%), the possibility of intense ablation of the lines could be suggested as well. To elucidate the actual nature of the chemical and physical transformation, the Raman spectra need to be carefully analyzed.

4.3.2.2 Compositional changes

Figure 4.9 shows the representative Raman spectra of the carbon deposits (carbon line) at a single point, taken at room temperature which demonstrates all major features representing material under investigation: Sharp peaks between 1300 cm^{-1}-1600 cm^{-1} represent the characteristic D-band and G-band peaks of carbon as introduced above.

The extremely weak peak near 1050 cm^{-1} might be due to the vibration of monosubstituted benzene rings.[214] The height of the deposits (50-500 nm) is significantly smaller compared to the depth of focus (700 nm). Hence, the spectra obtained here accounts for the entire volume of the deposit, considering that focal plane coincides with the substrate. It should be noted that the spectra appears more noisy and without clearly defined shoulder owing to its collection from a single point on the carbon deposit (carbon line in this case), whereas all other spectra (discussed below) represents an average of several points over the deposit.

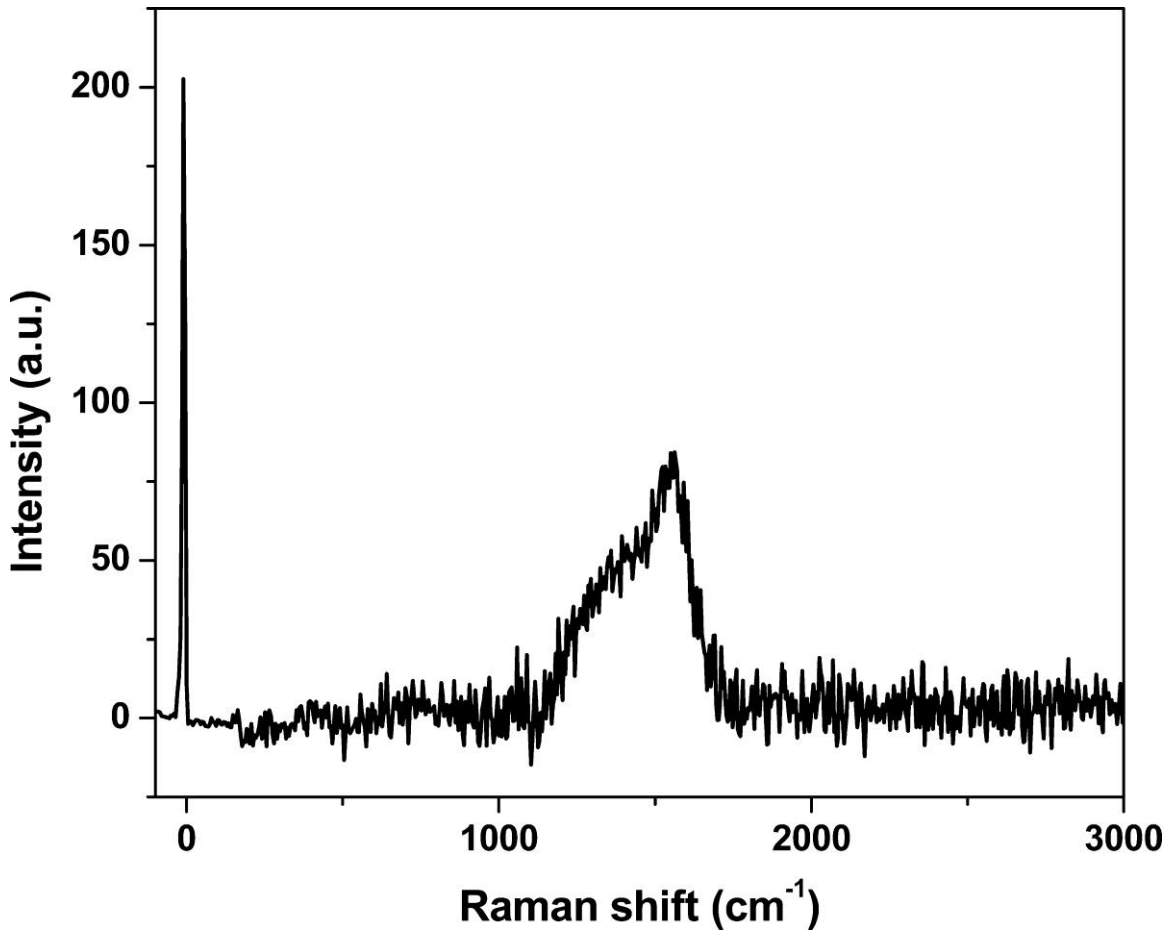

Figure 4.9 Representative integrated Raman spectra of amorphous carbon deposits (carbon line) at room temperature

The two major characteristic peaks which correspond to D-band and G-bands are difficult to analyze in this representative spectrum, but they can be clearly observed and deconvoluted when zoomed in a narrower window between 1000 cm^{-1} and 1800 cm^{-1} as apparent in Figure 4.10, which shows the evolution of the Raman spectra of a carbon line annealed at different temperatures. Similar trends can be observed for the spectra of carbon dots annealed at different temperatures. These spectra were utilized for further analysis after deconvoluting with the Lorentzian fits to clearly distinguish the characteristic G band and D band

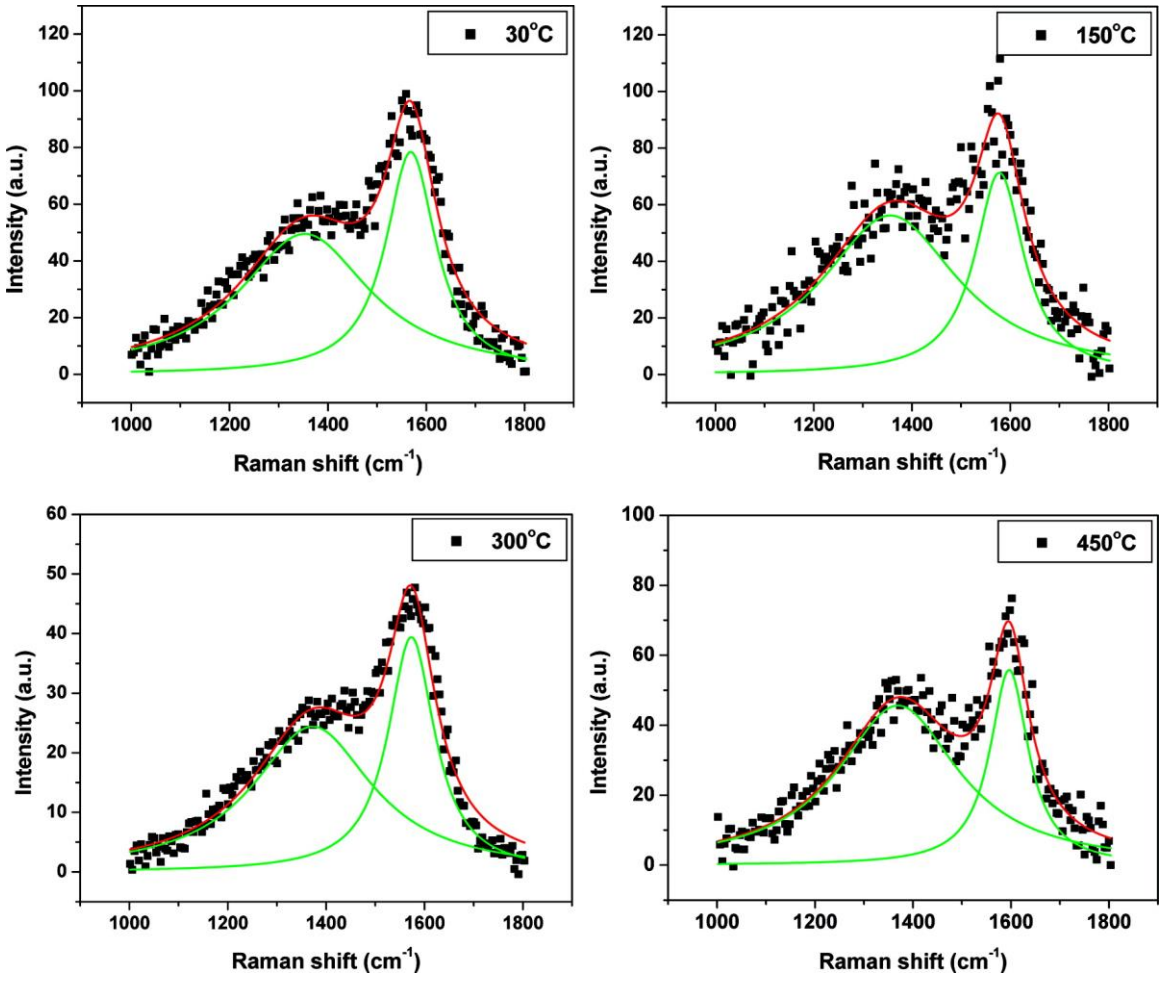

Figure 4.10 Evolution of Raman spectra of amorphous carbon deposits (carbon line) at different temperatures

As clear from Figure 4.10, the D band appears as a shoulder to the more intense G band at lower temperature. As the annealing temperature increases, the D band becomes more prominent in the spectra along with the increase in intensity of G band as well. Also, the full width at half maximum (FWHM) of the G-band was found to decrease by almost 35% (140 cm^{-1} to 90 cm^{-1}) as the annealing temperature increases. For further detailed analysis of the microstructure, we selected the positions of D and G bands as well as the ratio of their peak areas as commonly referred in literature. As mentioned earlier, D band correspond to the breathing mode of sp^2 sites in rings and G-band relates to the stretching vibration of any pair of sp^2 sites in chains or aromatic rings. In case of graphite, as the disorder increases, the cluster size and number decreases and gets more distorted until it opens up. Since, the G-peak is just related to the relative motion of C sp^2 atoms, the I(G) increases with respect to I(D) and the ratio decreases. On the contrary, in case of amorphous carbons having a small correlation length (L_a), the D-mode stretch is proportional to the probability of finding a six-fold ring in the cluster which in turn is proportional to the cluster area. Thus, in amorphous carbons, the development of a D peak indicates ordering, exactly opposite from the case of graphite.[240,241]

Figure 4.11 indicates that the D/G ratio undergoes significant variation with increasing annealing temperature, showing a gradually increase from 1.0-1.4 to 2.0-2.2 for both carbon dots and lines. Moreover, overall behavior for dots and lines is similar within standard deviations indicating that shrinking dimensions do not significantly affect the thermally-induced phase transformations. Thus general trends will be analyzed after averaging for all dots and all lines with different sizes as represented by the solid black lines (averaging over all data points) in the subsequent figures. The smaller dots (< 140nm in height) and lines (< 15nm in height) were excluded from the averaging owing to their low signal to noise ratio. However, the data points are included in the figures for consistency.

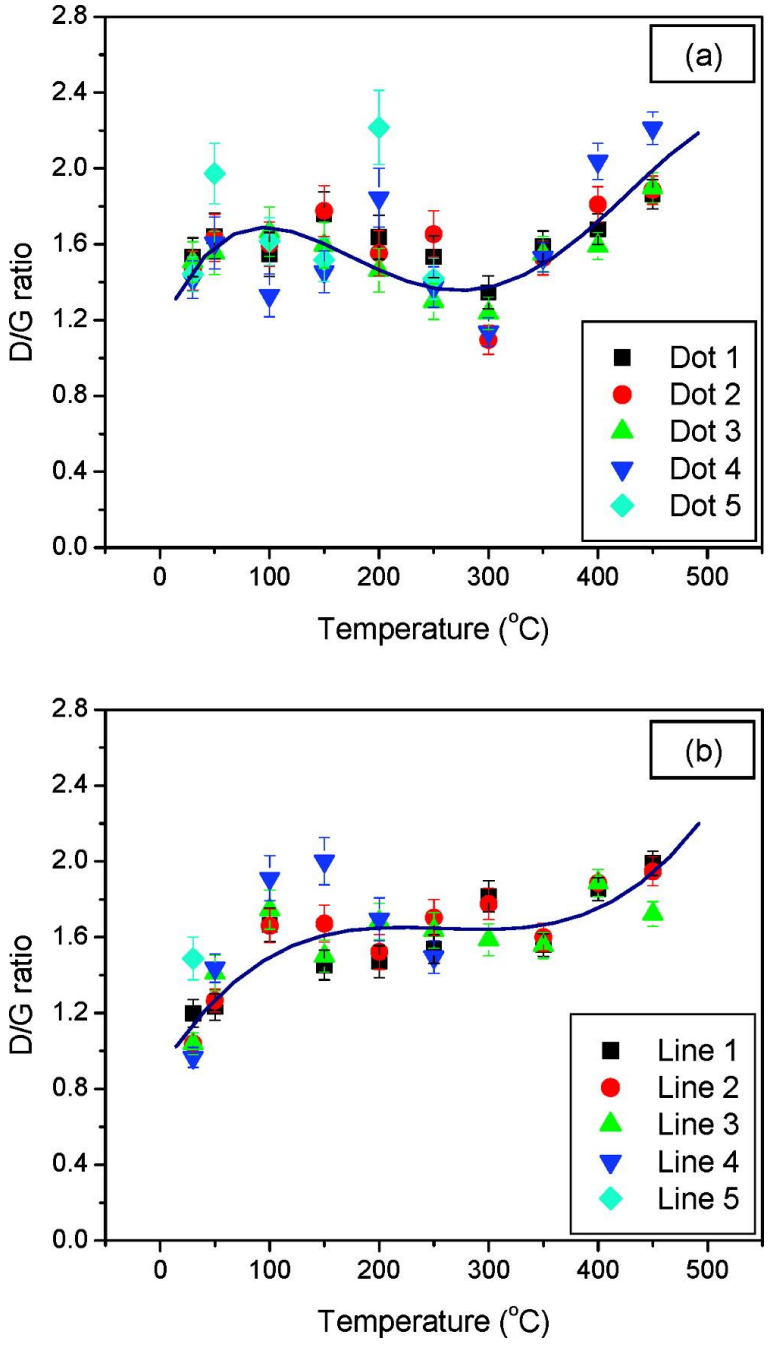

Figure 4.11 D/G ratio analysis of (a) amorphous carbon dots, and (b) amorphous carbon lines at different annealing temperatures. Solid line represents the average of the data points for all sizes at a given annealing temperature

D/G ratio has been known to be a quantitative factor in determining the size of graphitic crystallites in any carbon structure.[233] It is accepted that the increase in the D/G ratio

corresponds to the increase in the correlation length of the graphitic crystallites. Ferrari *et al.* showed that the D/G ratio for amorphous carbon materials varies between 0 and 2.5; 0 being a characteristic of 100% amorphous structure and 2.5 corresponding to a more graphitic structure.[242] At room temperature, the D/G ratio for all the dots occurred between 1.2 and 1.4, suggesting a mixed sp^2 and sp^3 character typical for hydrogenated amorphous carbon (Figure 4.11a). As annealing temperature increased, the D/G shows a 22% increase around 100^{o}C followed by a gradual decrease which extends to 300^{o}C. This change can be assigned to removal of adsorbed/absorbed moisture, dehydrogenation (annealing at ambient conditions) and stress-relaxations occurring inside the carbon structures deposited at metal surface.[254] At annealing temperatures between 100^{o}C and 300^{o}C, the Raman bands for dots show a 22% decrease in their D/G ratio. This implies the initiation of structural changes inside the dots. After reaching shallow minima at 300^{o}C, the D/G ratio shows a steep rise (36%), reaching around 2.5 at 450^{o}C. This sharp increase in the D/G ratio indicates the dramatic ordering of the graphitic domains and conversion into nano-crystalline graphitic material at the highest annealing temperature.

A similar variation in D/G ratio is observed for carbon lines annealed at different temperatures (Figure 4.11b). Indeed, the D/G ratio for lines at room temperature lies between 1.0 and 1.2, a little lower than the carbon dots. As temperature increased, the D/G ratio showed a steep increase (60%) for temperatures up to 150^{o}C corresponding to the process of moisture removal, dehydrogenation and stress relaxation similar to dots. The process is more prominent owing to the much pronounced structural response of the lines towards the heat transfer across the interface of the line as compared to the dots. This is also relates to the steady decrease in the dimensions of the lines witnessed from the AFM measurements. Further increasing the annealing temperature leads to no

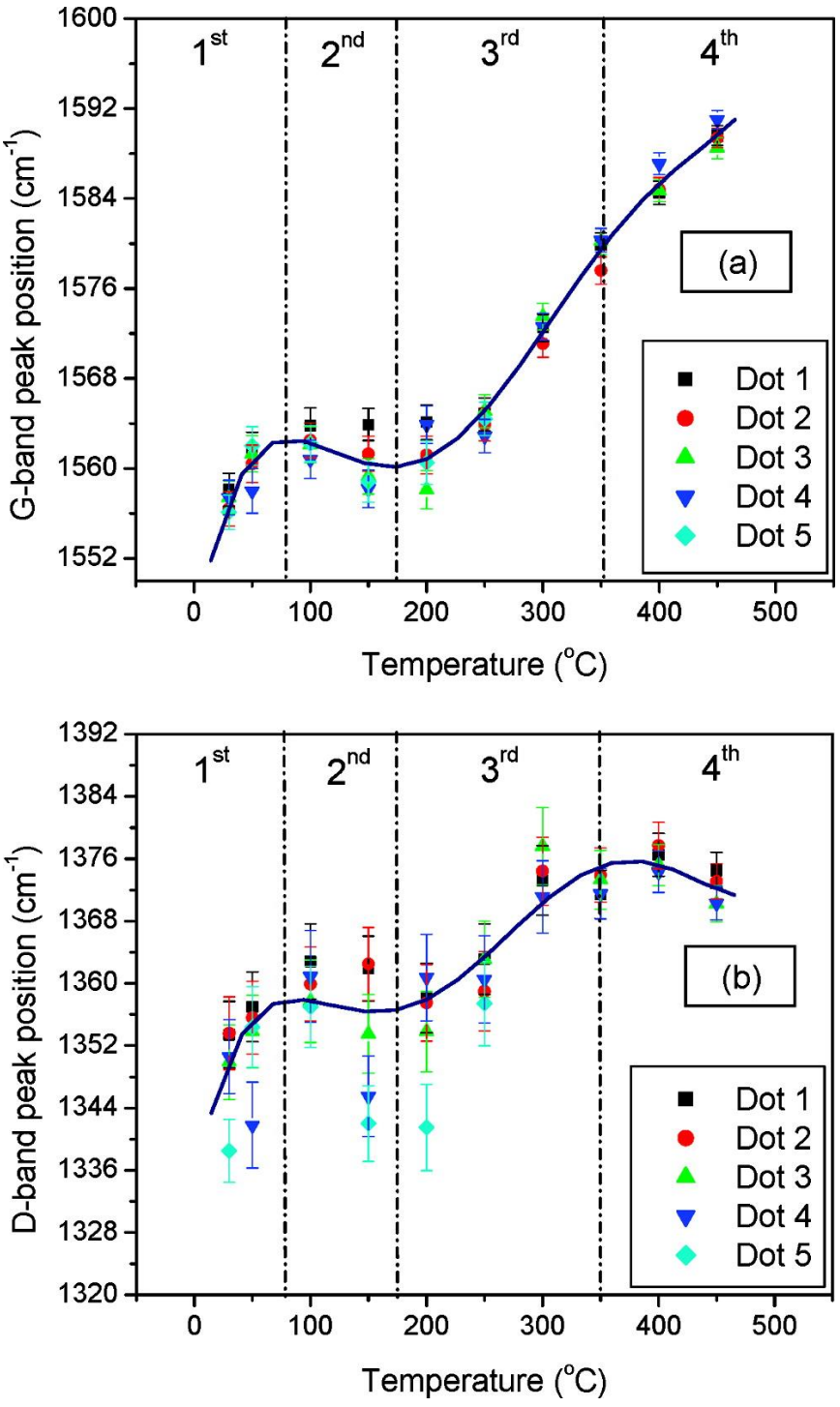

Figure 4.12 G-band peak position (a) and D-band peak position (b) for amorphous carbon dots annealed at different temperatures. Solid lines represent the average of the data points for all sizes at a given annealing temperature

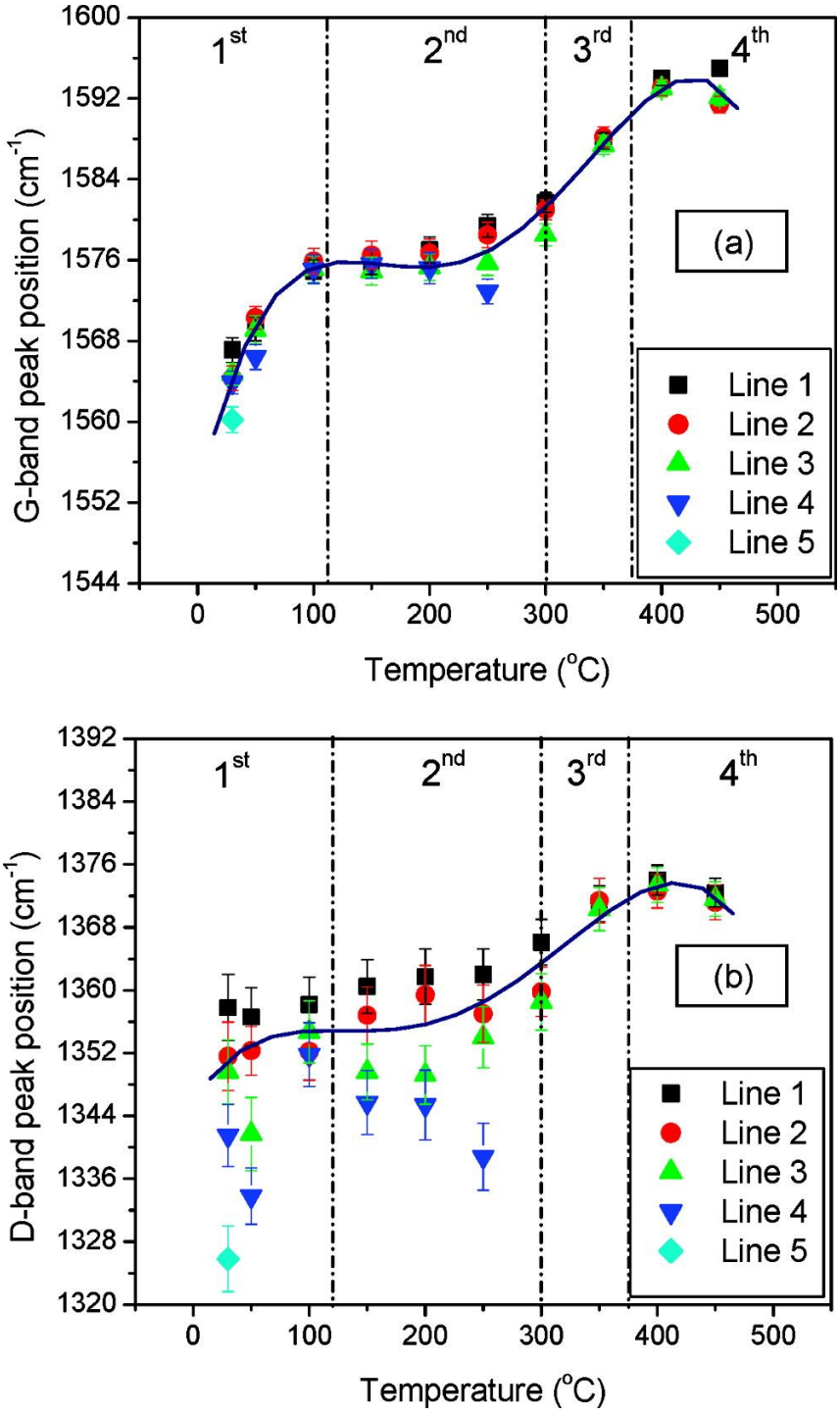

Figure 4.13 G-band peak position (a) and D-band peak position (b) for amorphous carbon dots annealed at different temperatures. Solid lines represent the average of the data points for all sizes at a given annealing temperature

apparent changes in the D/G ratio up to 350^{o}C, suggesting the formation and clustering of the graphitic crystals inside the deposits without significant changes in composition and density. Above 350^{o}C, the D/G ratio showed a gradual increase up to 2.2 at 450^{o}C. This also corresponds to the temperature range at which lines show a dramatic decrease in their height. Thus, from the AFM and Raman measurements it appears that the carbon lines are fully graphitized and densified around 400^{o}C.

Although, the dots show a similar trend in their Raman spectra variations, stress relaxation which occurs in carbon dots at intermediate annealing temperatures is completely absent in corresponding lines. This difference suggests that the long lines studied here are a subject of lower initial stresses related to the limited contribution from small volume of carbon in direct contact with the substrate.

To further elaborate the above suggestion made based upon densification dynamics and D/G ratio variation, we analyze the G and D-band positions of the deposits annealed at different temperatures (Figures 4.12, 4.13). G-band is known to have a strong dependence on the amount of the graphitic crystallites present in the carbon structure. It is known to vary from 1520 cm^{-1} to 1600 cm^{-1} depending on the amount and ordering of the graphitic nanocrystallites. A red shift of the G-band towards higher wavenumbers corresponds to the increase graphitization and ordering of nanocrystals.[240]

Figure 4.12a shows the variation of G-band peak position for the carbon dots annealed at different temperatures. As deposited, the EBID dots show G-band peak position around 1556 cm^{-1} at room temperature suggesting a significant presence of sp^3 content in the system with disordered microstructure, a characteristic of amorphous carbon as was indicated above. As the annealing temperature increases up to 100^{o}C, the G-band shows a shift towards higher wavenumbers, reaching 1560 cm^{-1} followed by a slight down shift

and a further increase above 200^{o}C. At higher annealing temperatures, the G-band position linearly increases to 1580 cm^{-1} (at 350^{o}C), which is related to the formation of ordered graphite nanostructures. With the further increase in temperature, the G-band position reaches 1590 cm^{-1} suggesting the formation of a nanocrystalline graphitic phase above 400^{o}C. A similar trend in the peak position is observed for the D-band (Figure 4.12b). It starts at 1344 cm^{-1} and steeply increases towards 1358 cm^{-1}, followed by a further linear shift, reaching 1372 cm^{-1} at 450^{o}C, indicating clustering and ordering of the crystallites as discussed earlier.

Interestingly, a similar trend in G-band position is observed in case of carbon lines annealed at different temperatures (Figure 4.13a). It can be seen that the G-band position starts at 1564 cm^{-1} (higher than for dots) and continues to shift up to 1576 cm^{-1} at 150^{o}C followed by a small plateau region between 150-250^{o}C. Further increase in the annealing temperature above 250^{o}C leads to the formation of a graphitic phase as indicated by the G-band position reaching 1580 cm^{-1}. Yet, even further increase in the temperature leads to the nucleation of nanocrystalline domains implying the formation of nanocrystalline graphite as can be concluded from band shift above 1590 cm^{-1}. Correspondingly, the D-band position follows similar trend with increasing annealing temperature, further implying the formation of a more ordered graphitic phase (Figure 4.13b). Overall, a continuous increase in the G band and D band positions with increasing annealing temperature strongly supports the argument made above about the formation of nanocrystalline graphitic carbon domains based upon the morphological changes and D/G analysis. The slight decrease in the G-band and D-band peak position near 450^{o}C is difficult to validate by the experimental measurements. However, it might suggest the disruption of the nanocrystalline domains caused by the process of ablation at the highest temperature exploited here.

Thus, our study demonstrates that three distinct structural transformations take place inside the carbon EBID deposits during annealing within a temperature range from 100^{o}C to 450^{o}C as presented in Figures 4.11 and 4.12. These transformations involves loss of adsorbed/absorbed moisture around 100^{o}C, dehydrogenation and stress relaxation at temperatures within 100-200^{o}C, followed by the intense graphitization and the formation of nanocrystalline graphitized nanostructures at the annealing temperatures, above 350^{o}C. By comparing these thermally-induced transformations in the nanoscale EBID deposits with those typically observed for the bulk amorphous carbon films, one can conclude that generally, they follow known transformation for bulk carbon materials except for several significant features as mentioned below.

Firstly, dehydration and dehydrogenation occurs at lower annealing temperatures (100^{o}C -200^{o}C) which significantly affect the physical state of nanoscale deposits. Secondly, at relatively low temperatures, within 150^{o}C-250^{o}C, nanoscale carbon deposits undergo significant stress relaxation, (usually not observed for bulk materials) owing to the significant confinement effects resulting from the large contribution of surface and interfacial regions. Finally, increase in annealing temperature leads to the similar transformations for both carbon dots and lines but it tends to be more gradual in carbon lines as compared to the dots. This difference further supports the argument that the heat transfer process occurs more efficiently in the lines than the dots owing to their higher interfacial area with the metal underneath. It is worth to note that overall trends in phase transformation of carbon deposits stay unchanged for different volumes over four orders of magnitude ranging from few μm^3 for the largest line down to 10^{-3} μm^3 for the smallest dot.

Considering the fact that electronic devices generally fabricated at relatively low temperatures to avoid any thermal effects to adversely affect the properties of the device

components. Thus, in order to use these materials for electronic device applications, it is critically important that ultimate phase transformations for carbon deposits occur *at much lower annealing temperatures* (300^{o}C-350^{o}C) than the bulk materials. This difference makes EBID carbon deposits more attractive than those prepared by different methods such as physical vapor deposition, chemical vapor deposition and sputtering.

Indeed, for these carbon materials complete graphitization and formation of nanocrystalline carbon occurs at significantly lower temperatures than that observed for amorphous carbon films (600^{o}C-800^{o}C). [238,249] We suggest that this significant difference is caused by the fact that the specific surface area for the nanoscale deposits is significantly larger than that for the bulk films, with annealing at ambient conditions also contributing. Moreover, the presence of a heterogeneous interface along with significant surface phonon vibrations on a nanoscale largely influence the physical and chemical properties of the material.[255,256] Moreover, EBID carbon differs from these commonly used techniques primarily in terms of its physical composition and structure by having imbedded volatile species (hydrogen and CH_x). Thus, upon annealing the EBID deposits and the resulting ablation, the formation of a porous structure might occur from the release of hydrogen and other embedded volatile species in contrast with traditional carbon films. Such porous structure may further collapse resulting in post-thermal-processing volume which is much smaller than that based on just change in density of graphite vs amorphous carbon.

Finally, as we suggested in the beginning, these nanoscale carbon deposits might be exploited for making carbon-metal interconnect elements of future microdevices. The results of our study suggest that modest thermal annealing can dramatically increase conductivity of these deposits due to its intense graphitization, important for establishing a robust interconnect. However, the size of the deposits limits the use of most

characterization methods for simple measurements of the conductivity of these nanostructures. Studies are ongoing to address this issue in near future by using conductive atomic force microscopy but it is a very challenging study which will be discussed separately.

In summary, the shape of the deposits and interfacial areas play an important role in the phase transformation behavior of amorphous nanoscale EBID carbon and needs to be considered for its prospective applications in high-performance multifunctional devices. In fact, the ability to graphitize nanoscale amorphous carbon deposits at much lower temperatures compatible with fabrication and packaging microelectronic process allows to effectively control the microstructure of the deposits for creating highly conductive ohmic interconnects across heterogeneous junctions. This further facilitates the need to produce the localized annealing of the nanosize deposits which will be the focus of our future studies.

CHAPTER 5

LIGHT-INDUCED TRANSFORMATION OF CARBON ON METAL NANOPARTICLES

5.1 Introduction

Light-induced transformation of materials is a common phenomenon observed in our day-to-day life for generating energy to sustain life processes.[257,258] Over the years, studies on light-matter interactions have led to the discovery of many light-induced reactions such as photoisomerization,[259] photopolymerization,[260] and photoionization[261]. Also, light-based phenomena such as the photoelectric effect,[262] photomagnetic effect,[263] photoacoustic effect,[264] and photothermal effect,[265] have made their way into many device applications. In fact, photothermal phenomena at the nanoscale have been studied in the efforts to develop and control biochemical reactions[266,267,268,269] induce photomechanical actuation,[270] manipulate the precise growth of nanostructures,[271] improve the efficiency of heterogeneous catalysis,[272,273] and for therapeutic applications.[274,275] This area can also open up opportunities to bring about controlled and localized heating with nanoscale precision for inducing confined phase transition in different materials such as patterning graphene oxide with conductive domains[276]. With the miniaturization of electronic devices, these methods can be used to develop complex phase and interconnect architectures for the semiconductor applications.

In chapter 4, we showed that the phase transformation in nanoscale EBID amorphous carbon deposits takes place between 100-400^{o}C. It has been observed that at lower temperature, stress relaxation and dehydrogenation takes place, followed by partial graphitization and formation of a disordered graphitic phase at temperatures above 300^{o}C. However, these transformations involve subjecting the entire substrate to high

temperatures and are relatively slow, thereby limiting its use for several applications, including fabrication of electronic devices. As known, bulk carbon materials can absorb light more efficiently and have been known to ignite or show a strong thermal emission upon excitation.[277,278] However, nanoscale carbon deposits with sub-micron dimensions cannot be directly employed for light-induced transformations because these structures are light transparent and most of the incident light is not absorbed if special designs are not implemented.

One of the approaches is the exploitation of metal nanostructures to induce local heating at metal-carbon interfaces. Indeed, noble metal nanostructures exhibit a strong absorption in the visible region owing to the surface plasmon resonances in response to the external electromagnetic radiation[279]. This strong light absorption causes a local increase in the temperature of the nanoparticles and can increase the rate of photochemical reaction.[272] Recently, the heat generated by surface plasmons was utilized for bringing about rippling of polymer surfaces and inducing phase transformations.[280,281,282] Brongersma *et. al* showed localized photothermal growth of carbon nanotubes and silicon nanowires due to localized thermal effects.[271]

Herein, we demonstrate a fast and highly localized phase transformation of amorphous carbon deposits on nanoparticulate metal films without global thermal treatment and the subsequent improvements in the deposited carbon's electrical conductivity. We suggest the critical role of surface plasmons excited by the laser source in bringing about a large local increase in the temperature, sufficient to partially graphitize amorphous carbon deposits and quickly convert them to disordered graphitic phase. The annealing kinetics of the carbon deposits on different metal films clearly demonstrates the role of the substrate on the carbon nanodeposit phase transformation.

In this study, EBID was used to make zero-dimensional (dots) and two-dimensional (square) carbon nanostructures on silicon substrate, gold film and silver film. The change in the composition and microstructure of the deposits on different substrates after exposure to the incident light at 514 nm was evaluated using Raman spectroscopy. Also, the effect of the localized heating on the morphology of the substrate was analyzed using atomic force microscopy (AFM). Further, to confirm the increase in electrical conductivity of these deposits associated with the amorphous to graphitic phase transition, conductive force microscopy (CFM) imaging was used to contrast the enhanced electrical conductivity of regions of the carbon deposits selectively exposed to laser irradiation.

5.2 Experimental details

Silicon (100) wafers were cleaned in pirhana solution (3:1 mixture of H_2SO_4/H_2O_2, *hazardous solution*) for 1 hr and then rinsed thoroughly with Nanopure water (18 MΩ-cm).[283] Gold and silver was sputtered on these cleaned silicon substrates for 2 mins and copper was sputtered for 10 mins at 30% setpoint in a Denton Vacuum Desk IV sputterer under argon atmosphere at a pressure of 50 mbar. The average thicknesses of the gold, silver and copper films as measured from ellipsometry were 14.4 $\pm$ 0.2 nm, 10.2 $\pm$ 0.18 nm and 17.0 $\pm$ 0.12 nm, respectively.

Residual hydrocarbons and acetone were used as sources of precursor molecules to induce the growth of carbon deposits over the substrates as discussed in chapter 3. The cone-shaped carbon deposits shown in Figure 5.3 were deposited by keeping the electron beam in spot mode for a period of 10 minutes. Electron beam energy of 25 keV with the electron beam current in the ~20 pA (spot size 3) was used for deposition. The square carbon deposits shown in Fig. 5.11 and Fig. 5.12 were made by scanning the electron

beam at energy of 25 keV and current of ~250 pA (spot size 5), using the 'NPGS' (Nanometer Pattern Generation System) program with 1300 mC/cm^2 of electron beam area dose. In order to keep the thickness of the squares similar, the deposition time per square was 45 mins and 90 mins on gold and silver films, respectively. Silver films shown in Fig. 5.8 were annealed in a Barnstead Thermolyne furnace for 5 sec at different temperatures under normal atmospheric conditions.

As discussed in chapter 3, AFM was used for the surface characterization of the metal films and the carbon deposits. Also, Raman microscopy was used to analyze the changes in the composition of the carbon deposits deposited on the metal films.

5.3 Results and Discussion

5.3.1 Metal nanostructures

Three different common substrates were utilized for this study: silicon (Si) wafer, gold (Au) and silver (Ag) films (see Experimental). Fig. 5.1 shows topographical AFM images of these substrates along with their corresponding cross-sections. Bare silicon and gold films appear to be relatively smooth with a root mean square (RMS) microroughness of 0.17 nm and 0.51 nm respectively, over a surface area of 1 μm^2 (Figures 5.1a and 5.1b). In contrast, silver film show a significantly rough surface with an RMS roughness of 3.6 nm and dense granular morphology with nanoparticles measured to be 12 $\pm$ 0.9 nm in diameter (Figure 5.1c). The gold film shows the presence of continuous island like morphology.

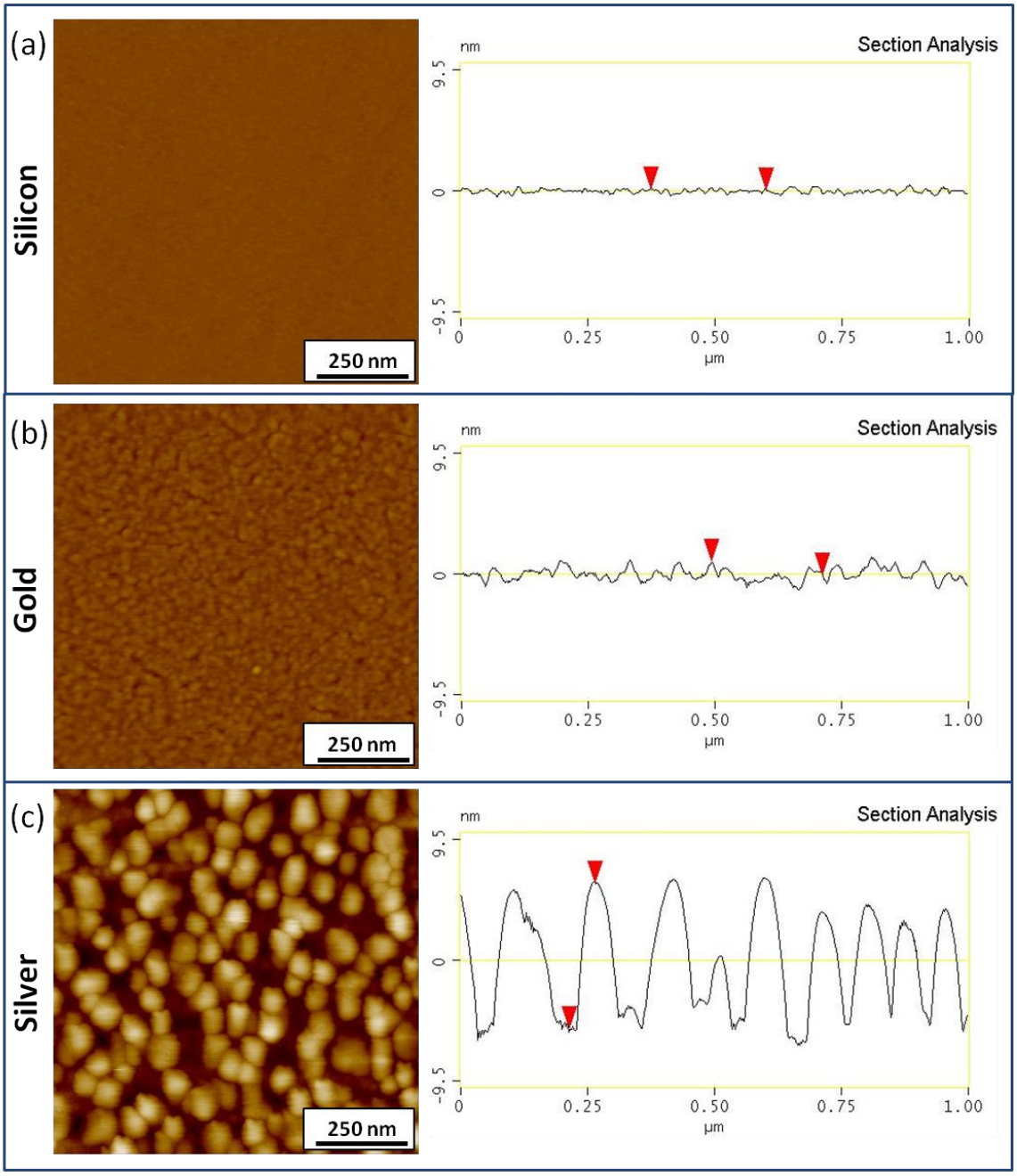

Figure 5.1 AFM images showing the morphology and sectional analysis of different films: (a) silicon substrate, (b) gold film, and (c) silver film. The z-scale is 20 nm for all the images

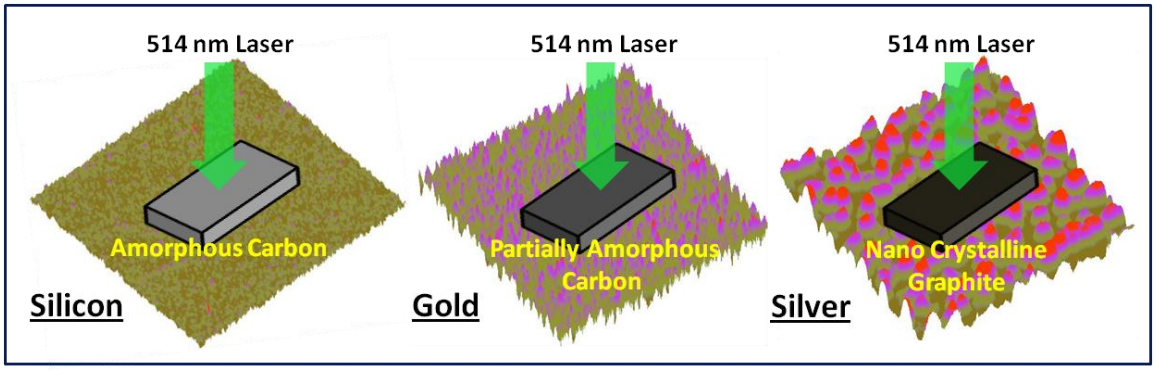

Figure 5.2 EBID carbon nanostructures (grey blocks) fabricated on substrates with different composition (silicon, gold, and silver) and surface morphologies and their physical state on exposure to a 514 nm laser source

5.3.2 Amorphous carbon deposits fabrication

After analyzing the surface morphology of different substrates, EBID carbon deposits of similar shapes and sizes were deposited over these substrates (Figure 5.2). The schematic shows the formation of selected areas with graphitized carbon within carbon films on substrates with different morphologies as will be discussed in detail below. Electron beam focused at a spot for a prolonged period of time lead to the formation of "dot" like structures from residual hydrocarbons ("contamination") as a precursor. SEM images of deposits upon tilting the substrate at 45^{o} with respect to the electron beam reveal a pillar like morphology for the dots (Figure 5.3a). Although, the substrate would have an influence on the morphology of the EBID deposits owing to the difference in the secondary electron yield and surface diffusion coefficient, the dimensions of the deposits on the different substrates were within $\pm$ 200 nm.

The size and structure of the EBID carbon deposits over different substrates were quantified using AFM imaging. Figure 5.3b shows the AFM image of the dots along

with the corresponding 3-dimensional (3D) image (Figure 5.3c) and cross-sectional profile (Figure 5.3d). 3D image of the dots also reveals a pillar like morphology in agreement with the SEM image (Figure 5.3a). The height of the dots is about 1.2 $\pm$ 0.2 µm and its width is 0.72 $\pm$ 0.15 µm, for an electron beam exposure time of 10 mins. The shape and size of the deposits can be varied by adjusting the SEM deposition settings and exposure time as has been discussed in chapter 3.

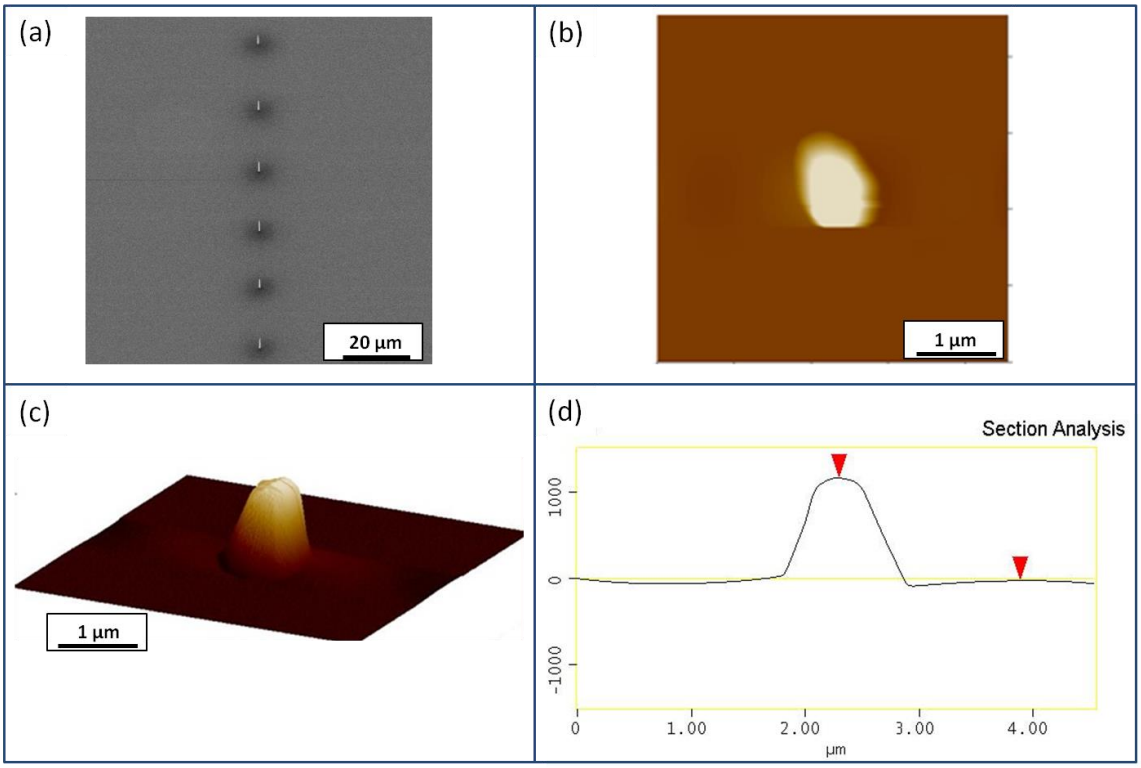

Figure 5.3 Morphology of the EBID carbon deposit. (a) SEM image obtained at 45^{o} viewing showing an array of carbon deposits, (b) AFM image of one of the carbon deposit (z-scale: 1.5 µm), (c) corresponding 3D image showing its pillar like morphology (z-scale: 1.5 µm) and (d) sectional analysis

5.3.3 Phase composition

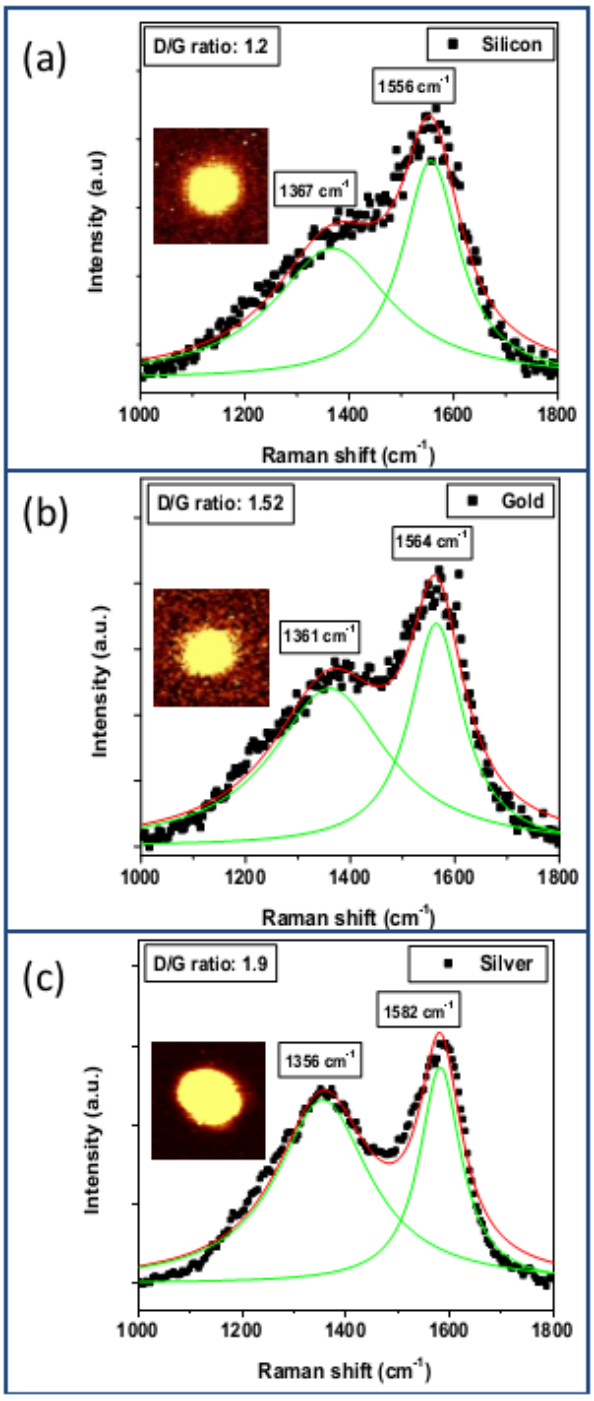

Figure 5.4 Raman spectra of carbon deposits (inset showing the Raman map) on (a) silicon substrate, (b) gold film and (c) silver film

The intrinsic physical state of carbon deposits was analyzed from the Raman spectra collected from individual carbon structures using confocal Raman micromapping under minimum laser power (<1mW) to avoid any laser induced heating. All carbon materials show characteristic D-band and G-band between 1350-1380 cm^{-1} and 1560-1590 cm^{-1} respectively, which relates to the sp^2 and sp^3 content of the system.[241,242] Generally, the Raman spectrum of carbon materials is dominated by the sp^2 sites owing to their higher scattering cross-section.[284] Thus, depending on the peak positions and the intensity ratio of these bands, the microstructure of the material can be identified.[285] Briefly, amorphous and graphitized carbon show G-band peaks around 1520 cm^{-1} and 1580 cm^{-1} respectively and increase in the disorder of a graphitized system leads to the breakdown of the large graphitic domains into smaller moieties, thereby further shifting the G-band peak to 1590-1600 cm^{-1}. This phase is termed as 'nanocrystalline graphite' and represents carbon material with a disordered graphitic microstructure with short-range ordering of graphitic planes.1

Figure 5.4 shows the high resolution Raman map and the corresponding Raman scattering obtained from averaging over 400 individual spectra of the EBID carbon dots on different substrates. The images were obtained by integrating the intensity of the peaks between 1000 cm^{-1} and 1800 cm^{-1} to account for the characteristic D-band and G-band peaks for carbon dots. Interestingly, the carbon dots on different substrates showed significantly different Raman characteristics. The G-band peak position and the D/G ratio of the dots deposited on silicon substrate lies around 1556 $\pm$ 1 cm^{-1} and 1.2, respectively (Figure 5.4a). For carbon deposits on gold film, the G-band peak position is slightly higher than on silicon (1564.6 $\pm$ 1.5cm^{-1}) with the D/G ratio around 1.5 (Figure 5.4b). The sight difference in the G-band peak positions of the carbon dots on silicon and gold substrate may be due to the difference in the internal stresses. These stresses are

formed during fabrication, owing to the difference in the secondary electron yield and surface diffusion coefficient.

In contrast, the Raman spectrum for the carbon deposits on silver film showed the G-band and D-band peaks completely distinguishable from one another. The G-band peak position for dots deposited on silver film reached 1582 cm^{-1} (Figure 5.4c). Also, the D/G ratio is significantly higher (1.9) than the deposits on silicon (1.2) and gold (1.5). This suggests that although the carbon deposits were fabricated under identical conditions, they exhibit different microstructure when exposed to the laser source at 514nm.

The analysis of Raman data suggests that as-deposited carbon dots on silicon substrate are partially amorphous with some sp^2 content. However, the deposits on silver film show G-band peak position shifted significantly above 1580 cm^{-1}, implying an increase in the graphitic ordering with the formation of the nanocrystalline carbon phase inside the structure upon laser exposure, a unique phenomenon revealed in this study.

As is known, an amorphous to graphitic transformation usually requires exposure to high temperature or high pressure.[246,285] However, in this study, the amorphous carbon deposits were subjected to an extremely low laser power (<1mW) under normal atmospheric conditions. This phenomenon suggests that the substrate must be influencing the phase transformation process of the as-deposited amorphous carbon deposits under laser illumination. Particularly, bare silicon substrate shows no effect on the properties of the amorphous carbon deposits. However, noble metal films seem to influence the characteristics of the as-deposited carbon deposits in the presence of a laser source. Thus, the interaction of electromagnetic waves with the metal film needs to be studied in order to understand the laser-assisted phase transformation.

5.3.4 Optical properties of sputtered metal films

Figure 5.5 represents refractive index and extinction coefficient of gold and silver films used in this study. The gold film showed a slight variation of refractive index up to 450 nm, followed by a steady decrease with an increase in wavelength (Figure 5.5a).

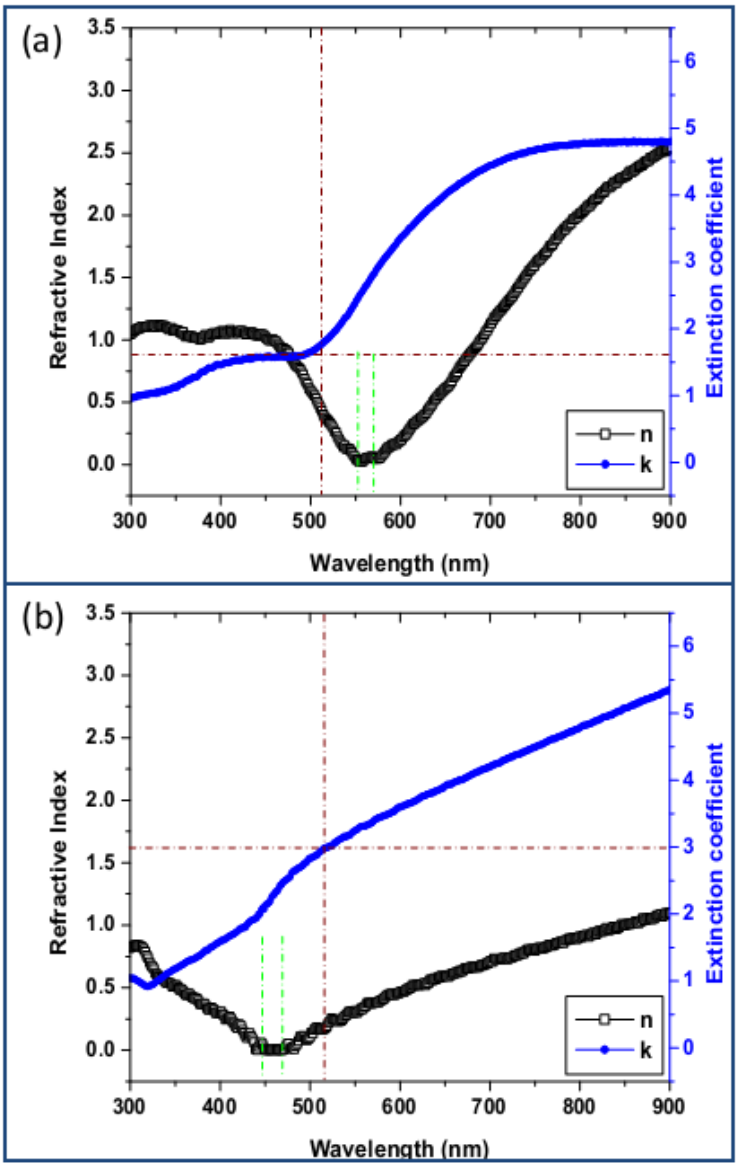

Figure 5.5 Variation of refractive index (n) and extinction coefficient (k) with wavelength of (a) gold film, and (b) silver film

It shows a near zero refractive index at wavelengths between 550-580 nm and continues to rise thereafter. A similar trend is observed for the silver film (Figure 5.5b). The refractive index show a slight variation in the near UV wavelengths followed by a steady decrease, approaching zero between 550-580 nm and continues to steadily increase up to 900 nm. These results correlate well with the optical properties of evaporated metal films reported by Sennett *et al*.[286] At shorter wavelengths, bound electrons contribute towards the absorption whereas at higher wavelengths, the absorption is more dominant. This transition occurs in the visible region and UV region of the electromagnetic spectrum for gold and silver films, respectively. In the case of gold films, the absorption increases at wavelengths above 550 nm whereas silver film strongly absorbs at all wavelengths.

Figure 5.5 also gives the variation of extinction coefficient of the metal films with the wavelength. The extinction coefficient for the gold film shows an increase up to 500 nm with a small bump around 420 nm and sharply increases up to 700 nm (Figure 5.5a). Above 700 nm, the extinction coefficient for the gold film saturates. For the silver film, the extinction coefficient shows a near linear increase from 300 nm to 450 nm and undergoes a transition between 450-480 nm and continues to linearly increase up to 900 nm (Figure 5.5b). It is interesting to note that the extinction coefficient of these films shows little variation at wavelengths where the refractive index approaches a minimum.

The sudden drop in the refractive index of the metal films is caused by the free electron transition which occurs due to the resonant coupling between the surface plasmons and incident electromagnetic wave and can be described using the Drude model for free electron oscillations.[287,288,289,290] At the resonant frequency, the real part of permittivity approaches zero and consequently the refractive index approaches zero. A refractive index of less than 1 represents a pure metal-like behavior of the sputtered films.

However, these resonances occur at slightly different wavelength than that of our laser source.

Comparing the absolute values of the extinction coefficient at 514 nm, the absorptive index of silver (3.0) is significantly higher than that for gold (1.75), suggesting that the silver film absorbs light more efficiently than the gold film. Thus, on exposure to the incident light, the surface plasmons of silver nanoparticles oscillate near its resonant frequency and absorb the incident light more efficiently than the gold surface, though the plasmon resonance of gold is also close to the laser wavelength.

Such localized electromagnetic enhancement of light is achieved by excitation of the surface plasmons of metal nanoparticles at or near their resonant frequency.[291,292,293] As a result, metal nanoparticles are known as nano-heat generators, absorbing incident light and converting it into thermal energy.[273,294,295,296] This heating effect is especially strong under the plasmon resonance conditions when the energy of the incident photons is close to the plasmon frequency of metal nanoparticles. Thus, the optical properties of metal films demonstrated above, we suggest that this thermal energy generated might be responsible for bringing about the phase transformation of amorphous carbon deposits.

5.3.5 Effect laser exposure on sputtered metal films

To further consider the effect of the laser illumination on the metal films, we studied the silver and gold films under identical direct light exposure. Figure 5.6 shows the topographical AFM images of these exposed areas along with the corresponding phase images. It can be clearly seen that the surface morphology of the silver film changes significantly in the areas exposed to the laser, whereas the gold film does not show any apparent change in its surface features. A high resolution AFM image in Figure 5.7

shows that the nanoparticles within the laser-exposed regions of the silver film became significantly reduced in size, indicating intense changes in silver nanoparticle morphology after exposure to light. The average size of the silver nanoparticles in the exposed areas is 2.3 nm, as compared to 12 nm in the unexposed areas.

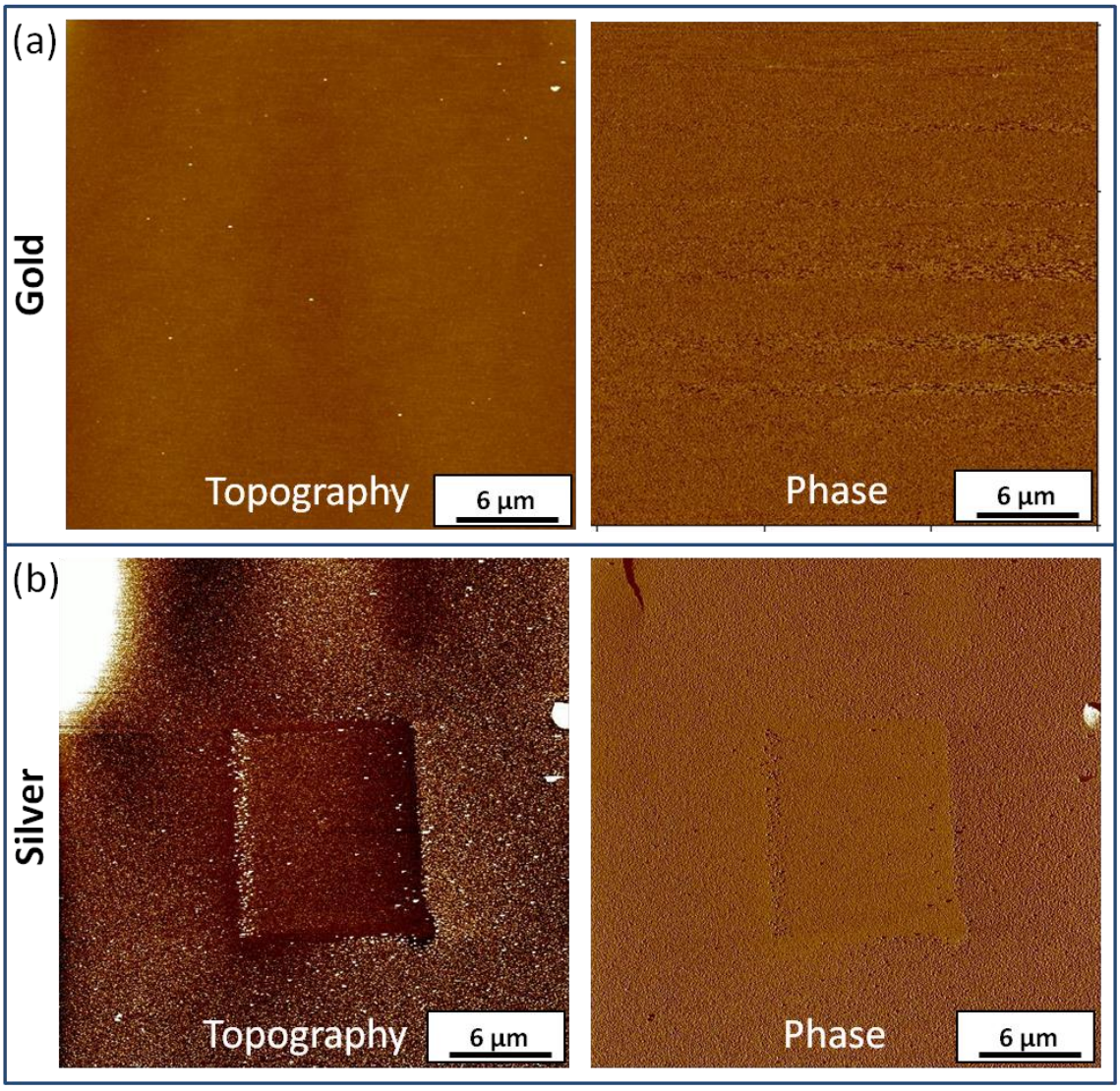

Figure 5.6 AFM image of the metal films after exposure to the laser showing the topography (z-scale: 20 nm) and phase (z-scale: 60^{o}) of (a) gold film and (b) silver film

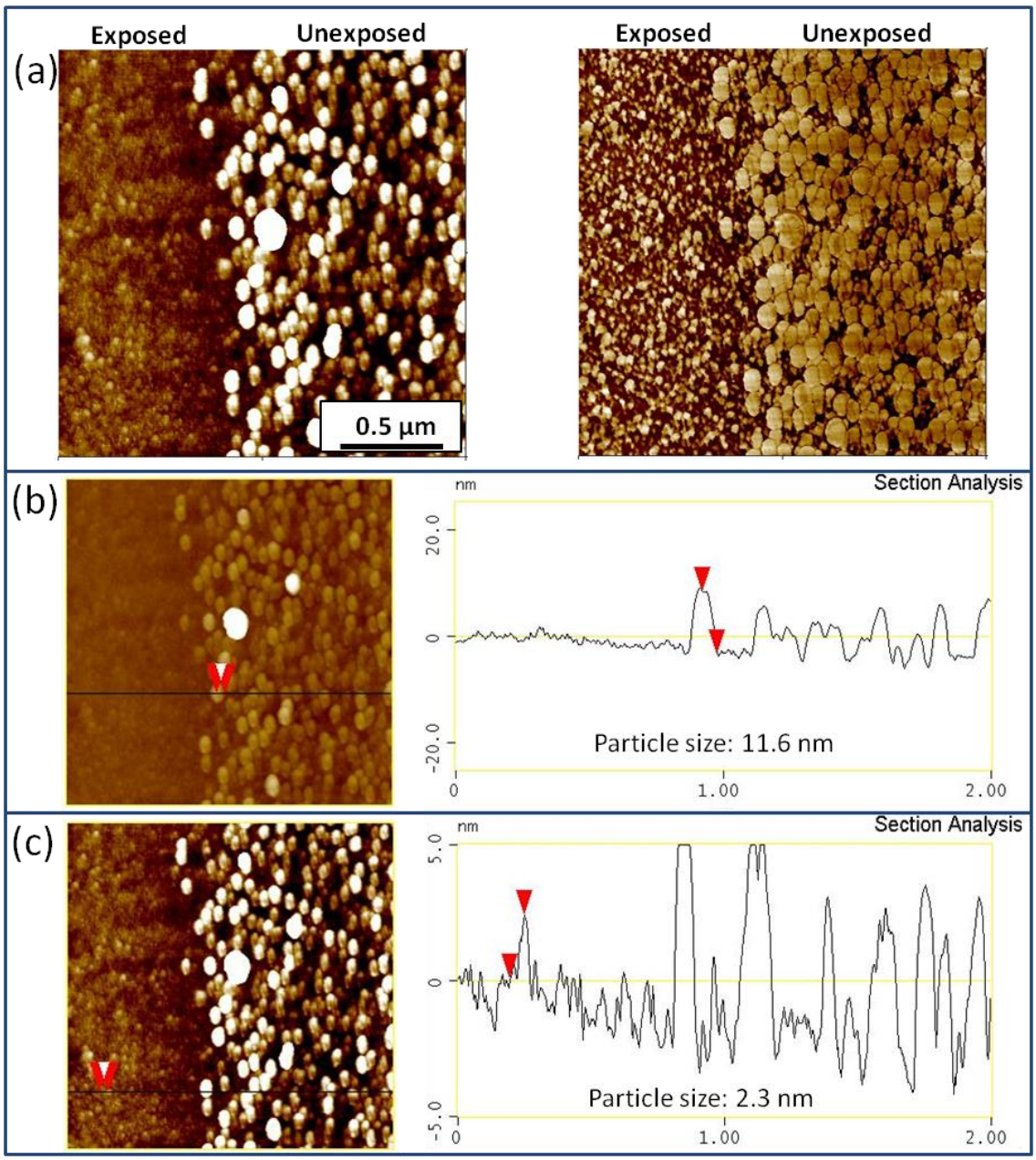

Figure 5.7 High resolution AFM image showing the difference between the laser exposed and unexposed areas of silver film. (a) topography (left; z-scale: 10 nm) and phase (right; z-scale: 60^{o}). Sectional analysis showing the height variation in the (b) unexposed and (c) exposed areas

Ablation of metal nanostructures using a high powered laser source is well known in the literature.[297,298,299] However, the laser used in this research is a low-power continuous laser and the power density used in this study is several orders of magnitude (at least four) lower than that reported.[300] Thus, direct light-induced ablation of the metal nanoparticles is improbable under our experimental conditions. We speculate that the localized excitation of surface plasmons of the silver film that possess absorption near the incident laser frequency causes temperature to dramatically in the exposed areas, to a value high enough to affect the surface morphology of the area. Also, it is well established from our previous work that a temperature of around 350-400^{o}C would be required for the EBID amorphous carbon deposit to graphitize completely. Although the exact temperature at the surface of the nanoparticles on laser exposure is a challenge to measure with our current experimental conditions, an estimate of the temperature required for silver nanoparticle morphology changes would be necessary.

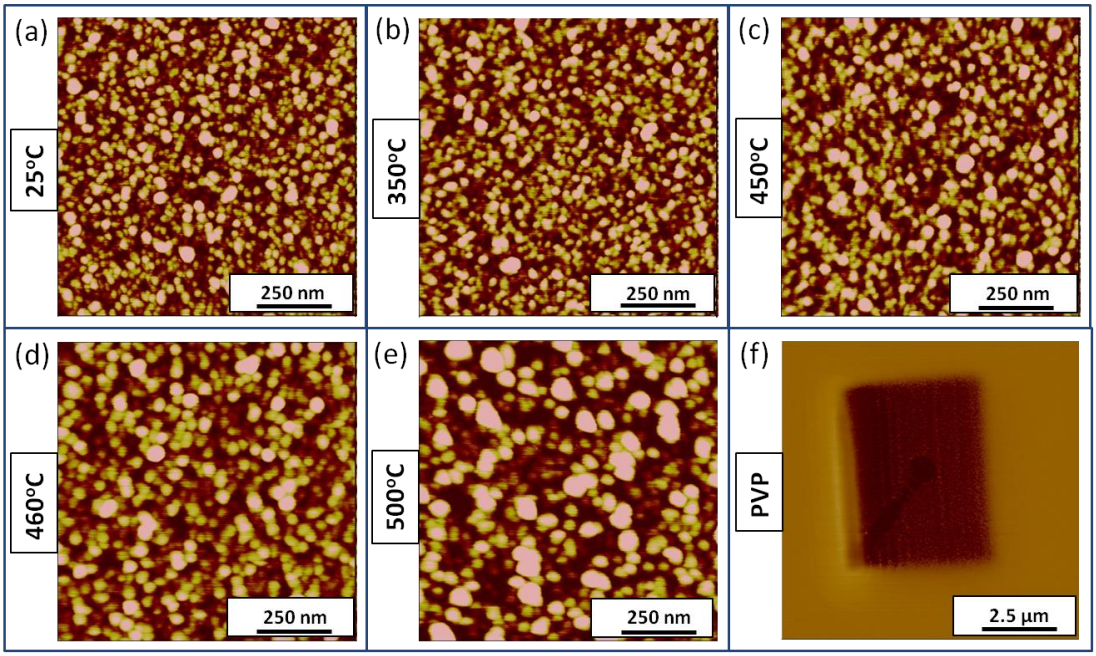

Figure 5.8 High resolution AFM image showing the morphology of the silver film at different temperatures. The z-scale is 10 nm for all images

5.3.6 Local temperature estimation

Figure 5.8 shows the morphology of the silver film annealed at different temperatures. It can be seen that the surface morphology of the silver film remains unaltered on annealing up to 450^{o}C, with a uniform particle size distribution over the entire surface. Annealing above this temperature results in an increase in the lateral dimensions of the silver nanoparticles with the height decreasing to 7.3 $\pm$ 1.1 nm. These changes suggest that the silver nanoparticles melt on annealing above 450^{o}C. Thus, exposing the substrate to the highest temperature results in local melting causing the silver nanoparticles to aggregate and grow in size. On the contrary, in case of the sputtered silver film exposed to the laser source, the particles are in a state of confinement in the exposed areas and account for the excess temperature by reduction of size and increasing specific surface area.

It is logical to assume that the temperature required for bringing about a change in morphology of silver nanoparticles would be similar for thermal-based annealing and laser-based transformation. To further confirm this independently, thin films of common polymers, such as poly(4-vinylphenol), with well known thermal decomposition temperature above 360^{o}C,[301] were deposited on noble metal substrates and exposed to the laser under identical conditions. As a result, we observed an intense and highly localized thermal decomposition of a 100 nm thin film of the selected polymers deposited on silver substrate in areas exposed to the laser, whereas the morphology remained unaffected for a similar polymer film deposited on silicon. Such thermal decomposition additionally confirms a localized plasmon-assisted laser-induced thermal heating on silver surface with temperature well exceeding 360^{o}C.

5.3.7 Application of laser-induced phase transformation of carbon on copper substrate

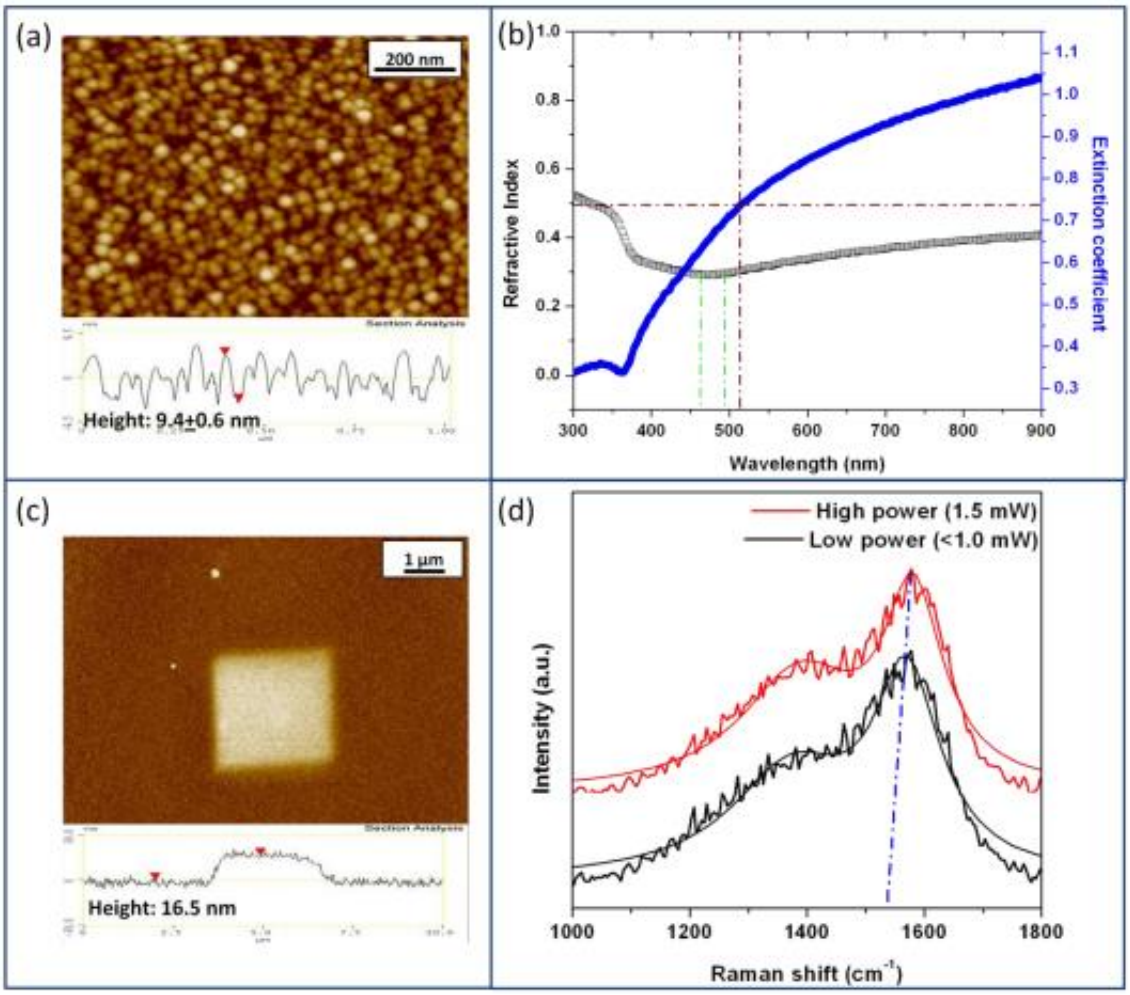

Figure 5.9 (a) morphology of the copper film showing granular morphology along with the cross-sectional profile (z-scale: 20 nm), (b) The variation of refractive index (n) and absorption coefficient (k) with wavelength of copper film, (c) topography of the EBID carbon square deposited on the copper film along with the cross-sectional profile (z-scale:40 nm), (d) Raman spectra of the carbon square at different laser power (dotted blue line indicates the blue shift in G-band position

As a proof of concept, we studied the effect of laser exposure on the physical state of the carbon deposits fabricated on top of a copper substrate, a commonly used material in the semiconductor industry. Figure 5.9a shows the morphology of the copper substrate along with the corresponding cross-sectional analysis. Similar to the silver substrate, the copper substrate also showed the presence of a granular surface topography with a particle size of 9.4 $\pm$ 0.6 nm. Further, on measuring the optical properties of the copper film, it was observed that the refractive index of the film approaches a minimum between 460-500 nm corresponding to the free electron oscillations of the surface plasmons as a response to the incident electromagnetic radiation (Figure 5.9b). Thus, the surface plasmon resonance of the copper film was also near the laser excitation wavelength as observed for the gold and silver film.

However, on comparing the extinction coefficient of the copper film with the gold and silver films, it was observed that the copper film absorbs 2.5 times less light than the gold film and 5 times less light than the silver film at 514 nm wavelength. Thus, according to our hypothesis put forth in the earlier sections, the carbon deposits should not graphitize on the copper film. In order to prove this, we fabricated carbon squares on top of the copper film. Figure 5.9c shows the morphology of the carbon square along with the corresponding cross-sectional profile. The height of the square was around 16.5 nm with lateral dimensions of ~ 3 um x 3 um. On exposing the deposit to the Raman laser at 514 nm, it was observed that the deposit showed amorphous behavior as expected with the G-band position around 1568 cm^{-1} (Figure 5.9d).

This suggests that the surface plasmons of the copper film do not absorb enough light at 514 nm to bring about a local increase in the temperature, high enough for graphitization of the carbon deposit. However, in order to increase the effective absorption of light at 514 nm, the laser power can be increased. Thus, we exposed another carbon square

fabricated under similar conditions as before to the laser source at slightly higher power (~1.5 mW) and monitored the Raman spectra. On analysis, it was observed that the G-band peak position blue shifts towards the graphitic peak position at 1580 cm^{-1} (Figure 5.9d). This further validates the role of surface plasmons in bringing about a localized phase transition in amorphous carbon deposits on exposure to the light.

5.3.8 Kinetics of laser-induced phase transformation

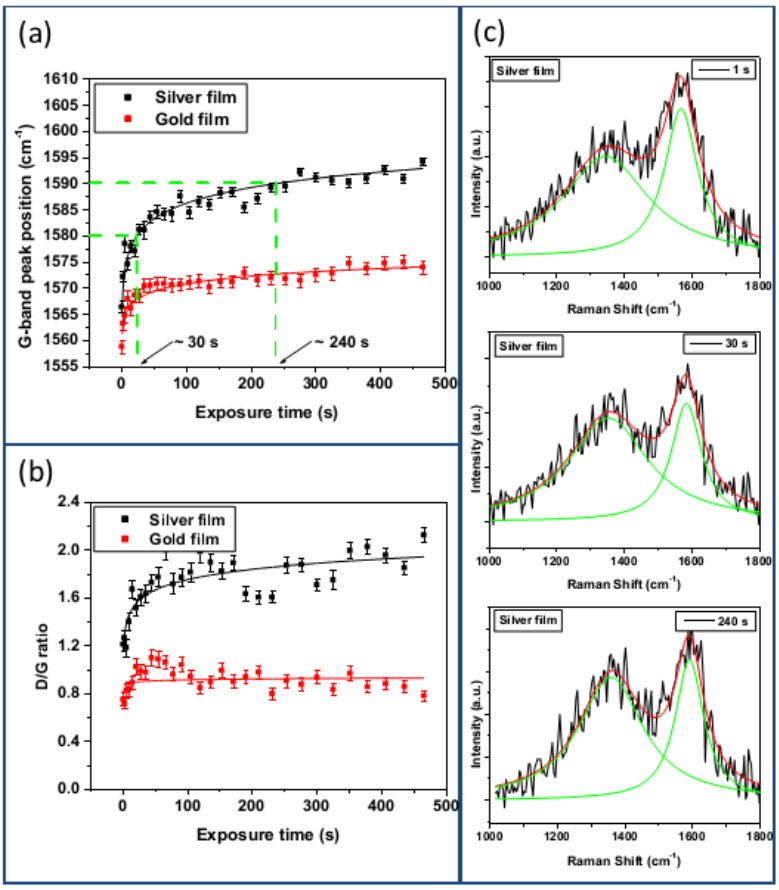

Figure 5.10 Kinetics of phase transformation of the carbon deposit on different metal films on exposure to 514 nm laser source. (a) G-band peak position of the carbon deposit at different exposure time (Solid lines represent average of the data points) (b) corresponding D/G ratio (Solid lines represent average of the data points) and (c) Raman spectra of the carbon deposit on silver at different time intervals

The carbon dots on different metal films were exposed to the laser illumination under minimum power (<1mW) for increasing periods of time and spectra were recorded after each exposure interval to monitor kinetics of graphitization transformation. Figure 5.10 shows the variation of G-band peak position and the D/G ratio for the dots deposited on silver and gold films. It can be seen that initially the deposits are amorphous with the G-band peak position around 1558 cm^{-1} and 1567 cm^{-1}, on gold and silver films, respectively (Figure 5.10a).

Also, the D/G ratio for deposits occurs around 0.8 on gold and 1.2 on silver films (Figure 5.10b). As the exposure time increases, the G-band peak position for carbon deposits on silver films steadily increases, and reaches 1580 cm^{1} after ~30 seconds of light exposure with D/G ratio increasing to 1.6. Further increase in the exposure time results in the steady shift of G-band peak position towards 1590 cm^{-1}, suggesting the formation of a nanocrystalline graphitic phase. Thus, the carbon deposits on silver film undergo a rapid (tens of seconds) transition from amorphous to graphitic to nanocrystalline graphitic phase (Figure 5.10c).

The G-band peak position of deposits on gold films shows a sharp increase up to 1572 cm^{-1}, during the initial exposure followed by a plateau region (Figure 5.10a). This minor shift suggests that the carbon deposits on gold undergo only partial graphitization to disordered graphitic phase, without a complete transformation. The D/G ratio of carbon deposits on gold film remains about constant around 0.9 (Figure 5.10b).

5.3.9 Electronic properties of carbon deposits upon laser exposure

In order to address the practical implication of amorphous to graphitic phase transformation in controlling electrical properties of carbon-metal interfaces, we

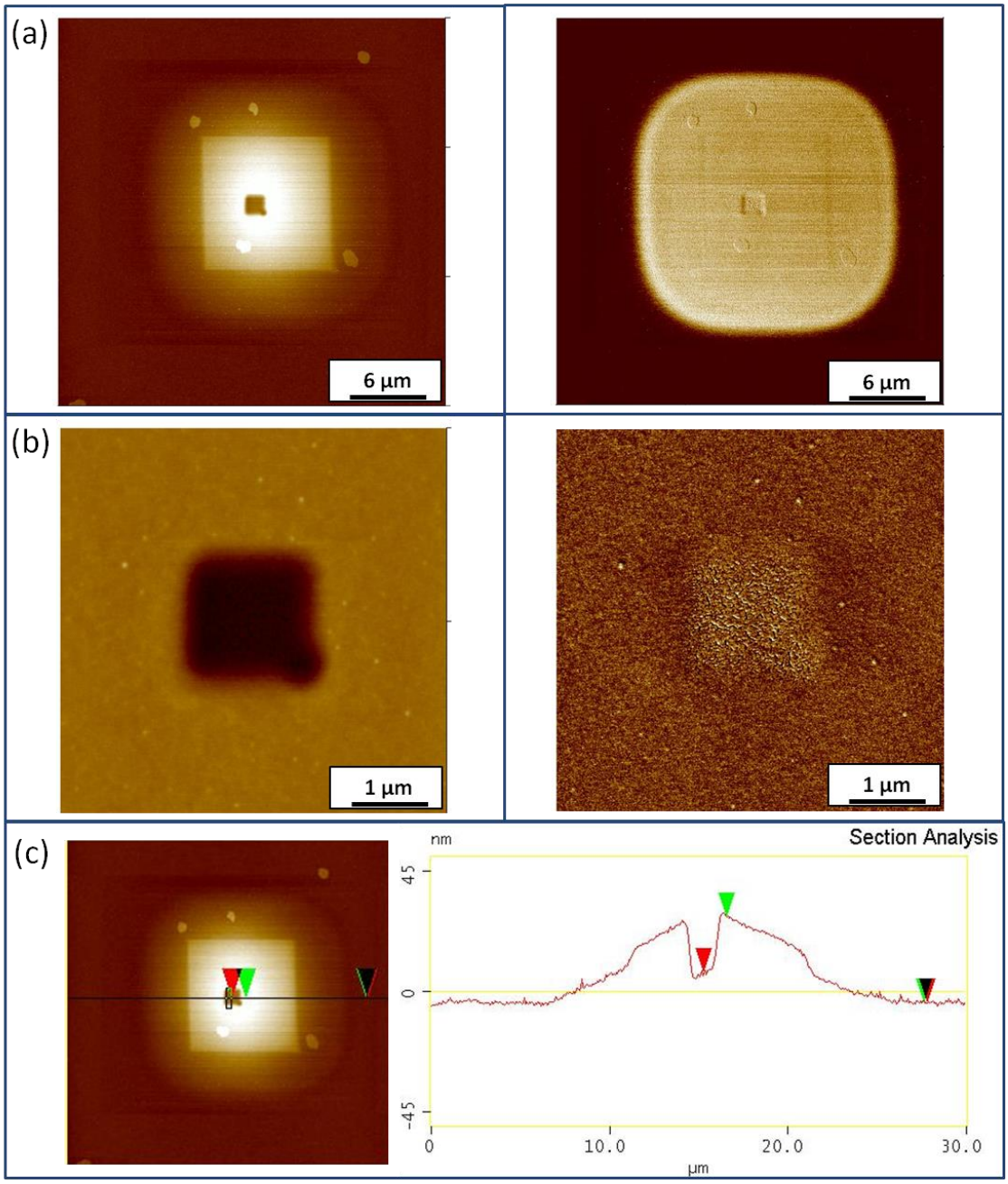

Figure 5.11 Morphology of amorphous carbon square on gold film. (a) topography (z-scale: 100 nm) and the corresponding phase (z-scale: 90^{o}) showing the square and the laser exposed area at the center, (b) high resolution topography (z-scale: 50 nm) and phase (z-s cale: 50 nm) and phase (z-scale: 30^{o}) of the laser exposed areas showing the difference in morphology and (c) sectional analysis of laser exposed area

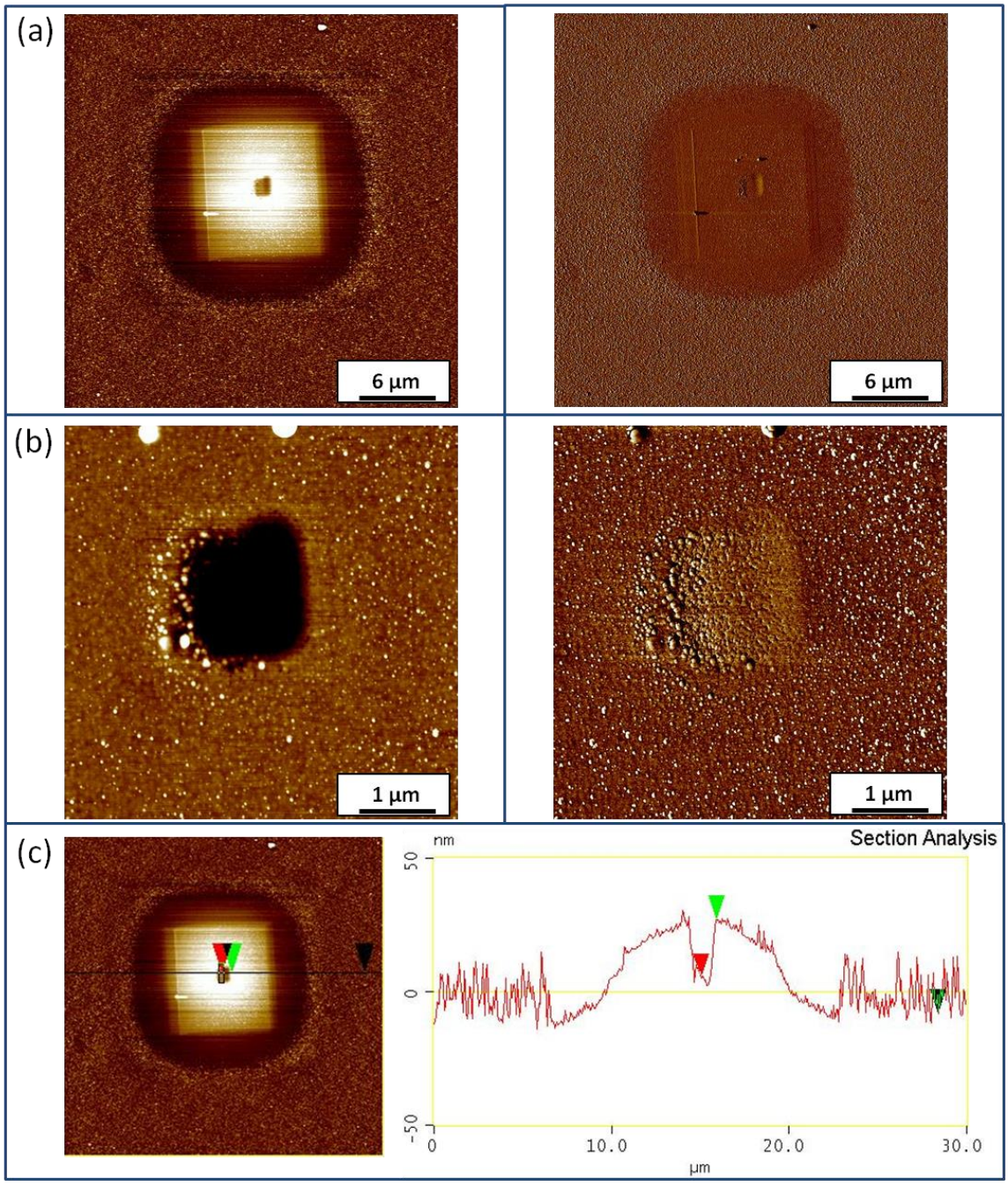

Figure 5.12 Morphology of amorphous carbon square on silver film. (a) topography (z-scale: 100 nm) and the corresponding phase (z-scale: 90^{o}) showing the square and the laser exposed area at the center, (b) high resolution topography (z-scale: 50 nm) and phase (z-scale: 50 nm) and phase (z-scale: 30^{o}) of the laser exposed areas showing the difference in morphology and (c) sectional analysis of laser exposed area

performed CFM measurements of laser-exposed amorphous carbon deposits. Here, an electrically biased metal coated tip rasters across the surface of carbon deposits and the current flowing through the system is recorded.[211] The current flow will thus depend on the contact resistance between the tip and the surface and the resistance of the material itself. In order to have a valid comparison between the amorphous and graphitic domains, we used the same tip to scan both areas within the same sample. However, the shape of the dots is not ideal for such measurements because the pillar-like morphology can be easily destroyed by the large forces used during the CFM scanning process. Therefore, we exploited flat squared carbon deposits for CFM experiments.

Figure 5.11a shows the amplitude (morphology) and phase (stiffness) of EBID square carbon deposit on a gold film for CFM experiments. It can be seen that the carbon square shows some non-uniformity in its thickness with its center being higher than the periphery, with the height of the square ~32 nm at the center. Inside the square, a smaller dark square can be seen, which represents the surface area which was exposed to laser illumination under similar conditions as before. High resolution AFM imaging around the exposed region shows that the laser ablates a part of the deposit (Figure 5.11b). The laser exposure resulted in the ablation of the deposit forming a crater up to 20 nm deep. This suggests the oxidation of sp^3 carbon from the deposit. However, a thin layer of the material (~12 nm) still remains intact after exposure to laser irradiation. The phase image also reveals the formation of an area with different surface properties within the exposed region.

Figure 5.12a shows similar topographical features of the EBID square carbon deposit on a silver film as seen on gold film. Exposure to the laser illumination resulted in the ablation of the carbon deposit with initial thickness of 35 nm (dark square at the center). High resolution AFM images near the exposed areas reveal changes in morphology of the

initially amorphous carbon (Figure 5.12b). The laser exposure resulted in a significant reduction in its size due to material ablation with a residual (~13 nm) carbon film left within the laser exposed "crater". The phase image shows the formation of carbon material with different physical structure in the areas exposed to the laser beam. This similarity suggests that the laser exposure has similar effect on the morphology of the amorphous carbon deposits on different substrates.

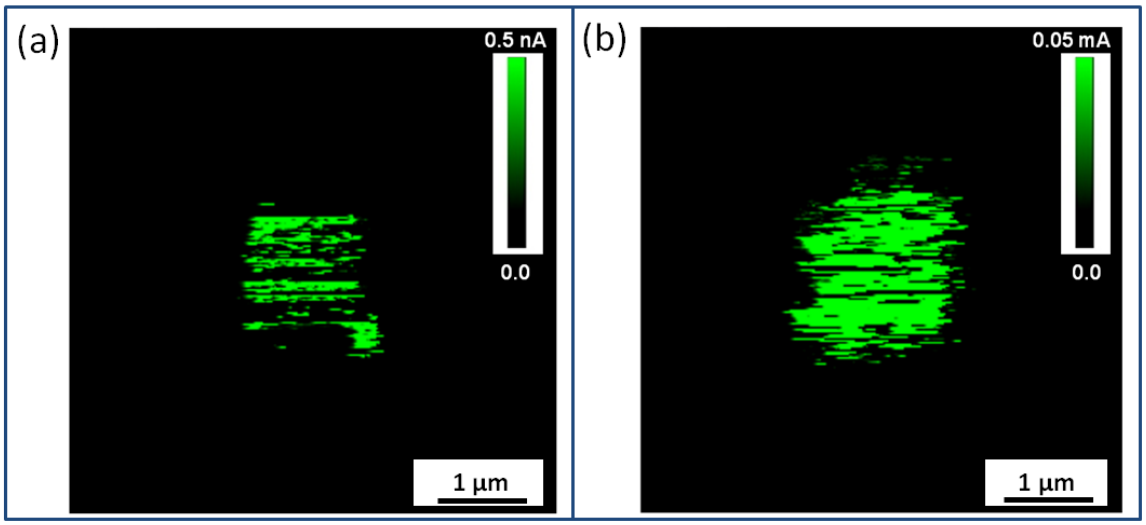

Figure 5.13 Conductive atomic force microscopy imaging of the deposit on (a) gold film and (b) silver film

According to the arguments put forth earlier based upon Raman scattering studies, it is expected that the areas exposed to the laser irradiation would consist of disordered and nanoscale graphitic domains while the remaining film should consist of amorphous carbon. Figure 5.13 shows the conductivity map of these deposits on different metal films obtained via CFM. The deposit on the gold film shows much improved conductivity at the laser exposed areas. However, the surrounding area shows practically no current flow, i.e., carbon film remains nearly insulating. Exact values of the resistance cannot be obtained quantitatively owing to the unknown contact resistance. However,

qualitatively the CFM images clearly identify the graphitic and amorphous domains and degree of graphitization. Moreover, the area of amorphous carbon exposed to the laser on the silver film shows a much greater electrical conductivity (Figure 5.13b, current of 0.05 mA flows from the CFM tip to the substrate on applying a sample bias of 3.0V) as compared to the deposits on gold film (Figure 5.13a, current of 0.5 nA flows from the CFM tip to the substrate on applying a sample bias of 9.0V). It is difficult to estimate or compare the electrical conductivity of the amorphous carbon in the unexposed areas of the square deposit since it shows no measurable current even after applying a maximum sample bias of 10 V. However, since the amorphous carbon maintains its identity in the unexposed areas, irrespective of the underlying substrate, it can be said that the electrical conductivity of amorphous carbon is significantly lower than that of partially graphitized carbon on the gold film. The electrical conductivities of gold (4.2×10^7 S/m) and silver (6.2×10^7 S/m) are large and almost identical at room temperature.[302]

Thus, assuming the contact resistance between the sample and the tip to be same in both cases, presence of the silver film resulted in an increase in electrical conductivity by over six orders of magnitude (resistance of the laser exposed carbon film is ~ 60 kΩs on silver substrate, compared to ~14 GΩs on gold substrate), and thus much improved overall electrical contact conductivity (or dramatically decreased resistivity) at carbon-silver interface after laser-induced transformation.

CHAPTER 6

SCANNING THERMAL TWIST MICROSCOPY – A NOVEL TECHNIQUE FOR NANOSCALE THERMAL IMAGING

6.1 Introduction

Scanning thermal microscopy (SThM) is a critical technique in the analysis of thermal, electronic, and photonic transport at dimensions approaching the mean free path of phonons and other quasi particles.[303,304] Unfortunately, commercial probes are typically limited to sub-micron spatial resolution and thermal sensitivity of a fraction of a degree.[305,306,307] Over the years many different thermal sensing mechanisms have been explored for SThM including the Seebeck effect,[308,309,310,311,312] temperature dependant resistance,[313] and thermal bimorph bending.[314] The thermal bimorph mechanism utilizes the difference in thermal expansion of two materials intimately bound to cause bending stresses in response to heat.[315] Thermal bimorph bending has very promising properties, but has remained impractical for SThM because the thermal bending directly interferes with topography imaging. Here, we re-examine the bimorph mechanism for SThM and address this major limitation by introducing scanning thermal twisting microscopy. The thermal-topographical signal interference issue is solved by creating a probe with an asymmetrical bimorph geometry that twists, instead of bends, in response to heat.

Since the introduction of thermal probes,[316] there have been major improvements in SThM, but the widespread use has unfortunately been hindered by the high cost of commercial probes, as well as their modest spatial (typically~100nm) and thermal resolution(~0.1^{o}K).[317,318,319,320,321] Furthermore, commercial resistive-based probes can also suffer from cross-talk between thermal and electrical signals when imaging electrical circuits. Thermal bimorphs do not suffer from these setbacks. In fact, thermal bimorphs

transduced with an AFM quadrant photodetector have a theoretical limit of thermal resolution on the order of 10^{-5} K, two orders of magnitude better than the theoretical limit of electrical techniques.[314] As mentioned, the impediment to this approach is that the thermal signal and the topographical signal utilize the same signal transduction channel, namely normal deflection of the laser spot in the quadrant photodiode (Figure 6.1a). In order for SThM to function properly, the tip-surface distance must be accounted for by performing SThM in conjunction with atomic force microscopy (AFM). The topography imaging of the AFM is critical to maintaining the thermal probe/sample distance, thereby enabling the inherent thermal properties to be mapped. Therefore, typically the thermal bimorph effect is considered a nuisance, despite promising properties. While the thermal bimorph effect interferes with the topographical signal, this has not stopped researchers from trying to utilize this transduction mechanism for SThM. For instance, in order to circumvent the signal overlap issue, Majumdar and co-workers used a microfabricated resistive heating substrate to sinusoidally heat the sample at a frequency on the order of 100 Hz.[314] While this technique worked fairly well, it unfortunately requires a microfabricated substrate and complicated electronics and therefore did little to address cost issues associated with SThM.

Scanning thermal twisting microscopy (STTM) addresses the thermal-topographical signal interference issue by creating an assymetrical bimorph geometry that twists the microfabricated cantilever with thermal changes, thereby using the lateral deflection signal ((A+C)-(B+D)) for thermal imaging, while maintaining the normal deflection signal ((A+B)-(C+D)) for concurrent topographical imaging (Figure 1b). This design does not require complicated and expensive electronic equipment; instead the imaging technique relies only on the hardware already typically provided by AFM manufacturers.

Inherently, the lateral (twisting) spring constants of cantilevers are much higher than the normal spring constants. V-shaped cantilevers have lateral (twisting) spring constants that are roughly 500 times more stiff than normal bending spring constants.[322] Therefore, to realize thermal twisting probes it is critical to maximize the thermal expansion mismatch between the materials to overcome the inherently high lateral stiffness. Most thermal bimorph work thus far has involved ceramic/metal composites with rather poor sensitivity due to a small thermal expansion difference of the two materials making up the bimorph. Instead, polymer/ceramic composites have proven to be much more sensitive due to high thermal expansion coefficient of the polymeric materials.[323] LeMieux et al. developed highly sensitive probes through the use of plasma polymer-silicon bimorphs with high mismatch of thermal properties.[324,325,326] These cantilevers had an unprecedented thermal resolution of 0.2 mK. Furthermore, this work demonstrated plasma polymers have excellent adhesion to silicon and excellent long-term stability.

6.2 Experimental details

Probe Fabrication and STTM: Mikromasch NSC-11 (Al-BS) probes were coated with a 90 nm thick plasma polyacrylonitrile films on the top side and underside of the probe. The plasma enhanced chemical vapor deposition was done in a custom PECVD chamber.[324] Argon was used as a plasma carrier gas, which entered the chamber 20 cm upstream of the plasma generation zone at a flow rate of 20 cc/min. The plasma was generated with a capacitive coupled radio frequency discharge source with a frequency of 13.56 MHz and a power of 20W. The acrylonitrile monomer vapor entered the chamber approximately 10 cm downstream of the plasma source at a flow rate of 1 cc/min. The cantilever chips (Mikromasch NSC-11 Al-BS) were mounted on a silicon wafer substrate that was mounted to the chamber chuck about 3 cm downstream from the monomer inlet

stream. Plasma polyacrylonitrile films (90 nm thick) were deposited on the each side of the probe in two separate identical deposition runs. The thickness was measured by ellipsometry on the silicon wafers. Focused ion beam milling (FEI DB-235) was used to remove opposing halves of the two polymer coatings. Typically, the polymer film was removed by raster scanning the FIB at an accelerating voltage of 30kV and a current of 20nA over a 130 x 115 μm rectangular area that included the polymer region targeted for removal for 3 minutes. Most of the STTM work (including the images presented was performed with a DI-3000 equipped with a Nanoscope IV controller (Veeco), but some was also performed with a DI3100 with a Nanoscope V controller. The sample temperature was controlled with 2510 TEC controller (Keithley) connected to a thermo-electric cooler with a surface mounted thermistor. Further details regarding the imaging procedure are presented in the supporting information.

Simulation: Finite element analysis (FEA) using COMSOL Multiphysics 3.2 software with a structural mechanics module have been used to understand the deflection of the cantilever in response to changes in temperature. The FEA modeling involves minimizing the energy of the individual mesh elements. The bimaterial structure was meshed into over 40,000 elements. The silicon cantilever modeled with the same dimensions as the Mikromasch NSC-11 cantilevers used in the study. The NSC-11 cantilevers have a thickness of 2 μm, a length (chip edge to tip of V) of 90 μm and an arm width of 40 μm. The material parameters for the cantilever were obtained from COMSOL as default values for silicon. The plasma polyacrylonitrile material properties were taken from previous work (see Refs. 322, 323). A modulus of 2 GPa, an absolute thermal expansion of 3.1×10^{-4} and a Poisson's ratio of 0.4 was used. The modeled thermal bending data presented in Figure 6.2 was produced by change the temperature from 20 ^{o}C to 30 ^{o}C. The output of the modeling process is a color map of cantilever

defection which was used to understand the normal and lateral bending with the changes in temperature.

6.3 Results and discussion

The thermal twisting probes presented here are fabricated by first depositing plasma polymerized film on both sides of commercially available V-shaped "tapping" cantilever ($f \approx 330$ kHz, $k_N \approx 48$ N/m) as schematically shown in Figure 6.1c. Half of the top-side coating is then removed via focused ion beam (FIB) milling, followed by removing the opposite half of the bottom-side coating (Figure 6.1c). This procedure leaves each leg of the v-shaped cantilever as a thermal bimorph, but with opposite orientations. The combined thermal actuation is a twisting motion, instead of the typical normal bending, as is depicted in Figure 6.1b. Scanning electron micrographs of a twisting bimorph cantilever are presented in Figure 6.1d-e.

Finite element modeling was used to explore the deformation of the twisting bimorph and the sensitivity dependence on the laser spot position with respect to the cantilever surface (Figure 6.2). The modeling of thermal bending V-shaped twisting cantilevers indicated that the cantilevers would provide the highest thermal lateral sensitivity $\left(\frac{\partial}{\partial T}\left(\frac{\partial x}{\partial z}\right)\right)$ when the laser spot was positioned near the center of the cantilever in the x-y plane (refer to Figure 6.2). Furthermore, in that center region, the thermal normal bending sensitivity $\left(\frac{\partial}{\partial T}\left(\frac{\partial y}{\partial z}\right)\right)$ would ideally be zero, thereby preventing interference with the topographical signal. On either side (offset in the x-axis) of the center point are saddle points (bright red and bright blue regions in Figure 6.2), which are regions where the cantilever is parallel with the horizon and thus are completely insensitive to thermal signal. Adjacent

to these saddle points along the y-axis are regions of enhanced normal bending sensitivity $\left(\frac{\partial}{\partial T}\left(\frac{\partial y}{\partial z}\right)\right)$ and thus increased interference with the topographical signal.

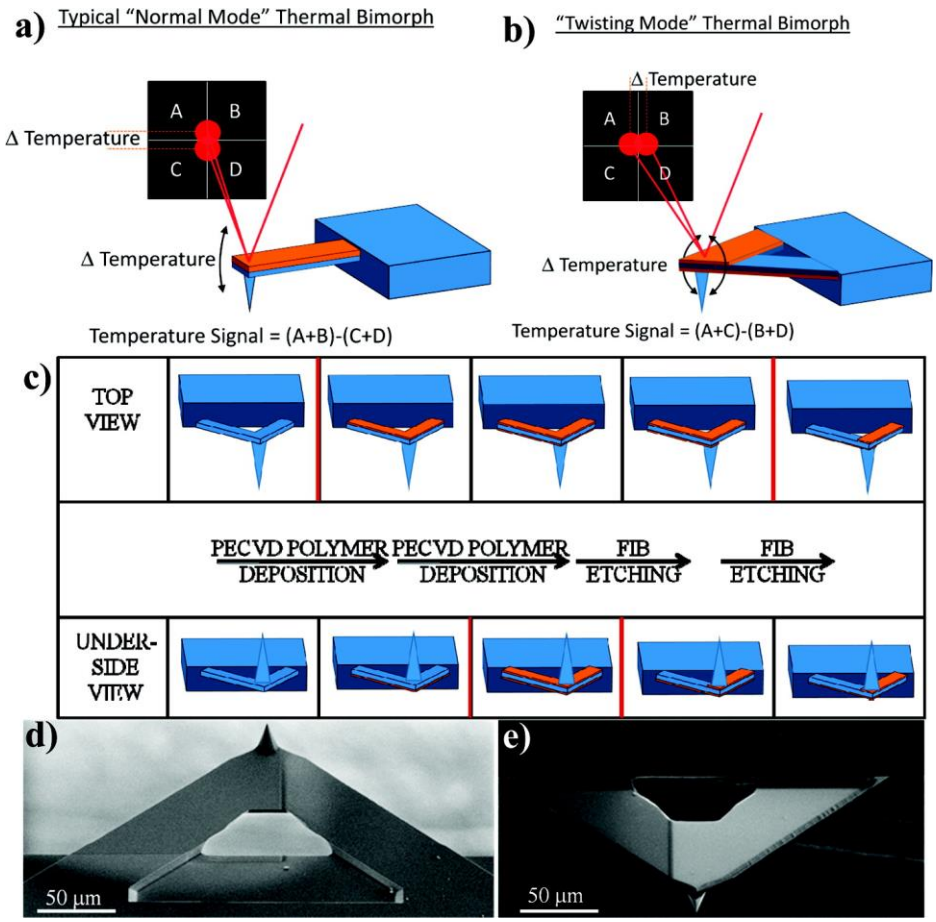

Figure 6.1 (a) A schematic of the bending motion of a typical thermal bimorph. The bimorph bending signal channel is the difference between the top two photodetectors and the bottom two photodetectors, which is the same as the topographical signal channel. (b) A schematic of the twisting motion of a thermal twisting bimorph. The bimorph twisting signal channel is the difference between the left two photodetectors and the right two photodetectors, which is different than the topographical signal channel. (c) A schematic indicating the fabrication process used for making V-shaped thermal twisting probes. (d) Tip-side oriented and (e) backside oriented scanning electron micrographs of a STTM probe

Therefore, it should be clear that positioning of the laser spot is critical to maximizing the lateral thermal sensitivity and minimizing the normal thermal sensitivity. Fortunately, centering the laser spot is a relatively simple and routine procedure with the use of an optical microscope associated with most AFMs.

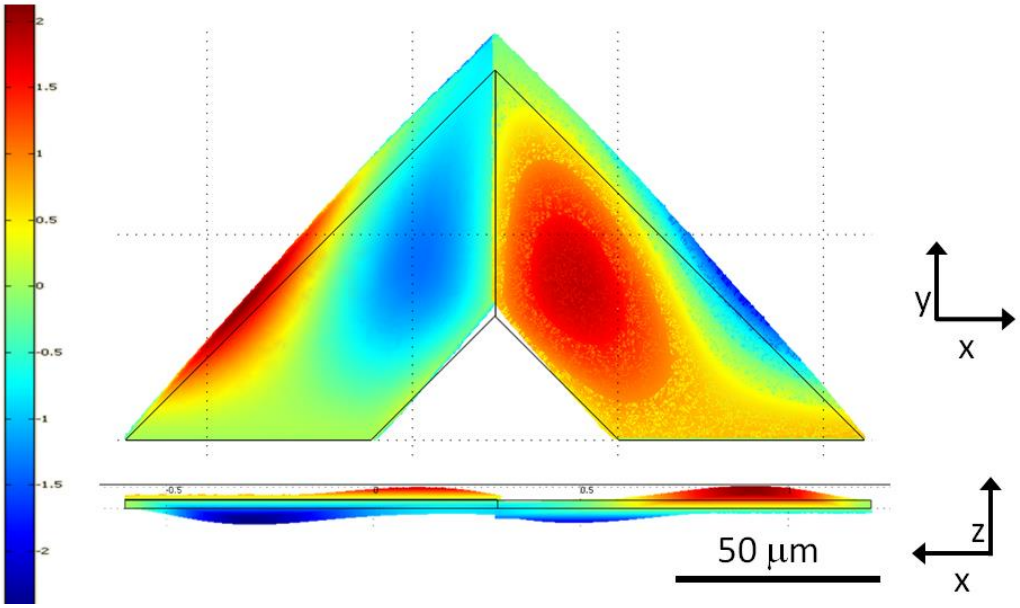

Figure 6.2 The result of modeling the thermal response of the twisting bimorph cantilever geometry shown from two different perspectives. The z-displacement color scale has units of nm

The thermal sensitivity of normal and lateral bending was quantified by suspending the cantilever above a thermal-electric cooler/heater, with a tip-surface distance of roughly 20 µm, as estimated by Z-stepper motor movement. The temperature was incrementally changed, while monitoring the normal and lateral photodiode signals. Figure 6.3 shows a plot of lateral and normal photodiode signal versus temperature. The lateral thermal sensitivity was measured to be 65.4 mV/K, whereas the absolute normal thermal sensitivity was measured to be 7.1 mV/K, almost an order of magnitude less. The lateral

signal noise was measured to be 1.8 mV, thereby leading to a noise-limited thermal resolution of 27 mK which is manifold better than thermal resolution of the traditional mode (0.11K as estimated for the same tip).

The STTM images presented here were obtained in "lift mode" to definitively show that frictional forces do not play a part in creation of the thermal image. Lift mode is a common non-contact scanning method used in several scanning probe imaging techniques including magnetic force microscopy and electrostatic force microscopy. Furthermore, lift-mode has also recently been used in a calibration approach to account for environmental thermal losses in order obtain quantitative SThM images.

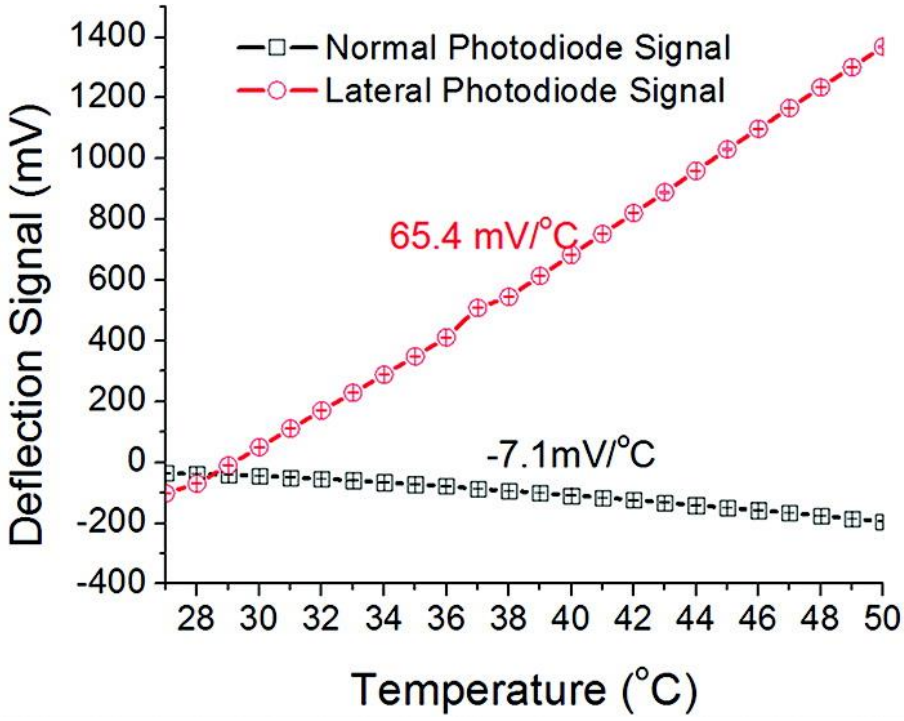

Figure 6.3 A plot of lateral and normal deflection of a representative twisting bimorph cantilever versus surrounding temperature

The images presented here were acquired by recording surface topography in the first pass of the probe and the lateral thermal signal was obtained while retracing the

topography profile with a set lift height above the surface. Lift-mode maintains a constant tip-surface distance, which minimizes surface damage and lateral friction forces that interfere with the thermal signal. As the temperature was raised the maximum stable lift height decreased. This behavior indicates that the predominant thermal conduction mechanism is a water bridge between the surface and the tip, which is typical of SThM performed at atmospheric conditions. Thermal images were not significantly affected by scanning speeds as high as 2 Hz with a resolution of 512 points per line, indicating that the thermal equilibration time is on the order of milliseconds. While lift-mode essentially eliminates frictional contributions, imaging was also performed at different scanning angles to confirm that frictional forces were not contributing to the thermal image.

To further demonstrate that the lateral deflection signal is in fact imaging thermal properties and the normal deflection signal is imaging topography independent of one another, the sample temperature was changed from heating to cooling (with respect to room temperature) in the middle of the imaging, expecting to see a contrast inversion in the lateral deflection image and no change in the topographical image. The results of this so-called "litmus test" on a rough surface serve as a strong indicator of the characteristics of the system. The contrast inversion in the lateral image is expected because the absolute magnitude of the image contrast is directly related to the thermal conductivity of the sample. As shown in Figure 6.1, the lateral signal is comprised of the output from the left photodetectors minus the output of the right photodetectors ((A+C)-(B+C)). In this case the cantilever the cantilever twists to the left upon heating, creating a lighter image contrast. Thus in the sample heating regime, regions with higher thermal conductivity will appear lighter than regions with lower conductivity because the tip is being heated more in the higher thermal conductivity regions. Whereas in the sample cooling regime, regions with higher thermal conductivity will appear darker than regions with lower

conductivity because more heat is being drawn from the tip in the higher thermal conductivity regions.

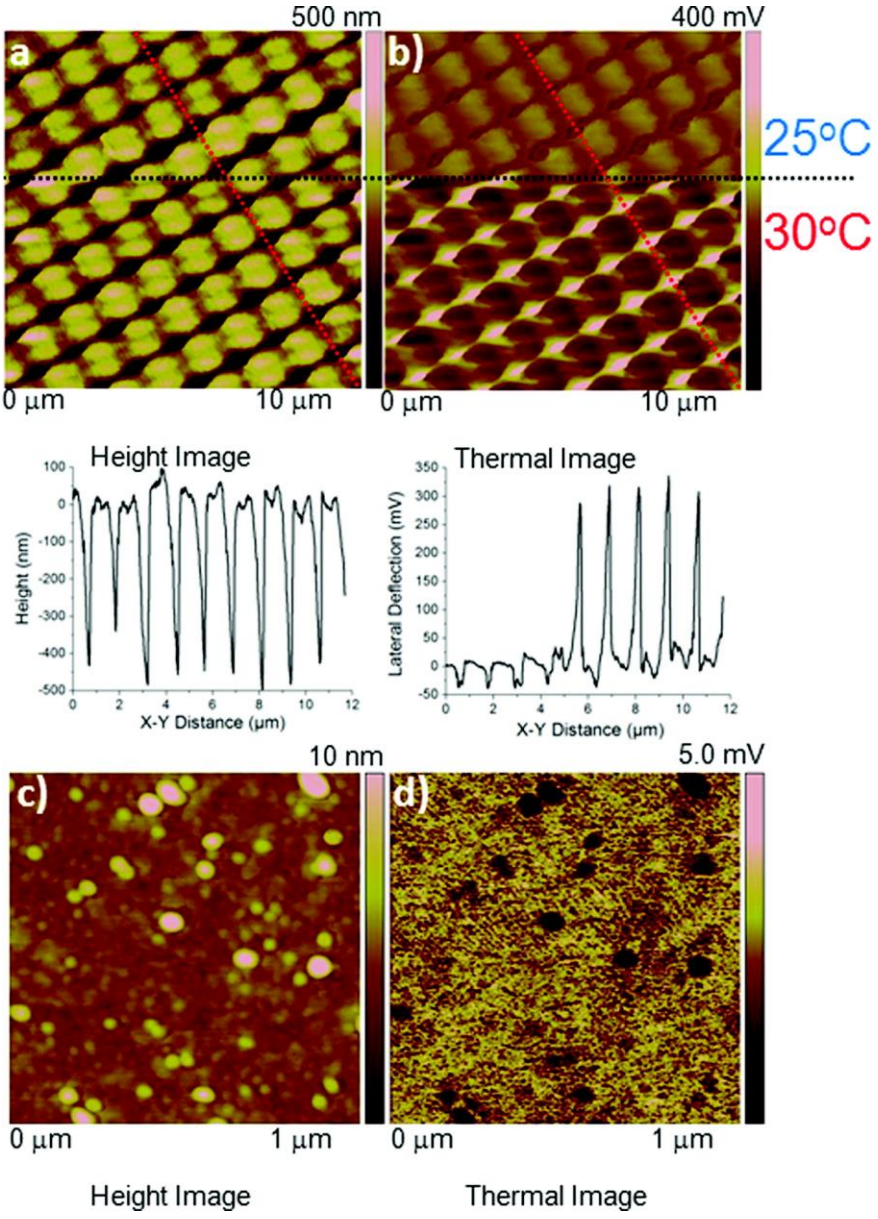

Figure 6.4 (a) Height image and (b) Lateral deflection thermal image of patterned SU-8 with respective slice plots. The temperature was changed from 25°C to 30°C half way through the acquisition of the images. The black dotted line indicates the location at which the temperature was changed. The red dotted lines indicate the location that the respective slice plots are from. (c) Height image and d) Lateral deflection thermal image of gold nanoparticles taken at 26°C. The thermal images in (b) and (d) were captured with lift heights of 50 nm and 10 nm, respectively

The images resulting from this litmus test, taken from a sample patterned with interference lithography (SU-8 at 1.25 μm periodicity), are shown in Figure 6.4a-b. The tip/sample thermal conductivity is much higher in the sample depressions because the tip-sample contact area is much higher and because the glass substrate has a higher thermal conductivity than the SU-8 photoresist. It is evident that the height image (Figure 6.4a) does not change considerably upon changing from heating to cooling, whereas the contrast inverts in the lateral deflection image (Figure 6.4b) after the temperature change.

The spatial resolution of thermal microscopy was quantified from the STTM images using the following equation,

$$\Delta x = \frac{\Delta T_n}{(dT_t/dx)_{max}}$$

where $\Delta T_n$the noise of the temperature signal and $(dT_t/dx)_{max}$ is defined as the largest temperature gradient signal measured.[2,28] STTM images of interference lithography samples show a max thermal signal gradient of 2977 mV/μm and the noise of 1.8 mV leading to a spatial resolution of 0.61 nm, which is about two orders of magnitude better than that of conventional SThM. Therefore, STTM spatial resolution is limited by the radius of curvature of the tip and not the thermal sensitivity of the cantilever. In order to confirm the lateral spatial resolution of the thermal imaging a standard gold nanoparticle sample (5 nm radius) was imaged (Figure 6.4c-d) at 26^{o}C. The lateral feature sizes of the topographical image and the thermal image are essentially identical indicating a tip dilation effect. Therefore, the spatial resolution of the thermal imaging is in fact limited by the tip radius which can be as low as 5 nm for microfabricated tips.

In summary, we developed a novel method of mapping of nanoscale thermal properties of complex devices, scanning thermal twisting microscopy. The approach utilizes a novel asymetrical bimorph geometry that induces a twisting motion in the thermal probe. This twisting motion allows the thermal signal to be isolated from the normal deflection caused by surface topography thus facilitating nanoscale spatial resolution and mK thermal resolution. STTM simplifies thermal imaging with significant improvement of the spatial and thermal resolution. STTM does not use electronics for signal transduction and therefore does not suffer from the same current leakage issues as other methods, making it ideal to study thermal and electronic transport simultaneously. The fabrication of the miniature assymetrical bimorph cantilevers is simple and therefore stands as a possible mass-production of cheap and highly sensitive thermal imaging probes with nanoscale spatial resolution and mK thermal resolution not existing now.

CHAPTER 7

MAPPING CHARGE DISTRIBUTION ON GRAPHENE OXIDE SURFACE

7.1 Introduction

Numerous studies have been reported on understanding the structure, morphology, and composition of graphene oxide. Most popular has been the Lerf-klinowski (LK) model that suggests graphene oxide to be composed of randomly distributed graphitic domains with sp^2 hybridized carbon atoms and oxidized domains with epoxide, carboxyl, and hydroxyl functionalities.[327,328,329] Bulk composition and chemical structure of graphene oxide has been verified using spectroscopic techniques such as FTIR, Raman, and X-ray photoelectron spectroscopy (XPS).[330] However, all these optical techniques are resolution limited by the diffraction-limit of light and provide average information of the sample over a given area.

Scanning Tunneling Microscopy (STM) and Transmission Electron Microscopy (TEM) have been used to locally probe the presence of defects sites on the graphene oxide surface.[76,77,331] The studies have clearly shown that the surface of graphene oxide consists of defects due to chemical functionalities as well as bond disorder. In particular, the use of STM has been demonstrated to probe the different functional groups such as carboxyl, epoxy, and hydroxyl over a given area along the surface. Although these techniques are powerful in probing the local defects, they requires the material to be deposited on special substrates (conductive films or TEM grids) which limits their use for characterizing graphene oxide on a device or application platform. Also, these techniques either give information of the bulk sample or over a small area. Thus, the overall composition and distribution of oxygenated functionalities over an entire surface of graphene oxide flake is still missing.

EFM - an AFM based technique, has emerged to be a powerful tool for mapping the charge distribution, surface potential, or dielectric properties of metal or semiconductor surface. It has been used for imaging charge distribution in carbon nanotubes and DNA, interfacial properties of self-assembled monolayers on metals, measuring charge transfer in semiconductor materials and conductive polymer blends and even for measuring the charge within a single molecule.[332,333,334,335,336] However, measuring a charge within a single molecule requires the measurement to be performed under extremely low temperatures (5K) and is not always feasible.[337] In this technique, the conductive AFM tip and the substrate form a capacitor system and the dielectric properties of the substrate at different points can be mapped as the tip scans across the surface.

EFM studies have been reported for identifying the different layers of graphene, detect the electrical dipoles from polymer residues and water on the surface of graphene, probe the surface potential and charge distribution in graphene films, and identify the contact potential difference between a single layer graphene and the substrate.[338,339,340,341,342] It has been used to measure the electric potential fluctuations on the surface of highly oriented pyrolytic graphite (HOPG) as well as study the dielectric response of reduced graphene oxide.[343,344,345] In a recent study, Gomez-Herrero *et al.* studied the surface potential distribution of few layer graphene oxide deposited on different substrates and a step-like decrease in the surface potential was observed with the increase in the number of layers. The surface potential distribution was uniform on the surface of graphene oxide and the oxidized areas were indistinguishable from the conductive domains.[346] However, TEM and STM studies suggest that the surface of graphene oxide is comprised of conductive graphitic domains interconnected by a disordered oxidized matrix. Thus, graphene oxide is expected to show a different response to the conductive tip at different areas owing to the different dielectric and charge characteristics along the surface.

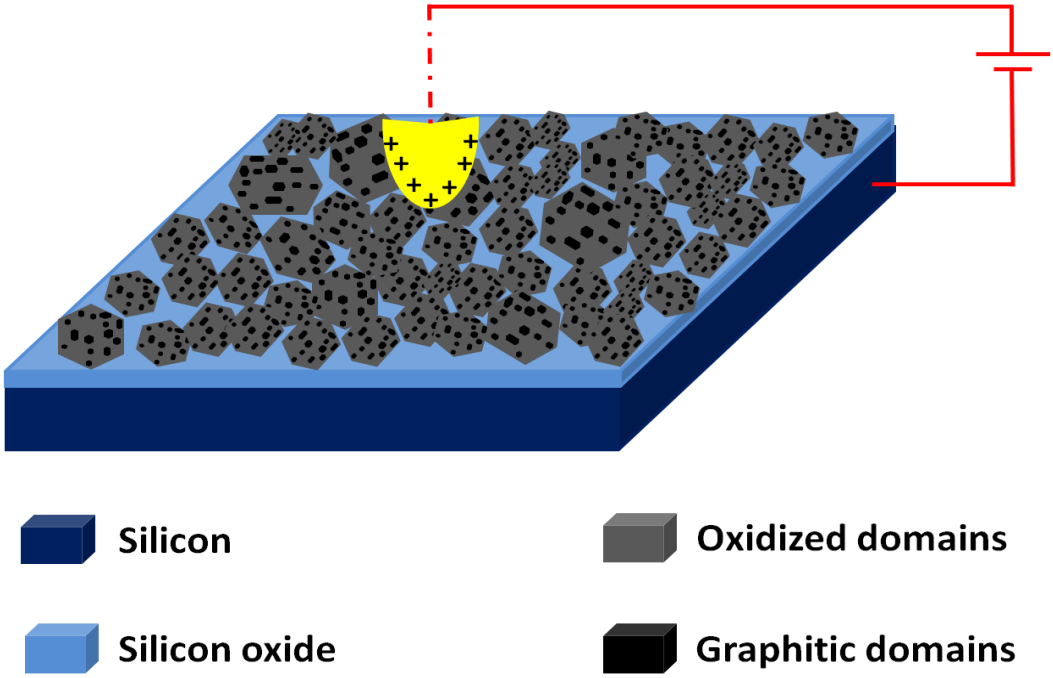

Figure 7.1 Representation of the EFM-setup showing the graphene oxide flakes uniformly distributed over the silicon oxide surface scanned using a charged AFM charged tip above the surface

In this work, we investigate the use of the EFM technique in mapping the graphitic and oxidized areas on the surface of an individual graphene oxide flake. A typical setup is shown in Figure 7.1. Prior to the local characterization, a majority of monolayer graphene oxide flakes were uniformly deposited over the surface and analyzed using the conventional spectroscopic techniques for estimating the average concentration of oxygen functionalities on the surface. Contact angle measurements were also performed to estimate the degree of oxidation of the graphene oxide flakes deposited over a substrate.

Next, EFM measurements were demonstrated on a single graphene oxide and the oxidized areas were found to be clearly distinguishable from the graphitic domains

especially under low humidity conditions. Interestingly, the synthesis process was found to result in a non-homogeneous mixture of graphene oxide flakes with a significant variation in the different degree of oxidation. Although a majority of the surface was covered with the oxygenated functionalities, the density varied from 50% to 80% for different flakes. We believe that this is the first report which analysis the degree of oxidation over individual graphene oxide flakes. Further, the reduction process of graphene oxide was explored and the effect of reduction time on the EFM-phase image of different flakes was analyzed. Similar to the non-homogenous oxidation of the graphene flakes, the reduction process also resulted in flakes with different degree of reduction.

Finally, the EFM images were quantified by analyzing the changes in the cantilever phase shift over different areas of graphene oxide with the change in tip bias. Interestingly, it was observed that the oxidized areas and graphitic domains show a similar response, however, the oxidized areas show a higher absolute surface potential than the graphitic domains. Another important aspect observed in this study was the positive charge on the graphitic domains imparted by the negatively charged oxidized domains. Thus, overall the graphene oxide was found to consist of positive and negative domains, however, the negative oxidized areas dominated the surface and also account for the negative z-potential of graphene oxide reported in literature. Moreover, Chemical reduction of graphene oxide was found to eliminate the oxygen functionalities and showed a uniform surface composition with a high dielectric constant. We believe that this is the first report that scrutinizes the properties of a predominantly monolayer graphene oxide film deposited on a substrate rather than bulk as well as monitors the surface composition of individual graphene oxide flakes, qualitatively and quantitatively.

7.2 Experimental details

Graphene oxide sheets were synthesized and assembled on silicon oxide substrate using LB technique. SEM, AFM, and EFM were used to characterize the structure of graphene oxide. Raman microscopy and XPS were used to identify the composition of graphene oxide flakes. Additional details can be found in chapter 3.

7.3 Results and Discussion

Graphene oxide prepared by Hummer's method functionalizes the surface of graphene with epoxy, carboxyl, and hydroxyl groups, allowing it to disperse in several organic and aqueous solvents. A uniform deposition of the graphene oxide flakes can be achieved using the LB technique.

7.3.1 Structural characterization of graphene oxide flakes

Figure 7.2a shows the optical image of the graphene oxide flakes assembled on a 300 nm SiO_2/p-Si substrate. Graphene oxide flakes are quite visible in the optical image and the 300 nm SiO_2 layer was found to give a better contrast than the bare silicon substrate. The optical image shows a majority of monolayer graphene oxide flakes uniformly deposited on the substrate over large areas and can be used to get a good estimate of the coverage. The graphene oxide coverage was also verified using SEM and areas with different surface coverage density were observed. However, several SEM images taken over substrate revealed the surface coverage to be in the range of $80\pm6\%$. (Figure 7.2b).

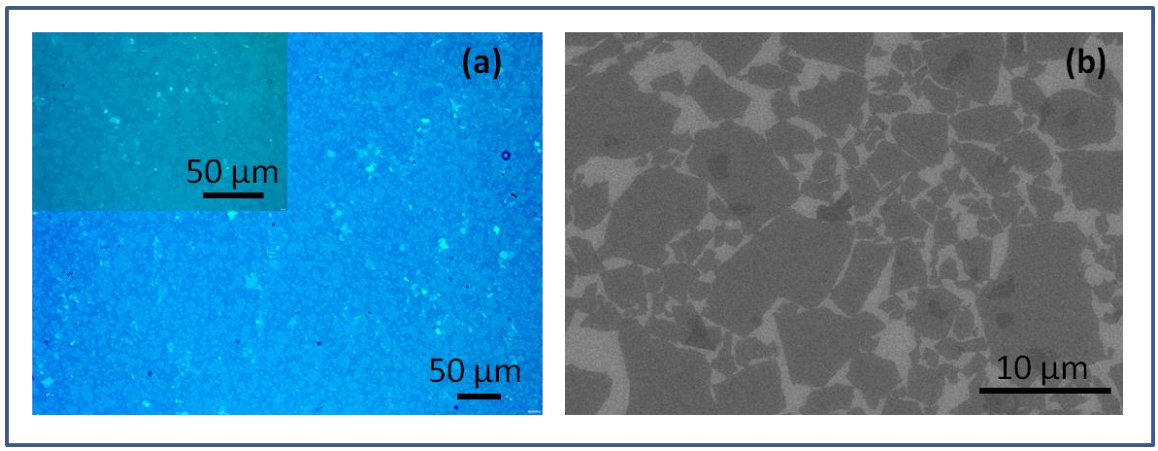

Figure 7.2 Estimation of the surface coverage of graphene oxide on the silicon oxide surface. (a) Optical image with inset showing the zoomed-in image representing the uniform high density coverage of graphene oxide, and (b) representative SEM image showing the areal density to be 80± 6%

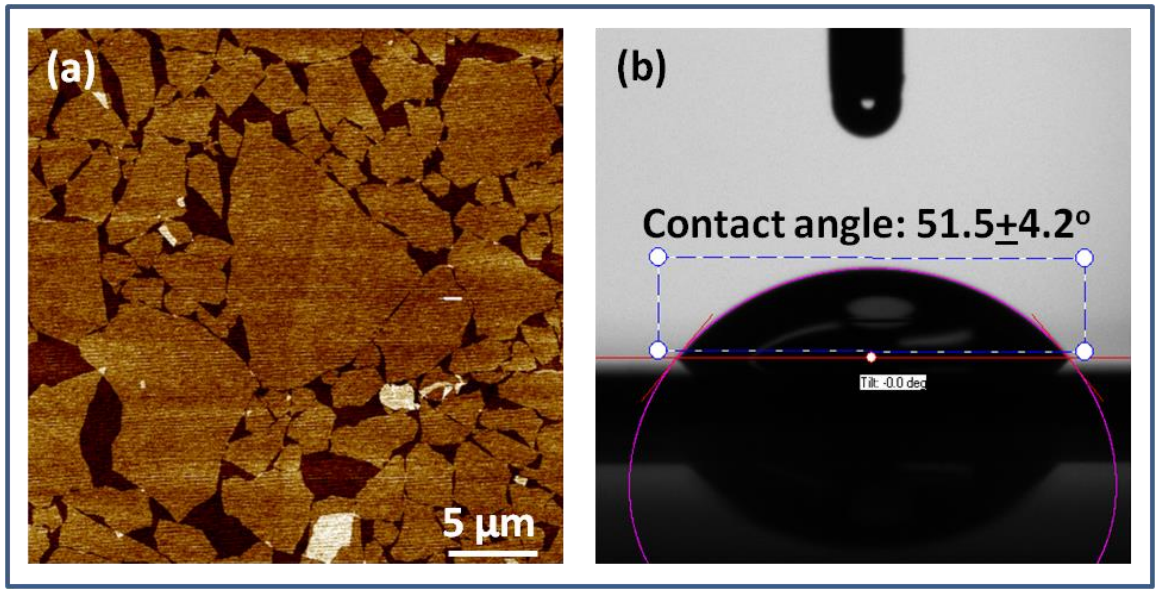

Figure 7.3 Surface morphology and contact angle measurements. (a) AFM image showing a densely packed area of graphene oxide flakes on the surface, and (b) representative contact angle profile of the surface

The morphology, dimensions, and distribution of the graphene oxide flakes was also analyzed from the AFM topography images. Figure 7.3a shows a typical AFM topography of the graphene oxide flakes transferred over the SiO_2 substrate. Majority of graphene oxide flakes show a smooth surface morphology and a uniform thickness profile. The AFM image was taken in a densely packed area and shows a better surface coverage than the one represented in the SEM image (Figure 7.2b). Sectional analysis of different flakes suggests a polydispersity in the lateral size ranging from a few μm to over 10 μm. However, the thickness of the flake was quite uniform around 0.9 ± 0.2 nm implying that majority of the graphene oxide flakes were monolayer in nature.

7.3.2 Bulk compositional characterization of graphene oxide flakes

The sample was stored under ambient conditions after the LB transfer process to remove any residual water on the surface. Thus, there is a possibility of contaminants from the atmosphere being adsorbed on the surface. In order to verify this hypothesis, we measured the contact angle of the substrate at three different locations. The contact angle depends on the surface chemistry and can be used to estimate the concentration of the functional groups on the surface of graphene oxide. It was found that the average contact angle for the graphene oxide deposited on the SiO_2 surface was ~51.5^o (Figure 7.3b). The contact angle value depends on the surface coverage of graphene oxide and was much lower than the contact angle bulk graphene oxide reported in literature (62.8^o).[347] Also, the values of the contact angle of bulk graphene oxide reported in literature depends on the C:O content which varies from 1.8 to 2.5 depending on the method used for synthesis (Staudinger's/ Hummer's/ modified Hummer's).[330] However, we will use this value for estimating the average degree of oxidation in the graphene oxide flakes.

According to Cassie's law,[348] the effective contact angle θ_c for a liquid droplet on a composite surface is given by

$$\cos(\theta_c) = f_{GO}\, cos(\theta_{GO}) + f_{SiO_2} \cos\left(\theta_{SiO_2}\right)$$

where f_{GO} is the coverage of graphene oxide, θ_{GO} is the contact angle of bulk graphene oxide, f_{SiO_2} is the coverage of SiO_2, and θ_{SiO_2} is the contact angle of bulk graphene oxide. Contact angle for a freshly cleaned piece of SiO_2 surface was found to be around 15° and the substrate with 80±6% coverage of graphene oxide showed a contact angle of 51.5±4.2°. Thus, based on these parameters, the effective contact angle of graphene oxide (θ_{GO}) was calculated to be 57.6±4.5° and was close agreement with the values reported in the literature. Also, the low contact angle of water at the surface negates the possibility of any adsorbed contaminants (organic), which generally tend to increase contact angle of the surface.

Graphene oxide surface consists of the graphitic domains and the oxidized areas. Based on the contact angle measurements, the concentration of oxygenated groups on the graphene oxide can also be estimated using Cassie's law. Assuming, the oxygenated domains on the graphene oxide show a hydrophilic character with low contact angle (~15±5°) and the sp^2 graphitic domains behave as a graphite surface with a contact angle of 98.3°,[349] the oxygenated domains would constitute 62.6±6.12% of the graphene oxide surface. Thus, based on these measurements, it was speculated that a significant area of the graphene oxide surface was oxidized and supports the values reported in literature.

Further, the chemical composition of the graphene oxide was confirmed using spectroscopic techniques. Figure 7.4a shows the Raman map of the surface obtained by recording the intensity of the G-band (1550-1650 cm^{-1}) and the average Raman spectra of graphene oxide flakes. The spectrum showed all the characteristic peaks corresponding

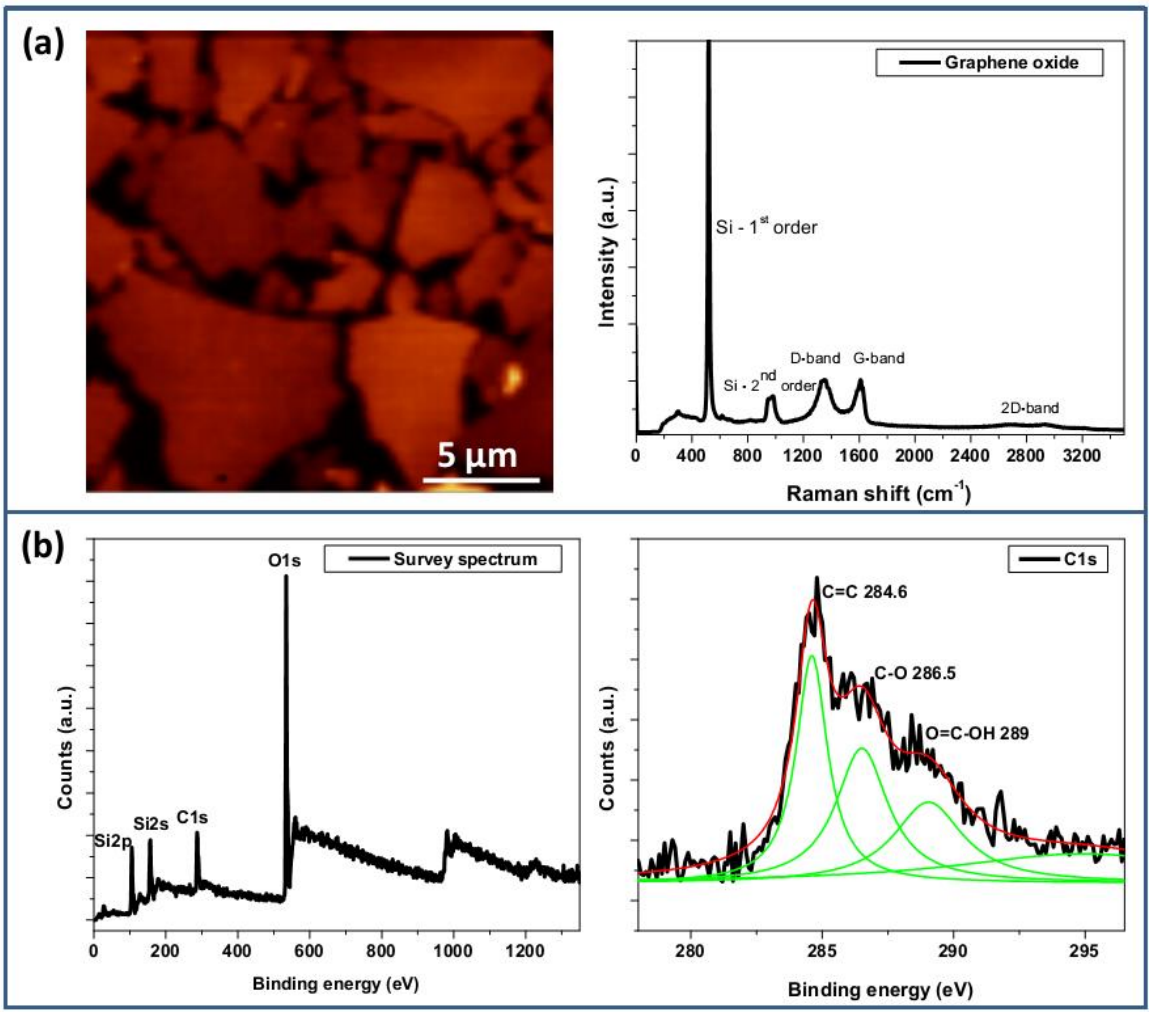

Figure 7.4 Spectroscopic characterization of graphene oxide flakes. (a) Raman map showing the uniform deposition of monolayer graphene oxide and the corresponding Raman spectrum, (b) XPS survey spectrum and the C1s spectrum showing the elemental composition of an area over the substrate

to the silicon substrate (1st order at 520 cm^{-1} and 2nd order between 950-1000 cm^{-1}) and the graphene oxide (D-band at 1357 cm^{-1}, G-band at 1608 cm^{-1}, and a broad 2D band between 2500-3000 cm^{-1}).[350,351] A uniform intensity of the G-band and the D-band was observed over the surface of graphene oxide. This further supports the presence of a majority of monolayer graphene oxide flakes on the surface. The D-band in the Raman spectrum is a result of the defects and disruption of the C=C lattice in graphene. Thus, a

significant intensity of the D-band suggests that the surface of graphene oxide surface consists of a high concentration of oxygenated functionalities. However, the spectroscopic technique is limited the diffraction-limit of light and cannot resolve the distribution of the nanoscale defects areas on the surface.

Figure 7.4b shows the XPS survey spectra and the C1s spectra of the substrate. The survey spectrum shows all the expected peaks corresponding to the silicon oxide substrate and graphene oxide. In particular, the C1s spectra can be deconvoluted into three peaks corresponding to the sp^2 domains (C=C with a binding energy of 284.6 eV) and the oxidized sp^3 domains (C-O with binding energy of 286.5 eV and O=C-OH with binding energy of 289 eV).[351] The ratio of areas under the peaks suggests that 69.1$\pm$4.5% of the graphene oxide surface is oxidized, similar to the values obtained with the contact angle measurements. However, the minimum spot size of XPS being is limited to 30 μm and mapping the distribution of the oxidized domains is difficult. The XPS spectrum represents the average distribution of the functional groups and fails to probe the distribution over the surface. However, the uniformity of the G-band intensity in the Raman map and the XPS survey spectrum do confirm the absence of any adsorbed impurities on the surface.

So far, we have looked at the macroscopic properties of the graphene oxide flakes deposited on a 300 nm silicon oxide surface supported on doped silicon. Also, contact angle measurements and XPS analysis suggested that 62-69% of the graphene oxide surface is decorated with the oxygenated groups and the conductive sp^2 domains occupy only a small portion of the graphene oxide surface. However, these measurements reveal an average behavior of the surface and precise understanding of the distribution and changes during the reduction process is lacking. From here onwards, we will focus on a

single flake of graphene oxide and study the characteristics of its surface using EFM technique.

7.3.3 EFM imaging of individual graphene oxide flakes

The surface of graphene oxide consists of oxygenated functionalities which impart a negative charge to the surface. z-potential measurements of graphene oxide solution reported in reveal a pH dependence but show a negative surface charge irrespective of the solution pH.[352] Thus, EFM can be a promising technique to probe the surface charges and measure the changes in the surface potential between the graphitic domains and conductive domains across the surface of graphene oxide. In this technique, a conductive tip oscillating at its resonant frequency traces the topography of the sample at a fixed height above the sample. Any interaction between the sample and the tip results in a change in the amplitude of oscillation and phase which is plotted against the lateral movement of the piezo system.

7.3.3.1 Effect of humidity on EFM imaging

Figure 7.5a shows the topography and the corresponding EFM phase image of graphene oxide flakes deposited on SiO_2/Si substrate obtained at a relative humidity (R.H) of 27%. These images were obtained using a heavily doped silicon tip. Conventionally used silicon tips coated with conductive metals (eg., Pt/Ir) were avoided to reduce any wear and tear of the coating during the scanning process. The topography image shows a majority of monolayer graphene oxide flakes with uniform morphology, however, the EFM-phase image appears quite uniform. Light features are observed in the areas covered with graphene oxide but are not pronounced enough to resolve the distribution of chemical functionalities over the surface.

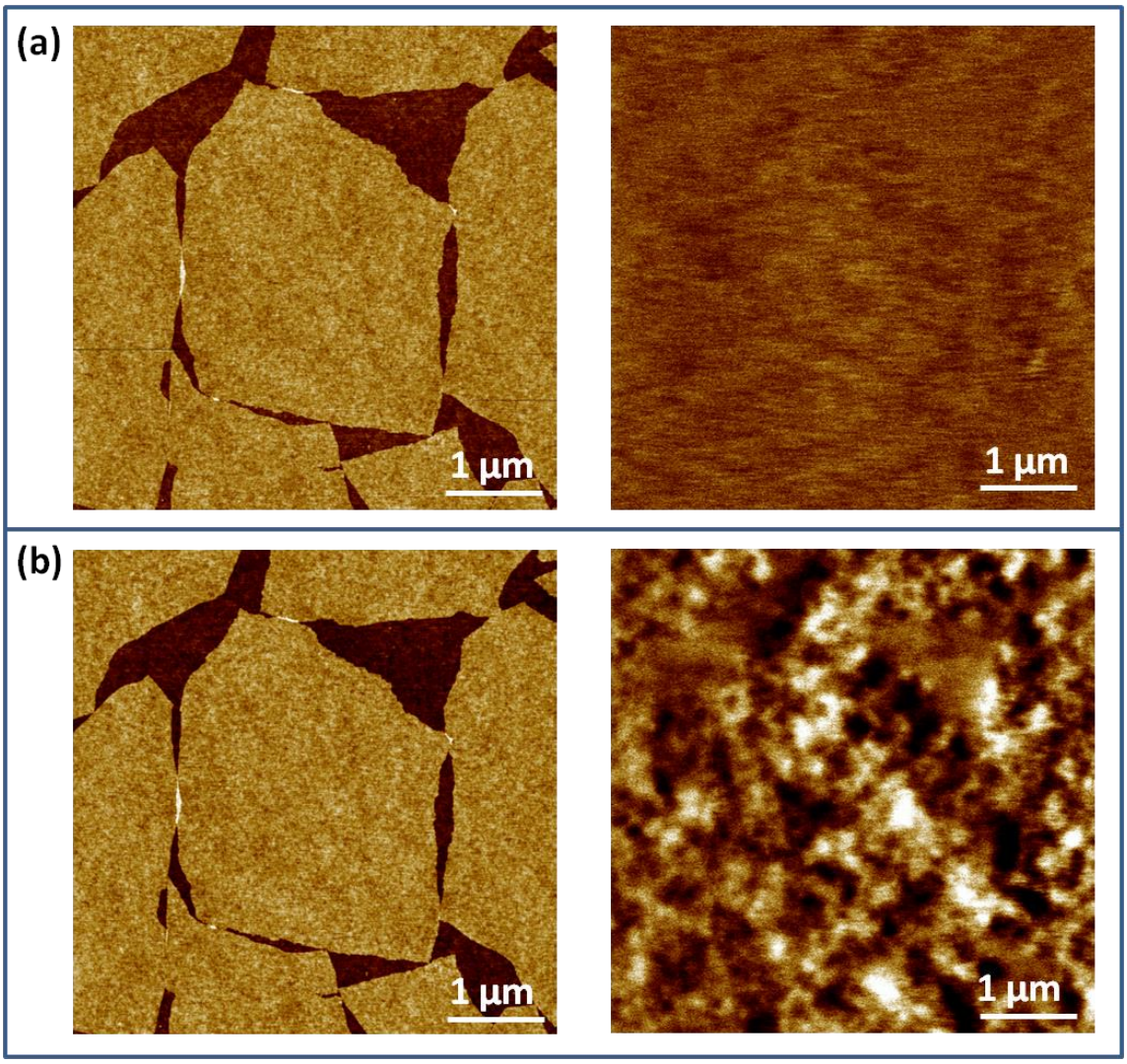

Figure 7.5 Effect of humidity on the EFM-phase image of graphene oxide. Topography (z-scale = 3 nm) and corresponding EFM-phase image (z-scale: 1°) of the same area obtained at a tip bias of 5V and a lift height of 50 nm under (a) 27% R. H., and (b) 2% R.H. conditions

We speculated that the high relative humidity conditions during the scanning process might be responsible to screening the chemical functionalities on the surface. It is a well known fact that a layer of water is always present between the tip and sample during scanning.[338,353,354] Also, the presence of highly polar water molecules can influence the electrostatic interaction between the tip and the sample. Presence of residual water on the sample can screen the surface charges and thus the EFM imaging depends on the

environmental conditions around the sample. We also observed that scanning the sample immediately after the transfer of graphene oxide from the LB setup (prior to drying) showed a uniform but enhanced EFM contrast between the graphene oxide and SiO_2 surface.

Thus, to confirm this hypothesis and reduce the presence of water on the sample, imaging was performed at a reduced humidity environment. Figure 7.5b shows the topography and the EFM phase image of the same area but collected at a R.H of 2%. The topography showed the same surface features irrespective of the humidity conditions and the apparent height of the flakes was 1.0 nm irrespective of the humidity conditions. However, the EFM phase image obtained at lower humidity clearly shows pronounced bright and dark areas within the graphene oxide flake itself. We believe that these areas of contrast represent the chemical non-uniformity on the surface of graphene oxide. The presence of randomly distributed oxygenated domains over the graphene oxide surface results in a non-uniform electrostatic interaction as the tip rasters across the surface. This causes a shift in the phase of the oscillation of the cantilever as can be seen from the EFM image. The silicon oxide surface shows a uniform phase shift whereas the graphene oxide surface shows areas with a higher or lower phase shift with respect to the silicon oxide surface. Slightly darker areas are also seen which probably correspond to the functional groups underneath the surface. However, the exact correlation between the functional groups and the phase shift is unclear and will be discussed in the subsequent sections.

Interestingly, statistical analysis of the different domains seen in the EFM-phase images over different graphene oxide flakes revealed that the dark domains covered $64\pm15\%$ of the surface. This value is in agreement with the average distribution of functional groups estimated from the contact angle and XPS measurements and probably corresponds to the oxygenated functionalities on the surface. A significant standard deviation was observed

in the distribution and can be due to the lack of control over the different parameters during the synthesis and processing steps. Inconsistencies in the graphene oxide surface chemistry can occur during the sonication, centrifugation, and exfoliation process of graphene as well as during the synthesis due to the non-uniform size of the graphite flakes and the variations in the size of grain boundaries which can act as active centers for oxidation. This further validates the significance of the EFM technique in characterizing the surface of graphene oxide compared to other conventional techniques.

7.3.3.2 High resolution adhesion and EFM mapping

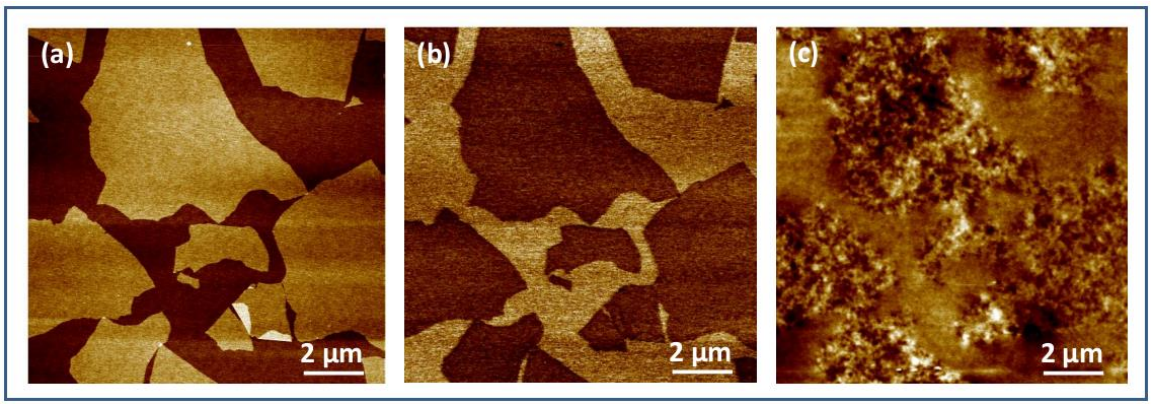

Figure 7.6 (a) AFM topography (z-scale: 2.4 nm) along with the (b) adhesion map (z-scale: 2.1 nN), and (c) EFM-phase image (z-scale: 1.6^{o}) at tip bias of 5V and 50 nm light height under reduced humidity (2% R.H.)

Adhesion between the AFM tip and the surface also depends on the surface chemistry and can be effective in probing the functionalities on the surface of graphene oxide. Figure7.6 shows the topography, adhesion, and EFM phase image of the same area taken using the same AFM tip under reduced humidity conditions. The adhesion map clearly distinguishes the different adhesion properties of the graphene oxide and silicon oxide surface with respect to the hydrophilic silicon tip. A lower adhesion force was observed between the silicon tip and the graphene oxide surface compared to the silicon tip and the

silicon oxide surface. This suggests that the silicon oxide surface is more hydrophilic than the graphene oxide surface which was also evident from the contact angle measurements. However, the adhesion maps were not able to differentiate between the oxidized and graphitic domains on the surface of graphene oxide. This can be due to the adhesion forces below the AFM resolution experienced by the tip (k = 3N/m) as it comes in the vicinity of the functional groups. However, mapping the adhesion forces using softer functionalized AFM probes can be promising to address this issue.

On the other hand, the EFM-phase image taken over the same area clearly shows the different domains on the graphene oxide flake. Also, the silicon oxide surface shows a uniform EFM response suggesting that the areas of contrast observed over the graphene oxide flake result from the chemical inhomogeneity of the surface. If we assume that the contrast in the EFM image is due to the adsorbed organic contaminants (typically hydrophobic) then a similar contrast should have been observed on the silicon oxide surface. Also, the adhesion map over the graphene oxide flake would have shown a different response between the adsorbed hydrophobic contaminants and the hydrophilic areas. Thus, we believe that the contrast within a single graphene oxide flake seen in the EFM phase image is indeed due a difference in the surface potentials and non-uniform charge distribution along the oxidized and graphitic areas.

Surface functionalization of graphene has been known to the reason for the increase in the d-spacing from 0.34 nm to 0.72 nm. Thus, an apparent increase in the thickness over the surface should be evident from the AFM topography. Figure 7.7 shows high resolution topography, adhesion, and EFM phase images of the surface of graphene oxide

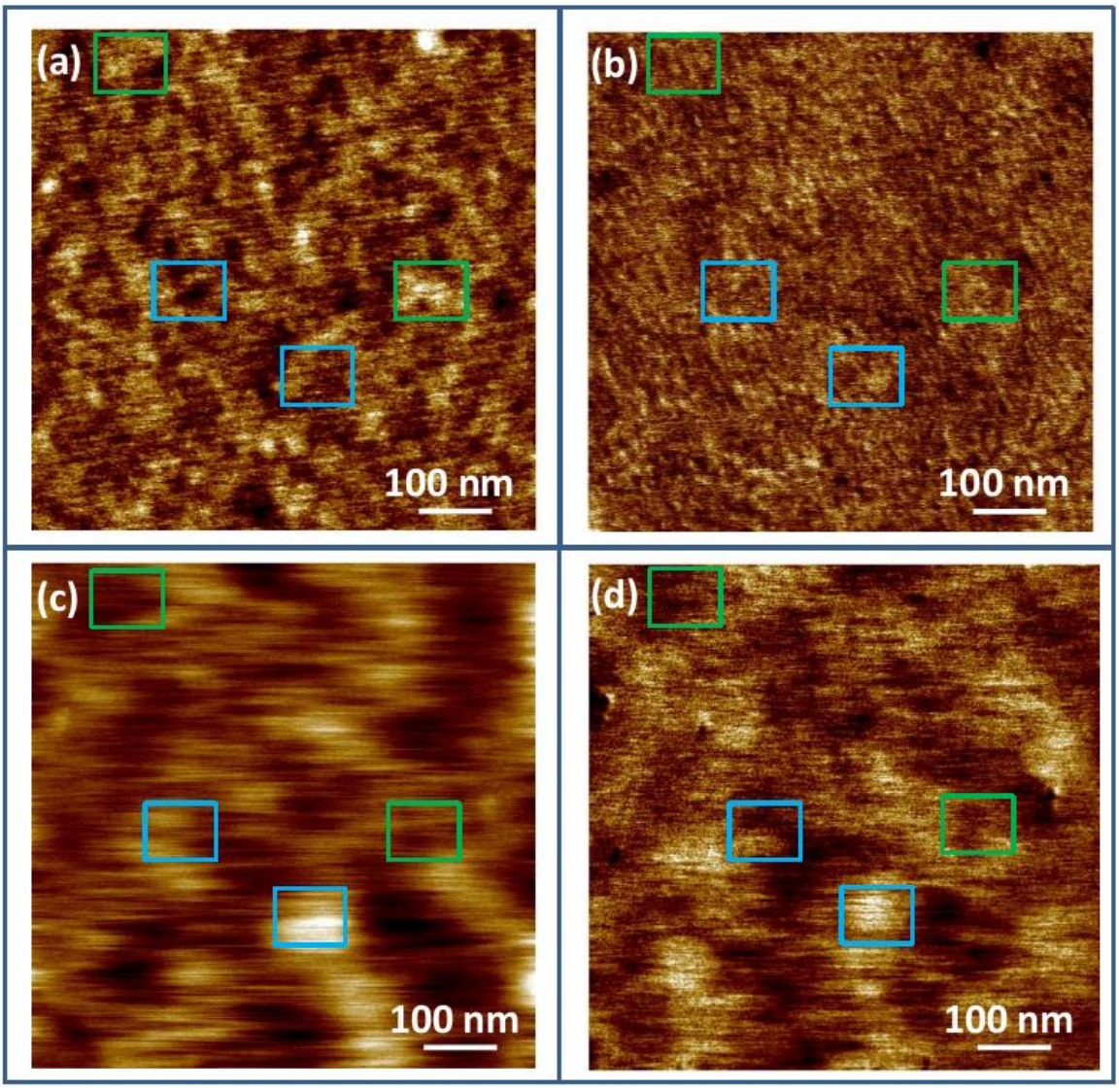

Figure 7.7 High resolution (a) AFM topography (z-scale: 1nm), (b) AFM adhesion map(z-scale: 2nN), (c) EFM-phase image (z-scale = 2^{o}) at tip bias of 5V and lift height of 50 nm, and (d) EFM phase image (z-scale: 4^{o}) at tip bias of 5V and light height of 20 nm

taken at reduced humidity conditions (RH <2%). This ensures a resolution per pixel of < 1nm and reduced water bridge at the tip-sample junction to get a good estimate of the surface features. Figure 7.7a shows the surface morphology of the graphene oxide surface along with the corresponding adhesion map (Figure 7.7b) and EFM-phase images

(Figures 7.7c and 7.7d). The topography image showed some variation along the surface on the order of 0.13 nm whereas the adhesion map was quite uniform. The EFM image showed a higher degree of contrast over the surface but looks skewed along the scan direction. This can be due to wider area of electrostatic influence of the charged probe due to the combination of a large tip curvature and higher lift heights compared to the spatial distribution of charges along the surface. In order to verify this hypothesis, the light height was lowered to 20 nm and Figure 7.7d shows the EFM-phase image of the same area. It is evident that the lateral resolution is much improved and gives a better perspective of the surface.

Graphene surface is known to be rippled and the presence of functional groups on either side further perturbs the surface leading to non-uniform topography.[355] Exact correlation between the topography, adhesion, and EFM-phase image was difficult to estimate due to the similar roughness of the silicon oxide surface underneath (RMS roughness ~ 0.14 nm over a 500nm x 500 nm area). However, some of the apparent areas are highlighted in all the images and there seems to be a trend between the surface topographic features and the EFM-phase images. If we compare, Figure 6a and 6d then it seems that the areas which appear higher in the topography appear darker in EFM-phase image and vice-a-versa. Also, based on our previous understanding, darker areas in the EFM-phase image should correspond to the oxygenated functionalities on the surface. However, the changes in the surface topography are not so obvious and cannot be used directly to probe the distribution of functionalities on the graphene oxide surface.

7.3.3.3 Effect of lift-height on EFM imaging

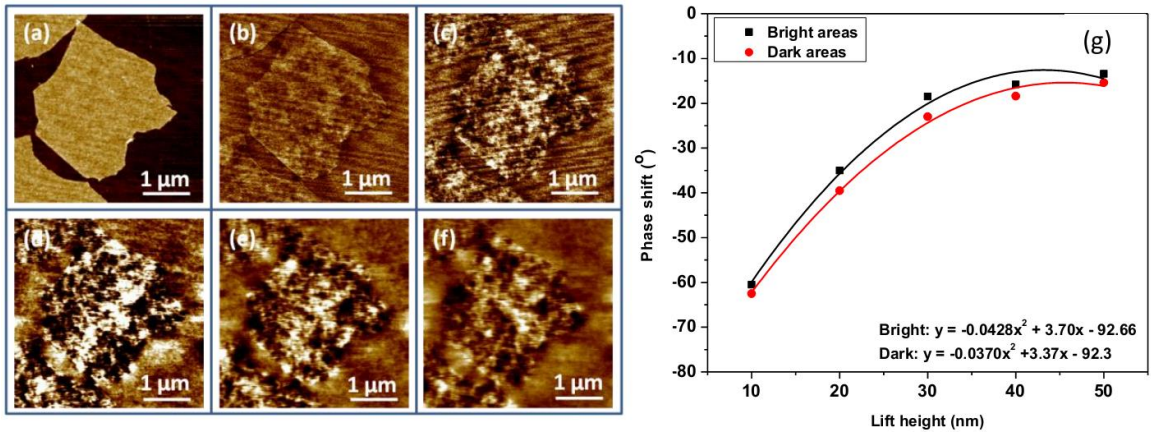

Figure 7.8 Effect of lift height on EFM imaging. (a) Representative topography image (z-scale: 3nm), (b-f) EFM-phase images with lift heights varying from 10 nm to 50 nm in 10 nm intervals (z-scale: 4° for (b)-(e) and 2° for (d)-(f)), and (g) phase shift v/s lift height trend for the bright and dark areas

An important factor witnessed from Figure 7.7 was the effect of lift height on the EFM-phase imaging. This was understood further by obtaining the EFM-phase images of the same area at the same tip bias but different lift heights as shown in Figure 7.8. As evident, the topography of graphene oxide was smooth and uniform but the EFM-phase image clearly showed the different domains on the graphene oxide surface. On plotting the change in phase with the changes in the lift height, it was observed that the phase shift showed a parabolic dependence on the lift height. At a lift height of 50nm, the dependence of the phase shift on the lift height was minimum. This suggests that the phase shift at lower lift heights is primarily contributed by the van der Waals forces whereas the electrostatic forces are dominant the phase shift at higher lift heights. Also, the lift height was found to be dependent on the scan area and the resolution. Lower lift height gives better resolution images for smaller scan areas whereas a lift height of 30 nm or more was found to be reasonable for scan areas above 5 µm. In the subsequent EFM

images, a lift height of 50 nm was maintained to negate the effect of light height on the electrostatic forces.

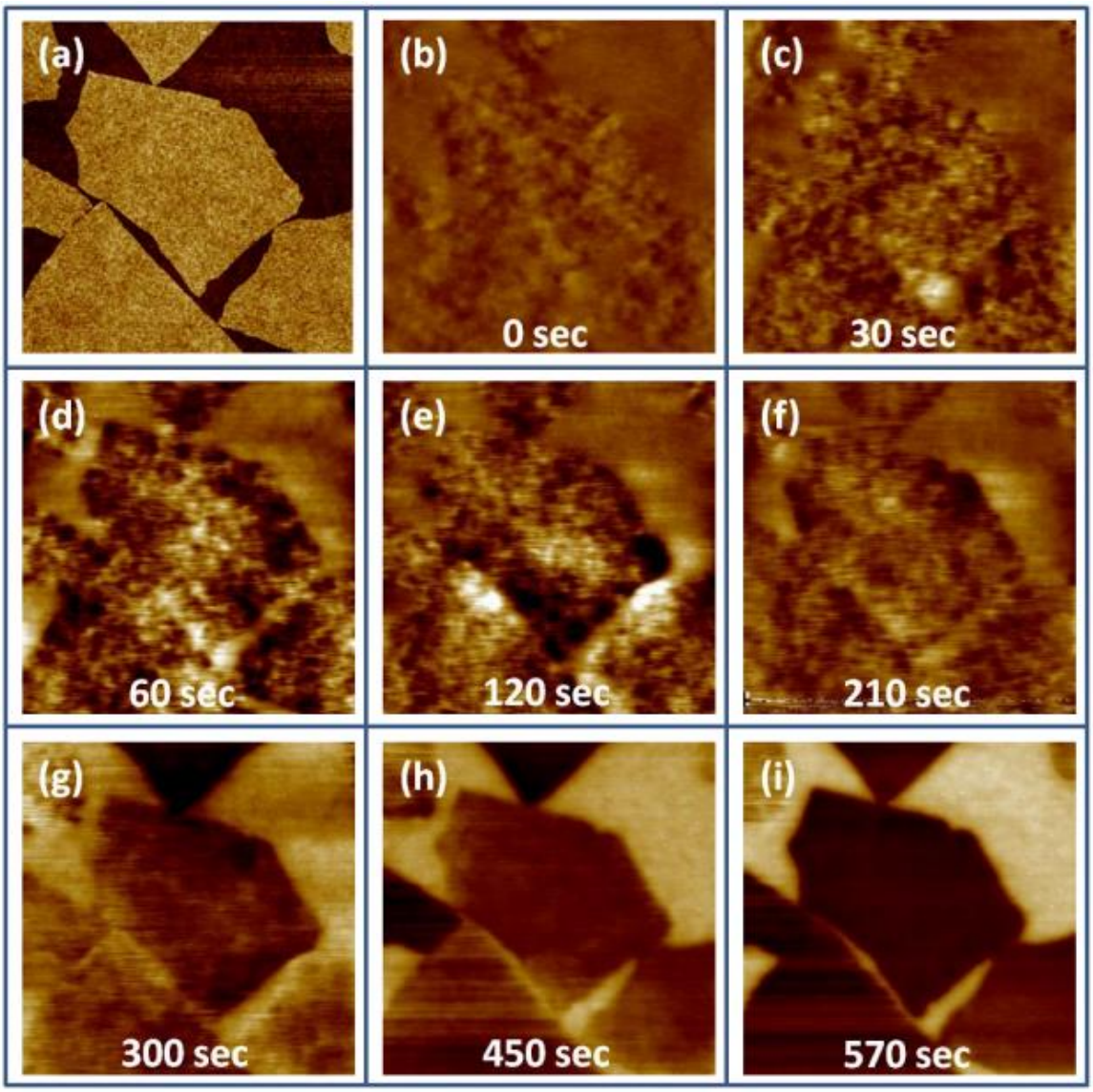

Figure 7.9 Effect of reduction time on graphene oxide composition. (a) AFM topography (z-scale: 3nm) and (b)-(i) EFM-phase images at different times (z-scale: 4^{o} for (b)-(g) and 6^{o} for (h)-(i))

7.3.4 Monitoring the reduction process of graphene oxide

Graphene oxide can be chemically reduced to strip off the oxygenated functionalities on the surface. Thus, the charge distribution on the surface can be varied depending on the degree of reduction. To understand the reduction process of graphene oxide and also to verify our hypothesis, EFM-phase images were obtained for the same flake upon subjecting the substrate to reducing environment for different periods of time. Figure 7.9 shows the changes in the EFM-phase image of the same area subjected to reduction with the increase in time. No significant changes in the topography were observed during the reduction process. However, the EFM images clearly showed a trend. Before reduction, the EFM-phase image showed some distribution of the bright and dark areas with the bright area covering ~27% of the graphene oxide surface. As the reaction time progresses, the dark areas were found to be dominant in the EFM-phase images and eventually a uniform phase shift was observed over the surface of graphene oxide.

Interestingly, different flakes showed different contrast in the EFM-phase upon reduction. This can be due to the different rate of reduction of graphene oxide flakes with a wide chemical inhomogeneity over the surface, as was discussed in the earlier sections. According to our previous observations, a negative phase shift with respect to the silicon oxide substrate at a positive tip bias (darker areas) suggest the presence of oxygen functionalities which should be absent after the reduction process. Thus, to understand this contradiction, additional analysis of the EFM-phase data was required.

7.3.5 Quantitative analysis of the EFM images.

The electrostatic interaction between the conductive tip and the sample can be explained mathematically using the equation[213,341]

$$F_z = \frac{1}{2}\frac{\partial C}{\partial z}\left(V_{tip} - \varphi\,(x,y)\right)^2 \quad (1)$$

where V_{tip} is the voltage applied to the cantilever and $\varphi\,(x,y)$ is the potential distribution along the surface. The electrostatic force is positive since $\frac{\partial C}{\partial z}$ is negative. However, our EFM measurements monitor the changes in the phase and amplitude of oscillation of a mechanically driven cantilever and measures the changes in the force gradient, dF/dz. For small changes in force gradient, the resonant frequency and phase shift are described as follows[213]

$$\Delta\omega = \frac{\omega_0}{2\kappa}\frac{\partial F}{\partial z} \quad (2)$$

$$\Delta\phi = -\arcsin\left(\frac{Q}{2\kappa}\frac{\partial F}{\partial z}\right) \quad (3)$$

where κ is the spring constant (~3 N/m) and Q is the quality factor of the cantilever (~240). Thus, combining equations 1 and 3, the phase shift varies with the electrostatic gradient as [213]

$$\Delta\phi = -\arcsin\left(\frac{Q}{2\kappa}\frac{\partial^2 C}{\partial z^2}\left(V_{tip} - \varphi\,(x,y)\right)^2\right) \quad (4)$$

Or

$$\sin(-\Delta\phi) = \frac{Q}{2\kappa}\frac{\partial^2 C}{\partial z^2}\left(V_{tip} - \varphi\,(x,y)\right)^2 \quad (5)$$

The phase shift is always negative because $\frac{\partial^2 C}{\partial z^2}$ is positive. If a constant voltage is applied to the tip and the tip-sample distance is also maintained constant then the measured electrostatic interaction corresponds to the changes in surface potential along the surface. Also, the electrostatic interaction is zero when the applied voltage equals the surface potential.

Surfaces having identical chemical composition (eg., graphene) and thus an equi-potential surface show a uniform response towards a conductive tip as it moves above the surface. However, the surface of graphene oxide is known to consist of conductive

graphitic domains within a randomly distributed non-conductive matrix consisting of oxidative areas and defects. Thus, it was expected that the chemically different areas along the surface of graphene oxide will show a different response to an electrically biased tip as it moves along the surface. In this study, we recoded the changes in the phase of oscillation because it is known to be more sensitive to the electrostatic forces than the amplitude of oscillation.

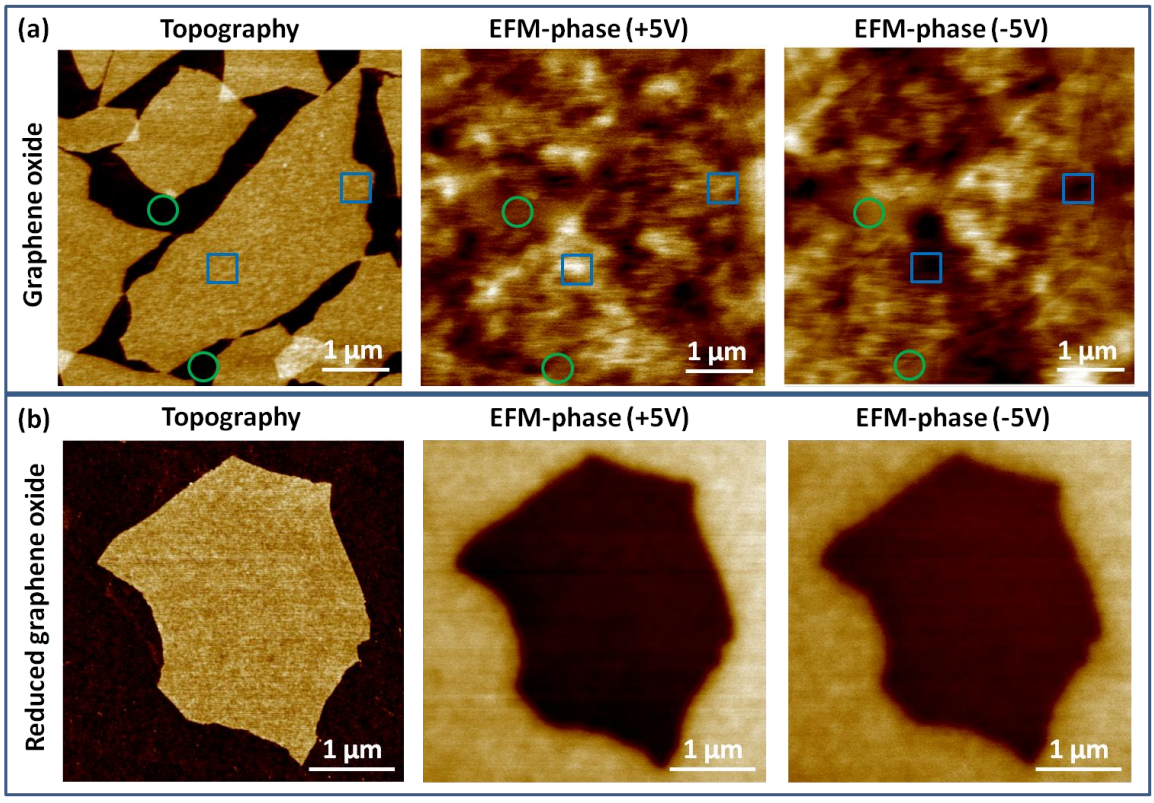

Figure 7.10 AFM topography and EFM-phase image of (a) graphene oxide and (b) reduced graphene oxide flake at a opposite tip polarities

Two factors which influence the EFM signal are the tip-sample capacitance and the tip-sample potential difference. The tip-sample capacitance primarily depends on the material properties (dielectric constant, geometry and tip-sample separation) whereas the

potential difference depends linearly on the sample potential (surface charges).[343] Reversing the polarization of tip is the simplest way to deconvolute effect of the two contributing factors towards phase imaging. The difference in capacitance or dielectric constant over the sample surface will result in a relative change in the phase contrast whereas the non-uniformity in the surface potential will result in a reversal of the phase contrast.

Thus, to verify this effect, EFM-phase images of graphene oxide were obtained at opposite tip polarities before and after reduction. Based on the above hypothesis, the graphene oxide flakes should show a reversal of contrast in the EFM-phase image if the different domains correspond to the charged functionalities and the reduced graphene oxide should show the same contrast irrespective of the tip polarity. Figure 7.10 shows the topography and corresponding EFM phase image of the same area of graphene oxide and reduced graphene oxide taken at a positive and negative tip bias under low humidity conditions (RH <2%). No apparent difference was observed in the topography. However, the EFM phase images of the graphene oxide clearly show a contrast reversal in the areas covered by graphene oxide upon changing the tip polarity (highlighted in blue squares). Also, areas covered by the silicon oxide appeared uniform and showed a relative decrease in the contrast upon changing the tip polarity (highlighted in green circles). This suggests that the observed EFM-phase contrast over the different areas is indeed due to the areas with different surface potential or the presence of charged species on the graphene oxide surface. On the other hand, the EFM-phase images of the reduced graphene oxide look similar irrespective of the tip polarity. This implies that the observed EFM-phase shift for graphene oxide was dominated by the tip-sample potential difference whereas the tip-sample capacitance was responsible for the phase shift in reduced graphene oxide.

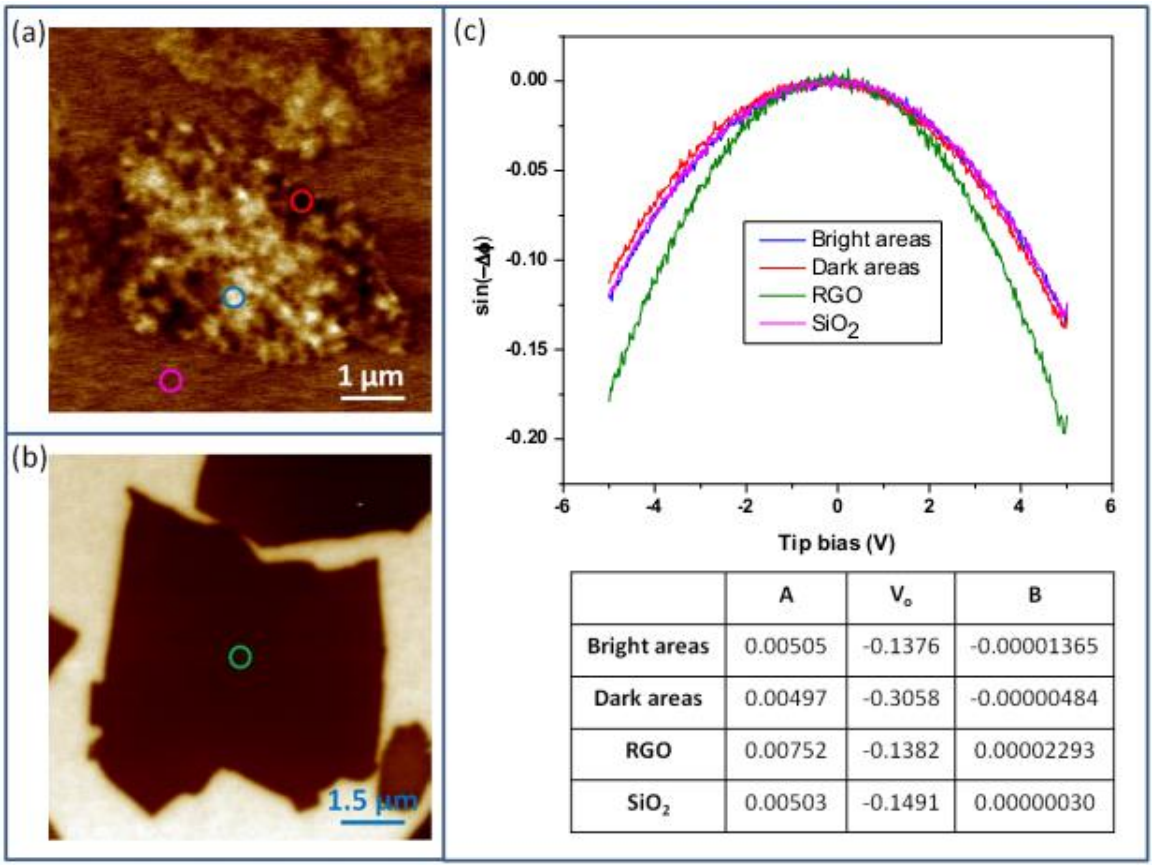

	A	V_o	B
Bright areas	0.00505	-0.1376	-0.00001365
Dark areas	0.00497	-0.3058	-0.00000484
RGO	0.00752	-0.1382	0.00002293
SiO_2	0.00503	-0.1491	0.00000030

Figure 7.11 EFM-phase images of (a) graphene oxide and (b) reduced graphene oxide (RGO), and (c) the corresponding phase shift v/s tip voltage plots at different points over the surface along with the table showing the fitting parameters

Further, to quantify the surface potential and distinguish the conductive and non-conductive domains on the surface of graphene oxide, we measured the phase shift due to electrostatic forces at a given point on the surface to the change in tip bias. Figure 7.11 shows EFM-phase image of graphene oxide and reduced graphene oxide. Also, the shift in the phase of oscillation of the cantilever as function of tip voltage is plotted at the two different areas (bright and dark) on the graphene oxide, the surface of reduced graphene oxide, and the silicon oxide surface. The areas corresponding to the plots are circled with the same color scheme for clarity. As expected from eq. 5, the phase shifts was negative over all the areas and showed a parabolic dependence on the tip bias. Judging from the

shape of the curves, the bright and dark areas showed a similar response to the changes in the tip bias as the silicon oxide surface whereas the reduced graphene oxide showed a higher curvature.

For quantitative calculations, the curves obtained over the different areas were fitted with a function of the form[341,213]

$$\phi = -\arcsin[A(V - V_0)^2] + B \quad (7)$$

Where A represents the constant parameter $\frac{Q}{2\kappa}\frac{\partial^2 C}{\partial z^2}$, B represents an offset to 0°, and V_0 represents potential difference between the sample and the tip ($V_0 = \phi_{sample} - \phi_{tip}$). Also, V_0 can be calculated from the plot itself since the minimum phase shift occurs when $V_0 = V_{tip}$. The values obtained after fitting the representative curves to equation 6 are given in the table shown in Figure 7.11. Additional areas over the substrate were analyzed to get a quantitative estimate of the electrostatic interaction.

A and V_0 are important parameters in quantifying the electrostatic interaction. A can be further used to calculate $\frac{\partial^2 C}{\partial z^2}$ by knowing the quality factor and spring constant. Comparing the bright and dark areas over the graphene oxide surface, it was observed that the A values showed a little variation with the bright areas showing a $\frac{\partial^2 C}{\partial z^2}$ of 0.000126 C/m^2 whereas the dark areas showed a $\frac{\partial^2 C}{\partial z^2}$ of 0.00012 C/m^2. Thus, it was not significant to account for the distribution of functionalities. However, V_0 which corresponds to the surface potential showed a clear difference with the values being 121$\pm$ 2.3 mV and 293$\pm$6.1 mV for the bright and the dark areas respectively. According to classical theory, the different functionalities (hydroxyl, epoxy, and carboxyl) consisting of an oxygen having a lone pair of electrons should have a higher surface potential than

the graphitic domains. Thus, a higher surface potential in the darker areas suggests that these areas correspond to the oxygenated functionalities over the surface.

On the other hand, reduced graphene oxide showed a higher value of $\frac{\partial^2 C}{\partial z^2}$ (0.00019 C/m^2) with very little deviation over the surface. Also, the surface potential of the reduced graphene oxide was found to be 133.6±9.3 mV which was in the range of the surface potential observed for the bright areas over the graphene oxide. A comparatively large standard deviation can be due to the different degree of reduction of graphene oxide flakes as was witnessed from Figure 7.9. This further confirms that the bright areas indeed correspond to the conductive graphitic domains on the surface. Another important noticeable aspect was the distinct curvature in the phase shift of the reduced graphene oxide compared to graphene oxide. This implies that the reduced graphene oxide experiences a higher electrostatic interaction at the same tip bias compared to graphene oxide and silicon oxide. As discussed earlier, the EFM-phase shift in graphene oxide is a result of the tip-sample capacitance which depends on the dielectric properties of the material. Higher dielectric constant would support high degree of polarizability and a higher phase shift at the same tip voltage. The reduction of graphene oxide is expected to restore the electronic properties of graphene. Thermally reduced graphene oxide have been reported to show a dielectric constant of 3.6,[356] close to the dielectric constant of silicon oxide (3.9) but graphite is known to exhibit a very high dielectric constant (10-15). Thus, the exact reason for the observed trend is unclear. However, higher values of capacitance per unit area ($\frac{\partial^2 C}{\partial z^2}$) for reduced graphene oxide suggest a higher dielectric constant, compared to graphene oxide and silicon oxide surfaces.

Several groups have reported similar parabolic dependence of the electrostatic force on the tip bias for different substrates. In particular, Salmeron *et al.* studied the EFM

response of glass, mica, silicon, and graphite.[357] They observed that curvature of the parabola followed the same trend as the dielectric constant (degree of polarizability) of these materials; graphite showing a pronounced polarization effect towards the change in tip bias whereas glass with the lowest dielectric constant showed the weakest response. The oxidized domains consisting of the oxygen atom with lone pair of electrons is highly polarizable and susceptible to the changes in the environment. Thus, upon varying the tip bias, oxidative areas are expected to show a dramatic phase shift in the cantilever oscillation and the resulting parabolic relationship (phase shift v/s tip bias) will have a higher degree of curvature.

In our study, a similar curvature was observed for the bright and dark areas but the bright areas showed a slightly higher phase shift at a negative tip bias and the darker areas showed a higher phase shift at a positive tip bias. This phenomenon again suggests that the darker areas in the EFM-phase image obtained at a positive tip bias should correspond to the oxygenated functionalities with high electronegativities. At the same time, it appears that the graphitic domains are positively charged and not neutral. However, a significant area of the graphene oxide surface is covered by the negatively charged oxygen functionalities. Thus, an overall negative charge is observed on the graphene oxide surface as evident from the z-potential measurements reported in literature.

A scanning probe microscopy technique similar to EFM known as Kelvin probe scanning microscopy (KPFM), has been widely used technique for mapping the changing in the surface potential along the surface. There have been several reports on the use of KPFM to characterize the graphene or graphene oxide surfaces. In particular, Gomez-Herrero *et al.* reported a detailed study on the KPFM measurements to understand the surface potential of graphene oxide flakes deposited on different substrates (gold, silicon, and HOPG).[346] Contrary to our results, they did not observe the variations in surface

potential along the surface of graphene oxide deposited even on silicon. We believe that the discrepancy in the results might be due to the presence of an additional 300 nm oxide layer on top of the doped silicon substrate. The doped silicon substrate with a high polarizability probably influences the surface potential of the 1nm thick graphene oxide by screening the charge distribution along the surface, similar to the presence of a highly polar water layer on the surface.

CHAPTER 8

GRAPHENE OXIDE-POLYMER NANOCOMPOSITES

8.1 INTRODUCTION

Much of the initial excitement around graphene, a one-atom thick layer of sp^2 hybridized carbon atoms, is related to its unique electronic structure in which the electrons behave as Dirac fermions and ballistically conduct, thereby presenting an intriguing truly two dimensional system.[58,66,169,358,359,] With the introduction of robust chemical approaches (vapor[170,171] and solution[66,172,173]) for large scale synthesis of high quality graphene, the real world application of this material excites broader scientific community. For example, graphene has suggested to be an excellent candidate for nanoelectronic devices, solid state gas sensors, ultra sensitive biodevices and nanomechanical actuators, prominent amongst them being as nanofiller in composite materials.[360,361,362,363] However, in order to use graphene as a efficient reinforcing component, it is paramount to incorporate non-aggregated, and non-crumpled graphene sheets with maximum interfacial interactions for efficient load transfer within the polymer matrix.

Recently, highly ordered ultrathin membranes (50-100 nm) containing nanostructures showing high elasticity and robustness have been fabricated using layer-by-layer (LbL) assembly, cast at air-water interfaces, and spin-coating on sacrificial layer. These membranes are known for controlled conformal orientation and stratification of the filler in the composite structure.[187,224,364,365,366] Excellent fracture toughness (~152 MJ/m^3) have been reported for CNT LbL nanocomposites.[367] Similar dramatic increase in the elastic modulus (~105 GPa) have been demonstrated for LbL nanocomposites with incorporated clay nanoplatelets with their content reaching 50 vol.%.[189]

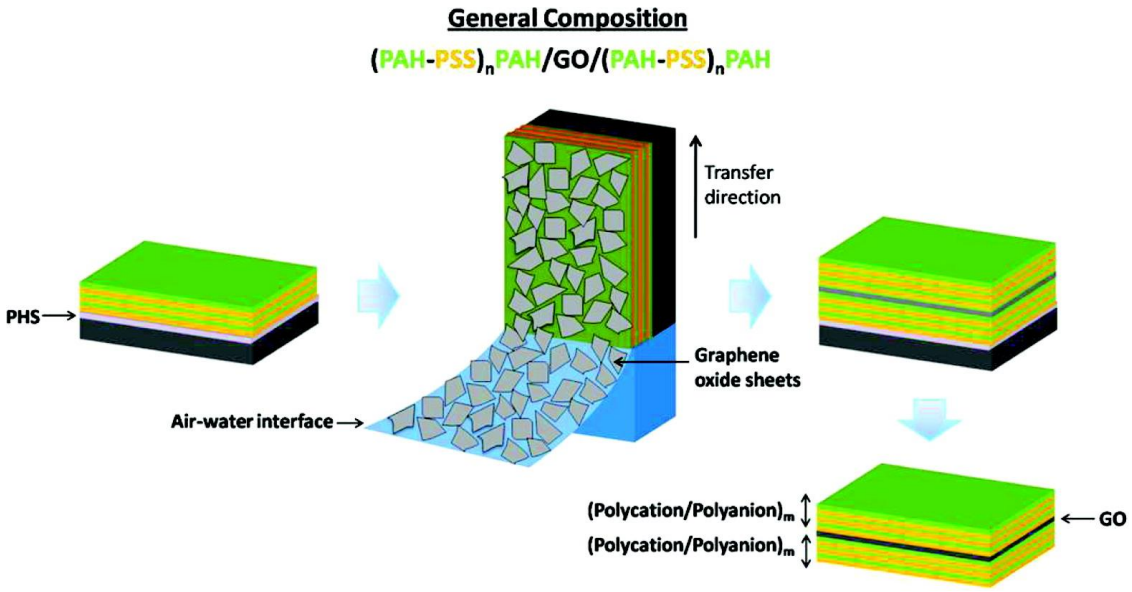

Figure 8.1 Fabrication and assembly of free-standing graphene oxide-LbL membranes

Here, we demonstrate the bottom-up fabrication of highly ordered, free-standing, layered nanocomposites with embedded graphene oxide sheets having excellent toughness and improved elastic modulus, reaching 1.9 MJ/m^3 and 20 GPa for low content of graphene oxide (about 8%). Graphene oxide sheets were uniformly incorporated inside the LbL polyelectrolyte matrix to have a well-ordered stratification. In order to minimize the folding and wrinkling of the graphene oxide sheets, their deposition was performed using Langmuir-Blodgett (LB) technique instead of regular adsorption and spin-casting (Figure 8.1). Folding and wrinkling of graphene oxide sheets due to its flexible nature can be substantially minimized when deposited using LB technique.[368] These free-standing nanoscale (~50 nm thick) multilayered nanomembranes with a monolayer of planar graphene oxide flakes with large lateral dimensions (few cm across) possess outstanding mechanical robustness facilitating their easy handling and facile transfer to any appropriate substrate for further integration with microelectomechanical devices.

8.2 Experimental details

Graphene oxide synthesis and assembly, fabrication of LbL films, fabrication of free-standing graphene oxide-polyelectrolyte composites, and their mechanical testing was done according to the methods discussed in Chapter 3.

8.3 Results and discussions

Graphene oxide sheets prepared by the oxidative exfoliation of graphite flakes gave a homogeneous dispersion appropriate for single-layer deposition. The concentration and size of the graphene oxide flakes was controlled by successive cycles of sonication followed by centrifugation. Sectional analysis of the AFM image revealed planar flakes up to few tens of microns across having modest polydispersity in thickness, 0.96 nm $\pm$ 0.15 nm.

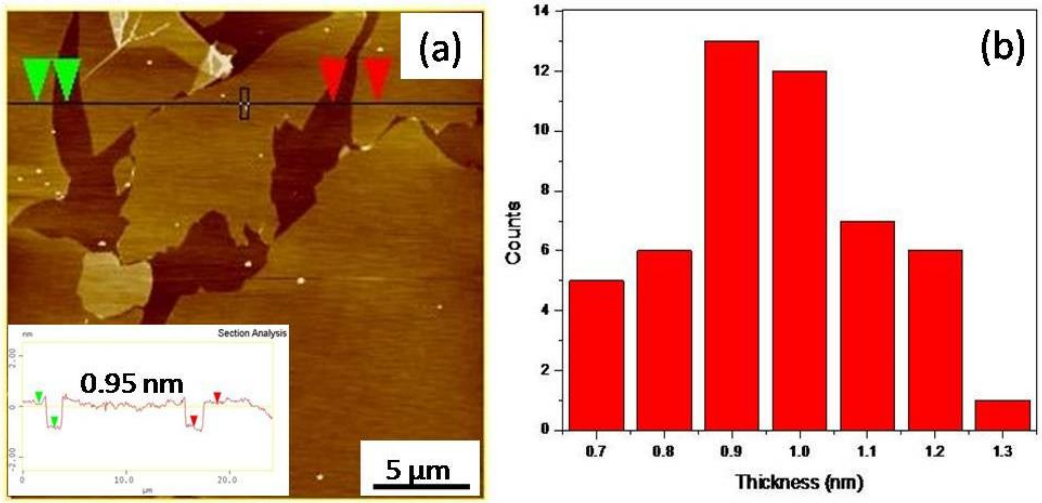

Figure 8.2 Characterization of graphene oxide sheets. (a) AFM image shows graphene oxide sheets deposited on silicon (inset showing the sectional image). (b) Histogram showing the variation of thickness for 50 different flakes with the average thickness: 0.96 $\pm$ 0.2 nm. z-scale: 5 nm

Thus, most of the exfoliated flakes are single layers and bilayers (Figure 8.2).[77,369,370] In order to verify this, we built up a molecular model of graphene oxide sheets with surface functional groups by considering the ratio of C:O to be ~2.2 as reported by Hummer's *et al.* Simple calculations using van der Waals radii for epoxy and hydroxyl surface groups, bond lengths, and bond angles give the effective thickness of a monolayer of graphene oxide to be 0.72 nm. Hydroxyl and epoxy groups in the basal plane, primarily account for this increased thickness of graphene oxide compared to graphene (0.34 nm) whereas carboxyl groups known to be present at the edges contribute insignificantly. It is worth to note that reports on the thicknesses of graphene oxide sheets have suggested that the thicknesses of mono-, bi- and trilayered graphene oxide sheets scale as 1:1.5:2.0 which is consistent with our estimations.

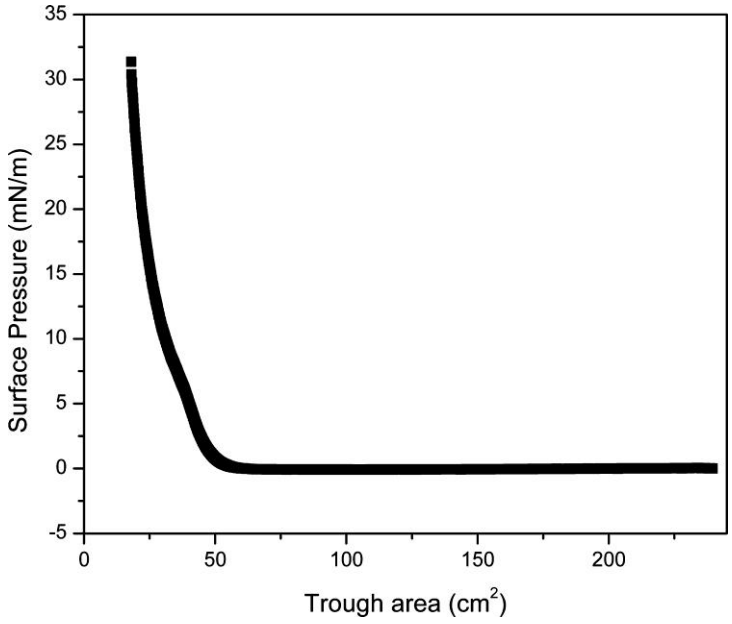

Figure 8.3 Langmuir Isotherm for graphene oxide monolayer deposition

Poly(allylamine hydrochloride) (PAH) and poly(sodium 4-styrene sulphonate) (PSS) PEMs fabricated here via spin-assisted LbL assembly showed uniform morphology with microroughness (within 1x1 μm^2) below 0.5 nm, common for LbL films.[371,372,373] LB

isotherm for graphene oxide solution shows a smooth rise in the surface pressure with the decrease in the surface area suggesting an increase in the packing density of the graphene oxide (Figure 8.3). By controlling the surface pressure, the surface coverage of the graphene oxide sheets was manipulated to give a uniform deposition with high density reaching 90% showing only occasional wrinkles and overlaps (Figure 8.2). High resolution AFM imaging showed that the graphene oxide sheets followed the morphology of the polyelectrolyte layers (Figure 8.4(a), (b)). The microroughness of graphene oxide sheets of 0.38 nm indicates the atomic smoothness. High contrast in phase image obtained at higher resolution showed large difference in surface properties of PEMs and graphene oxide sheets caused by their very different surface functionalities and stiffness (Figure 8.4(c), (d)). These graphene oxide-LbL films with total thickness within 50-70 nm depending upon composition and with 2mm x 2mm lateral dimensions were robust enough after being released to maintain their integrity during gentle handling, drying, and transfer onto different substrates. For instance, uniform deposition of graphene oxide-LbL membranes were obtained upon transfer onto a copper substrate with 150 μm aperture for further bulging mechanical tests and a PDMS compliant substrate for buckling mechanical tests (Figure 8.5).

The elastic modulus of the membrane under compressive stresses is calculated using the equation given below.[194,226]

$$\lambda = 2\pi d \left(\frac{E_f(1-v_s^2)}{3E_s(1-v_f^2)}\right)^{\frac{1}{3}} \quad (1)$$

where, λ is the periodicity of the buckles, v_s, v_f and E_f, E_S are the poisson's ratio and elastic modulus of the substrate (1.8 MPa) and film respectively. The free standing film transferred to elastomeric substrate showed a uniform buckling pattern with the periodicity (λ) of the wrinkles if the stress applied exceeded the threshold level (Figure 8.5(a),(b)). The average value of λ determined from the 2-D Fourier transform of optical

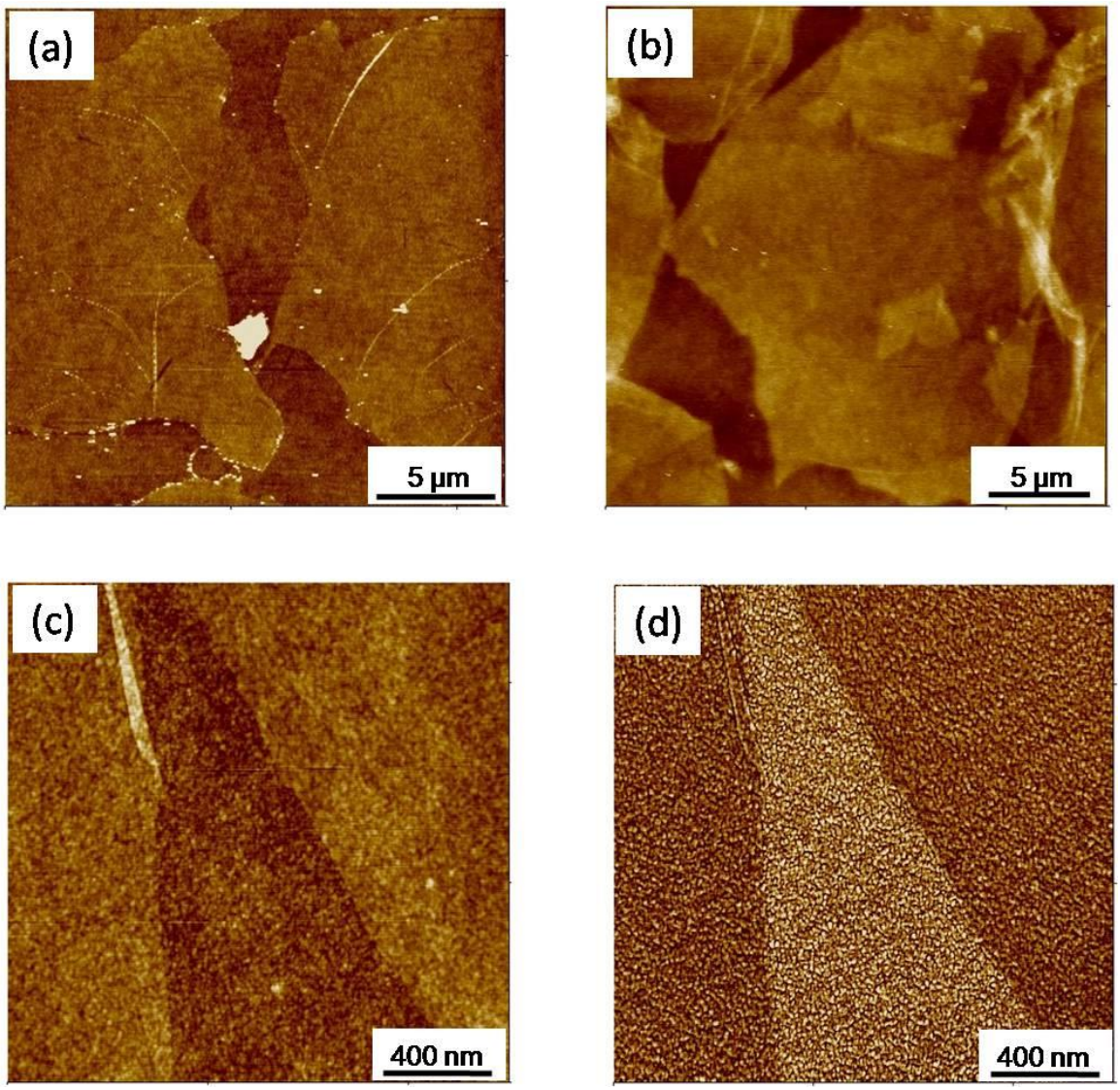

Figure 8.4 AFM images showing the morphology of graphene oxide-LbL membranes with composition (a) $(PAH/PSS)_9PAH$-GO and (b) $(PAH/PSS)_9PAH$-GO-$PAH(PSS/PAH)_9$. High resolution topography (c) and the corresponding phase image (d) of the membrane with composition $(PAH/PSS)_9PAH$-GO. z-scale for topographical images is 5 nm and for phase image is 5^o

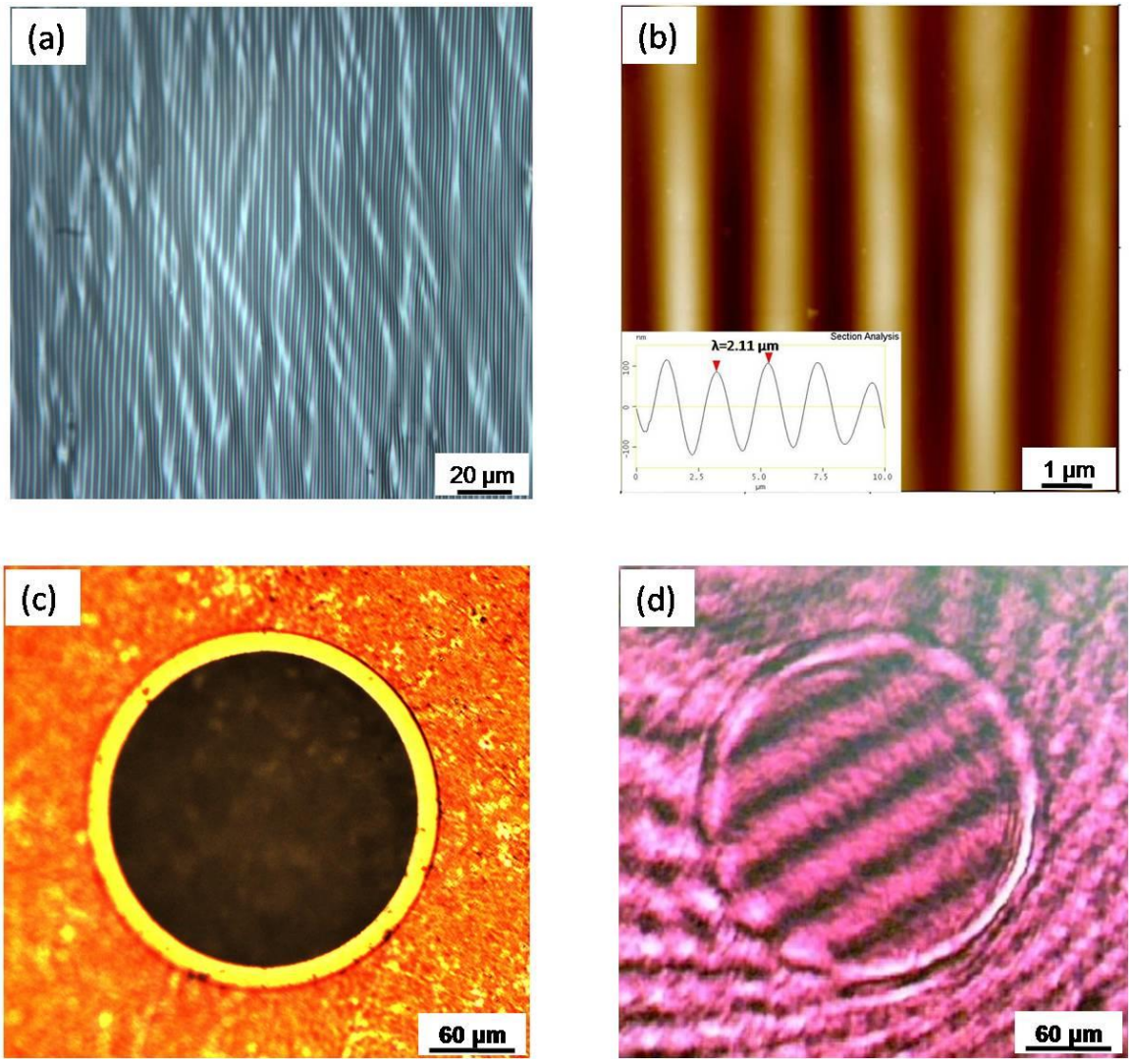

Figure 8.5 (a) Optical image of buckling pattern for LbL-LB film showing periodic wrinkles with spacing of 2.2 µm. (b) AFM image of the buckling pattern (inset showing the sectional image) z-scale: 1 µm, and (c) Optical image of the membrane suspended over a 150 µm

images and AFM cross-sections increased from 2.5 μm to 5.0 μm with increasing concentration of the graphene component and the corresponding Young's modulus increased from 1.5 to about 4.0 GPa (Table 8.1).

Table 8.1 Detailed mechanical properties of graphene oxide based nanomembranes as measured by buckling and bulging techniques

Volume fraction, φ (%)	Effective membrane thickness (nm)	Bulging Young's modulus (GPa)	Buckling Young's modulus (GPa)	Theoretical Young's modulus (GPa)	
				Random orientation	Parallel orientation
0	53 ± 2	1.9 ± 0.6	1.1 ± 0.5	-	-
1.7	52 ± 2	4.5 ± 1.4	1.2 ± 0.5	3.1	5.6
3.3	48 ± 2	8.2± 0.7	2.2 ± 0.3	4.7	9.7
4.9	54 ± 2	10.4 ± 1.5	2.6 ± 0.4	6.2	13.6
6.4	62 ± 2	15.4 ± 1.5	2.8 ± 0.5	7.6	17.4
8.0	74 ± 2	18.2 ± 2.6	3.9 ± 0.5	9.0	21.0

In the case of bulging measurements, a gradual increase in the applied pressure resulted in progressive membrane deflections as monitored with interference microscopy (Figure 8.5(c), (d)). The bulging test measures the deflection d (in μm) of a membrane subjected to a variable pressure P (Pa). The data obtained was analyzed using a theoretical model for a circular elastic plate clamped at stiff edges using equation given below:

$$P=P_0+\left[C_o\frac{E}{1-\nu^2}\frac{h^4}{a^4}+C_1\frac{\sigma_o h^2}{a^2}\right]\left(\frac{d}{h}\right)+C_2\frac{E}{1-\nu}\frac{h^4}{a^4}\left(\frac{d}{h}\right)^3 \quad (2)$$

Here, P_o is the initial pressure, E is the Young's modulus of the film, ν is its poisson's ratio, h is the film thickness, a is the diameter of the membrane, d is the membrane deflection and σ_0 is the residual stress. The tabulated coefficients C_0, C_1 and C_2 are found

to be primarily dependent on the membrane geometry as discussed by Markutsya *et al.*[374] A full pressure versus deflection curve obtained from the bulging data was converted into a stress versus strain curve using the relationships, $\sigma = Pr^2/4hd$ and $\varepsilon = 2d^2/3r^2$, where r is the radius of the opening (75 μm), d is the vertical deflection, and h is the films thickness.

The experimental data for the bulged membranes with different concentrations of graphene oxide component was fitted with the theoretical model for the determination of their Young's moduli in the elastic regime with other parameters (ultimate strength and toughness) calculated from stress-strain data derived from bulging test (Figure 8.6a).[374,375] For this analysis, the linear portion of the stress-strain curve which reflects elastic deformation can be fitted with expression, $\sigma = \sigma_o + [E/(1-\nu^2)]\varepsilon$, $\sigma = \sigma 0 + [E/(1-\nu 2)]\varepsilon$ to calculate the elastic modulus. The Young's modulus increased from 1.5 GPa for original PEM to about 20 GPa with increasing graphene oxide loading from 1.7 to 8.0 vol.% as will be discussed in detail below.

From the experimental data, it is worth to note a significant difference (about five times) in the elastic modulus obtained from buckling and bulging measurements which is highly unusual for bulk composite materials (e.g., 3.9 GPa vs. 18.2 GPa for 8% graphene oxide content). Considering that our membranes were primarily incorporated with bilayer graphene oxide sheets we suggest that the compressive stresses on the graphene oxide-LbL films initiate slippage of the individual graphene oxide sheets and their crumpling at threshold compression. Indeed, the individual layers of the graphene oxide might slip past one another under shearing due to weaker van der Waals interactions of single layers within bilayers as compared to stronger interfacial interactions of graphene oxide sheets with PAH layers facilitated by polar interactions and hydrogen bonding between epoxy/hydroxylic and amine groups. Due to the slippage and buckling, the stress applied

is not completely transferred to the filler and thus the reinforcing contribution of stiff but easily pliable graphene oxide sheets is significantly undermined resulting in the compressive elastic modulus to be many-fold lower than the theoretical estimations (see below). On the contrary, in bulging measurements, the graphene oxide-LbL nanocomposites are subjected to tensile stress which is evenly transferred across the thickness of the film. Thus, all the graphene sheets contribute to the reinforcement fully with minimum slippage.

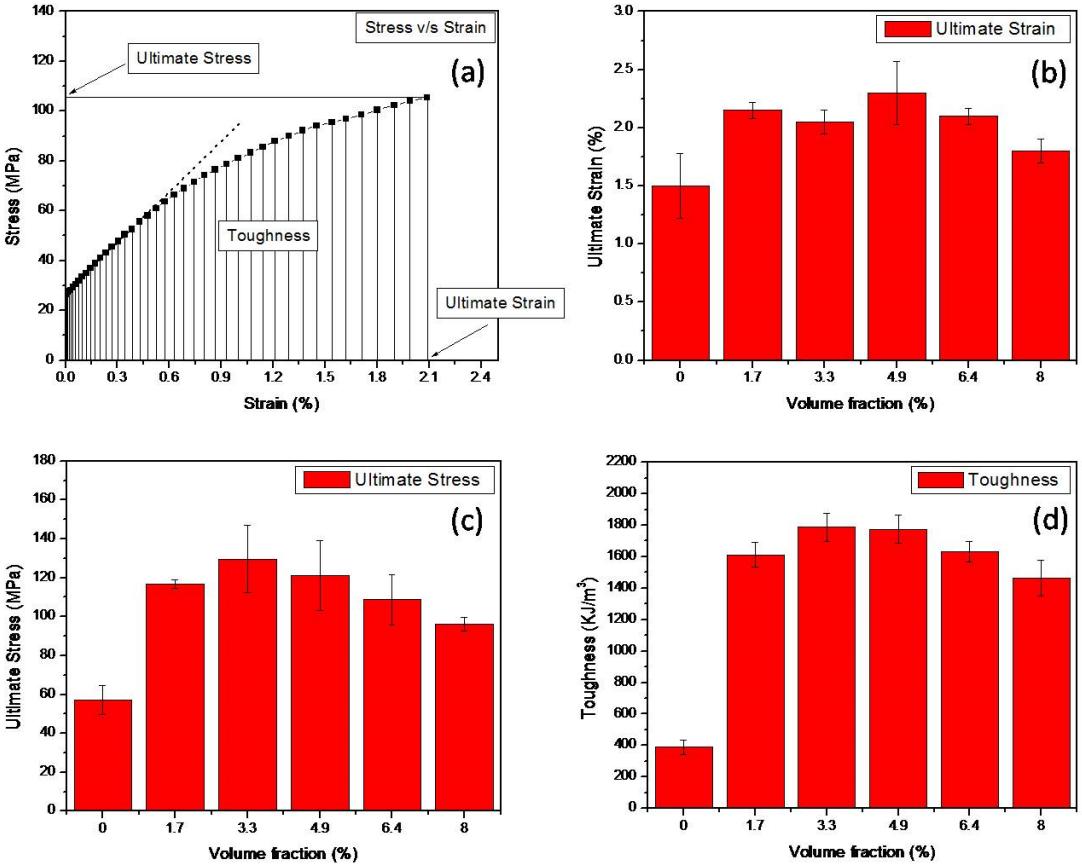

Figure 8.6 (a) Representative stress v/s strain plot showing the ultimate strain, ultimate stress and toughness values. Variation of (b) ultimate strain, (c) ultimate stress and (d) toughness with the volume fraction of graphene oxide component

The stress-strain data derived from bulging measurements was used to estimate the ultimate strength, ultimate strain and toughness in accordance with usual procedures. This analysis showed that the ultimate strain increased significantly from 1.4% to 2.2% after incorporating graphene oxide sheets, indicating surprisingly higher flexibility of graphene oxide-containing nanocomposite membranes (Figure 8.6(b)). In contrast, polyelectrolyte membranes with 50 wt% CNTs have been shown to withstand an ultimate strain of 1%. Moreover, PVA incorporated graphene oxide composites showed a 30% reduction in elasticity whereas PVA/clay polyelectrolyte membrane showed an elasticity of 0.3%.[376] On the other hand, the ultimate mechanical strength of reinforced graphene oxide-LbL nanomembranes increased even more dramatically, by a factor 2.5, and reached 135 MPa (about 150 MPa for some specimens) for very low graphene oxide content (Figure 8.6(c)). Remarkably, the maximum mechanical strength value obtained at a loading of 3.3 vol.% graphene oxide sheets is higher than that of "nacre" with extremely high content of inorganic laminates, one of the toughest known natural composite (~110 MPa).[365] Moreover, it is twice higher than that of high-performance industrial plastics (20-70 MPa) and reaches 2/3 of that recorded for CNT-LbL membranes with 50 wt.% loading of carbon nanotubes (220 MPa).

Even more significant observation is that the toughness of the graphene oxide containing nanomembranes (total energy required to fracture the specimen) increased dramatically, by almost 5-fold, up to about 1.9 MJ/m^3 (Figure 8.6(d)). The maximum toughness was again reached at very small, 3.3 vol.% content of graphene oxide component due to the combination of higher mechanical strength and the ultimate strain. The outstanding value recorded here is about three times higher than those reported for other reinforced LbL films containing metal nanowires and nanoparticles and for silk-clay LbL nanocomposites.[366]

To further verify the micromechanical parameters of the graphene oxide nanomembranes, theoretical predictions based upon Halpin-Tsai model were directly compared with experimental data for nanocomposites with a variable content of graphene oxide sheets.[377] This model is widely applicable to a variety of reinforcement geometries specifically to individual platelets with random or parallel spatial arrangement of reinforcing nanostructures.

Theoretical values of Young's modulus under random and parallel orientation for different concentration of graphene oxide were calculated using Halpin-Tsai model with the following equations.[377]

$$E_{random} = \left[\frac{3}{8}\frac{1+\left(\frac{2L_g}{T_g}\right)\eta_l V_g}{1-\eta_l V_g} + \frac{5}{8}\frac{1-2\eta_t V_g}{1-\eta_l V_g}\right] E_m \quad (3)$$

$$E_{parallel} = \left[\frac{1+\left(\frac{2L_g}{T_g}\right)\eta_l V_g}{1-\eta_l V_g}\right] E_m \quad (4)$$

$$\eta_l = \frac{\left(\frac{E_g}{E_m}\right)-1}{\left(\frac{E_g}{E_m}\right)+2\left(\frac{L_g}{T_g}\right)} \quad (5)$$

$$\eta_t = \frac{\left(\frac{E_g}{E_m}\right)-1}{\left(\frac{E_g}{E_m}\right)+2} \quad (6)$$

where, η_l and η_t are the Halpin-Tsai parameters reflecting the ratio of graphene oxide and matrix moduli in longitudinal and transversal directions, respectively. Young's modulus under random (E_{random}) and parallel ($E_{parallel}$) orientation was calculated by taking into account graphene oxide aspect ratio (l/d), graphene oxide volume fraction (V_g), matrix modulus (E_m =1.5$\pm$0.5 GPa for PAH/PSS film) and the modulus of graphene oxide (E_g = 250 GPa).[378]

The values thus obtained from the calculations for ideal parallel orientation of platelets and complete stress transfer scenario were remarkably close to those obtained

experimentally from the bulging measurements (Figure 8.7). This correlation confirms that the design experimentally elaborated here reaches the theoretical limit of reinforcing effect with highly parallel graphene oxide sheets confined and uniformly distributed within a layered nanocomposite matrix.

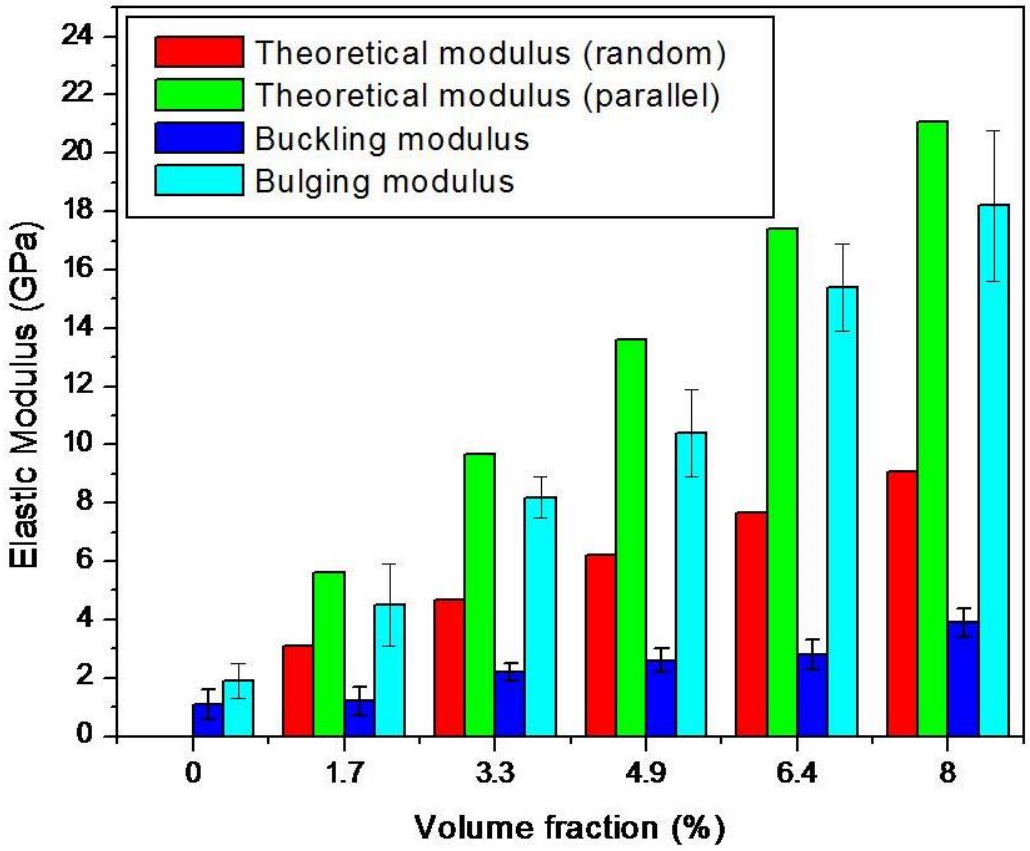

Figure 8.7 Plot showing the variation of elastic modulus calculated theoretically (under parallel and random orientation) and that calculated experimentally (using buckling and bulging measurements) with the volume fraction of graphene oxide

It is worth to note that out attempts to assemble complete LbL nanocomposite films with graphene oxide flakes assembled as a step in LbL routine were not successful due to significant curling, folding, and aggregation of graphene flakes in uncontrollable manner. The resulting fully LbL nanocomposites showed much less ordered and uniform

morphology which compromised their ultimate properties with elastic modulus being only modestly (factor of 2-3) improved. On the other hand, multilayering of graphene oxide flakes by adding second, third, etc LB layers and decreasing polyelectrolyte content did not show significant improvement and overall mechanical properties were compromised by increasing brittleness.

Mechanical properties of reinforced nanocomposites with graphene oxide and graphite flakes incorporated in different polymer matrices have already been reported in literature. However, unlike this study, only modest to substantial reinforcing effect has been observed for highly heterogeneous morphologies.[379] For instance, Shi *et al.* demonstrated a 128% increase in the Young's modulus and 70% increase in the tensile strength of PVA-graphene oxide composites with 3 wt.% graphene oxide.[376] Another study on PVA-graphene oxide composites reported a percolation threshold of 1.8 vol.% for graphene oxide, beyond which the mechanical performance of composite was reduced.[380] Graphene-containing films with thickness between 5-10 μm showed an average modulus of 13 GPa with a tensile strength of 72 MPa.[204] Higher mechanical properties have usually been found for composites with extremely high content of graphene oxide sheets (e.g., carbon paper) on expense, however, of overall flexibility and uniformity.[205,206,381] Altogether, modest reinforcing effect is usually related to easy crumpling and wrinkling of this reinforcing component that compromises its reinforcing role.[382]

CHAPTER 9

GENERAL CONCLUSIONS AND BROADER IMPACT

9.1 General conclusions and discussion

Efficient transport of charge carriers, phonons, and photons across the carbon-metal interface with minimum resistance is the key to fabricate efficient electronic or optoelectronic devices. Also, interfaces play a key role in transferring stress from the polymer to the filler material and dominate the mechanical properties of composite materials. In this work, we have investigated the different interfaces commonly encountered while fabricating carbon-based devices, monitored the changes in the physical structure and chemical composition of different materials, probed the effect of processing conditions, and developed techniques for optimizing the interface properties which would help in improving the device performance, eg., fabricating low-resistance carbon-based electrical interconnects and mechanically robust polymer composites. In particular, two different interfaces were the focus of study: 1) the interface between amorphous carbon and inorganic material (metal nanostructures and silicon), and 2) the interface between carbon (graphene oxide) and synthetic polymer matrix.

Localized carbon nanostructures were fabricated on silicon substrate and found to be amorphous with low electrical conductivity. To improve the electrical conductivity at the interface, structural and compositional transformation of the amorphous carbon deposits to graphitic nanostructures was achieved by thermal annealing and monitored using AFM and Raman microscopy. One of the significant finding of this study is that, c*ompared to bulk amorphous carbon films, the phase transformation in amorphous carbon nanostructures was achieved at a much lower temperature.* Furthermore, the shape of the deposits and interfacial areas was found to play an important role in the phase

transformation behavior of amorphous carbon deposits. However, the process involved subjecting the entire substrate to high temperature and the need to bring about a localized phase transformation of the nanosize carbon deposits was inevitable.

Thus, in the next level of complexity, localized phase transformation of the amorphous carbon nanostructures fabricated on metallic surfaces was achieved by increasing the local temperature using the photothermal effect of the surface plasmons upon excitation with the photons of the right wavelength. The carbon nanostructures fabricated on top of silicon and sputtered metal films showed different structural and compositional characteristics on different substrates upon laser exposure. The deposits on metal films showed partial or full graphitization whereas no compositional change was observed for deposits on the silicon substrate. Localized and dramatic increase in the electrical conductivity at the carbon-metal interface upon laser exposure was observed via current mapping using CFM technique. This *phase transformation was suggested to be brought about by localized surface plasmons that convert the incident light energy into heat and enable a localized phase transition in the amorphous carbon nanostructures to nanocrystalline carbon.* However, the local thermal characteristics and phonon transport at the carbon-metal interface were difficult to measure owing to the small area, thereby fostering the need to develop a sensitive technique for local thermal characterization.

We developed STTM technique in order to map the nanoscale thermal properties of complex devices and interfaces. The approach utilized a novel assymetrical bimorph geometry that induces a twisting motion in the thermal probe. As a proof of concept, thermal properties or phonon transport across inorganic-inorganic interfaces (metal nanoparticles on silicon) as well as organic-inorganic interfaces (patterned organic polymer on glass) at different temperatures was characterized along with their surface morphology. The twisting motion allowed the thermal signal to be isolated from the

normal deflection caused by surface topography thus facilitating nanoscale spatial resolution and mK thermal resolution. STTM simplified thermal imaging with significant improvement of the spatial and thermal resolution.

Next, we focused on the mechanical interface between graphene oxide and a synthetic organic polymer. Graphene oxide, a functionalized form of graphene was synthesized and uniformly deposited on different surfaces using LB technique. EFM technique was used to probe the distribution of oxygenated functionalities on the surface of graphene oxide. A detailed study was performed on characterizing the surface of graphene oxide using conventional methods, however, the EFM technique was found to be unique in mapping the surface functionality distribution on the graphene oxide. Interesting, AFM-based mechanical imaging of the graphene oxide surface was unable to resolve the functionalities but the EFM technique was clearly efficient in mapping the charge distribution over the same area with a sub-20nm lateral resolution. Further, changes in the surface composition of graphene oxide during reduction was also monitored and recorded using this technique.

Finally, graphene oxide flakes were precisely ordered and sandwiched inside a polymer matrix to achieve a high degree of vertical stratification and enable the fabrication robust freely standing membranes. LB technique in combination with LbL assembly ensured a planer, non-wrinkled, and high-surface area coverage of monolayer graphene oxide for the fabrication of layered carbon-based nanocomposites with outstanding mechanical properties facilitated by enhanced interfacial stress transfer between the functionalized groups of graphene oxide and the polymer matrix. Compared to the pristine polymer, incorporation of graphene oxide resulted in a dramatic enhancement in the elastic modulus, tensile strength, and toughness. These robust membranes were found to be highly compliant and could be easily transferred over different substrates.

9.2 Significance and broader impact

Ordered carbon nanomaterials like carbon nanotubes and graphene are known for their unique electronic, mechanical, and thermal properties and offer a promise towards fabrication of high-performance devices and ultra-strong materials. However, eventually it will be the interface between these carbon materials and other structures/materials in the device which would control the overall performance. Thus, *to truly realize and exploit the properties of carbon nanomaterials, it is essential to understand and fabricate interfaces which would enable an efficient transfer of charge carriers, phonons, and photons in devices and an efficient transfer of stress in structural materials.* The work highlighted here presents a novel design paradigm for lowering the electrical resistance of carbon-metal contact and improving the strength of carbon-polymer contact.

The table below taken from the ITRS 2011 interconnect handbook presents some of the key issues related to the scaling down of interconnect technology below 16 nm (table 9.1).[118] Carbon-based nanomaterials materials offer a promise to overcome some of these issues but problems with integration, reliability, and performance come in their way of being a part of electronic systems. Thus, efforts were being made to address some of these issues (highlighted in red) by the use of different materials and different technique. At the same time, developing processes and techniques compatible with the ITRS requirements for semiconductor manufacturing was also taken into consideration in this study. In particular, the challenges with processing, integration, and fabrication of 3D interconnect structures were the prime focus of this study.

Table 9.1 Critical issues challenges the scaling down of interconnect below 16 nm according to the ITRS[118]

Five Most Critical Challenges ***< 16 nm***	***Summary of Technical Issues***
Materials *Mitigate impact of size effects in interconnect structures*	*Line and via sidewall roughness, intersection of porous low-κ voids with sidewall, barrier roughness, and copper surface roughness will all adversely affect electron scattering in copper lines and cause increases in resistivity.*
Metrology *Three-dimensional control of interconnect features (with it's associated metrology) will be required* ***Focus of study***	*Line edge roughness, trench depth and profile, via shape, etch bias, thinning due to cleaning, CMP effects. The multiplicity of levels, com bined with new materials, reduced feature size and pattern dependent processes, use of alternative memories, optical and RF interconnect, continues to challenge .*
Process *Patterning, cleaning, and filling at nano dimensions*	*As features shrink, etching, cleaning, and filling high aspect ratio structures will be challenging, especially for low-κ dual damascene metal structures and DRAM at nano-dimensions.*
Complexity in Integration *Integration of new processes and structures including interconnects for emerging devices*	*Combinations of materials and processes used to fabricate new structures create integration complexity. The increased number of levels exacerbate thermomechanical effects. Novel/active devices may be incorporated into the interconnect.*
Practical Appraoch for 3D *Identify solutions which addresses 3D interconnect structures and other packaging issues*	*Three-dimensional chip stacking circum vents the deficiencies of traditional interconnect scaling by providing enhanced functional diversity. Engineering manufacturable solutions that meet cost targets for this technology is a key interconnect challenge.*

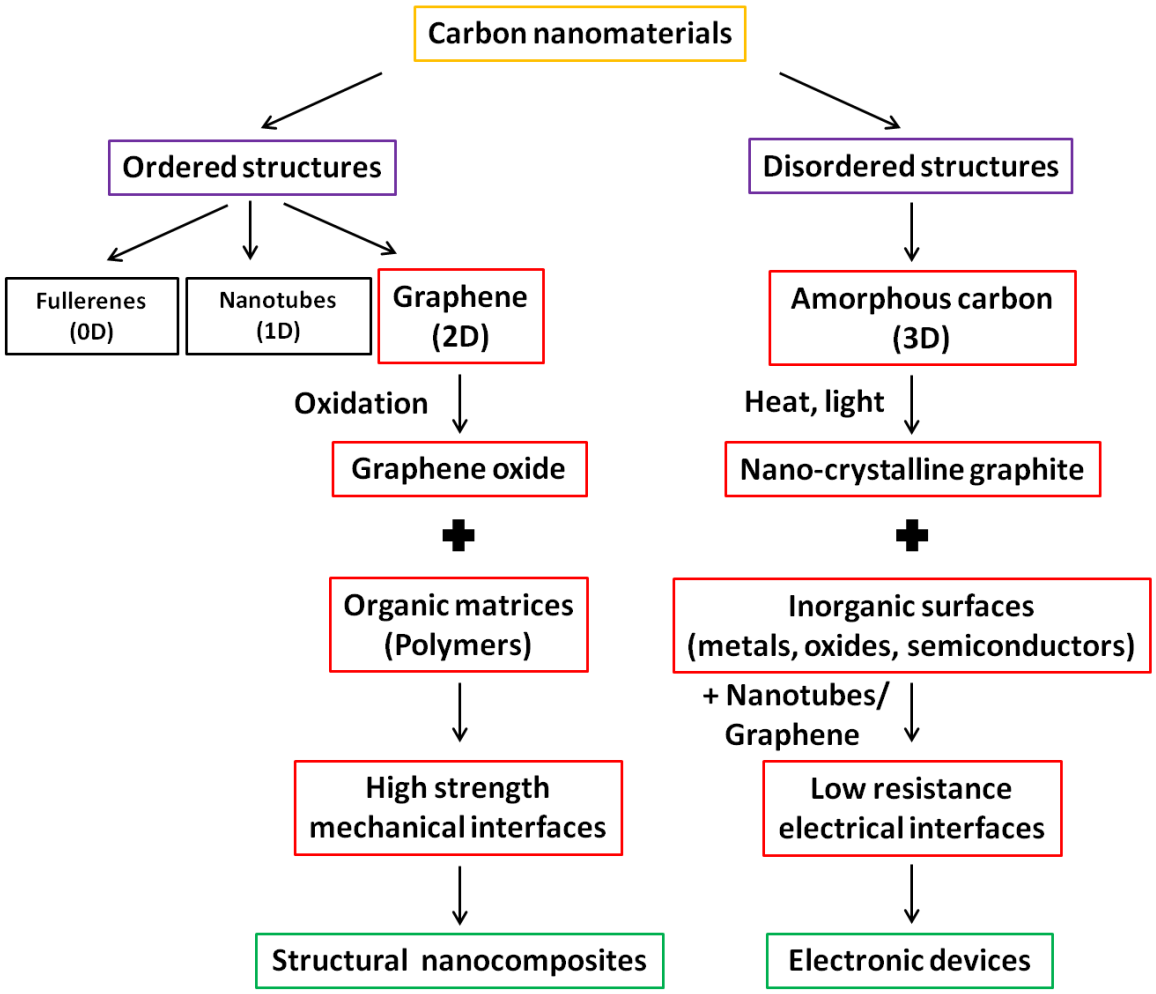

Figure 9.1 Flow-chart showing the structure, significance, and impact of this study

Nanoscale carbon deposits fabricated at the junction between the ordered carbon nanomaterial and metal can reduce the interfacial electrical resistance. However, these carbon deposits showed amorphous characteristics with low electrical conductivity. Thus, efforts to bring about a phase transformation of non-conductive amorphous carbon to conductive nanocrystalline graphitic nanostructures were necessary. This was achieved at low temperatures for the deposits and the processing was as per the requirements put-forth by the International Technology Roadmap for Semiconductors

(ITRS). Further, localized phase transformation was achieved by using the photothermal effect of surface plasmons induced by the light of right wavelength. *Thus, the study not only highlights a simple low temperature phase transformation process of amorphous carbon nanostructures but also demonstrates an efficient technique for faster, greener, less-expensive, and highly localized transformation of amorphous carbon into graphitic nanostructures.* Moreover, localized patterning of conductive domains within the amorphous carbon deposits was also demonstrated which can offer a wider control over the device design and fabrication compared to the conventional techniques.

Particularly for carbon-based electronic devices, deposition of localized carbon nanostructures offers an advantage to electrically connect multiple shells of a MWCNT or multiple layers of graphene with the contact metal on the substrate, previously not possible with the conventional metal deposition techniques. Moreover, contact fabrication using the same material i.e carbon, offers an advantage of having a strong mechanical adhesion and good electronic coupling at the amorphous carbon-carbon nanomaterial interface. Also, the technique can be further improved by using an organo-metallic precursor resulting in the formation of carbon nanostructures with metal nanoparticles embedded which can further lower the resistivity at the interface.

For instance, Prof. Fedorov's group at Georgia Tech is working on the fabrication of low-resistance carbon nanotube interconnects via deposition of amorphous carbon deposition at the carbon nanotube-metal interface. Indeed, the interconnect resistance was found to be lowered by three orders of magnitude after the deposition of amorphous carbon nanostructures itself (Figure 9.2). In order to further low the interfacial resistance, phase transition of the highly resistive amorphous carbon nanostructures towards low resistance graphitic nanostructures was necessary. Thus, collaborative efforts were made to further lower the resistance by tuning the structure and composition of the amorphous carbon

nanostructures deposited at the carbon nanotube-metal interface using the global and local low temperature phase transformation procedures discussed in this study. These phase transformation techniques in conjunction with the amorphous carbon nanostructure fabrication protocol to connect multiple shells of a multi-walled carbon nanotube with the metal underneath resulted in lowering the contact resistance by over eight orders of magnitude, down to a few 100 Ωs, the lowest recorded values ever achieved for carbon nanotube-metal interfaces (Figure 9.2).[27,383]

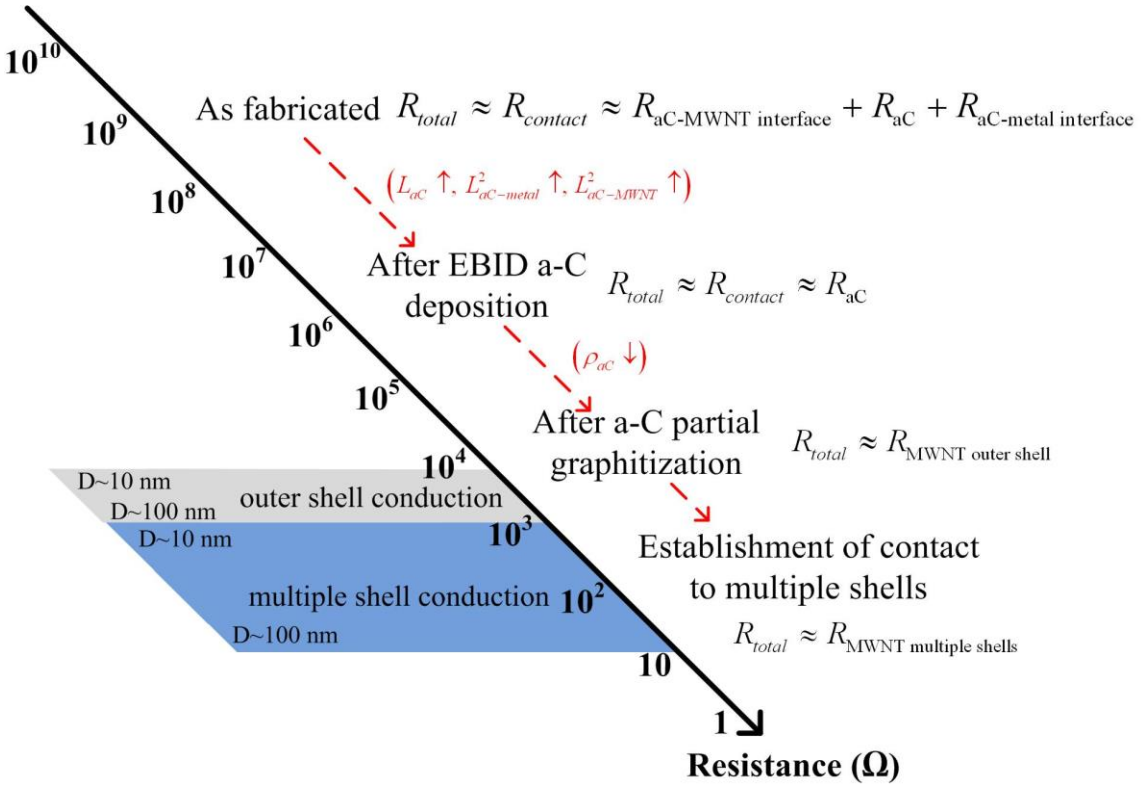

Figure 9.2 Chart summarizing the total resistance of multi-walled carbon nanotube interconnect at the different stages of EBID amorphous carbon deposition and processing[27]

Fabrication of a localized low-resistance multi-junction electrical interface also enables a local phonon transfer across the heterojunction. Thus, the efficiency of the interface can be monitored by the probing the local thermal characteristics of the interface. SThM is a

critical technique in the analysis of thermal, electronic, and photonic transport at dimensions approaching the mean free path of phonons and other quasi particles. However, this technique is limited by resolution, cost, and require additional electronics. *In this work, STTM - an SThM based technique was developed and demonstrated for characterizing the thermal properties of homogeneous and heterogeneous interfaces with nanoscale spatial resolution and high thermal sensitivity not existing now.* STTM technique flourishes near room temperature, thereby making it highly promising for biological imaging applications, mapping of electronic microdevices, and electromechanical systems.

Nanoscale structural, compositional, and defect characterization of a material is typically done using an STM or a TEM. Truly, these techniques can provide precise information of the surfaces with atomic resolution, however, relies on the use of a conductive substrate and an electron transparent carbon support respectively. This limits the use of these techniques for analyzing materials with 'on-substrate' configuration or for biological samples. In this study, we established protocol to use EFM for mapping the charge distribution on a single monolayer of oxidized graphene deposited on commonly used substrates for electronic device fabrication. The protocol was simple and showed its uniqueness in identifying the surface functionalities compared to other AFM-based techniques. This technique is widely applicable to different organic and inorganic materials and can be used to identify the defect sites and interface properties of any electronic substrate irrespective of the device configuration.

On the other hand, high-performance structural materials require a robust mechanical interface for efficient stress transfer between the filler and polymer matrix. Thus, the interface properties can be improved by incorporation of filler materials with chemical functionalities which can act as anchoring sites to the polymer matrix. In this study,

graphene oxide with different oxygenated functionalities on the surface was used for fabricating a robust polymer nanocomposite. Negatively charged graphene oxide and positively charged synthetic polymer incorporated in a LbL structrure enabled a solid control over the distribution of filler inside the polymer matrix. *High surface area of graphene oxide with electrostatically bound interface with the polymer resulted in excellent interfacial strength*. Easy fabrication of free-standing polymer composites was achieved which showed excellent toughness characteristics along with high elastic modulus, strength, and flexibility. These nanocomposite membranes can find wider application due to their prospective electrical, thermal and optical properties along with already outstanding mechanical properties unachievable in traditional clay-based nanocomposites. Electrically conductive, flexible and robust membranes can serve as a substrate for photovoltaics, membranes for heat sink in electronic devices, and can provide an alternative to replace stiff silicon in capacitive pressure sensors used in MEMS devices.

We believe that the understanding of the interface between carbon nanomaterials and organic-inorganic substrates combined with the fabrication and characterization processes discussed in this study can be important for the addressing some of the challenges facing the integration of carbon-based electronic, photonic, and thermal devices and structural materials.

ACKNOWLEDGEMENTS

Financial support for this work was provided by the Semiconductor Research Corporation (SRC) under contract 2008OJ1864.1281 and Air Force Office of Scientific Research (AFOSR) under FA9550-11-1-0233 grant.

DISSEMINATION OF WORK

This work has been conveyed to the scientific community by the following publications and presentations.

Publications

1. **D. D. Kulkarni**, S. Kim, A. G. Fedorov, V. V. Tsukruk. " Probing the defects on graphene oxide using EFM" in preparation

2. **D. D. Kulkarni**, S. Kim, A. G. Fedorov, V. V. Tsukruk. "Light-induced Plasmon-assisted phase transformation of carbon on metal nanoparticles" *Adv. Funct. Mater.* **2012**, *22*, 2129-2139.

3. M. E. McConney, **D. D. Kulkarni**, H. Jiang, T. J. Bunning, V. V. Tsukruk. "A new twist on Scanning Thermal Microscopy" *Nano Lett.* **2012**, *12*, 1218-1223.

4. **D. D. Kulkarni**, K. Rykaczewski, S. Singamaneni, S. Kim, A. G. Fedorov, V. V. Tsukruk. "Thermally Induced Transformations of amorphous carbon nanostructures fabricated by Electron Beam Induced Deposition" *ACS Appl. Mater. Inter.* **2011**, *3*, 710-720.

5. **D. D. Kulkarni**, I. Choi, S. Singamaneni, V. V. Tsukruk. "Graphene oxide-polyelectrolyte nanomembranes" *ACS Nano* **2010**, *4*, 4667-4676.

6. K. Rykaczewski, M. R. Henry, S. Kim, A. G. Fedorov, **D. D. Kulkarni**, S. Singamaneni, V. V. Tsukruk. "The effect of the geometry and material properties of a carbon joint produced by electron beam induced deposition on the electrical resistance of a multiwalled carbon nanotube-to-metal contact interface" *Nanotechnology* **2010**, *21*, 035202.

7. K. Rykaczewski, O. J. Hilderth, **D. D. Kulkarni**, M. R. Henry, S. Kim, C. P. Wong, V. V. Tsukruk, A. G. Fedorov. " Maskless and resist-free rapid prototyping of three-dimensional structures through Electron Beam Induced Deposition (EBID) of carbon in combination with Metal-Assisted Chemical Etching (MaCE) of silicon" *ACS Appl. Mater. Inter*. **2010**, *2*, 969-973.

The following publications are related to the work in this dissertation:

8 I. Choi, **D. D. Kulkarni**, W. Xu, C. Tsitsilianis, V. V. Tsukruk. "Binding of star polymer unimicelles on graphene oxide" *Langmuir*, Submitted

9 K. Hu, M. K. Gupta, **D. D. Kulkarni**, V. V. Tsukruk. "Ultra-robust graphene oxide-silk fibroin nanocomposite membranes" *Adv. Mater*. **2013**, *25*, 2301-2307.

10 M. K. Gupta, **D. D. Kulkarni**, R. Geryak, S. Naik, V. V. Tsukruk. "A robust and facile approach to assembling mobile and highly-open unfrustrated triangular lattices from ferromagnetic nanorods" *Nano Lett.* **2013**, *13*, 36-42.

11 S. Kim, **D. D. Kulkarni**, K. Rykaczewski, M. R. Henry, V. V. Tsukruk, A. G. Fedorov. "Fabrication of an ultra-low resistance ohmic contact to MWCNT-Metal interconnect using Graphitic carbon by Electron Beam Induced Deposition (EBID)" *IEEE Trans. Nano.* **2012**, *6*, 1223-1230.

12 B. Hu, Y. Ding, W. Chen, **D. D. Kulkarni**, Y. Shen, V. V. Tsukruk, Z. L. Wang. "External-strain induced insulating phase transition in VO_2 nanobeam and its application as flexible strain sensor" *Adv. Mater.* **2010**, *22*, 5134-5139.

Presentations

- "Light-induced Plasmon-assisted phase transformation of carbon on metal nanoparticles" Center for Organic Photonics and Electronics (COPE), Atlanta, GA, Apr 23, 2013.

- "Light-induced Plasmon-assisted phase transformation of carbon on metal nanoparticles" Georgia Tech Research & Innovation Conference (GTRIC), Atlanta, GA, Feb 2, 2013.

- "Electron Beam Induced Deposition of graphitic nanojoints for graphene interconnects, NMS patterning & Nanoengineered Materials Review, Denton, TX, June 12-13, 2012.

- “Plasmon-assisted graphitization of amorphous carbon nanostructures.” Materials Research Society (MRS) Fall meeting, Boston, MA, Nov 28 -Dec 2, 2011.

- “On the contact resistance of carbon nanotube-metal interface.” Materials Research Society (MRS) Fall meeting, Boston, MA, Nov-Dec 2011.

- “Graphene oxide-polyelectrolyte nanomembranes” Science Applications International Conference (SAIC), Atlanta, GA, Nov 8, 2011.

- “Development and characterization of low temperature ohmic contact between CNT metal interconnect using focused electron beam chemical vapor deposition.” NMS patterning & Nanoengineered Materials Review, Durham, NC, October 4-6, 2011.

- “Fundamentals of formation and nanoscale properties of carbon nanotube-metal conductor interfaces.” NMS patterning & Nanoengineered Materials Review, Amherst, MA, Nov 9, 2010.

- “Properties of electron beam induced deposited (EBID) carbon-multiwalled carbon nanotube (MWNT)-metal interface.” Materials Research Society Spring Meeting, San Francisco, CA, April 13-17, 2010.

- “Assembly of free-standing polyelectrolyte-graphene oxide nanomembranes.” Materials Research Society Spring 2010 Meeting, San Francisco, CA, April 13-17, 2010.

REFERENCES

[1] Silva, S. R. P. *Properties of Amorphous Carbon*; INSPEC, **2003**.

[2] Ruoff, R. S.; Lorents, D. C. *Carbon* **1995**, *33*, 925-930.

[3] Lee, C.; Wei, X.; Kysar, J.; Hone, J. *Science* **2008**, *321*, 385-388.

[4] Kelly, A.; MacMillan, N. H. *Strong Solids*, Oxford Univ. Press, London, **1986**.

[5] Brookes, C. A. *Philos. Mag. A* **1981**, *43*, 529

[6] Robertson, J. *Phys. Rev. Lett.* **1992**, *68*, 220-223.

[7] Gogotsi, Y.; Presser, V. (Eds.) *Carbon nanomaterials*, CRC Press, **2010**.

[8] Avouris, P.; Chen, Z.; Perebeinos, V. *Nat. Nano.* **2007**, *2*, 605-615.

[9] Ago, H.; Petritsch, K.; Shaffer, M. S.; Windle, A. H.; Friend, R. H.; *Adv. Mater.* **1999**, *11*, 1281-1285.

[10] Dai, L. *Carbon nanotechnology: recent developments in chemisty, physics, materials science and device applications*, Elsevier Science, **2006**.

[11] Sahoo, N. G.; Rana, S.; Cho, J. W.; Li, L.; Chan, S. H. *Prog. Poly. Sci*. **2010**, *35*, 837-867.

[12] Yang, W.; Ratinac, K. R.; Ringer, S. P.; Thordarson, P.; Gooding, J. J.; Braet, F. *Angew. Chem. Int. Ed.* **2010**, *49*, 2114-2138.

[13] Zanello, L. P. *Nano Lett.* **2006**, *6*, 562-567.

[14] Kin, W.; Javey, A.; Tu, R.; Cao, J.; Wang, Q.; Dai, H. *Appl. Phys. Lett.* **2005**, *87*, 173101.

[15] Yaish, Y.; Park, J. K.; Rosenblatt, S.; Sazanova, V.; Brink, M.; McEuen, P. L. *Phys. Rev. Lett.* **2004**, *92*, 046401.

[16] Heinze, S.; Tersoff, J.; Martel, R.; Derycke, V.; Appenzeller, J.; Avouris, P. *Phys. Rev. Lett.* **2002**, *89*, 106801.

[17] Tselev, A.; Hatton, K.; Fuhrer, M. S.; Paranjape, M.; Barbara, P. *Nanotechnology* **2004**, *15*, 1475.

[18] Chou, S. Y.; Krauss, P. R.; Zhang, W.; Guo, L.; Zhuang, L. *J. Vacuum Sci. & Tech. B: Microelec. & Nano. Struc.* **1997**, *15*, 2897-2904.

[19] Austin, M. D.; Ge, H.; Wu, W.; Li, M.; Yu, Z.; Wasserman, D.; Lyon, S. A.; Chou, S. Y. *Appl. Phys. Lett.* **2004**, *84*, 5299-5301.

[20] Lakshminarayanan, S.; Steigerwald, J.; Price, D. T.; Bourgeois, M.; Chow, T. P.; Gutmann, R. J.; Murarka, S. P. *IEEE Elect Dev. Lett.* **1994**, *15*, 307-309.

[21] Svizhenko, A.; Anantram, M. P. *Phys. Rev. B* **2005**, *72*, 085430.

[22] Svizhenko, A.; Anantram, M. P.; Govindan, T. R. *IEEE Trans. Nano*. **2005**, *4*, 557-562.

[23] Banhart, F. *Nanoscale* **2009**, *1*, 201-213.

[24] Banhart, F. *Nano Lett.* **2001**, *1*, 329-332.

[25] van Dorp, W. F.; van Someren, B.; Hagen, C. W.; Kruit, P.; Crozier, P. A. *Nano Lett.* **2005**, *5*, 1303-1307.

[26] Mitsuishi, K.; Shimojo, M.; Han, M.; Furuya, K. *App. Phys. Lett.* **2003**, *83*, 2064-2066.

[27] Rykaczewski, K.; Henry, M. R.; Kim S. K.; Fedorov, A. G.; Kulkarni, D. D; Singamaneni, S.; Tsukruk V. V. *Nanotechnology* **2010**, *21*, 035202.

[28] Kennedy, D. P. *J. App. Phys.* **1960**, *31*, 1490-1497.

[29] Wagner, H. D.; Vaia, R. A. *Materials Today* **2004**, *7*, 38-42.

[30] Velasco-Santos, C.; Martinez-Hernandez, A. L.; Castano, V. M. *Comp. Inter.* **2005**, *11*, 567-586.

[31] Giannelis, E. P. *Adv. Mater.* **1996**, *8*, 29-35.

[32] Vaia, R. A.; Vasudevan, S.; Krawiec, W.; Scanlon, L. G.; Giannelis, E. P. *Adv. Mater.* **1995**, *7*, 154-156.

[33] Moniruzzaman, M.; Winey, K. I. *Macromolecules* **2006**, *39*, 5194-5205.

[34] Wang, M. C.; Yan, C.; Ma, L. *Graphene Nanocomposites. Composites and Their Properties*, In Tech, Shanghai, **2012**.

[35] Fischer, H. *Mater. Sci. & Engg.: C* **2003**, *23*, 763-772.

[36] Iijima, S. *Nature* **1991**, *354*, 56-58

[37] Baughman, R. H.; Zakhidov, A. A.; de Heer, W. A. *Science* **2002**, *297*, 787-792.

[38] Dillon, A. C.; Jones, K. M.; Bekkedahl, T. A.; Kiang, C. H.; Bethune, D. S.; Heben, M. J. *Nature* **1997**, *386*, 377-379.

[39] Kreupl, F.; Graham, A. P.; Duesberg, G. S.; Steinhogl, W.; Liebau, M.; Unger, E.; Honlein, W. *Microelec. Engg.* **2002**, *64*, 399-408.

[40] Bianco, A.; Kostarelos, K.; Prato, M. *Curr. Opi. Chem Bio*. **2005**, *9*, 674-679.

[41] Sun, Y. P.; Fu, K.; Lin, Y.; Huang, W. *Acc. Chem. Res.* **2002**, *35*, 1096-1104.

[42] Katz, E.; Willner, I. *Chem. Phys. Chem.* **2004**, *5*, 1084-1104.

[43] http://www.lawandenvironment.com/tags/singlewalled-carbon-nanotubes/

[44] Li, H. J.; Lu, W. H.; Li, J. J.; Bai, X. D.; Gu, C. Z. *Phys. Rev. Lett.* **2005**, *95*, 086601

[45] Naeemi, A.; Sarvari, R.; Meindl, J. D. *IEEE Elec. Dev. Lett.* **2005**, *26*, 84-86.

[46] Pan, Z. W.; Xie, S. S.; Chang, B. H.; Wang, C. Y.; Lu, L.; Liu, W.; Zhou, W. Y.; Li, W. Z.; Qian, L. X. *Nature* **1998**, *394*, 631-632.

[47] Li, W. Z.; Xie, S. S.; Qian, L. X.; Chang, B. H.; Zou, B. S.; Zhou, W. Y.; Zhao, R. A.; Wang, G. *Science* **1996**, *274*, 1701-1703.

[48] Huang, S.; Cai, X.; Liu, J. *J. Am. Chem. Soc.* **2003**, *125*, 5636-5637.

[49] Wilder, J. W. G.; Venema, L. C.; Rinzler, A. G.; Smalley, R. E.; Dekker, C. *Nature* **1998**, *391*, 59-62.

[50] Odom, T. W.; Huang, J. L.; Kim, P.; Lieber, C. M. *Nature* **1998**, *391*, 62-64.

[51] Bachilo, S. M.; Strano, M. S.; Kittrell, C.; Hauge, R. H.; Smalley, R. E.; Weisman, R. B. *Science* **2002**, *298*, 2361-2366.

[52] White, C. T.; Todorov, T. N. *Nature* **1998**, *393*, 240-242.

[53] Treacy, M. M. J.; Ebbesen, T. W.; Gibson, J. M. *Nature* **1996**, *381*, 678-680.

[54] Salvetat, J. P.; Bonard. J. M.; Thomson, N. H.; Kulik, A. J.; Forro, L.; Benoit, W.; Zuppiroli, L. *App. Phys. A* **1999**, *69*, 255-260.

[55] Novoselov, K. S.; Geim, A. K.; Morozov, S. V.; Jiang, D.; Zhang, Y.; Dubonos, S. V.; Grigorieva, I. V.; Firsov, A. A. *Science* **2004**, *306*, 666-669.

[56] Berger, C.; Song, Z.; Li, T.; Li, X.; Ogbazghi, A. Y.; Feng, R.; Dai, Z.; Marchenkov, A. N.; Conrad, E. H.; First, P. N.; de Heer, W. A. *J. Phys. Chem. B* **2004**, *108*, 19912-19916.

[57] http://graphenelitreviews.blogspot.com/2009/02/electronic-and-magnetic-properties-of.html.

[58] Novoselov, K. S.; Geim, A. K.; Morozov, S. V.; Jiang, D.; Katsnelson, M. I.; Grigorieva, I. V.; Dubonos, S. V.; Firsov, A. A. *Nature* **2005**, *438*, 197-200.

[59] Geim, A. K.; Novoselov, K. S. *Nat. Mater.* **2007**, *6*, 183-191.

[60] Nair, R. R.; Blake, P.; Grigorenko, A. N.; Novoselov, K. S.; Booth, T. J.; Stauber, T.; Peres, N. M. R.; Geim, A. K. *Science* **2008**, *320*, 1308.

[61] Geim, A. K. *Science* **2009**, *324*, 1530-1534.

[62] Jariwala, D.; Sangwan, V. K.; Lauhon, L. J.; Marks, T. J.; Hersam, M. C. *Chem. Soc. Rev.* **2013**, *42*, 2824-2680.

[63] Kim, K. S.; Zhao, Y.; Jang, H.; Lee, S. Y.; Kim, J. M.; Kim, K. S.; Ahn, J. H.; Kim, P. Choi, J. Y.; Hong, B. H. *Nature* **2009**, *457*, 706-710.

[64] Alwarappan, S.; Erdem, A.; Liu, C.; Li, C. Z. J. *Phys. Chem. C* **2009**, *113*, 8853-8857.

[65] Ghosh, S.; Calizo, I.; Tewelderbrhan, D.; Pokatilov, E. P.; Nika, D. L.; Balandin, A. A.; Bao, W.; Miao, F.; Lau, C. N. *Appl. Phys. Lett.* **2008**, *92*, 151911.

[66] Hummers, W. S.; Offeman, R. E. *J. Amer. Chem. Soc.* **1958**, *80*, 1339.

[67] Stankovich, S.; Dikin, D. A.; Piner, R. D.; Kohlhaas, K. A.; Kleinhammes, A.; Jia, Y.; Wu, Y.; Nguyen, S. T.; Ruoff, R. S. *Carbon* **2007**, *45*, 1558-1565.

[68] Marcano, D. C.; Kosynkin, D. V.; Berlin, J. M.; Sinitskii, A.; Sun, Z.; Slesarev, A.; Alemany, L. B.; Lu, W.; Tour, J. M. *ACS Nano* **2010**, *4*, 4806-4814.

[69] Dreyer, D. R.; Park, S.; Bielwski, C. W.; Ruoff, R. S. *Chem. Soc. Rev.* **2010**, *39*, 228-240.

[70] Lerf, A.; He, H. Riedl, T.; Forster, M.; Klinowski, J. *Sol. State Ion.* **1997**, *101-103*, 857-862.

[71] He, H.; Klinowski, J, Forster, M.; Lerf, A. *Chem. Phys. Lett.* **1997**, *287*, 53-56.

[72] Sun, Z.; Kohama, S.; Zhang, Z.; Lomeda, J. R.; Tour, J. M. *Nano Res.* **2010**, *3*, 117-125.

[73] Zhu, Y.; Murali, S.; Cai, W.; Li, X.; Suk, J. W.; Potts, J. R.; Ruoff, R. S. *Adv. Mater.* **2010**, *22*, 3906-3924.

[74] Eda, G.; Fanchini, G.; Chhowalla, M. *Nat. Nano.* **2008**, *3*, 270-274.

[75] Gao, X.; Jang, J.; Nagase, S. *J. Phys. Chem. C* **2010**, *114*, 832-842.

[76] Erickson, K.; Erni, R.; Lee, Z.; Alem, N.; Gannett, W.; Zettl, A. *Adv. Mater.* **2010**, *22*, 4467-4462.

[77] Mkhoyan, K. A.; Contryman, A. W.; Silcox, J.; Stewart, D. A.; Eda, G.; Mattevi, C.; Miller, S.; Chhowalla, M. *Nano Lett.* **2009**, *9*, 1058-1063.

[78] Gomez-Navarro, C.; Meyer, J. C.; Sundaram, R. S.; Chuvilin, A.; Kurasch, S.; Burghard, M.; Kern, K.; Kaiser, U. *Nano Lett.* **2010**, *10*, 1144-1148.

[79] Robertson, J. *Adv. Phy.* **1986**, *35*, 317-374.

[80] Tersoff, J. *Phys. Rev. Lett.* **1988**, *61*, 2879-2882.

[81] Smith, F. W. *J. Appl. Phys.* **1984**, *55*, 764-771.

[82] Robertson, J.; O'rilley, E. P. *Phys. Rev. B* **1987**, *35*, 2946.

[83] Cuomo, J. J.; Pappas, D. L.; Bruley, J.; Doyle, J. P.; Saenger, K. L. *J. Appl. Phys.* **1991**, *70*, 1706-1711.

[84] Pappas, D. L.; Saenger, K. L.; Bruley, J.; Krakow, W.; Cuomo, J. J.; Gu, T.; Collins, R. W. *J. Appl. Phys.* **1992**, *71*, 5675-5684.

[85] Wachter, R.; Cordery, A. *Carbon* **1999**, *37*, 1529-1537.

[86] Aisenberg, S.; Chabot, R. *J. App. Phys.* **1971**, *42*, 2953-2958.

[87] Krishnaswamy, J.; Rengan, A.; Narayan, J.; Vedam, K.; McHargue, C. J. *App. Phys. Lett.* **1989**, *54*, 2455-2457.

[88] McKenzie, D. R.; Yin, Y.; Marks, N. A.; Davis, C. A.; Kravtchinkaia, E. Pailthorpe, B. A.; Amaratunga, G. A. J. *J. Non-Crys. Sol.* **1993**, *164*, 1101-1106.

[89] Tiainen, V. M. *Diam. & Rel. Mater.* **2001**, *10*, 153-160.

[90] Sullivan, J. P.; Friedman, T. A.; Hjort, K. *MRS Bulletin* **2001**, *26*, 309-311.

[91] Han, H. X.; Feldman, B. J. *Sol. State. Comm.* **1988**, *65*, 921-923.

[92] Choi, W. S.; Kim, K.; Yi, J.; Hong, B. *Mater. Lett.* **2008**, *62*, 577-580.

[93] Rykaczewski, K.; Henry, M. R.; Fedorov, A. G. *App. Phys. Lett.* **2009**, *95*, 113112.

[94] Fedorov, A. G.; Rykaczewski, K.; White, W. B. *Surf. Coat. Tech.* **2004**, *201*, 8808-8812.

[95] Ding, W.; Dikin, D. A.; Chen, X.; Piner, R. D.; Ruoff, R. S.; Zussman, E.; Wang, X.; Li, X. *J. App. Phys.* **2005**, *98*, 014905.

[96] Utke, I., Hoffmann, P.; Melngailis, J. *J. Vac. Sci. Tech. B* **2008**, *26*, 1197-1276.

[97] Silvis-Cividjian, N. *Electron beam induced nanometer scale deposition*, Dissertation, University of Delft: Netherlands, **2002**.

[98] Ando, A.; Shimizu, T.; Abe, H.; Nakayama, Y.; Tokumoto, H. *Physica E: Low-Dimens. Sys. & Nanostruc.* **2004**, *24*, 6-9.

[99] Rykaczewski, K.; Marshall, A.; White, W. B.; Fedorov, A. G. *Ultramicroscopy* **2008**, *108*, 989-992.

[100] Ueda, K.; Yoshimura, M. *Thin solid films* **2004**, *464-465*, 331-334.

[101] Rykaczewski, K.; White, W. B.; Fedorov, A. G. *J. App. Phys.* **2007**, *101*, 054307.

[102] Tao, J.; Cheung, N. W.; Hu, C. *IEEE Elec. Dev. Lett.* **1993**, *14*, 249-251.

[103] Lloyd, J. R.; Clement, J. J. *Thin Solid Films* **1995**, *262*, 135-141.

[104] Raychowdhury, A.; Roy, K. *IEEE Trans. Comp.- Aided Design of Integrated Circuits and Systems* **2006**, *25*, 58-65

[105] Naeemi, A.; Meindl, J. D. *IEEE Elec. Device Lett.* **2006**, *27*, 338-340.

[106] Li, J.; Ye, Q.; Cassell, A.; Ag, H. T.; Stevens, R.; Han, J.; Meyaappan, M. *App. Phys. Lett.* **2003**, *82*, 2491-2493.

[107] Tans, S. J.; Verschueren, A. R. M.; Dekker, C. *Nature* **1998**, *393*, 49-52.

[108] McEuen, P. L. *Nature* **1998**, *393*, 15-17.

[109] Avouris, P.; Hertel, T.; Martel, R.; Schmidt, T.; Shea, H. R.; Walkup, R. E. *Appl. Surf. Sci.* **1999**, *141*, 201-209.

[110] Avouris, P. *MRS Bulletin* **2004**, 403-410.

[111] Li, H.; Yin, W. Y.; Banerjee, K.; Mao, J. –F. *IEEE Trans. Elect. Dev.* **2008**, *55*, 1328-1337.

[112] Close, G. F.; Yasuda, S.; Paul, B.; Fujita, S.; Wong, H. S. P. *Nano Lett*. **2008**, *8*, 706-709.

[113] Xia, F.; Farmer, D. B.; Lin, Y. M.; Avouris, P. *Nano Lett.* **2010**, *10*, 715-718.

[114] Li, X.; Wang, X.; Zhang, L.; Lee, S.; Dai, H. *Science* **2008**, *319*, 1229-1232.

[115] Han, M. Y.; Ozyilmaz, B.; Zhang, Y.; Kim, P. *Phys. Rev. Lett.* **2007**, 206805.

[116] Wassmann, T.; Seitsonen, A. P.; Saitta, A. M.; Lazzeri, M.; Mauri, F. *Phys. Rev. Lett.* **2008**, *101*, 096402.

[117] Lin, Y. M.; Dimitrakopoulos, C.; Jenkins, K. A.; Farmer, D. B.; Chiu, H. Y.; Grill, A.; Avouris, P. *Science* **2010**, *327*, 662.

[118] www.ITRS.net

[119] Dean, C. R.; Young, A. F.; Meric, I.; Lee, C.; Wang, L.; Sorgenfrei, S.; Watanbde, K.; Taniguchi, T.; Kim, P.; Shepard, K. L.; Hone, J. *Nat. Nano.* **2010**, *5*, 722-726.

[120] Lee, K. H.; Shin, H. J.; Lee, J.; Lee, I. Y.; Kim, G. H.; Choi, J. Y.; Kim, S. W. *Nano Lett.* **2012**, *12*, 714-718.

[121] Bae, S.; Kim, H.; Lee, Y.; Xu, X.; Park, J. S.; Zheng, Y.; Balakrishnan, J.; Lei, T.; Kim, H. R.; Song, Y. L.; Kim, Y. J.; Kim, K. S.; Ozyilmaz, B.; Ahn, J. H.; Hong, B. H.; Iijima, S. *Nat. Nano.* **2010**, *5*, 574-578.

[122] Li, X.; Zhu, Y.; Cai, W.; Borysiak, M.; Han, B.; Chen, D.; Piner, R. D.; Colombo, L.; Ruoff, R. S. *Nano Lett.* **2009**, *9*, 4359-4263.

[123] Liu, Z.; Liu, Q.; Huang, Y.; Ma, Y.; Yin, S.; Zhang, X.; Sun, W.; Chen, Y. *Adv. Mater.* **2008**, *20*, 3924-3930.

[124] Wang, X.; Zhi, L.; Mullen, K. *Nano Lett.* **2008**, *8*, 323-327.

[125] Dimitrakakis, G.; Tylianakis, E.; Froudakis, G. E. *Nano Lett.* **2008**, *8*, 3166-3170.

[126] Pumera, M. *Ener. & Environ. Sci.* **2011**, *4*, 668-674.

[127] Yin, S.; Zhang, Y.; Kong, J.; Zou, C.; Li, C. M.; Lu, X.; Ma, J.; Boey, F. Y. C.; Chen, X. *ACS Nano* **2011**, *5*, 3831-3938.

[128] Stoller, M. D.; Park, S.; Zhu, Y.; An, J.; Ruoff, R. S. *Nano Lett.* **2008**, *8*, 3498-3502.

[129] Rice, P.; Wallis, T. M.; Russek, S. E.; Kabos, P. *Nano Lett.* **2007**, *7*, 1086-1090.

[130] Rykaczewski, K.; Hilderth, O. J.; Kulkarni, D. D.; Henry, M. R.; Kim, S. -K; Wong, C. P; Tsukruk, V. V.; Fedorov, A. G. *ACS Appl. Mater.Inter.* **2010**, *2*, 969-975.

[131] Guan, Y.; Fowlkes, J. D.; Retterer, S. T.; Simpson, M. L.; Rack P. D. *Nanotechnology* **2008**, *19*, 505302.

[132] Marchon, B.; Heiman, N.; Khan, M. R.; Lautie, A.; Ager J. W.; Veirs, D. K. *J. Appl. Phys.* **1991**, *69*, 5748-5750.

[133] Onodera, A.; Irie, Y.; Higashi, K.; Umermeura, J.; Takenaka, T. *J. Appl. Phys.* **1991**, *69*, 2611-2617.

[134] Zheng, M.; Takei, K.; Hsia, B.; Fang, H.; Zhang, X.; Ferralis, N.; Ko, H.; Chueh, Y. L.; Zhang, Y.; Maboudian, R.; Javey, A. *Appl. Phys. Lett.* **2010**, *96*, 063110.

[135] Yang, C.; Hazeghi, A.; Takei, K.; Chen H. Y.;Chan, P. C. H.; Javey, A.; Wong, P. H. S. *IEEE Trans. Elec. Devices* **2012**, *59*, 12-19.

[136] Barreiro, A.; Borrnert, F.; Avdoshenko, S. M.; Rellinghaus, B.; Cuniberti, G.; Rummeli, M. H.; Vandersypen, L. M. K. *Scientific Reports* **2012**, *3*, 1-6.

[137] Schadler, L. S.; Giannaris, S. C.; Ajayan, P. M. *App. Phys. Lett.* **1998**, *73*, 3842-3845.

[138] Qian, D.; Dickey, E. C.; Andrews, R.; Rantell, T. *App. Phys. Lett.* **2000**, *76*, 2868-2871.

[139] Ramasubramanium, R.; Chen, J.; Liu, H. *App. Phys. Lett.* **2003**, *83*, 2928-2931.

[140] Kymakis, E.; Alexandou, I; Amaratunga, G. A. *J. Syn. Metals* **2002**, *127*, 59-62.

[141] Ajayan, P. M.; Stephan, O.; Colliex, C.; Trauth, D. *Science* **1994**, *265*, 1212-1214.

[142] Bower, C.; Rosen, R.; Jin, L.; Han, J.; Zhou, O. *Appl. Phys. Lett.* **1999**, *74*, 3317-3320.

[143] Thostenson, E. T.; Chou, T. W. *J. Phys. D: Appl. Phys.* **2002**, *35*, L77-L80.

[144] McNally, T.; Potschke, P.; Halley, P.; Murphy, M.; Martin, D.; Bell, S. E.; Brennan, G. P.; Bein, D.; Lemoine, P.; Quinn, J. P. *Polymer* **2005**, *46*, 8222-8232.

[145] Andrews, R.; Jacques, D.; Qian, D. L.; Rantell, T. *Acc. Chem Res*. **2002**, *35*, 1008-1017.

[146] Sandler, J. K. W.; Kirk, J. E.; Kinloch, I. A.; Shaffer, M. S. P.; Windle, A. H. *Polymer* **2003**, *44*, 5893-5899.

[147] Stankovich, S.; Dikin, D. A.; Dommett, G. H.; Kohlhaas, K. M.; Zimney, E. J.; Stach, E. A.; Piner, R. D.; Nguyen, S. T.; Ruoff, R. S. *Nature* **2007**, *442*, 282-286.

[148] Kuilla, T.; Bhadra, S.; Yao, D.; Kim, N. H.; Bose, S.; Lee, J. H. *Prog. Poly. Sci.* **2010**, *35*, 1350-1375.

[149] Rafiee, M. A.; Rafiee, J.; Wang, Z.; Song, H.; Yu, Z. Z. Koratkar, N. *ACS Nano* **2009**, *3*, 3884-3890.

[150] Zhang, K.; Zhang, L. L.; Zhao, X. S.; Wu. *J. Chem Mater*. **2010**, *22*, 1392-1401.

[151] Jung, J. H.; Jeon, J. H.; Sridhar, V.; Oh, I. K. *Carbon* **2011**, *49*, 1279-1289.

[152] Brownson, D. A.; Kampouris, D. K.; Banks, C. E. *J. Pow. Sour.* **2011**, *196*, 4873-4885.

[153] Huang, X.; Qi, X.; Boey, F.; Zhang, H. *Chem. Soc. Rev.* **2012**, *41*, 666-686.

[154] Li, J.; Guo, S.; Zhai, Y.; Wang, E. *Electrochem. Comm.* **2009**, *11*, 1085-1088.

[155] Kim, H.; Miura, Y.; Macosko, C. W. *Chem. Mater.* **2010**, *22*, 3441-3450.

[156] Fang, M.; Wang, K.; Lu, H.; Yang, Y.; Nutt, S. *J. Mater. Chem.* **2009**, *19*, 7098-7105.

[157] Collins, P. G.; Arnold, M. S.; Avouris, P. *Science* **2001**, *292*, 706-709.

[158] Takagi, D.; Homma, Y.; Hibino, H.; Suzuki, S.; Kobayashi, Y. *Nano Lett.* **2006**, *6*, 2642-2645.

[159] Bhaviripudi, S.; Mile, E.; Steiner, S. A.; Zare, A. T.; Dresselhaus, M. S.; Belcher, A. M.; Kong, J. *J. Amer. Chem. Soc.* **2007**, *129*, 1516-1517.

[160] Dresselhaus, M. S.; Dresselhaus, G.; Avouris, P. *Carbon nanotubes: synthesis, structure, properties and applications*, Berlin; New York: Springer, **2001**.

[161] Li, Y.; Peng, S.; Mann, D.; Cao, J.; Tu, R.; Cho, K. J.; Dai. H. *J. Phys. Chem. B* **2005**, *109*, 6968-6971.

[162] Arnold, M. S.; Green, A. A.; Hulvat, J. F.; Stupp, S. I; Hersam, M. C. *Nat. Nano.* **2006**, *1*, 60-65.

[163] Zheng, M.; Jagota, A.; Strano, M. S.; Santos, A. P.; Barone, P.; Chou, S. G.; Diner, B. A. *Science* **2003**, *302*, 1545-1548.

[164] Krupke, R.; Hennrich, F.; Lohneysen, H. V.; Kappes, M. M. *Science* **2003**, *301*, 344-357.

[165] Hiura, H.; Ebbesen, T. W.; Tanigaki, K. *Adv. Mater.* **1995**, *7*, 275-276.

[166] Rinzler, A. G.; Liu, J.; Dai, H.; Nikolaev, P.; Huffman, C. B.; Rodriguez-Marcias, F. J.; Boul, P. J.; Lu, A. H.; Heymann, D.; Colbert, D. T.; Lee, R. S.; Fischer, J. E.; Rao, A. M.; Eklund, P. C.; Smalley, R. E. *Appl. Phys. A: Mat. Sci Process.* **1998**, *67*, 29-37.

[167] Nakada, K.; Fujita, M.; Dresselhaus, G.; Dresselhaus, M. S. *Phys. Rev. B* **1996**, *54*, 17954-17961.

[168] Berger, C.; Song, Z.; Li, X.; Wu, X.; Brown, N.; Naud, C.; Mayou, D.; Li, T.; Hass, J.; Marchenkov, A. N.; Conrad, E. H.; First, P. N.; de Heer W. A. *Science* **2006**, *313*, 1191-1196.

[169] Giem, A. K.; Novoselov, K. S. *Nat. Mater.* **2007**, *6*, 183-191.

[170] Reina, A.; Thiele, S.; Jia, X.; Ho, J.; Nezich, D.; Son, H.; Bulovic, V.; Dresselhaus, M. S.; Kong, J. *Nano Lett.* **2009**, *9*, 30-35.

[171] Wei, D.; Liu, Y.; Wang, Y.; Zhang, H.; Huang, L.; Yu, G. *Nano Lett.* **2009**, *9*, 1752-1758.

[172] Park, S.; Ruoff, R. S. *Nat. Nano.* **2009**, *4*, 217-224.

[173] Tung, V. C.; Allen, M. J.; Yang, Y.; Kaner, R. B. *Nat. Nano.* **2009**, *4*, 25-29.

[174] Nieuwoudt, A.; Massoud, Y. *IEEE Trans. Elec. Dev.* **2006**, 33, 2460-2466.

[175] Nihei, M.; Kondo, D.; Kawabata, A.; Sato, S.; Shioya, H.; Sakaue, M.; Iwai, T.; Ohfuti, M.; Awano, Y. *Proc. IEEE Int. Interconnect Tech. Conf.* **2005**, 234-236.

[176] Dong, L.; Youkey, S.; Bush, J.; Jiao, J.; Dubin, V. M.; Chebiam, R. V. *J. App. Phys.* **2007**, *101*, 024320.

[177] Frank, S.; Poncharal, P.; Wang, Z. L.; de Heer W. A. *Science* **1998**, *280*, 1744-1746.

[178] Sato, S.; Nihei, M.; Mimura, A.; Kawabata, A.; Kondo, D.; Shioya, H.; Iwai, T.; Mishima, M.; Ohfuti, M.; Awano, Y. *IEEE Int. Interconnect Tech. Conf.* **2006**, 230-232.

[179] Langford, R. M.; Wang, T. –X.; Thronton, M.; Heidelberg, A.; Sheridan, J. G.; Blau, W.; Leahy, R. *J. Vac. Sci. Tech. B* **2006**, *24*, 2306-2311.

[180] Dockendorf, C. P. R.; Steinlin, M.; Poulikakos, D.; Chaoi, T. –Y. *App. Phys. Lett.* **2007**, *90*, 193116.

[181] Tersoff, J. *App. Phys. Lett.* **1999**, *74*, 2122-2124.

[182] Lim, S. C.; Jang, J. H.; Bae, D. J.; Han, G. H.; Lee, S.; Yeo, I. S.; Lee, Y. H. *App. Phys. Lett.* **2009**, *95*, 264103.

[183] Barboza, A. M.; Carara, S. S.; Batista, R. J. C.; Chacham, H.; Neves, B. R. A. *Small* **2012**, *8*, 220-224.

[184] Matsuda, Y.; Deng, W. Q.; Goddard III, W. A. *J. Phys. Chem. C* **2010**, *114*, 17845-17850.

[185] Wang, M. S.; Goldberg, D.; Bando, Y. *Adv. Mater.* **2010**, *22*, 93-98.

[186] Ko, H.; Jiang, C.; Tsukruk, V. V. *Chem. Mater.* **2005**, *17*, 5489-5497.

[187] Gunawidjaja, R.; Jiang, C.; Pelshanko, S.; Ornatska, M.; Singamaneni, S.; Tsukruk, V. V. *Adv. Funct. Mater.* **2006**, *16*, 2024-2034.

[188] Mamedov, A. A.; Kotov, N. A. *Langmuir* **2000**, *16*, 5530-5533.

[189] Podsiadlo, P.; Kaushik, A. K.; Arruda, E. M.; Waas, A. M.; Shim, B.S.; Xu, J.; Nandivada, H.; Pumplin, B. G.; Lahann, J.; Ramamoorthy, A.; Kotov, N. A. *Science* **2007**, *318*, 80-83.

[190] Mamedov, A. A.; Kotov, N. A.; Prato, M.; Guldi, D. M.; Wickstead, J. P.; Hirsh, A. *Nat. Mater.* **2004**, *3*, 721-728.

[191] Coleman, J. N., Khan, U., Blau, W. J., Gun'ko, Y. K. *Carbon* **2006**, *44*, 1624-1652.

[192] Gong, X.; Liu, J.; Baskaran, S.; Voise, R. D.; Young, J. S. *Chem Mater.* **2000**, *12*, 1049-1052.

[193] Haque, A.; Ramasetty, A. *Comp. Struc.* **2005**, *71*, 68-77.

[194] Ko, H.; Jiang, C.; Shulha, H.; Tsukruk, V. V. *Chem. Mater.* **2005**, *17*, 2490-2493.

[195] Aroca, R. F.; Goulet, P. J. G.; dos Santos, D. S.; Alvarez-Puebla, R. A.; Oliveira, O. N. *Anal. Chem.* **2005**, *77*, 378-382.

[196] Kovtyukhova, N. I.; Marin, B. R.; Mbindyo, J. K. N.; Smith, P. A.; Razavi, B.; Mayer, T. S.; Mallouk, T. E. *J. Phys. Chem. B* **2001**, *105*, 8762-8769.

[197] Dai, H. *Science* **2002**, *500*, 218-241.

[198] Javey, A.; Guo, J.; Wang, Q.; Lundstrom, M.; Dai, H. *Nature* **2003**, *424*, 654-657.

[199] Chen, Z.; Appenzeller, J.; Knoch, J.; Lin, Y. M.; Avouris, P. *Nano Lett.* **2005**, *5*, 1497-1502.

[200] Bachtold, A.; Henry, M.; Terrier, C.; Strunk, C.; Schonenberger, C.; Salvetat, J. –P.; Bonard, J. –M.; Forro, L. *Appl. Phys. Lett.* **1998**, *73*, 274-276.

[201] Bussolotti, F.; D'Ortenzi, L.; Grossi, V.; Lozzi, L.; Santucci, S.; Passacantado, M. *Phys. Rev. B* **2007**, *76*, 125415.

[202] Molhave, K.; Madsen, D. N.; Dohn, S.; Boggild, P. *Nanotechnology* **2004**, *15*, 1047-1053.

[203] Chen, H.; Muller, M. B.; Gilmore, K. J.; Wallace, G. G.; Li, D. *Adv. Mater.* **2008**, *20*, 3557-3661.

[204] Chen, C.; Yang, Q.; Yang, Y.; Lv, W.; Wen, Y.; Hou, P.; Wang, M.; Cheng, H. *Adv. Mater.* **2009**, *21*, 3007-3011.

[205] Park, S.; Dikin, D. A.; Nguyen, S. T.; Ruoff, R. S. *J. Phys. Chem.C* **2009**, *113*, 15801-15804.

[206] Dikin, D. A.; Stankovich, S.; Zimney, E. J.; Piner, R. D.; Dommett, G. H. B.; Evmenenko, G.; Nguyen, S. T.; Ruoff, R. S. *Nature* **2007**, *448*, 457-460.

[207] Tsukuk, V. V.; Wendorff, J. H.; Karthaus, O.; Ringsdorf, H. *Langmuir* **1992**, *9*, 614-618.

[208] www.veeco.com.

[209] Tsukruk, V. V. *Rubber Chem. Technol.* **1997**, *70*, 430.

[210] McConney, M. E.; Singamaneni, S.; Tsukruk, V. V. *Poly. Rev.* **2010**, *50*, 235-286.

[211] Tsukruk, V. V.; Singamaneni, S. *Scanning probe microscopy of soft matter: Fundamentals and Practices*, Wiley-VCH, Weinheim, Germany **2012**.

[212] Young, S. L.; Gupta, M.; Hanske, C.; Fery, A.; Scheibel, T.; Tsukruk, V. V. *Biomacromolecules* **2012**, *13*, 3189-3199.

[213] Lei, C. H.; Das, A.; Elliot, M.; Macdonald, J. E. *Nanotechnology* **2004**, *15*, 627-634.

[214] Kuptsov, A. H.; Zhizhin, G.N. *Handbook of Fourier Transform Raman and Infrared spectra of polymers;* Elsevier, **1998**.

[215] Raravikar, N. R.; Keblinski, P.; Rao, A. M.; Dresselhaus, M. S.; Schadler, L. S.; Ajayan, P. M. *Phys. Rev. B.* **2002**, *66*, 235424.

[216] Jiang, C.; Ko, H.; Tsukruk, V. V. *Adv. Mater.* **2005**, *17*, 2127-2131.

[217] Ko, H.; Pikus, Y.; Jiang, C.; Jauss, A.; Hollricher, O.; Tsukruk, V. V. *Appl. Phys. Lett.* **2004**, *85*, 2598-2600.

[218] Wang, Y.; Alsmeyer, D. C.; McCreery, R. L. *Chem. Mater.* **1990**, *2*, 557-563.

[219] Singamaneni, S.; Gupta, M. K.; Yang, R.; Tomczak, M.; Naik, R. R.; Wang, Z. L.; Tsukruk, V. V. *ACS Nano* **2009**, *3*, 2593.

[220] Anderson, K. D.; Slocik, J. M.; McConney, M. E.; Enlow, J. O.; Jakubiak, R.; Bunning, T. J.; Naik, R. R.; Tsukruk, V. V. S*mall* **2009**, *5*, 741-749.

[221] Azzam, R. M. A.; Bashara, N. M. *Ellipsometry and Polarized Light*, Elsevier Science Pub Co, **1987**.

[222] Tompkins H. G.; McGahan, W. A. *Spectroscopic Ellipsometry and Reflectometry*, John Wiley & Sons Inc, **1999**.

[223] Tompkins, H. G.; Irene, E. A. Eds., *Handbook of Ellipsometry* William Andrews Publications, Norwich, NY, **2005**.

[224] Jiang, C.; Markutsya, S.; Pikus, Y.; Tsukruk, V. V. *Nat. Mater.* **2004**, *3*, 721-728.

[225] Mallwitz, F.; Goedel, W. A. *Angew. Chem. Int. Ed*. **2001**, *40*, 2645-2647.

[226] Volynskii, A. L.; Bazhenov, S.; Lebedeva, O. V.; Bakeev, N. F. *J. Mater. Sci.* **2000**, *35*, 547-554.

[227] Stafford, C. M.; Harrison, C.; Beers, K. L.; Karim, A.; Amis, E. J.; Vanlandingham, M. R.; Kim, H. C.; Volksen, W.; Miller, R. D.; Simonyi, E. E. *Nat. Mater.* **2004**, *3*, 545-550.

[228] Jiang, C.; Singamaneni, S.; Merrick, E.; Tsukruk, V. V. *Nano Lett.* **2006**, *6*, 2254-2259.

[229] Zhang, W.; Catherine, Y. *Surf. Coat. Technol.* **1991**, *47*, 69-83.

[230] Rother, B.; Siegel, J.; Breuer, K.; Muhling, I.; Deutschmann, S.; Vetter, J.; Trommer, G.; Rau, B.; Heiser, C. *J. Mater. Res.* **1991**, *6*, 101-111.

[231] Voevdin, A. A.; Donley, M. S. *Surf. Coat. Tech.* **1996**, *82*, 199-213.

[232] Onoprienko, A. A.; Yanchuk, I. B. *Powder Metallurgy and Metal Ceramics* **2006**, *45*, 190-195.

[233] Robertson, J. *J. Mater. Sci. Eng. R.* **2002**, *37*, 129-281.

[234] Rossi, F.; Andre, B.; Veen, A. V.; Mijnarends, P. E.; Schut, H.; Delplanke, M. P.; Gissler, W.; Haupt, J.; Lucazeau, G.; Abello, L. *J. Appl. Phys.* **1994**, *75*, 3121-3129.

[235] Urso, L. D.; Compagnini, G.; Puglisi, O. *Carbon* **2006**, *44*, 2096-2098.

[236] Chu, P. K.; Li, L. *Mater. Chem. Phys.* **2006**, *96*, 253-277.

[237] Schwan, J.; Ulrich, S.; Batori, V.; Ehrardt, H.; Silva, S. R. P. *J. Appl. Phys.* **1996**, *80*, 440- 447.

[238] Reinke, P.; Oelhafen, P. *J. App. Phys.* **1997**, *81*, 2396-2399.

[239] Nemanich, R. J.; Solin, S.A. *Phys. Rev. B* **1981**, *20*, 392-401.

[240] Ferrari, A. C.; Robertson, J.; *Phys. Rev. B* **2000,** *61*, 14 095-14 107.

[241] Tuinstra, F.; Koenig, J. L. *J. Chem. Phys.* **1970**, *53*, 1126-1130.

[242] Ferrari, A. C.; Robertson, J. *Phil. Trans. R. Soc. Lond. A* **2004**, *362*, 2477-2512.

[243] Kelly, B.T. *Physics of Graphite*; Applied Science Publishers: London, **1993**.

[244] Koidl, P.; Wagner, C.; Dischler, B.; Wagner, J.; Ramsteiner, M. *Mater. Sci. Forum* **1990**, *52*, 41.

[245] Hart, R. K.; Kassner, T. F.; Maurin, J. K. *Philos. Mag.* **1970**, *21*, 453-467.

[246] Onodera A.; Yasushi I.; Higashim K.; Umemura J.; Takenaka T.; *J. Appl. Phys.* **1991**, *69*, 043512-1.

[247] Mounier, E.; Bertin, F.; Adamik, M.; Pauleau, Y.; Barna, P. B.; *Diam. Relat. Mater.* **1996**, *5*, 1509-1515.

[248] Cho. N. H.; Veirs, D. K.; Ager J. W.; Rubin, M. D.; Hopper, C. B.; Bogy, D. B. *J. Appl. Phys.* **1992**, *71*, 2243-2248.

[249] Jiu J. T.; Wang, H.; Cao, C.-B.; Zhu, H. S. *J. Mater. Sci.* **1999**, *34*, 5205-5209.

[250] Takabayashi, S.; Okamoto, K.; Sakaue, H.; Takahagi, T.; Shimada, K.; Nakatani, T. *J. Appl. Phys.* **2008**, *104*, 043512.

[251] Walters, J. K.; Fox, D. M.; Burke, T. M.; Weedon, O. D.; Newport, R. J.; Howells, W. S. *J. Chem. Phys.* **1994**, *101*, 4288-4300.

[252] Osswald, S.; Yushin, G.; Mochalin, V.; Kucheyev, S. O.; Gogotsi, Y. *J. Am. Chem. Soc*. **2006**, *128*, 11635-11642.

[253] Singamaneni, S.; Gupta, M. K.; Yang, R.; Tomczak, M.; Naik, R. R.; Wang, Z. L.; Tsukruk, V. V. *ACS Nano* **2009**, *3*, 2593.

[254] Sullivan, J. P.; Friedmann, T. A.; Baca, A. G. *J. Elec. Mater.* **1997**, *26*, 1021-1029.

[255] Buffat. Ph.; Borel, J. -P. *Phys. Rev. A* **1976**, *13*, 2287-2298.

[256] Shi, F. G. *J. Mater. Res.* **1994**, *9*, 1307-1313.

[257] Smith, A. D., *Oxford Dictionary of Biochemistry and Molecular Biology*, Oxford University Press, Oxford, New York **1997**.

[258] Bryant, D. A.; Frigaard, N. U. *Trends Microbio.* **2006**, *14*, 488.

[259] Waldeck, D. H. *Chem. Rev.* **1991**, *91*, 415.

[260] Fouassier, J. P. *Photoinitiation, Photopolymerization, and Photocuring: Fundamentals and Applications*, Hanser Publishers, Cincinnati **1995**.

[261] Berkowitz J. *Photoabsorption, Photoionization, and Photoelectron Spectroscopy*, Academic Press, New York **1979**.

[262] Ryvkin S. M. *Photoelectric Effects in Semiconductors*, Consultants Bureau, New York **1964**.

[263] Fisher, W. M.; Rand, S. C. *J. App. Phys.* **2011**, *109*, 064903.

[264] Rosencwaig, A. *Photoacoustics and Photoacoustic Spectroscopy*, Wiley, New York **1980**.

[265] Almond, D. P.; Patel, P. M. *Photothermal Science and Techniques*, Chapman & Hall, London **1996**.

[266] Jain, P. K.; Huang, X.; El-Sayed, I. H.; El-Sayed, M. A. *Acc. Chem. Res.* **2008**, *41*, 1578.

[267] Elghain, R.; Storhoff, J. J.; Mucic, R. C.; Letsinger, R. L.; Mirkin, C. A. *Science* **1997**, *277*, 1078.

[268] Haes, A. J.; Van Duyne, R. P. *J. Am. Chem. Soc.* **2002**, *124*, 10596.

[269] Hirsch, L. R.; Stafford, R. J.; Bankson, J. A.; Sershen, S. R.; Rivera, B.; Price, R. E.; Hazle, J. D.; Halas, N. J.; West, J. L. *Proc. Natl. Acad. Sci. U.S.A.* **2003**, *100*, 13549.

[270] Sidorenko, A.; Houphouet-Boigny, C.; Villavicencio, O.; Hashemzadeh, M.; McGrath, D. V.; Tsukruk V. V. *Langmuir*, **2000**, *16*, 10569.

[271] Cao L.; Barsic, D. N.; Guichard, A. R.; Brongersma, M. L. *Nano Lett.* **2007**, *7*, 3523.

[272] Nitzan, A., Brus, L. E. *J. Chem. Phys*. **1981**, *75*, 2205.

[273] Stamplecoskie, K. G.; Pacioni, N. L.; Larson, D., Scaiano, J. C. *J. Am. Chem. Soc.* **2011**, *133*, 9160.

[274] Jain, P. K.; El-Sayed, I. H.; El-Sayed, M. A. *Nano Today* **2007**, *2*, 18.

[275] Hu, M.; Chen, J.; Li, Z.; Au, L.; Hartland, G. V.; Li, X.; Marquez, M.; Xia, Y.; *Chem. Soc. Rev.* **2006**, *35*, 1084.

[276] Wei, Z.; Wang, D., Kim, S.; Kim, S. Y.; Hu, Y.; Yakes, M. K.; Laracuente, A. R.; Dai, Z.; Marder, S. R.; Berger, C.; King, W. P.; de Heer, W. A.; Sheehan, P. E.; Riedo, E. *Science* **2010**, *328*, 1373.

[277] Ajayan, P. M.; Terrones, M.; de la Guardia, A.; Huc, V.; Grobert, N.; Wei, B. Q., Lezec, H.; Ramanath, G.; Ebbesen, T. W. *Science* **2002**, *296*, 705.

[278] Osswald, S.; Behler, K.; Gogotsi, Y. *J. App. Phys*. **2008**, *104*, 074308.

[279] El-Sayed, M. A., *Acc. Chem. Res*. **2001**, *34*, 257.

[280] Rontzsch, L.; Heinig, K. H.; Schuller, J. A.; Brongersma, M. L. *Appl. Phys. Lett.* **2007**, *90*, 044105.

[281] Govorov, A. O.; Zhang, W.; Skeini, T.; Richardson, H.; Lee, J.; Kotov N. A. *Nanoscale Res. Lett.* **2006**, *1*, 84.

[282] Soares, B. F.; Johnson F.; Zheludev, N. I. *Phys. Rev. Lett*. **2007**, *98*, 153905.

[283] Sheller, N. B.; Petrash, S.; Foster, M. D.; Tsukruk, V. V. *Langmuir* **1998**, *14*, 4535.

[284] Nemanich, R. J.; Solin, S. A. *Phys. Rev. B* **1979**, *20*, 392.

[285] Kulkarni, D. D.; Rykaczewski, K.; Singamaneni, S.; Kim, S.; Fedorov, A. G.; Tsukruk, V. V. *ACS Appl. Mater. Inter.* **2011**, *3*, 710-720.

[286] Sennett, R. S., Scott, G. D. *J. Opt. Soc. Am.* **1950**, *40*, 203.

[287] Kreibig, U.; Vollmer, M. *Optical Properties of Metal Clusters*, Springer, Berlin **1995**.

[288] Jain, P. K.; El-Sayed, M. A. *Chem. Phy. Lett.* **2010**, *487*, 153.

[289] Maaroof, A. I.; Cortie, M. B.; Smith, G. B. *J. Opt. A: Pure Appl.* **2005**, *7*, 303.

[290] Dixon, M. C.; Daniel, T. A.; Hieda, M.; Smilgies, D. M.; Chan, M. H. W.; Allara, D. L. *Langmuir* **2007**, *23*, 2414.

[291] Liedberg, B., Nylander, C.; Lundstrom, I. *Sens. Act.* **1983**, *4*, 299.

[292] Ko, H. H.; Singamaneni, S.; Tsukruk, V. V. *Small* **2008**, *4*, 1576.

[293] Jain, P. K.; Huang, X.; El-Sayed, I. H.; El-Sayed, M. A. *Plasmonics* **2007**, *2*, 107.

[294] Govorov, A. O.; Richardson, H. H. *Nano Today* **2007**, *2*, 30.

[295] Richardson, H. H.; Carlson, M. T.; Tandler, P. J.; Hernandez, P.; Govorov, A. O. *Nano Lett.* **2009**, *9*, 1139.

[296] Baffou, G.; Quidant, R.; Girard, C. *App. Phys. Lett.* **2009**, *94*, 153109.

[297] Kamat, P. V.; Flumiani, M.; Hartland, G. V. *J. Phys. Chem. B* **1998**, *102*, 3123.

[298] Takami, A.; Kurita, H.; Koda, S. *J. Phys. Chem. B* **1999**, *103*, 1226.

[299] Stietz, F. *Appl. Phys. A: Mater. Sci. Process.* **2001**, *72*, 381.

[300] Tarasenko, N. V.; Butsen, A. V.; Nevar, E. A. *Appl. Surf. Sci.* **2005**, *247*, 410.

[301] Poly (4-vinyl phenol); Available from Sigma-Aldrich database. http://www.sigmaaldrich.com/catalog/ProductDetail.do?D7=0&N5=SEARCH_CONCAT_PNO|BRAND_KEY&N4=436224|ALDRICH&N25=0&QS=ON&F=SPEC.

[302] Russell, A. M.; Lee, K. L. *Structure- Property Relations in Nonferrous Metals*, John Wiley & Sons Inc., Hoboken, New Jersey **2005**.

[303] Gmelin, E.; Fischer, R.; Stitzinger, R. *Thermochimica Acta* **1998**, *310*, 1-17.

[304] Shi, L.; Majumdar, A. *Microscale Thermophysical Engineering* **2001**, 5, 251-265.

[305] Menczel, J. D.; Prime, R. B. *Thermal Analysis of Polymers*. John Wiley & Sons, Inc.: **2008**.

[306] Gorbunov, V. V.; Fuchigami, N.; Hazel, J. L.; Tsukruk, V. V. *Langmuir* **1999**, *15*, 8340-8343.

[307] Tsukruk, V. V.; Gorbunov, V. V.; Fuchigami, N. *Thermochimica Acta* **2002**, *395*, 151-158.

[308] Majumdar, A.; Carrejo, J. P.; Lai, J. *Applied Physics Letters* **1993**, *62*, 2501-2503.

[309] Shi, L.; Kwon, O.; Miner, A. C.; Majumdar, A. *J. Microelectromechanical Sys.* **2001**, *10*, 370-378.

[310] Shi, L.; Majumdar, A. *J. Heat Trans.* **2002**, *124*, 329-337.

[311] Pollock, H. M.; Hammiche, A.; Song, M.; Hourston, D. J.; Reading, M. *J. Adhesion* **1998**, *67*, 217-234.

[312] Patrick, C. F.; Byeonghee, L.; William, P. K. *Nanotechnology* **2012**, *23*, 035401.

[313] Pylkki, R. J.; Moyer, P. J.; West, P. E. *Jap. J. Appl. Phys.* **1994**, *33*, 3785-3790.

[314] Nakabeppu, O.; Chandrachood, M.; Wu, Y.; Lai, J.; Majumdar, A. *Appl. Phys. Lett.* **1995,** *66*, 694-696.

[315] Singamaneni, S.; LeMieux, M. C.; Lang, H. P.; Gerber, C.; Lam, Y.; Zauscher, S.; Datskos, P. G.; Lavrik, N. V.; Jiang, H.; Naik, R. R.; Bunning, T. J.; Tsukruk, V. V. *Adv. Mater.* **2008**, *20*, 653-680.

[316] Williams, C. C.; Wickramasinghe, H. K. *Appl. Phys. Lett.* **1986**, *49*, 1587-1589.

[317] Majumdar, A. *Ann. Rev. Mater. Sci.* **1999**, *29*, 505-585.

[318] Pollock, H. M.; Hammiche, A. *J. Phys. D: Appl. Phys.* **2001**, *34*, R23.

[319] Hammiche, A.; Polloch, H. M.; Song, M.; Hourston, D. J. *Measurement Science and Technology* **1996**, *7*, 142.

[320] Reading, M. *Trends in Poly. Sci.* **1993**, *1*, 248-253.

[321] Hinz, M.; Marti, O.; Gotsmann, B.; Lantz, M. A.; Durig, U. *Appl. Phys. Lett.* **2008**, *92*, 043122-3.

[322] Hazel, J. L.; Tsukruk, V. V. *J. Tribology* **1998**, *120*, 814-819.

[323] Lin, Y. H.; McConney, M. E.; LeMieux, M. C.; Peleshanko, S.; Jiang, C.; Singamaneni, S.; Tsukruk, V. V. *Adv. Mater.* **2006**, *18*, 1157-1161.

[324] LeMieux, M. C.; McConney, M. E.; Lin, Y. H.; Singamaneni, S.; Jiang, H.; Bunning, T. J.; Tsukruk, V. V. *Nano Lett.* **2006**, *6*, 730-734.

[325] Singamaneni, S.; Le Mieux, M. C.; Jiang, H.; Bunning, T. J.; Tsukruk, V. V. *Chem. Mater.* **2007**, *19*, 129-131

[326] Singamaneni, S.; McConney, M. E.; LeMieux, M. C.; Jiang, H.; Enlow, J. O.; Bunning, T. J.; Naik, R. R.; Tsukruk, V. V. *Adv. Mater.* **2007**, *19*, 4248-4255.

[327] He, H.; Riedl, T.; Lerf, A.; Klinowski, J. *J. Phys. Chem.* **1996**, *100*, 19954-19958.

[328] He, H.; Klinowski, J.; Forster, M.; Lerf, A. *Chem. Phys. Lett.* **1998**, *287*, 53-56.

[329] Lerf, A.; He, H.; Forster, M.; Klinowski, J. *J. Phys. Chem. B* **1998**, *102*, 4477-4482.

[330] Dimiev, A.; Kosynkin, D. V.; Alemany, L. B.; Chaguine, P.; Tour, J. M. *J. Amer. Chem. Soc.* **2010**, *39*, 228-240.

[331] Gomez-Navarro, C.; Weitz, R. T.; Bittner, A. M.; Scolari, M.; Mews, A.; Burghard, M.; Kern, K. *Nano Lett.* **2007**, *7*, 3499-3503.

[332] Bachtold, A.; Fuhrer, M. S.; Plyasunov, S.; Forero, M.; Anderson, E. H.; Zettl, A.; McEuen, P. L. *Phys. Rev. Lett.* **2000**, *84*, 6082.

[333] Gomez-Navarro, C.; Moreno-Herrero, F.; de Pablo, P. J.; Colchero, J.; Gomez-Herrero, J.; Baro, A. M. *Proc. Natl. Acad. Sci. USA* **2002**, *99*, 8484.

[334] Jesperson, T. S.; Nygard, J. *Nano Lett.* **2005**, *5*, 1838-1841.

[335] Zaniewski, A. M.; Loster, M.; Sadtler, B.; Alivisatos, A. P.; Zettl, A. *Phys. Rev. B* **2010**, *82*, 155311.

[336] Paillet, M.; Poncharal, P.; Zahab, A. *Phys. Rev. Lett.* **2005**, *94*, 186801.

[337] Mohn, F.; Gross, L.; Moll, N.; Meyer, G. *Nat. Nano.* **2012**, *7*, 227-231.

[338] Moser, J.; Verdaguer, A.; Jimenez, D.; Barreiro, A.; Bachtold, A. *App. Phys. Lett.* **2008**, *92*, 123507.

[339] Burnett. T.; Yakimova, R.; Kazakova, O. *Nano Lett.* **2011**, *11*, 2324-2328.

[340] Zhao, S.; Lv, Y.; Yang, X. *Nanoscale Res. Lett.* **2011**, *6*, 1-6.

[341] Shi, Y.; Dong, X.; Chen, P.; Wang, J.; Li, L.-J. *Phys. Rev. B.* **2009**, *79*, 115402.

[342] Datta. S. S.; Strachan, D. R.; Mele, E. J.; Charlie Johnson, A. T. *Nano Lett.* **2009**, *9*, 7-11.

[343] Lu, Y.; Munoz, M.; Steplecaru, C. S.; Hao, C.; Bai, M.; Garcia, N.; Schindler, K.; Esquinazi, P. *Phys. Rev. Lett.* **2005**, *97*, 076805.

[344] Ekiz, O. O.; Urel, M.; Guner, H.; Mizrak, A. K.; Dana, A. *ACS Nano* **2010**, *5*, 2475-2482.

[345] Gomez-Navarro, C.; Guzman-Vazquez, F. J.; Gomez-Herrero, J.; Saenz, J. J.; Sacha, G. M. *Nanoscale* **2012**, *4*, 7231-7236.

[346] Jaafar, M.; Polin, G.L.; Gomez-Navarro, C.; Gomez-Navarro, J. *Appl. Phys. Lett.* **2012**, *101*, 263109.

[347] Moon, I. K.; Lee, J.; Ruoff, R. S.; Lee, H. *Nat. Comm.* **2010**, *1*, 1-6

[348] Cassie, A. B. D.; Baxter, S. *Trans. Faraday Soc.* **1944**, *40*, 546-551.

[349] Wang, S.; Zhang, Y.; Abidi, N.; Cabrales, L. *Langmuir* **2008**, *25*, 11078-11081.

[350] Ferrari, A. C.; Meyer, J. C.; Scardaci, V.; Casiraghi, C.; Lazzeri, M.; Mauri, F.; Piscanec, S.; Jiang, D.; Novoselov, K. S.; Roth, S.; Geim, A. K. *Phys. Rev. Lett.* **2006**, *97*, 187401.

[351] Yang, D.; Velamakanni, A.; Bozoklu, G.; Park, S.; Stoller, M.; Piner, R. D.; Stankovich, S.; Jung, I.; Field, D. A.; Ventrice Jr., C. A.; Ruoff, R. S. *Carbon* **2009**, *47*, 145-152.

[352] Li, D.; Muller, M. B.; Gilje, S.; Kaner, R. B.; Wallace, G. G. *Nat. Nano.* **2008**, *3*, 101-105.

[353] Domansky, S.; Leng, Y.; Williams, C. C.; Janata, J.; Petelenz, *Appl. Phys. Lett.* **1993**, *63*, 1513-1515.

[354] Zhao, M.; Gu, X.; Lowther, S. E.; Park, C.; Jean, Y. C; Nguyen, T. *Nanotechnology* **2010**, *21*, 225702.

[355] Fasolino, A.; Los, J. H.; Katsnelson, M. I. *Nat. Mater.* **2007**, *6*, 858-861.

[356] Joung, D.; Chunder, A.; Zhai, L.; Kondaker, S. I. *Appl. Phys. Lett.* **2010**, *97*, 093105.

[357] Hu, J.; Xiao, X.; Salmeron, M. *Appl. Phys. Lett.* **1995**, *67*, 476-478.

[358] Rao, C. N. R.; Sood, A. K.; Subramanyam, K. S.; Govindraj, A. *Angew. Chem. Int. Ed.* **2009**, *28*, 7752-7777.

[359] Novoselov, K. S.; Jiang, D.; Schedin, F.; Booth, T. J.; Khotkevich, V. V.; Morozov, S. V.; Giem, A. K. *Proc. Natl. Acad. Sci. U.S.A. 2***005**, *102*, 10451-10453.

[360] Bunch, J. S; Zande, V.; Verbridge, S. S.; Frank, I. W.; Tanebaum, D. M.; Parpia, J. M.; Craighead, H. G.; McEuen, P. L. *Science* **2007**, *315*, 490-493.

[361] Park, S.; An, J.; Suk, J. W.; Ruoff, R. S. *Small* **2009**, *6*, 210-222.

[362] Schedin, F.; Giem, A. K.; Morozov, S. V.; Hill, E. W.; Blake, P.; Katsnelson, M. I.; Novoselov, K. S. *Nat. Mater.* **2007**, *6*, 652-655.

[363] Stankovich, S.; Dikin, D. A.; Dommett, G. H. B.; Kohlhass, K. M.; Zimney, E. J.; Stach, E.A; Piner, R. D.; Nguyen, S. T.; Ruoff, R. S. *Nat. Nano.* **2009**, *4*, 217-224.

[364] Lutkenhaus, J. L.; Hrabak, K. D.; McEnnis K.; Hammond, P. T. *J. Am. Chem. Soc.* **2005**, *127*, 17228-17234.

[365] Tang, Z.; Kotov, N. A.; Magonov, S.; Ozturk, B. *Nat. Mater.* **2003**, *2*, 413-148.

[366] Kharlampieva, E.; Kozlovskaya, V.; Gunawidjaja, R.; Shevchenko, V.; Vaia, R.; Naik, R.; Kaplan, D.; Tsukruk, V. V. *Adv. Funct. Mater.* **2010**, *20*, 840-846.

[367] Shim, B.S.; Zhu, J.; Jan, E.; Critchley, K.; Ho, S.; Podsiadlo, P.; Sun, K.; Kotov, N.A. *ACS Nano* **2009**, *3*, 1711-1722.

[368] Cote, L. J.; Kim, F.; Huang, J. *J. Am. Chem. Soc.* **2009**, *131*, 1043-1049.

[369] Medhekar N. V.; Ramasubramaniam, A.; Ruoff, R. S.; Shenoy, V. B. *ACS Nano* **2010**, *4*, 2300-2306.

[370] Nakajima, T.; Mabuchi, A.; Hagiwara, R. *Carbon* **1988**, *26*, 357-361.

[371] Jiang, C. Y.; Tsukruk, V. V. *Adv. Mater.* **2006**, *18*, 829-840.

[372] Jiang, C. Y.; Tsukruk, V. V. *Soft Matter*, **2005**, *1*, 334-337.

[373] Jiang, C. Y.; Markutsya, S.; Tsukruk, V. V. *Adv. Mater.* **2004**, *16*, 157-161.

[374] Markutsya, S.; Jiang, C.; Pikus, Y.; Tsukruk, V. V. *Adv. Funct. Mater.* **2005**, *15*, 771-780.

[375] Jiang, C.; Markutsya, S.; Shulha, H.; Tsukruk, V. V. *Adv. Mater.* **2005**, *17*, 1669-1673.

[376] Xu. Y.; Hong, W.; Bai, H.; Li, C.; Shi, G. *Carbon* **2009**, *47*, 3538-3543.

[377] Agarwal, D. D.; Broutman, L. J. *Analysis and Performance of Fiber Composites*, 2nd ed., Wiley: New York, **1990**.

[378] Gomez-Navarro, C.; Burghard, M.; Kern, K. *Nano Lett.* **2008**, *8*, 2045.

[379] Kovtyukhova, N. I.; Ollivier, P. J.; Martin, B. R.; Mallouk, T. E.; Chizhik, S. A.; Buzaneva, E. V.; Gorchinskiy, A. D. *Chem. Mater.* **1999**, *11*, 771-778.

[380] Zhao, X.; Zhang, Q.; Chen, D. *Macromolecules* **2010**, *43*, 2357-2363.

[381] Shen, J.; Hu, Y.; Li, C.; Qin, C.; Shi, M.; Ye, M. *Langmuir* **2009**, *25*, 6122-6128.

[382] Kim, H.; Macosko, C. W. *Macromolecules* **2008**, *41*, 3317-3327.

[383] Kim, S. K.; Kulkarni, D. D.; Rykaczewski, K.; Henry, M.; Tsukruk, V. V.; Fedorov, A. G. *IEEE Trans. Nano*. **2012**, *11*, 1223-1230.

VITA

DHAVAL D. KULKARNI

Dhaval Kulkarni was born in Thane in Maharashtra, India on March 26, 1987 to Deepak and Jyoti Kulkarni. He attended Saraswati Education Society's High School and Junior college from 1st grade to 12th grade. He got a Bachelor degree in Chemical Technology and Engineering, with specialization in Fibres and Textile Processing from University Institute of Chemical Technology (UICT), Mumbai, India in 2008. He pursued a Ph.D. in Materials Science and Engineering at Georgia Institute of Technology with Prof. Vladimir V. Tsukruk. After graduating, Dhaval will begin as a Process Engineer at the Intel Corporation facility in Portland, Oregon.